Ligand isotope vibrational spectroscopic and

DFT studies of Pt(II) and Cu(I) complexes

A thesis submitted to
Rhodes University
in fulfilment of the requirements for the degree of
Doctor of Philosophy

by

Gerardo Juan Medina

Rhodes University
Grahamstown, South Africa
2004

ABSTRACT

Ligand-isotope labelling studies were performed on Zeise's salt derivatives with pyridine *N*-oxide and quinoline *N*-oxide, their perdeuterated and O-18 isotopomers, C_2D_4 and ^{13}CO, and the results of the vibrational analyses are reported. The isotopomers are modelled utilizing DFT calculations at the B3LYP level with the 6-31 G** basis set, and a pseudopotential level for the Pt atom. The calculated and observed structure and vibrational spectra correlate well. The crystal structures of $[Pt(C_2H_4)(pyO)Cl_2]$ and $[Pt(CO)(quinO)Br_2]$ are reported.

The frequency for the νPt-O vibration, ambiguously assigned in the literature, is here assigned unequivocally at 400 cm^{-1}. Previously observed, but inadequately described phenomena are addressed: the νN-O vibration in substituted quinoline *N*-oxides has been assigned previously at significantly different frequencies, depending on the nature of the substituent. This suggests that there is no specific mid-ir band associated with a high N-O character. A suitable explanation is presented for this phenomenon, showing that in low symmetry systems (*eg*. quinO) the N-O stretch is dispersed among several modes, whereas in high symmetry systems (*eg*. pyO) only a few limited modes have a high N-O character.

A theoretical study of Cu(I) carbonyl compounds with macrocyclic ligands is presented. Local and global HSAB parameters applied to the donor and Cu atoms are used to explain the observed reactivities and the available spectroscopic data. Extended to $[Cu(CO)\{H_2N(CH_2)_nNH(CH_2)_m NH_2\}]BPh_4$ (where n = 2, m = 2, 3 and n =3, m = 3, 4) and their -d_5 and ^{13}CO isotopomers, subtle differences obtained experimentally for the CO stretching frequency in this series have been reproduced in the DFT calculations at the B3LYP level, using the 6-31 G* and 6-31 G** basis sets. Several properties (ligand pK_a values, νCO frequencies, *etc*.) correlate with some HSAB descriptors.

Vibrational analyses are presented of Cu(I) carbonyl Schiff-base derivatives of *N*-Benzylidene-*N'*-[2-(benzyilidene-amino)-ethyl]-ethane-1,2-diamine, $\{2,2N3(C_6H_4R)_2\}$, and their -d_5 and ^{13}CO isotopomers. The crystal structure of $[Cu(CO)\{2,2N3(C_6H_5)_2\}]BPh_4$ is reported. From geometry optimizations and the HSAB descriptors, spectroscopic trends (νCu-N and νCO) are related to calculated global hardness and the Hammett substituent parameters, and are discussed in terms of σ-donation and π-backbonding of Cu- CO.

Acknowledgements

I am particularly thankful to Edith Antunes, Linda Jacobs and Emmanuel Lamprecht for all their help and support. Edith's help and patience recording the nmr spectra for the Zeise's salt derivatives, especially the labelled species, proved invaluable in the elaboration of this work. Special thanks to Linda for her help with the calculations and to Emmanuel for his assistance and aid during the long runs involving the discharge tube, as well as his assistance with all computer-related difficulties.

Special thanks go to Professor S.O. Paul at UNISA for running the Raman spectra of the Zeise's salt derivatives.

Thanks to Mr. A.W. Sonemann and Mr. A. Adriaan for their help in the construction and proper performance of the discharge tube.

Thanks to my supervisor Dr. G. M. Watkins.

I am particularly grateful to CONACYT in Mexico for the bursary awarded to pursue my PhD studies.

Thanks to staff and friends at Rhodes University.

Abbreviations

ν	=	stretch
α	=	in-plane bend (of heterocyclic ring).
γ	=	out-of-plane bend (of heterocyclic ring).
δ	=	inplane bend (of aliphatic ligand or metal complex).
π	=	out-of-plane bend (of aliphatic ligand or metal complex).
τ	=	twist or torsion.
ω	=	wag.
ρ	=	rock.
B3LYP	=	Becke's method in DFT using Lee-Yang-Parr's gradient-corrected exchange-correlation density functionals.
CSD	=	Cambridge Structural Database, maintained by the Cambridge Crystallographic Data Centre.
DFT	=	Density Functional Theory.
HSAB	=	Hard and Soft Acid and Base Theory.
ir	=	infrared.
6-31 G**	=	a fully flexible split valence basis set with polarisation d function applied to heavy atoms and polarisation p function applied to hydrogen atoms.
6-31 + G*	=	a fully flexible split valence basis set with polarisation d function applied to heavy atoms, and diffuse p function applied to heavy atoms.
6-31 + G**	=	a fully flexible split valence basis set with polarisation d function applied to heavy atoms, polarisation p function applied to hydrogen atoms and diffuse p function applied to heavy atoms.

Index

1. Introduction

The use of density functional theory (DFT) calculations has become increasingly important in recent years. The correct prediction of many of the observables for chemical systems has encouraged ongoing research in different areas to ascertain the reliability of the calculation methods with surprisingly good results. The present work is focused mainly on the vibrational analyses for Pt(II) and Cu(I) compounds, where the use of DFT calculations has proven an invaluable tool in the study of Zeise's salt derivatives and Cu(I) triamine carbonyl systems.

A brief introduction with an overview of DFT and HSAB descriptors obtained from DFT opens the present work. The remaining text is divided into three parts.

The first deals with the vibrational analyses of the *N*-oxide ligands employed in the syntheses of Zeise's salt derivatives, *viz*. pyridine *N*-oxide and quinoline *N*-oxide and their isotopomers, and concludes with the vibrational analyses of Zeise's salt derivatives of the aforementioned *N*-oxide ligands. In both sections mentioned, DFT calculations and vibrational analyses have been employed in order to perform the assignments for the various isotopomers modelled and prepared. The major aim in this part of the project was to establish the frequency for the νPt-O vibration, which has been ambiguously assigned in the literature. However, in the process of the elaboration of this point, several interesting features arose that have shed some light on phenomena that had been previously observed, but poorly described. Such is the case for the N-O stretching frequency in the low symmetry quinoline *N*-oxide ligand, for which there appears to be no specific band in the mid-ir spectra that can be associated to a high character N-O stretching vibration. More so, N-O stretching vibrations were previously assigned at significantly different frequency values depending on the presence of electron-withdrawing or electron-releasing substituents in substituted quinoline *N*-oxide systems. A suitable explanation for this phenomenon has been explored in this work. It will be shown that with low symmetry systems, a vibration like the N-O stretch is shared among several modes, whereas a high symmetry system like pyO will have a high character νN-O vibration which can only occur in a few limited modes of a particular symmetry. A final comment to the first part of this work that deals with Zeise's salt derivatives regards the employment of calculations at a pseudopotential level for the Pt(II) atom. Excellent results have been obtained in the comparison of the calculated and observed structure and vibrational spectra of these compounds and their isotopomers.

The second part deals with Cu(I) carbonyl compounds. The first section is a theoretical study for Cu(I) carbonyl compounds with macrocyclic ligands with a particular interest in associating local and global HSAB parameters to the donor and the Cu(I) atoms in an effort to explain the reactivities observed and the spectroscopic data available. The second section deals with triamine systems where subtle differences obtained experimentally for the CO stretching frequency in a series of Cu(I) carbonyl triamine complexes have been reproduced in the calculations. Several properties such as ligand pK_a values and νCO frequencies have been found to correlate with some HSAB descriptors.

Cu(I) carbonyl Schiff base derivatives, prepared and modelled, are also discussed in the second section. Unfortunately, although all compounds prepared were modelled by DFT calculations, geometric optimization failed to converge for these systems, hence the vibrational analyse could not be performed. The computational difficulties associated with systems with a large number of electrons still need to be overcome in order to perform a more thorough study. Nonetheless, the results arrived at from geometry optimizations and HSAB descriptors are satisfactory.

The third and final part of the work describes the relevant synthesis and instrumental procedures.

The present work will hopefully make a contribution, however small, to vibrational spectroscopy in inorganic chemistry, where the use of molecular modelling by means of DFT based methods has proven of excellent accuracy in its prediction of many of the properties of inorganic compounds.

1.1. Molecular modelling: DFT calculations [1]

DFT methods are based on the density-functional theory of Hohenberg, Kohn and Sham, and allow for the theoretical study of material properties [2]. They are called parameter-free methods as they, in principle, require as input only the types and positions of the nuclei in a system. DFT theory proves an advantageous method for predicting chemical systems, and in order to understand its similarities and differences to other computational methods employed, a brief introduction dealing with how the solution to multielectronic systems has been approached follows.

The Schrödinger equation in the static, time-independent case, for a system constituted of M nuclei and N electrons is

$$\hat{H}\Psi(\vec{x}_1,...,\vec{x}_N,\vec{X}_1,...,\vec{X}_M) = E\cdot\Psi(\vec{x}_1,...,\vec{x}_N,\vec{X}_1,...,\vec{X}_M) \quad (1)$$

where

$$\hat{H} = -\sum_{k=1}^{M}\frac{1}{2M_k}\nabla_{\vec{R}_k}^2 - \sum_{i=1}^{N}\frac{1}{2}\nabla_{\vec{r}_i}^2 + \frac{1}{2}\sum_{k\neq l=1}^{M}\frac{Z_k Z_l}{\left|\vec{R}_k-\vec{R}_l\right|} + \frac{1}{2}\sum_{i\neq j=1}^{N}\frac{1}{\left|\vec{r}_i-\vec{r}_j\right|} - \sum_{k=1}^{M}\sum_{i=1}^{N}\frac{Z_k}{\left|\vec{r}_i-\vec{R}_k\right|}, \quad (2)$$

is the Hamiltonian operator for the system.

The equation is given in Hartree atomic units ($m_e = |e| = 4\pi\varepsilon_0 = \hbar \equiv 1$), and $\vec{x}_i$ and $\vec{X}_k$ are the combined position and spin coordinates for the ith electron and kth nucleus, $\vec{r}_i$ and $\vec{R}_k$ are the positions of the ith electron and kth nucleus respectively, and M_k and Z_k are the mass and charge of the kth nucleus. In the above equation, the terms in the Hamiltonian are, from left to right, the kinetic energy for the nuclei, kinetic energy for the electrons, Coulombic interaction between the nuclei, Coulombic interaction between electrons and finally Coulombic interaction between electrons and nuclei.

By means of the Born-Oppenheimer approximation [1], the wavefunction can be factorized into a nuclear and an electronic part. The electronic part depends parametrically on the nuclear coordinates, but functionally on the electronic coordinates. The electronic Schrödinger equation hence becomes

$$\hat{H}_e\Psi_e(\vec{R}_1,...,\vec{R}_M;\vec{x}_1,...,\vec{x}_N) = E_e\cdot\Psi_e(\vec{x}_1,...,\vec{x}_N;\vec{X}_1,...,\vec{X}_M), \quad (3)$$

where the electronic Hamiltonian operator is

$$\hat{H}_e = -\sum_{i=1}^{N}\frac{1}{2}\nabla_{\vec{r}_i}^2 + \frac{1}{2}\sum_{i\neq j=1}^{N}\frac{1}{\left|\vec{r}_i-\vec{r}_j\right|} - \sum_{k=1}^{M}\sum_{i=1}^{N}\frac{Z_k}{\left|\vec{r}_i-\vec{R}_k\right|}. \quad (4)$$

Neglecting the kinetic energy of the nuclei, the total energy for the system can be expressed in terms of the electronic energy and the Coulombic interaction energy between the nuclei:

$$E = E_e + \frac{1}{2}\sum_{k\neq l=1}^{M}\frac{Z_k Z_l}{\left|\vec{R}_k - \vec{R}_l\right|}. \quad (5)$$

1.2. The Hartree-Fock approximation [1-3]

The solution of the multielectronic wave function can only be achieved by means of approximations. One of the most employed approximations is the Hartree-Fock 'self-consistent field' approximation, in which this is achieved by approximating the multielectronic wave function to *N*-one electron wave functions by means of a single Slater determinant Φ_0,

$$\Psi_e\left(\vec{R}_1,...,\vec{R}_M\,;\vec{x}_1,...,\vec{x}_N\right) \approx \Phi_0\left(\vec{x}_1,...,\vec{x}_N\right) = \frac{1}{\sqrt{N!}}\begin{vmatrix} \phi_1(\vec{x}_1) & \phi_2(\vec{x}_1) & \cdots & \phi_N(\vec{x}_1) \\ \phi_1(\vec{x}_2) & \phi_2(\vec{x}_2) & \cdots & \phi_N(\vec{x}_2) \\ \vdots & \vdots & \ddots & \vdots \\ \phi_1(\vec{x}_N) & \phi_2(\vec{x}_N) & \cdots & \phi_N(\vec{x}_N) \end{vmatrix}. \quad (6)$$

The one electron functions $\phi_i(\vec{x}_i)$ are called spin orbitals and they are each composed of a spatial orbital function and one of the two possible spin functions.

The solution of the Slater determinant through the application of the variational principle yields the *N* Hartree-Fock single-particle equations where the ε_k values have the physical interpretation of orbital energies,

$$\hat{F}_k\phi_k = \varepsilon_k\phi_k, \quad (7)$$

with $\hat{F}$, the Fock operator, defined by

$$\hat{F} = -\frac{1}{2}\nabla^2 + \sum_{k=1}^{M}\frac{Z_k}{\left|\vec{r} - \vec{R}_k\right|} + V_{HF}. \quad (8)$$

The first two terms in the Fock operator are the kinetic and potential energy of the electron in the presence of the nuclei and the V_{HF} term is the Hartree-Fock potential composed of the Coulomb operator and the exchange operator,

$$V_{HF} = \sum_{i=1}^{N}\left(\hat{J}_i - \hat{K}_i\right). \quad (9)$$

The Coulomb operator describes the classical Coulomb interaction of electrons and represents the potential that an electron at position $\vec{x}_1$ experiences due to the average charge distribution of another electron in spin orbital ϕ_k. The Coulomb operator is expressed as

$$\sum_{i=1}^{N} \hat{J}_i \phi_k(\vec{x}_1) = \sum_{i=1}^{N} \int \frac{|\phi_i(\vec{x}_2)|^2}{|\vec{r}_2 - \vec{r}_1|} d\vec{x}_2 \phi_k(\vec{x}_1) = V_C(\vec{r}_1)\phi_k(\vec{x}_1). \quad (10)$$

The exchange operator has no classical interpretation. Its effect can be described in terms of operating on a spin orbital, which leads to an exchange of the variables in the two spin orbitals by means of the permutation operator $\hat{P}_{12}$, which interchanges the arguments of the two subsequent functions,

$$\sum_{i=1}^{N} \hat{K}_i \phi_k(\vec{x}_1) = \sum_{i=1}^{N} \int \frac{\phi_i^*(\vec{x}_2)\hat{P}_{12}[\phi_i(\vec{x}_2)\phi_k(\vec{x}_1)]}{|\vec{r}_2 - \vec{r}_1|} d\vec{x}_2 . \quad (11)$$

It is the exchange term that causes the major problems in the solution of the Hartree-Fock equations and several approximations to overcome the computational difficulties have been sought.

The electron density within the HF approximation becomes

$$\rho(\vec{r}) = \sum_{i=1}^{N} |\phi_i(\vec{r})|^2 . \quad (12)$$

The chosen ϕ_i orbitals are those for which the lowest orbital energy values ε_i are obtained.
The solution of the Hartree-Fock equations (7) usually yields more than N orbitals and improved approximate wavefunctions called CI (configuration-interaction) wavefunctions can be constructed as

$$\Psi_e \approx c_0 \Phi_0 + \sum_{i=1}^{N} \sum_{\alpha=N+1}^{P} c_i^{\alpha} \Phi_i^{\alpha} + \sum_{i,j=1}^{N} \sum_{\alpha,\beta=N+1}^{P} c_{i,j}^{\alpha,\beta} \Phi_{i,j}^{\alpha,\beta} + \cdots, \quad (13)$$

$\Phi_{i,j,\cdots}^{\alpha,\beta\cdots}$ is the Slater determinant obtained from Φ_0 but the occupied orbitals ϕ_i, ϕ_j, … are substituted with the unoccupied orbitals ϕ_α, ϕ_β, …, and P is the total number of both occupied and unoccupied orbitals. The coefficients $c_{i,j,\cdots}^{\alpha,\beta,\cdots}$ are then optimized

.

Using this approximation, the electron density of the system hence becomes

$$\rho(\vec{r}) = \sum_{i,j=1}^{P} n_{ij}\phi_i^*(\vec{r})\phi_j(\vec{r}) = \sum_{i=1}^{P} \tilde{n}_i \left|\tilde{\phi}_i(\vec{r})\right|^2 , \quad (14)$$

$\tilde{\phi}_i$ and $\tilde{n}_i$ are the natural orbitals and their occupancies (which lie in the interval [0, 1]). The improvements obtained when equation (6) is replaced by equation (13) are the correlation effects.

The solution of the Hartree-Fock equations is usually performed by expanding the solutions into a finite set of basis functions as shown below, and determining the coefficient c_{pi} while the basis functions χ_p remain fixed,

$$\phi_i(\vec{r}) = \sum_{p=1}^{P} \chi_p(\vec{r}) c_{pi} . \quad (15)$$

The functions usually employed are Slater type orbitals and Gaussian type orbitals, which will be discussed later.

The Hartree-Fock equations are solved iteratively by choosing the initial orbitals and defining the Fock operator. The solution of these equations provides a new set of orbitals and the procedure is repeated until self-consistency is attained.

The main drawback of the HF approximation is the fact that the equations employed are highly complicated and the computational efforts scale as N^4 and up to N^7 for those methods that include correlation effects. Approximations have been introduced due to the fact that the many-particle wavefunction actually includes much more information than is necessary for the calculation of any observable. It is in this aspect that DFT calculations prove to be considerably better in principle, as they are not approximations to the calculation of the exact quantum mechanical problem, but rather are based on an exact theory as will be discussed in the following section.

1.3. Density functional theory [1-3]

Density functional theory contains two fundamental theorems. The first of the Hohenberg and Kohn theorems states that any ground state property is a functional of the electronic density. This is to say that through the knowledge of the electronic density of a ground state system one can construct the Hamiltonian operator for that system.

The second Hohenberg and Kohn theorem states that $E_e[\rho(\vec{r})] \geq E_e[\rho_0(\vec{r})]$. This is to say that if $\rho(\vec{r})$ is an approximation to the exact ground state electronic density $\rho_0(\vec{r})$ of a system, then the energy obtained through this approximation will be greater than the energy associated to the exact ground state electronic density of the system with the equality holding for $\rho(\vec{r}) = \rho_0(\vec{r})$. The aforementioned electronic densities have to obey the following relation

$$\int \rho(\vec{r})d\vec{r} = \int \rho_0(\vec{r})d\vec{r}\,, \quad (16)$$

which is a constraint on the system of interest that must follow that

$$\int \rho(\vec{r})d\vec{r} = N\,, \quad (17)$$

where N is the total number of electrons in the system.

Combining both equations (16) and (17) and using a variational principle for the density functionals, the following relation can be established

$$\frac{\delta}{\delta(\vec{r})}\left\{E_e[\rho] - \mu \cdot \left[\int \rho(\vec{r}')d\vec{r}' - N\right]\right\} = 0\,. \quad (18)$$

This relation, which uses the Lagrange multiplier μ for the constraint established by equation (16), is of extreme importance in DFT and will be further discussed below.

The theorems themselves state the existence of certain relations, but they do not give the forms of these relations. Hence, Hohenberg and Kohn observed that E_e for a given system could be expressed in terms of the electronic density. The model employed is that of non-interacting particles which move in some external effective potential $V_{eff}(\vec{r})$ that would have the same density and energy as the real system. Under this assumption, the energy is expressed as

$$E_e = \sum_{i=1}^{N}\left\langle \psi_i \left| -\frac{1}{2}\nabla^2 \right| \psi_i \right\rangle + \int V_{eff}(\vec{r})\rho(\vec{r})d\vec{r}. \quad (19)$$

In the above equation ψ_i are the orbitals of the model system that has a total density

$$\rho(\vec{r}) = \sum_{i=1}^{N} |\psi_i(\vec{r})|^2 , \quad (20)$$

which equals that of the electrons. The expression obtained for the density is similar to the one arrived at by means of the HF approximation, but an important difference is that equation (20) includes correlation effects, whereas equation (12) does not, and would thus be identical to equation (14) in the limit $P \to \infty$.

The electronic energy for a real system would hence be expressed as

$$E_e = \sum_{i=1}^{N} \left\langle \psi_i \left| -\frac{1}{2}\nabla^2 \right| \psi_i \right\rangle + \frac{1}{2}\iint \frac{\rho(\vec{r}_1)\rho(\vec{r}_2)}{|\vec{r}_1 - \vec{r}_2|} d\vec{r}_1 d\vec{r}_2 + \int V_{ext}(\vec{r})\rho(\vec{r}) d\vec{r} + E_{xc}[\rho]. \quad (21)$$

In the above equation, the first term corresponds to the kinetic energy of the non-interacting particles, followed by the Coulomb energy for the electrons, then the interaction energy with external fields and finally a term that includes all unknown parts of the electronic energy as a functional of the density

.

In the ground state, both the real and the model system have the same density. Hence, equations (19) and (21) can be equated, and lead to an expression for the effective potential

$$V_{eff}(\vec{r}) = V_C(\vec{r}) + V_{ext}(\vec{r}) + V_{xc}(\vec{r}), \quad (22)$$

with the Coulomb potential and exchange-correlation potential defined by

$$V_C(\vec{r}) = \int \frac{\rho'(\vec{r})}{|\vec{r} - \vec{r}'|} d\vec{r}' , \quad (23)$$

$$V_{xc}(\vec{r}) = \frac{\delta}{\delta\rho(\vec{r}')} E_{xc}[\rho]. \quad (24)$$

The particles in the DFT model are non-interacting, and hence the Hartree-Fock approximation is exact and the Hartree-Fock equations that are solved in the so-called density-based methods are simply

$$\hat{h}_{eff}\psi_i(\vec{r}) \equiv \left[-\frac{1}{2}\nabla^2 + V_{eff}(\vec{r}) \right] \psi_i(\vec{r}) = \varepsilon_i \psi_i(\vec{r}). \quad (25)$$

The construction of the model described, allows for the study of non-interacting particles as opposed to the real system of interacting electrons. Although the theory is exact, the lack of knowledge dealing with the true form of $E_{xc}[\rho]$ means that one is left with an exact framework where approximate methods can be developed.

1.4. Descriptors obtained by DFT [1]

An important aspect of DFT is derived from the interpretation of the Lagrange multiplier μ that appears in equation (18). This equation is associated with the constraint $N(\rho') = N(\rho)$ [4]. The multiplier is hence the derivative with respect to the value of the constraint, N, of the minimum of the functional $E_e[\rho]$, *i.e.*,

$$\mu = \left(\frac{\partial E_e}{\partial N} \right)_v , \quad (26)$$

and it is called the electronic chemical potential at a fixed external potential v.

This relation is equivalent to the negative of the electronegativity χ [4], as defined by Iczkowski and Margrave so the following relation can be made,

$$\chi = -\mu = -\left(\frac{\partial E}{\partial N} \right)_v . \quad (27)$$

It is interesting to note that the electronic chemical potential has an important consequence when studying the chemical reactivity of two systems of interest, as it is this difference in chemical potentials that will drive a given reaction between two species.

A finite difference approximation for equation (27) yields the Mulliken electronegativity,

$$\chi_M = \frac{I + A}{2} \approx \chi = -\mu , \quad (28)$$

where I and A are the ionization potential and the electron affinity of the system of interest.

Due to the fact that equalization of the chemical potential between two reacting species is a driving force in the reaction if it is to take place, then the chemical potential of the reacting species will change both in the number of electrons and in the external potential V_{eff}. If only infinitesimal changes in μ are considered, the following relation is established

$$d\mu = \left(\frac{\partial^2 E}{\partial N^2} \right)_{V_{eff}(\vec{r})} dN + \int \left(\frac{\delta \mu}{\delta V_{eff}(\vec{r})} \right)_N \delta V_{eff}(\vec{r}) d\vec{r} . \quad (29)$$

The first term in this relation has been defined as the chemical hardness according to

$$\eta = \frac{1}{2} \left(\frac{\partial \mu}{\partial N} \right)_{V_{eff}(\vec{r})} = \frac{1}{2} \left(\frac{\partial^2 E}{\partial N^2} \right)_{V_{eff}(\vec{r})} \approx \frac{I - A}{2}, \quad (30)$$

the final relation, obtained as a function of the ionization potential and the electron affinity, is arrived at by a finite difference approximation of the differential.

The chemical hardness of a given system is, as can be seen by equation (30), a resistance of the chemical potential to change in its number of electrons [5-11] and is an important factor governing the reactivity of two chemical species as will be discussed below.

The global chemical softness, *S*, is simply defined as the inverse of the chemical hardness η,

$$S = \frac{1}{2\eta} = \left(\frac{\delta N}{\delta \mu} \right)_{V_{eff}(\vec{r})} . \quad (31)$$

The second term in the differential of the chemical potential, equation (29), is related to the Fukui function $f(\vec{r})$, which is defined as

$$f(\vec{r}) \equiv \left(\frac{\delta \mu}{\delta V_{eff}(\vec{r})} \right)_N = \left(\frac{\partial \rho(\vec{r})}{\partial N} \right)_{V_{eff}(\vec{r})} . \quad (32)$$

The Fukui function, unlike the hardness, is a local quantity which has different values at different points [12] and it is indicative of how the electronic density varies at a constant external potential when there is a change in the number of electrons in the system.

However, the density as a function of *N* has slope discontinuities as electrons are added to the LUMO but removed from the HOMO, hence three different reaction indices can be defined, $f^+(\vec{r})$, $f^-(\vec{r})$ and $f^0(\vec{r})$, which are the Fukui functions for nucleophilic attack, for electrophilic attack and for radical attack, respectively. The following relations define these,

$$f^+(\vec{r}) = \left(\frac{\partial \rho(\vec{r})}{\partial N^+} \right)_{V_{eff}(\vec{r})} \approx \rho_{N+1}(\vec{r}) - \rho_N(\vec{r}), \quad (33)$$

$$f^-(\vec{r}) = -\left(\frac{\partial \rho(\vec{r})}{\partial N^-} \right)_{V_{eff}(\vec{r})} \approx \rho_N(\vec{r}) - \rho_{N-1}(\vec{r}), \quad (34)$$

$$f^0(\vec{r}) = \left(\frac{\partial \rho(\vec{r})}{\partial N^0} \right)_{V_{eff}(\vec{r})} \approx \frac{1}{2}\left[\rho_{N+1}(\vec{r}) - \rho_{N-1}(\vec{r}) \right] = \frac{1}{2}\left[f^+(\vec{r}) + f^-(\vec{r}) \right]. \quad (35)$$

The quantities $\rho_{N+1}(\vec{r})$, $\rho_N(\vec{r})$ and $\rho_{N-1}(\vec{r})$ are the electronic densities for the systems with *N + 1*, *N* and *N – 1* electrons, respectively.

Equation (29) can be expressed in terms of the parameters defined above as

$$d\mu = 2\eta dN + \int f(\vec{r})\delta V_{eff}(\vec{r})d\vec{r}\,. \qquad (36)$$

It may be hypothetically assumed that a reagent R will react with a species S. If R *approaches* S, then the direction preferred will be that for which the initial $|d\mu|$ value for S is a maximum [12]. However, the change in chemical potential $d\mu$ stated above, is constituted in the first term by a global quantity, which is less direction sensitive than the second term. Hence, it may be stated that the Fukui function is a good measure of reactivity in a chemical species. Furthermore, the fact that it is a local property allows for its calculation at different sites within a molecule.

If $\mu_S > \mu_R$ (alternatively stated, $\chi_S < \chi_R$), then the species S, an electrophile, will be attacked by the nucleophile R and the electron flow will be from R to S. Reactive sites at S would hence be obtained by means of f^+.

If $\mu_S < \mu_R$ ($\chi_S > \chi_R$), then the species S is a nucleophile that will react with the electrophile R and the electron flow will be from S to R. Reactive sites at S would be measured by means of f^-.

Finally, if $\mu_S \sim \mu_R$ ($\chi_S \sim \chi_R$), then the species R and S will react with each other as radicals and the reactive sites would be obtained by means of f^0.

An alternative and considerably more simple procedure to obtain information about the reactivity sites in a chemical system, is to calculate the condensed Fukui function for the atoms in a given system A with N_A electrons. The electronic density is condensed to the charge of each atom in the molecule and is differentiated with respect to the total number of electrons in the system [13]. For a system A consisting of *K* atoms, the finite differences approximations to the condensed Fukui functions for nucleophilic, electrophilic and radical attack, f_{Ak}^+, f_{Ak}^- and f_{Ak}^0 respectively, yield the following relations,

$$f_{Ak}^+ = q_{Ak}(N_A + 1) - q_{Ak}(N_A), \qquad (37)$$

$$f_{Ak}^{-} = q_{Ak}(N_A) - q_{Ak}(N_A - 1), \qquad (38)$$

$$f_{Ak}^{0} = \frac{1}{2}\left[q_{Ak}(N_A + 1) - q_{Ak}(N_A - 1)\right] = \frac{1}{2}\left[f_{Ak}^{+} + f_{Ak}^{-}\right]. \qquad (39)$$

In these relations, q_{Ak} is the gross electronic population of the *k*th atom in the system A and q_{Ak} (N_A + 1), q_{Ak} (N_A) and q_{Ak} (N_A – 1) are the corresponding values of the *k*th atom in system A with N_A + 1, N_A and N_A – 1 electrons respectively. There exist several ways to obtain the q_{Ak} value, the most common of these is to make use of a Mulliken population analysis.

Although the global properties that characterize a chemical system can explain some of the properties observed for these systems, much more information is obtained through the analysis of local properties. In this respect, the global hardness, η, and softness, S, have been defined. However, a considerable amount of information can be obtained by the study of the local descriptors in a chemical system. The condensed Fukui function allows for the study of these properties, and through it one may construct the condensed local softness which will be discussed, together with the local hardness, below.

It can be assumed that for two reacting species, the interaction that is to take place will consist of electron-donating and electron-accepting for the reacting species. From the global softness, a local softness $s(\vec{r})$ can be defined in terms of the electronic density as

$$s(\vec{r}) = \left(\frac{\delta\rho(\vec{r})}{\delta\mu}\right)_{V_{eff}(\vec{r})}. \qquad (40)$$

A local hardness can be equivalently defined as

$$\eta(\vec{r}) = \frac{1}{N}\int \frac{\delta^2 E}{\delta\rho(\vec{r})\delta\rho(\vec{r}')}\rho(\vec{r}')d\vec{r}'. \qquad (41)$$

The local hardness and local softness are related by

$$\int s(\vec{r})\eta(\vec{r})d\vec{r} = 1. \qquad (42)$$

It is the local softness that is of particular interest as it can easily be expressed in terms of the global softness and the Fukui function, equation (32), through the following relation

$$s(\vec{r}) = \left(\frac{\partial \rho(\vec{r})}{\partial \mu}\right)_{V_{eff}(\vec{r})} = \left(\frac{\partial N}{\partial \mu}\right)_{V_{eff}(\vec{r})} \left(\frac{\partial \rho(\vec{r})}{\partial N}\right)_{V_{eff}(\vec{r})} = Sf(\vec{r}). \quad (43)$$

Condensed and uncondensed local softness values can easily be calculated in terms of the global softness and the condensed and uncondensed Fukui functions respectively. The condensed local softness for nucleophilic, electrophilic and radical attack, s_{Ak}^{+}, s_{Ak}^{-} and s_{Ak}^{0} respectively, are shown below.

$$s_{Ak}^{+} = S_A f_{Ak}^{+}, \quad (44)$$

$$s_{Ak}^{-} = S_A f_{Ak}^{-}, \quad (45)$$

$$s_{Ak}^{0} = S_A f_{Ak}^{0}, \quad (46)$$

where S_A is the global softness of species A and the Fukui function value is calculated for the *k*th atom in species A depending on whether it will react with a nucleophile, an electrophile or a radical. Large values of local softness of the condensed Fukui function are associated with an increased reactivity at those sites.

As a first approximation, interaction energies and the number of electrons transferred from one species to another, ΔN, may be calculated by use of some of the descriptors obtained by DFT. An expansion of the energy in terms of the number of electrons in a system yields [7]

$$E = E^0 + \left(\frac{\partial E}{\partial N}\right)_0 \Delta N + \frac{1}{2}\left(\frac{\partial^2 E}{\partial N^2}\right)_0 (\Delta N)^2 + \cdots . \quad (47)$$

The derivative of the energy with respect to the number of electrons, gives, to the first order, the following relation

$$\mu = \mu^0 + 2\eta^0 \Delta N, \quad (48)$$

in which the zeroeth-order quantities correspond to the neutral atom and ΔN is the number of electrons transferred during bond formation.

As a first approximation, and using the electronegativity equalization principle, it can be assumed that two species A and B with chemical potentials μ_A and μ_B will react with each order in order to yield a species AB with a chemical potential μ_{AB}. Electron transfer will occur from the species with a larger value of chemical potential to that of lower chemical potential. Alternatively formulated, it can be said that electrons will flow from the species with lower χ to that of higher χ [5-8]. If it assumed that $\mu_B > \mu_A$, then electrons will flow from B to A and $(\Delta N)_B < 0$ and $(\Delta N)_A > 0$. Hence, equation (48) for each system becomes

$$\mu_A' = \mu_A^0 + 2\eta_A^0 \Delta N , \qquad (49)$$

and

$$\mu_B' = \mu_B^0 - 2\eta_B^0 \Delta N , \qquad (50)$$

where $\mu_A' = \mu_B' = \mu_{AB}$, the chemical potential of the AB species upon reaction completion.

The number of electrons transferred, as a first approximation, will obey the following relation

$$\mu_A' = \mu_A^0 + 2\eta_A^0 \Delta N = \mu_B' = \mu_B^0 - 2\eta_B^0 \Delta N = \mu_{AB} \qquad (51)$$

and it follows that

$$\Delta N = \frac{\mu_B^0 - \mu_A^0}{2\left(\eta_A^0 + \eta_B^0\right)} . \qquad (52)$$

This is to say, that a difference in chemical potentials (or electronegativities) drives the electron transfer and the sum of the hardness values acts as a resistance to this transfer. Hard species will have a large value for the $\eta_A^0 + \eta_B^0$ term and soft species will have a small value associated to this sum. This is in agreement with HSAB theory [8-11] that states that soft species are highly polarizable whereas hard ones are not. However, it must be noted that the sum of hardness values must be taken into account together with the differences in chemical potentials for the species involved.

It is important to mention that equation (52) is only an approximation, as it is based on equation (48) which ignores all other terms higher than first order. The chemical potential of a species is also a function of external fields, and hence the values for μ_A and/or μ_B will be affected as a function of the distance.

Equation (47) can be written in terms of the hardness and the chemical potential of each of the two reacting species A and B. If the previous assumption dealing with electron transfer from B to A (*i.e.*, $\mu_B > \mu_A$) is kept, the following equations result,

$$E_A = E_A^0 + \mu_A^0 \Delta N + \frac{1}{2}\eta_A^0 (\Delta N)^2 + \cdots, \qquad (53)$$

$$E_B = E_B^0 - \mu_B^0 \Delta N + \frac{1}{2}\eta_B^0 (\Delta N)^2 - \cdots. \qquad (54)$$

The energy change at a constant external potential due to the interaction of species A and B, is related to the charge transfer between the reacting species and can be expressed as

$$\Delta E_v = (E_A + E_B) - (E_A^0 + E_B^0) = (E_A - E_A^0) + (E_B - E_B^0), \qquad (55)$$

$$\Delta E_v \approx \left[\mu_A^0 \Delta N + \eta_A^0 (\Delta N)^2\right] + \left[-\mu_B^0 \Delta N + \eta_B^0 (\Delta N)^2\right], \qquad (56)$$

where only the expansion to the second order terms has been considered.

Substitution of the value obtained for ΔN (equation 52) yields

$$\Delta E_v \approx -\frac{1}{4}\frac{(\mu_B^0 - \mu_A^0)^2}{(\eta_A^0 + \eta_B^0)}. \qquad (57)$$

This reiterates that it is a difference in chemical potential (or electronegativity) of the interacting species that drives the electron transfer while the sum of the hardness values of the species involved acts as a resistance to it.

A more detailed analysis [8] of the interaction between two species A and B can be made assuming that the interaction occurs in two sequential steps, the first at a constant external potential and for which the driving force for the charge transfer is the chemical potential equalization. The second step occurs at a constant chemical potential and involves a reshuffling of charge distribution. The interaction energy ΔE_{int} becomes,

$$\Delta E_{int} = \Delta E_{v} + \Delta E_{\mu}. \quad (58)$$

Employing global softness values instead of global hardness, by substituting $S = 1/(2\eta)$ accordingly, equation (57) can be written as shown below,

$$\Delta E_{v} \approx -\frac{1}{2}\frac{(\mu_A - \mu_B)^2}{(S_A + S_B)} S_A S_B. \quad (59)$$

Superindices indicating the parameters in the unreacted A and B species have been omitted for simplicity in equation (59) and the following equations.

The term at a constant chemical potential is basically a manifestation of the maximum hardness principle [9, 13-16] and it is expressed as

$$\Delta E_{\mu} \approx -\frac{1}{2}\frac{\lambda}{(S_A + S_B)}, \quad (60)$$

where λ is a constant related to the effective number of valence electrons that participate in the interaction between both species [13, 16].

The interaction energy hence becomes

$$\Delta E_{int} \approx -\frac{1}{2}\frac{(\mu_A - \mu_B)^2}{(S_A + S_B)} S_A S_B - \frac{1}{2}\frac{\lambda}{(S_A + S_B)}. \quad (61)$$

Méndez and Gázquez [13] assumed that in a given chemical system, certain atoms will be more reactive than others in a particular type of chemical reaction. They used a global viewpoint for species B and a local one for any of the *k* atoms that compose species A, as the interaction between the reacting species will occur through the *k*th atom of species A when B approaches it. Hence, it will principally be this atom that will participate in the charge transfer and reshuffling

of charge distribution expressed in the ΔE_{int} equation. In this approximation, the global softness for species A is substituted by the condensed local softness for the *k*th atom in species A, *i.e.*, by s_{Ak}^{+}, s_{Ak}^{-} or s_{Ak}^{0}, depending on the reaction that will take place.

From a local point of view, the interaction energy for the *k*th atom of species A reacting with species B can be expressed as

$$\left(\Delta E_{int}\right)_{Ak} \approx -\frac{1}{2}\frac{\left(\mu_A - \mu_B\right)^2}{\left(S_A f_{Ak} + S_B\right)} S_A f_{Ak} S_B - \frac{1}{2}\frac{\lambda}{\left(S_A f_{Ak} + S_B\right)}, \qquad (62)$$

where f_{Ak} is the condensed Fukui function.

Equation (61) can only be used qualitatively as the value and nature of the constant λ are still not well known. But in spite of this drawback, it can still be usefully employed to study the behaviour of a reactive site within a molecule when reacted with a group of reagents as characterized by their S_B values.

Chandrakumar and Pal [16] have proposed a way of calculating the value of λ as the difference of electron densities in either of the A or B species, before and after the interaction,

$$\lambda_A = \sum_{k=1}^{M} \rho_{A_k}^{eq} - \sum_{k=1}^{M} \rho_{A_k}^{0}, \qquad (63)$$

$$\lambda_B = \sum_{k=1}^{M} \rho_{B_k}^{eq} - \sum_{k=1}^{M} \rho_{B_k}^{0}, \qquad (64)$$

where ρ^{eq} and ρ^{0} are the electron densities for the atoms in A (or B) in the AB compound and the A (or B) compound respectively and the sum runs over all of the M atoms in the species mentioned. For most practical cases, λ is approximately the difference in electron densities for the *k*th atom in A or B that is the reacting centre.

1.5. Basis sets [2, 17]

Basis sets, $\{\eta_\mu\}$, are employed for Hartree-Fock and DFT calculations and are almost universally constituted by Gaussian-type-orbitals (GTO) which are closely related to the solutions for the

hydrogen atom. They are expressed as a polynomial function in the Cartesian coordinates and an exponential in r^2.

$$\eta^{GTO} = N\, x^l\, y^m\, z^n \exp[-\alpha r^2]. \qquad (65)$$

N is a normalization constant, such that $\langle \eta_\mu | \eta_\mu \rangle = 1$, α is an orbital component that determines how compact or diffuse the resulting function is, and the relation $L = 1 + m + n$ is used to classify the GTO as s (L = 0), p (L = 1), d (L = 2) functions, etc. The η_μ functions are not orthogonal, *i.e.*, $\langle \eta_\mu | \eta_\nu \rangle \neq 0$ for $\mu \neq \nu$.

GTO basis sets are usually preferred due to the computational advantages they offer.

Slater-type-orbitals (STO) are also used as basis sets as they mimic the exact functions of the hydrogen atom. They are simple exponentials that can typically be expressed as

$$\eta^{STO} = N\, r^{\,n-1} \exp[-\zeta r\,]\, Y_{lm}(\Theta,\phi). \qquad (66)$$

In the above equation n is the principal quantum number, ζ is the orbital term exponent and Y_{lm} are the spherical harmonics used to express the angular part of the function.

In order to achieve a given level of accuracy, three times as many GTO functions have to be used as STO functions. However, the difficulties encountered at the computational level, when using STO functions account for the almost universal choice of GTO functions.

Basis sets may be classified as minimal basis sets and split-valence basis sets. The STO-3G basis set is an example of the former, while the 3-21G, 6-31G and 6-311G basis sets are examples of the latter.

Minimal basis sets make use of only those functions needed to accommodate all of the electrons of the atom maintaining a spherical geometry. These functions are the 1s function (for H and He) and a set of five functions: 1s, 2s, $2p_x$, $2p_y$ and $2p_z$ for Li to Ne. As a consequence, those molecules that have atoms with spherical environments will be better represented than those that have non-spherical environments.

The split valence basis sets incorporate sets of valence basis functions whereby the resulting orbitals can better represent anisotropic electron distribution in molecules in terms of both σ and π bonds. This is achieved by including two sets of valence basis functions that will account for orbitals involved in σ and π bonding in terms of linear combinations of the said functions. In these basis sets, atoms are represented by one set of functions that account for the inner-shell electrons, and two sets of functions that account for bonding electrons. Split valence basis sets may be a minimal split-valence basis set (like the 3-21g*), or a fully flexible split valence basis set (like the 6-31G*).

Displacement of electron distribution away from the nuclei can be achieved by providing p-type functions on H, and d-type functions for heavier atoms. These sets are termed polarization basis sets and the d-type functions, are known as polarization functions.

Polarization basis sets such as 6-31G*, 6-31G** and 6-311G* are constituted by a set of functions that represents the core electrons, two or more sets of functions that represent valence electrons and a set of d-type polarization functions that account for electronic distribution between nuclei. The polarisation functions adjust the orbital shape by adding an orbital angular momentum one quantum level higher than the valence orbitals. An * adds d function to heavy atoms, while ** adds p function to H, in addition to adding d function to heavy atoms.

Other possible basis sets, like 6-31 + G* and 6-311 + G**, incorporate diffuse functions which are employed for electrons with large radial extent, and hence are useful in describing anions, molecules with lone pairs, excited states and transition states, and in absolute acidity calculations. The Gaussian primitives have the same angular momentum as valence orbitals but have much small exponents, so allowing for some electron density at large distances from the nuclei. In these basis sets, normally only the heavy atoms (and occasionally hydrogen) are provided with diffuse functions. A + adds larger p function to heavy atoms, while ++ adds p and s type function to the heavy atom and to H, respectively.

1.6. Calculation procedure

One of the most successful density functionals applied to small molecules, B3LYP employs Becke's method of using Lee-Yang-Parr's gradient-corrected exchange-correlation density

functionals, which include a hybrid of the Hartree-Fock exchange and the DFT exchange. Thus the B3LYP is semi-empirical to an extent [18].

In the present work, DFT calculations were performed in all cases using the Spartan02 program package at the B3LYP level with the basis sets 6-31 G**, 6-31 + G* and/or 6-31 + G**. The basis set 6-31 G** was employed most widely, as it yielded satisfactory results and includes basis sets for the Cu atom (6-31 + G** does not). For calculations involving Pt(II), the lighter atoms were modelled by means of the 6-31 G** basis set while a pseudopotential (LACVP**) was employed for Pt(II).

For a given molecule A, geometry optimization for the ground state was carried out until the convergence criterion was met. From this calculation the values of the energy for the system with N electrons, $E_A(N)$, and the Mulliken charges on the kth atoms of system A, $q_{Ak}(N)$, were obtained. Once the calculation had completed, the optimized geometry obtained for the system was frozen and single point calculations were performed on species A with $N - 1$ and $N + 1$ electrons. From these calculations, the values $E_A(N-1)$, $q_{Ak}(N-1)$ and $E_A(N + 1)$, $q_{Ak}(N+1)$ are accordingly obtained.

Ionization potentials and electron affinities for system A, I_A and A_A, are calculated as

$$I_A = E_A(N-1) - E_A(N), \quad (67)$$

$$A_A = E_A(N+1) - E_A(N). \quad (68)$$

From these values obtained for the system of interest A, absolute electronegativity, absolute hardness and absolute softness values, χ_A, η_A and S_A respectively, can be calculated as

$$\chi_A = \frac{1}{2}(I_A + A_A), \quad (69)$$

$$\eta_A = \frac{1}{2}(I_A - A_A), \quad (70)$$

$$S_A = \frac{1}{2\eta_A}. \quad (71)$$

Mulliken charges for each of the *k*th atoms in species A with *N*, *N – 1*, and *N + 1* electrons, allow for the calculation of the condensed Fukui function according to equations (37), (38) and (39) mentioned above.

$$f_{Ak}^{+} = q_{Ak}\left(N_A + 1\right) - q_{Ak}\left(N_A\right), \quad (37)$$

$$f_{Ak}^{-} = q_{Ak}\left(N_A\right) - q_{Ak}\left(N_A - 1\right), \quad (38)$$

$$f_{Ak}^{0} = \frac{1}{2}\left[q_{Ak}\left(N_A + 1\right) - q_{Ak}\left(N_A - 1\right)\right] = \frac{1}{2}\left[f_{Ak}^{+} + f_{Ak}^{-}\right]. \quad (39)$$

1.7. References

1. Springborg, M; "Density-Functional Theory", in Hinchliffe, A.; *Chemical Modelling Applications and Theory, Volume 1;* RSC, UK, 2000, pp. 306–361.
2. Koch, W.; Holthausen, M.C.; *A Chemist's Guide to Density Functional Theory*, 2nd edition, Wiley-VCH, Weinheim, Federal Republic of Germany, 2000, pp. 3–64, pp. 93–104.
3. Jensen, F.; *Introduction to Computational Chemistry*, John Wiley & Sons Ltd., Chichester, Great Britain, 1999, pp. 150–193.
4. Parr, R.G.; Donnelly, R.A.; Levy, M.; Palke, W.E.; *J. Chem. Phys.*; **68**, 1978, 3801–3807.
5. Pearson, R.G.; *J. Org. Chem.*; **54**, 1989, 1423–1430.
6. Parr, R.G.; Pearson, R.G.; *J. Am. Chem. Soc.;* **105**, 1983, 7512–7516.
7. Mortier, W.J.; Ghosh, S.K.; Shankar, S.; *J. Am. Chem. Soc.;* **108**, 1986, 4315–4320.
8. Pearson, R.G.; *Inorg. Chem.*, **23**, 1984, 4675–4679.
9. Pearson, R.G.; *J. Chem. Ed.*; **64**, 1987, 561–567.
10. Pearson, R.G.; *Inorg. Chim. Acta*; **240**, 1995, 93–98.
11. Pearson, R.G.; *J. Am. Chem. Soc.*; **107**, 1985, 6801–6806.
12. Parr, R.G.; Yang, W.; *J. Am. Chem. Soc.*; **106,** 1984**,** 4049–4050.
13. Méndez, F.; Gázquez, J.L.; *J. Am. Chem. Soc.*; **116,** 1994, 9298–9301.
14. Parr, R.G.; Gázquez, J.L.; *J. Phys. Chem.*; **97**, 1993, 3939–3940.
15. Parr, R.G.; Chattaraj, P.K.; *J. Am. Chem. Soc.*; **113**, 1991, 1854–1855.
16. Chandrakumar, K.R.S.; Pal, S.; *J. Phys. Chem. A*; **106**, 2002, 11775–11781.
17. Hehre, W.J.; Yu, J.; Klunzinger, P.E.; Lou, L.; *A Brief Guide to Molecular Mechanics and Quantum Chemical Calculations*, Wavefunction, Inc., Irving, California, USA, 1998, pp. 1–110.
18. Janoschek, R., *Pure & Appl. Chem.,* **73,** 2001, 1521-1553.

2. Zeise's salt derivatives with aromatic *N*-oxide ligands

2.1. Vibrational spectra of pyridine *N*-oxide and its isotopomers

The vibrational spectra for the pyridine *N*-oxide ligand (pyO), substituted derivatives and coordination compounds have been extensively studied by several groups in previous years [1-13]. However, very little work has been published dealing with assignments for the perdeuterated analogue. Most of these involve coordination compounds with py-d_5O, in which the assignments seem in most cases to have been carried out by using the ν_D/ν_H ratios obtained for pyridine and pyridine-d_5 [14-18] and employ the assignments of Shindo [5, 6] which, although erroneous [11], have been shown to be widely accepted.

A re-examination of this system was carried out in the present work in order to review the assignment of Zeise's salt derivatives with pyO that have been reported in the past [14, 15]. Ambiguities regarding the assignment of the νPt-O stretching frequency have been pointed out for several *N*-oxide Zeise's salt derivatives [19-21]. The possibility exists of incorrectly assigning a low energy fundamental vibration of the pyO ligand as the νPt-O stretching frequency, and thus a thorough investigation of the ligand employed is required. A good understanding of the pyO/py-d_5O system is considered necessary, in order to have a theoretical foundation for assignments of the py-d_5O fundamentals and to clear up ambiguities in the far ir region, especially regarding the νPt-O vibration. As part of this study, the O-18 labelled pyridine *N*-oxide ligand was also prepared to be used in the preparation of Zeise's salt derivatives (chapter 4). Although the compound obtained is a mixture of the O-16/O18 *N*-oxides, several conclusions can be drawn from the appearance of two bands for the O-18 sensitive vibrations.

DFT calculations were carried out on benzene-d_0, benzene-d_6, pyO, py-d_5O, py-^{18}O and py-$d_5{}^{18}$O at the B3LYP level using the 6-31 G** basis set as previously described. In examining the sensitivity of the vibrations to the N-O bond length, the calculated frequencies are reported as obtained (*i.e.*, unscaled). In employing the calculated frequencies to the assignment problem, the calculated frequencies are rescaled using those obtained experimentally. In all cases, a linear relationship was obtained between experimental and calculated frequencies.

2.1.1. Benzene-d_0 and benzene-d_6

Assignments for the fundamentals of the benzene system have been well established in the past [22-24]. The systems were modelled in this study by means of DFT calculations in order to

ascertain the reliability of the calculated frequency values. The results obtained are in very good agreement with the observed values and are shown in table 2.1.1. Only one of the fundamentals in both the benzene-d_0 and benzene-d_6 systems is slightly underestimated. In benzene-d_0, Wilson mode 12 (the Star of David ring breathing mode) is observed at a higher wavenumber than mode 1 (the ring breathing mode), with the assigned frequencies of 1010 and 992 cm^{-1} respectively[29], while the trend is inverted in the calculated frequencies with mode 1 occurring higher than mode 12. In benzene-d_6, both modes are calculated following the experimentally observed trend, *i.e.*, mode 12 occurring before mode 1. However, the calculated frequency values for these vibrations are at 953 and 948 cm^{-1} respectively whereas the experimental values are observed at 970 and 945 cm^{-1} respectively. Regardless of the underestimated value for mode 12 in both isotopomers, the experimental and calculated ν_D/ν_H ratios yield the same value of 0.960.

Table 2.1.1. Experimental [22, 23] and calculated rescaled frequencies (in brackets) for benzene-d_0 and benzene-d_6. All frequency values in cm^{-1}.

Wilson mode	D_{6h}	C_6H_6	C_6D_6	ν_D/ν_H
2	A_{1g}	3062 [3073]	2294 [2296]	0.749 [0.747]
1		992 [995]	945 [948]	0.953 [0.953]
3	A_{2g}	1346 [1342]	1055 [1046]	0.784 [0.779]
5	B_{2g}	991 [987]	830 [817]	0.838 [0.828]
4		707 [705]	599 [606]	0.847 [0.860]
10	E_{1g}	849 [845]	663 [660]	0.781 [0.781]
7	E_{2g}	3047 [3048]	2267 [2266]	0.744 [0.743]
8		1595 [1604]	1553 [1558]	0.974 [0.971]
9		1177 [1172]	868 [859]	0.737 [0.733]
6		607 [613]	579 [585]	0.954 [0.954]
11	A_{2u}	675 [680]	497 [504]	0.736 [0.741]
13	B_{1u}	3048 [3039]	2275 [2254]	0.746 [0.742]
12		1010 [993]	970 [953]	0.960 [0.960]
14	B_{2u}	1309 [1319]	1282 [1306]	0.979 [0.990]
15		1146 [1150]	824 [823]	0.719 [0.716]
20	E_{1u}	3057 [3063]	2276 [2285]	0.744 [0.746]
19		1479 [1481]	1330 [1332]	0.899 [0.899]
18		1035 [1041]	812 [813]	0.784 [0.781]
17	E_{2u}	969 [950]	789 [774]	0.814 [0.815]
16		404 [413]	351 [363]	0.869 [0.879]

2.1.2. Pyridine *N*-oxide, pyridine-d_5 *N*-oxide and O-18 labelled pyridine *N*-oxide

Pyridine *N*-oxide is a commonly used ligand in coordination chemistry. The issue of the wide acceptance of Shindo's erroneous 'characteristic' *N*-oxide frequencies has been dealt with previously [11]. This is the consequence of strong vibrational coupling within the system, the

nature of which has been elucidated by normal coordinate analyses, the most comprehensive of which is that of Gambi and Ghersetti [1].

Figure 2.1.1 shows the labelling scheme for bond distances and angles for the pyO ligand and experimental and calculated values are shown in table 2.1.2. The analysis of the calculated frequencies for the pyO ligand shows that the νN-O frequency is over-estimated by *ca.* 70 cm^{-1} when the optimized geometry obtained by means of the DFT calculations is employed in the vibrational analysis. All other calculated frequencies, including the one related to the αN-O vibration are in good agreement with the experimental values. However, in pyO there can be no ambiguity regarding the assignment of the frequency at which the νN-O frequency occurs in the free ligand. It has been assigned at 1252 cm^{-1} and a normal coordinate analysis of the ligand performed by Gambi and Ghersetti provides a calculated value of 1254 cm^{-1} [1]. This band is also characterized by a strong intensity, sensitivity to solvents, and linearity with Hammett's parameters in 2- and 4- substituted derivatives [1, 3].

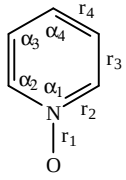

Figure 2.1.1. Labelling scheme for bond distances and bond angles as shown in table 2.1.2.

Table 2.1.2. Experimental and calculated bond distances (Å) and angles (degrees) for pyO. Experimental values for pyO taken from reference 25.

	experimental			Calculated			
	Molecule I	Molecule II	$[Pt(C_2H_4)(pyO)Cl_2]^{\dagger}$	rN-O = 1.27 Å	rN-O = 1.30 Å	RN-O = 1.33 Å	rN-O = 1.36 Å
r_1	1.33	1.37	1.3672	1.2741	1.3000	1.3300	1.3600
r_2	1.34	1.34	1.3236, 1.3430	1.3746	1.3709	1.3671	1.3635
r_3	1.37	1.38	1.3761, 1.3947	1.3826	1.3830	1.3834	1.3838
r_4	1.35	1.39	1.3971, 1.3621	1.3959	1.3960	1.3962	1.3964
α_1	120	124	122.52	118.4068	118.8775	119.3980	119.8875
α_2	120	119	119.02, 120.64	121.3711	121.1711	120.9580	120.7586
α_3	121	120	118.29, 119.36	120.5726	120.5043	120.3945	120.2869
α_4	118	118	120.14	117.7058	117.7717	117.8971	118.0216

† Relative error in distances 0.0002 Å

The optimized geometry of the pyO ligand exhibits a N-O bond distance of 1.2741 Å, considerably shorter than the bond distances obtained by means of X-ray diffraction studies, in which two crystallographically independent pyO molecules are found [25]. The observed N-O bond lengths are of 1.33 and 1.37 Å. The shorter bond distance obtained by means of the DFT calculations increases the bond order and hence the νN-O stretching frequency (mode $6A_1$) increases as well. In order to overcome this problem, the N-O bond distance was constrained to the values of 1.30, 1.33 and 1.36 Å and geometry optimizations and vibrational analyses were performed subject to the constraint. The results obtained show a linear relationship between the N-O bond distance and the calculated νN-O frequency over the range 1.27 and 1.33 Å. Minor changes are observed for most of the remaining calculated frequencies, as is shown in figures 2.1.2 and 2.1.3, for pyO and py-d_5O respectively, although several crossovers occur which are worth discussing further.

The most significant changes on varying the N-O bond length in pyO are observed for the $6A_1$, $6B_1$, $7A_1$, $10A_1$ and $6B_2$ vibrations. These agree with earlier reports of N-O and metal sensitivity of each of these vibrations [5, 6, 11]. In fact, modes 6 and $7A_1$ are the most sensitive to a variation in the N-O bond length and, upon varying the N-O bond distance, the νN-O stretching frequency occurs predominantly in one mode over the other. The normal modes obtained for the different bond lengths are shown in figure 2.1.4, together with the magnitude of the N-O displacement vector along the *z* axis of the molecule and the calculated shifts expected upon O-18 labelling. As can be seen in figure 2.1.4, for rN-O between 1.2741 to 1.3600 Å, mode $6A_1$ is initially the highest νN-O character vibration as reflected in O-18 sensitivity ($\Delta\nu$), whereas the νN-O character increases for mode $7A_1$ as the bond length is increased. Consequently, the νN-O stretching frequency is best described by mode $6A_1$ for short N-O bond lengths, is shared between both modes $6A_1$ and $7A_1$ for a distance of 1.33 Å, and is best described by mode $7A_1$ for long N-O bond distances.

It is also interesting to note that the position for mode $6A_1$ with respect to mode $6B_1$ is rN-O dependent. To a lesser extent, this is also observed for modes $7A_1$ and $7B_1$, and for modes $10A_1$ and $2A_2$.

Calculations for the py-d_5O system subject to the same bond length constraints also show an interesting dependence of the frequencies as a function of the N-O bond length. The most affected

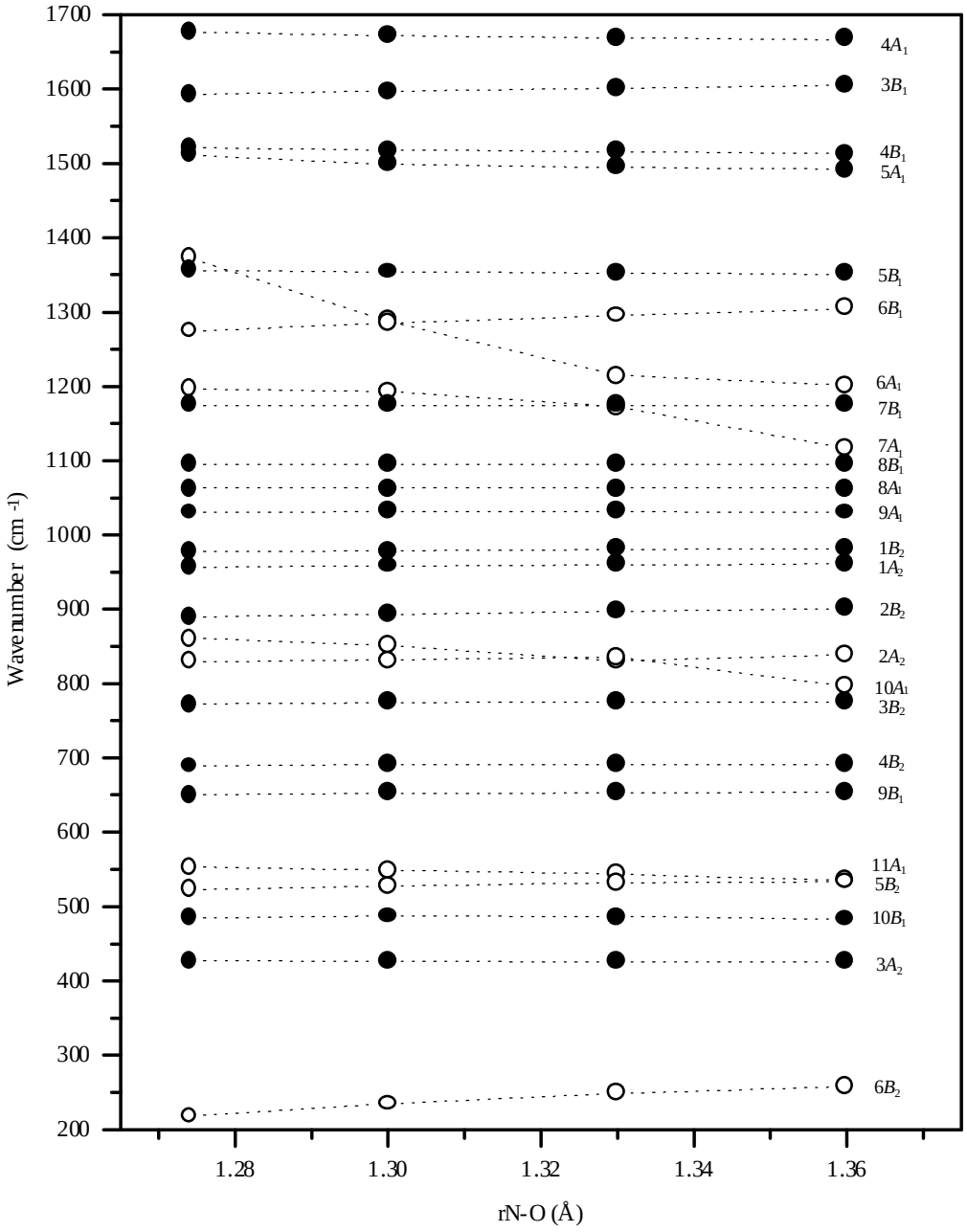

Figure 2.1.2. Calculated unscaled frequencies for the in-plane and out-of-plane modes in pyO as a function of the N-O bond length.

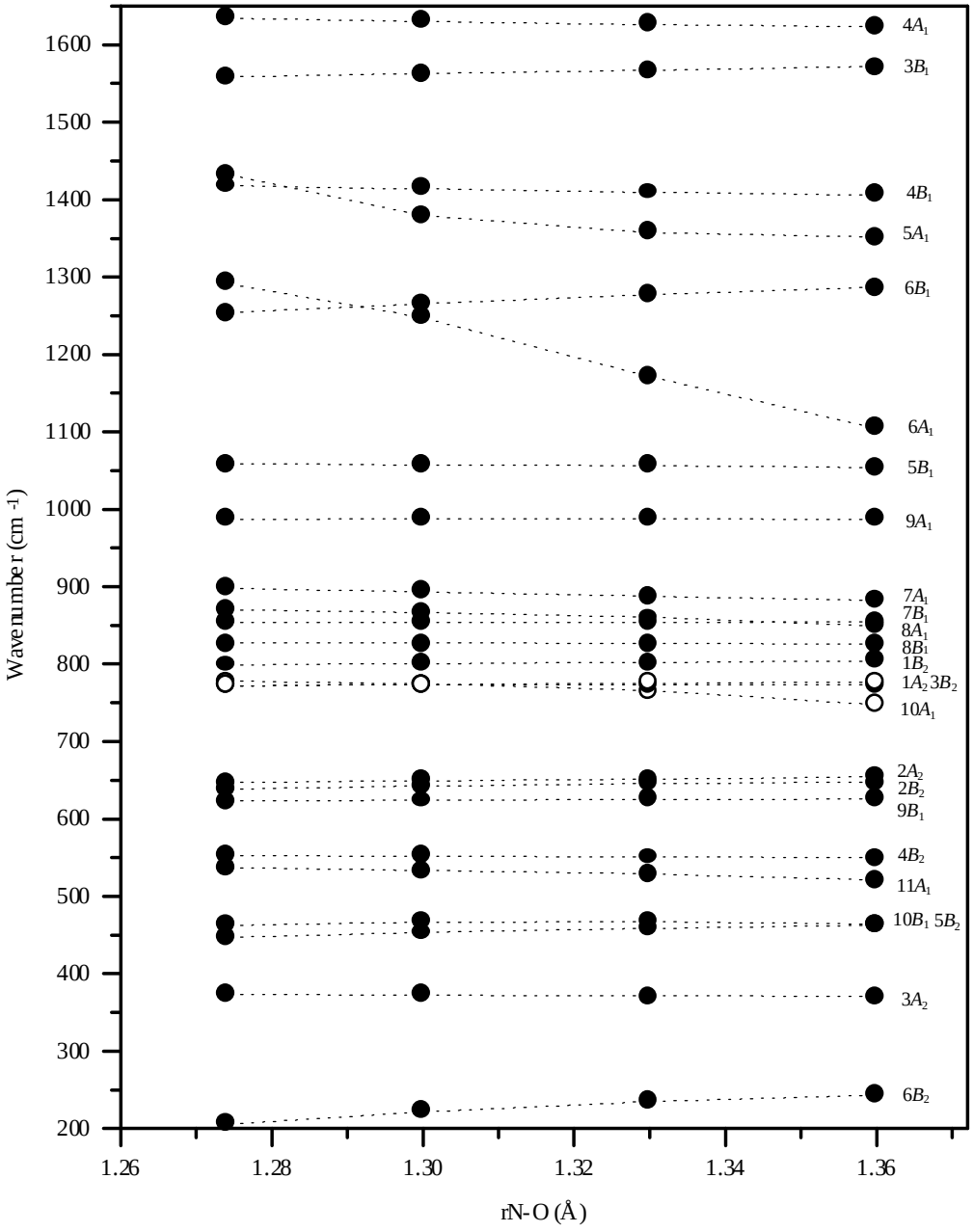

Figure 2.1.3. Calculated unscaled frequencies for the in-plane and out-of-plane modes in py-d_5O as a function of the N-O bond length.

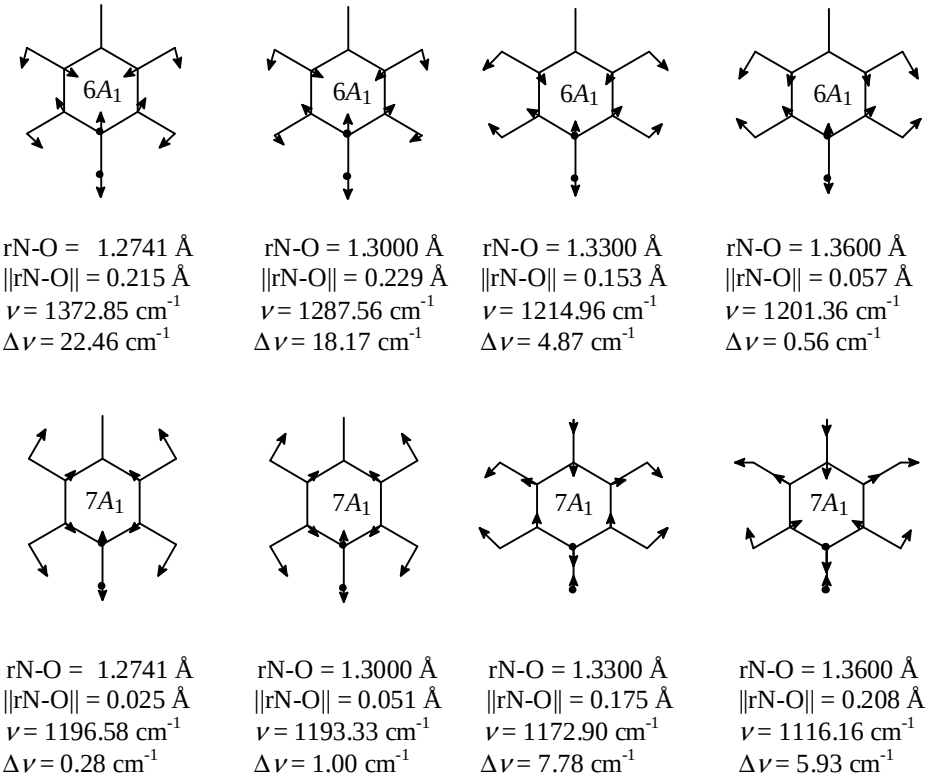

Figure 2.1.4. Affected νN-O modes for pyO as the N-O bond length is modified. Calculated frequencies are unscaled and $\Delta\nu = \nu_{\text{pyO}} - \nu_{\text{py-18O}}$.

modes are $5A_1$, $6B_1$, $6A_1$, $7B_1$, $8A_1$, $1A_2$, $10A_1$, $5B_2$ and $6B_2$, as is shown in figure 2.1.3. The νN-O stretching frequency is again shared by two modes of A symmetry, $5A_1$ and $6A_1$. The normal modes obtained for the different bond lengths are shown in figure 2.1.5 together with the magnitude of the N-O displacement vector along the z axis of the molecule and the calculated shifts expected upon O-18 labelling. For short N-O bond lengths, the νN-O stretch occurs mainly as mode $5A_1$ at the higher frequency, although mode $6A_1$ reflects a coupled vibration with considerable νN-O character. As the bond length increases the νN-O stretching frequency is shared between both modes, and finally for a bond distance of 1.36 Å it appears principally as the $6A_1$ mode. As mode $6A_1$ gains more N-O character, it has an extremely noticeable decrease in energy, while mode $6B_1$ increases only slightly on loss of N-O character.

Eight fundamentals are calculated to occur in the region 900-700 cm^{-1} for py-d_5O and, due to the proximity at which these occur, several crossovers are observed with increasing bond length.

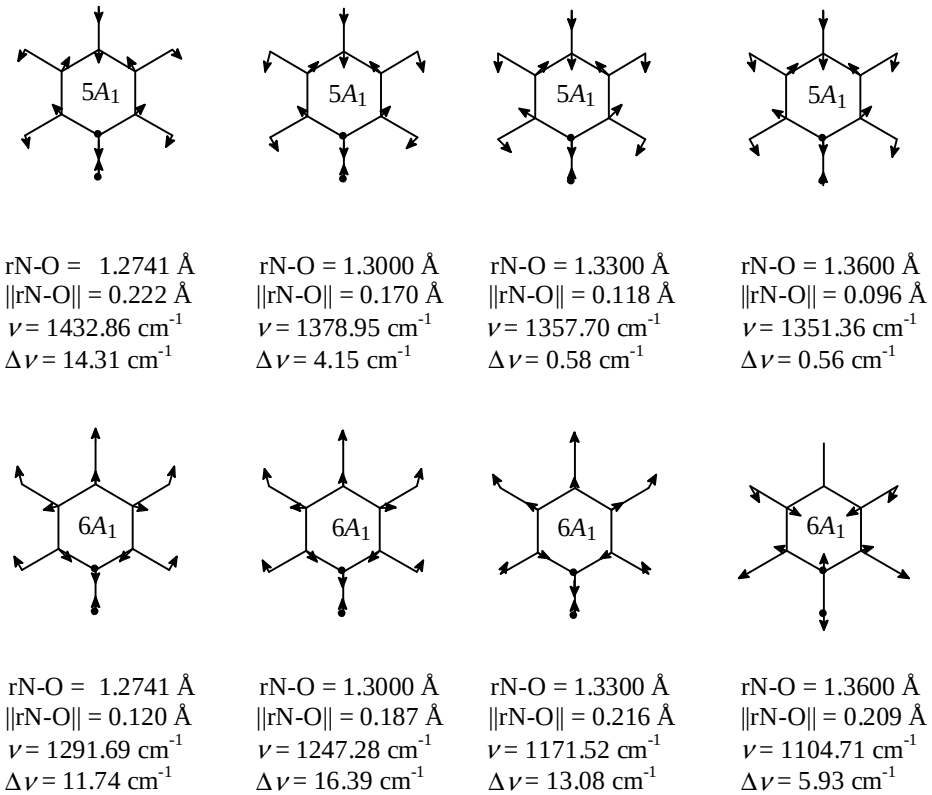

Figure 2.1.5. Affected νN-O modes for py-d_5O as the N-O bond length is modified. Calculated frequencies are unscaled and $\Delta\nu = \nu_{\text{py-}d5\text{O}} - \nu_{\text{py-}d5\text{18O}}$.

Such is the case for modes $7B_1$ and $8A_1$ and for the three modes occurring close to 750 cm^{-1}, modes $1A_2$, $3B_2$ and $10A_1$. For a N-O bond length of 1.30 Å the three latter modes are accidentally degenerate, occurring at almost the same frequency value. However, as the bond length increases, this accidental degeneracy is lifted by a slight upward shift of mode $1A_2$ and a noticeable downward shift of mode $10A_1$, with mode $3B_2$ remaining impervious to the N-O bond length.

The frequency of the low energy out of plane mode $6B_2$ is raised with increasing N-O bond length for both isotopomers.

The present DFT study confirms the earlier identification of the N-O sensitive modes and normal coordinate analyses for the -d_0 isotopomer and extends a subtle understanding of the pyridine *N*-oxide system in two areas. The first, missed in the earlier studies employing the ν_D/ν_H ratio, is the isotope sensitivity of the vibrational coupling within the molecule, *viz*. -d_5 induced coupling of

modes $5A_1$, $7B_1$, $8A_1$ and $1A_2$ and the $-d_5$ induced decoupling of mode $7A_1$. The second is a better measure on a change in the electronic distribution in the N-O bond.

Due to the fact that a change in the electronic distribution in the N-O bond is expected upon coordination to a metal ion, the frequencies that have been observed to be sensitive to the N-O distance may be expected to shift more than those that are impervious to a change in bond length. The previous consideration may prove useful in the assignment of the frequencies for coordination compounds involving *N*-oxide derivatives, where the experimental N-O bond distances are slightly longer than in the free ligand, and where significant changes in the N-O bond order are expected due to coordination to a metal centre.

The effect produced by a variation in the mass of a substituent X has been previously described by Várs anyi and Szöke [19] in substituted benzene derivatives. Although the above considerations deal with a variation of bond order and hence of the force constants involved for the N-O bond, a similar behaviour can be expected regarding the modes that should be most affected. For monosubstituted benzenes, C_6H_5X, the principal C-X vibrations were shown to affect three Wilson modes basically, depending on whether the X substituent was light (less than 25 a.m.u.) or heavy. Having classified the normal modes of benzene as radial, tangential and out-of-plane, according to the atomic displacements, light substituents show the C-X modes occurring in Wilson modes 13 (νC-X), 9b (αC-X) and 17b (γC-X), while the affected modes for heavy substituents are 7a (νC-X), 9b (αC-X) and 10b (γC-X). In the discussion above, the affected modes that share the νN-O stretch are modes $6A_1$ (13) and $7A_1$ (9a) for the pyO molecule, which has been considered to behave in a similar way to the monosubstituted benzenoid system, fluorobenzene. It is indeed the mode assigned as Wilson mode 13 that shows the highest νN-O character. However, as the bond length increases, the νN-O stretching frequency appears in mode $7A_1$ (9a), which is considered a tangential mode and not a radial mode as is the case with mode 13. As can be seen from figure 2.1.4, mode $7A_1$ experiences noticeable changes in the displacement of the H atoms as the bond length increases, to the extent that for long N-O bond lengths, the mode obtained ceases to resemble the Wilson mode 9a but can be interpreted as a mode of high νN-O character that can then be associated to one of the radial modes from the higher energy region.

The αN-O vibration occurs as mode $10B_1$ (9b) and it is interesting to note that it is basically impervious to a change in bond length, in good agreement with the fact that it is this same mode that is observed to produce the αC-X vibration for both light and heavy substituents.

Only minor changes are observed for the γN-O vibration, mode $6B_2$ (17b) when the bond length is varied. The significant out-of-plane displacements are kept, and the magnitude of the N-O displacement out of the *xz* plane is of 0.145, 0.141, 0.138 and 0.136 Å, respectively for rN-O distances of 1.2741, 1.3000, 1.3300 and 1.3600 Å. Mode $2B_2$ (10b), associated with the γC-X vibration for heavy X substituents, remains impervious to a change in the N-O bond length.

The changes observed for the pyO ligand as the bond length is varied can be extended to the py-d_5O system. The main difference is that the νN-O vibrations appear in modes $5A_1$ (19a) and $6A_1$ (13) for short and long N-O bond lengths respectively.

The best fit to experimental values was obtained with the 1.30 Å constraint, and hence this value was consistently used for the calculations involving pyO, py-d_5O, py-^{18}O and py-$d_5{}^{18}$O in this work. Although the value employed is shorter than the observed bond lengths for this molecule, it is quite close to that of 1.29 Å employed by Gambi and Ghersetti in their normal coordinate treatment for pyO [1]. It must also be borne in mind that the calculations provide a molecule in the gaseous state, and the bond lengths and angles are expected to vary in the solid state.

The calculations yield a molecule with C_{2v} symmetry and 30 modes of vibration, 21 in plane modes and 9 out of plane modes. Table 2.1.3 shows the assignment carried out in this work for the pyO and py-d_5O fundamentals and their relation to the Wilson modes for benzene. The assignment of the modes follows the order obtained for the molecules with a constrained N-O bond length of 1.30 Å and with the pyO molecule lying on the *xz* plane with the N-O bond along the *z* axis. Displacement diagrams showing in-plane and out-of-plane vibrations for both isotopomers are shown in figures 2.1.6 and 2.1.7, and the spectra for both compounds are shown in figure 2.1.8.

Due to the fact that the py-d_5O system has previously not been as extensively studied as the pyO system, assignments were performed by means of the calculated values obtained, the ν_D/ν_H ratio obtained for the calculated frequencies, and by the information provided by the coordination spectra of the Zeise's salt derivatives with the perdeuterated analogue. These prove particularly

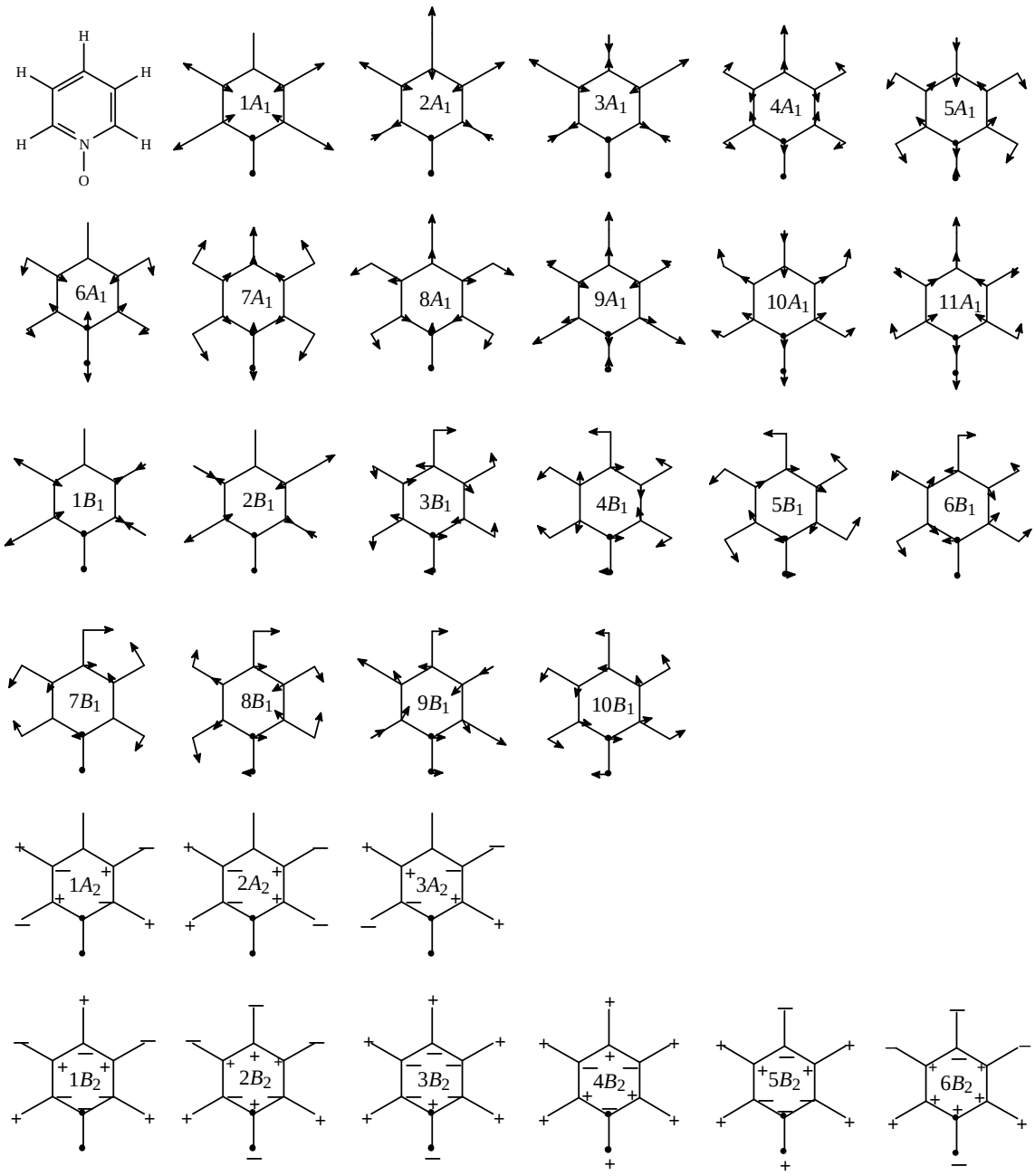

Figure 2.1.6. In-plane and out-of-plane vibrations for pyO.

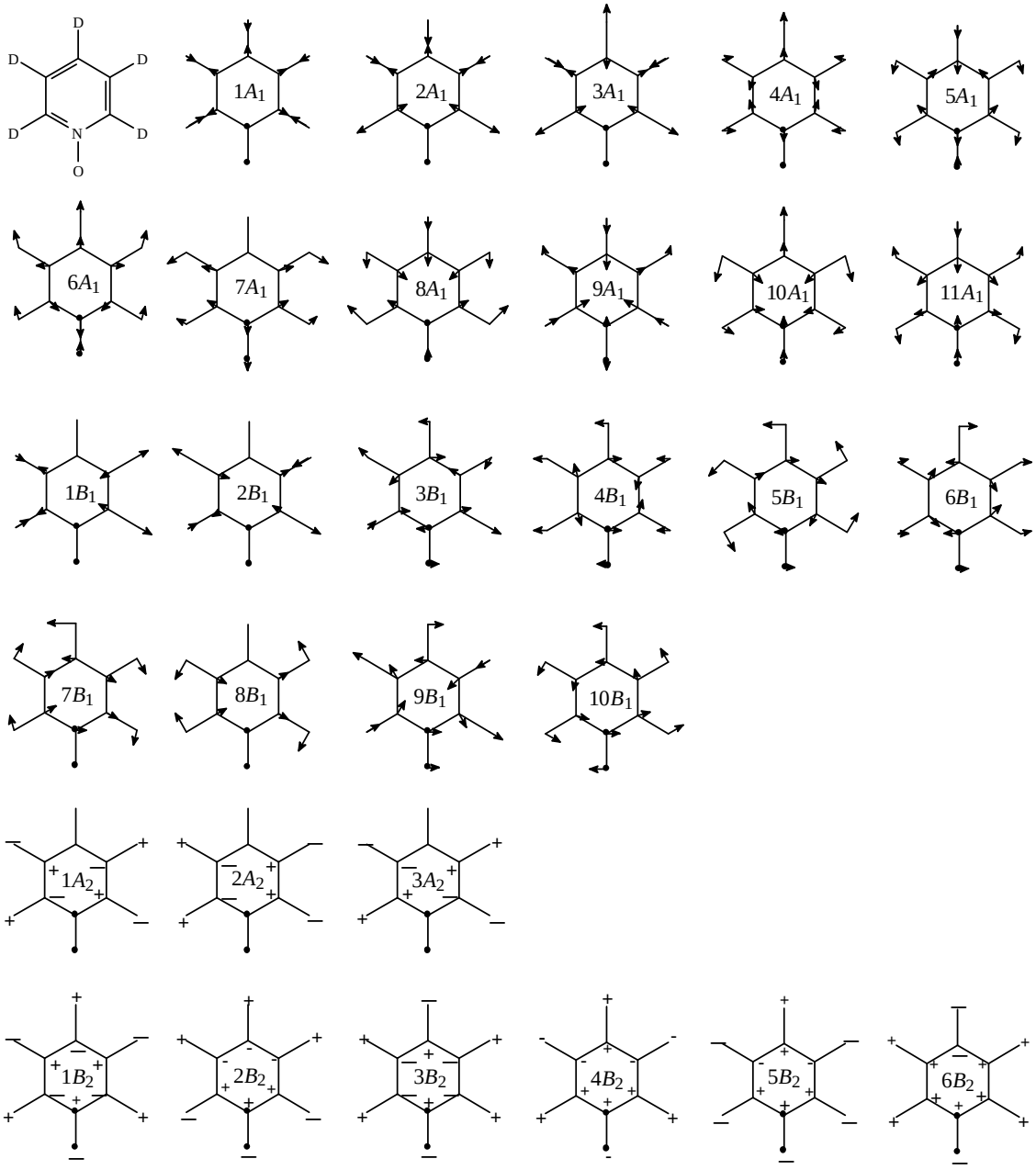

Figure 2.1.7. In-plane and out-of-plane vibrations for py-d_5O.

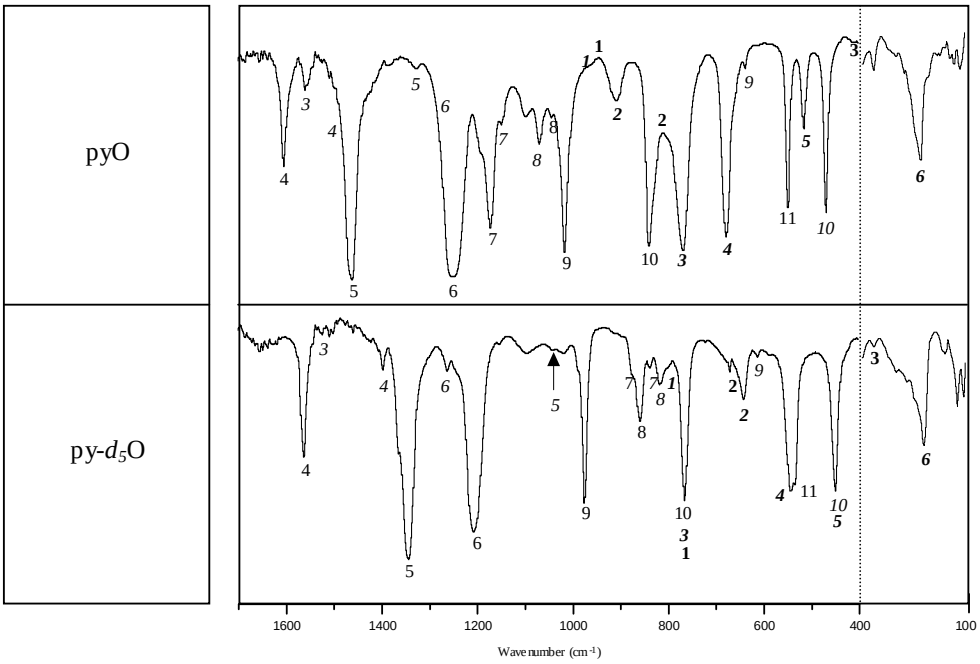

Figure 2.1.8. Infrared spectra for pyO and py-d_5O in the 1700-100 cm^{-1} region.
In-plane modes shown by corresponding number (A_1) and italics (B_1).
Out-of-plane modes in bold (A_2) and bold italics (B_2)

useful in the assignment of certain weak intensity fundamentals, as the combination bands observed in the spectra for the coordination compounds are less intense than those observed in the spectrum for the free ligand.

2.1.2.1. In-plane vibrations

Eleven modes of A_1 symmetry and ten of B_1 symmetry are expected for pyridine *N*-oxide and pyridine-d_5 *N*-oxide. The observed frequencies for C-H/D stretching vibrations for the pyO and py-d_5O systems (modes 1, 2 and 3A_1 and 1 and 2B_1) are in good agreement with the calculated values and with previous work performed on the pyO system. Their assignment in terms of the Wilson modes has been the subject of numerous works [19], and hence will not be discussed further.

All of the in-plane fundamentals of A_1 symmetry agree with Gambi and Ghersetti's work. However, several re-assignments have been performed for some of the B_1 fundamentals, namely modes 5 and 6B_1. All other modes of B_1 symmetry coincide with the aforementioned work.

Table 2.1.3. Experimental and calculated rescaled frequencies (in brackets) for pyO and py-d_5O. All frequency values in cm^{-1}. Experimental values A_2 vibrations for the pyO from reference 4.

Wilson mode	C_{2v}		pyO	py-d_5O	ν_D/ν_H
20a	A_1	1	3098 [3108]	2361 [2357]	0.762 [0.758]
2		2	3066 [3073]	2342 [2330]	0.764 [0.758]
7a		3	3045 [3052]	2294 [2302]	0.753 [0.754]
8a		4	1604 [1630]	1561 [1590]	0.973 [0.975]
19a		5	1461 [1462]	1342 [1347]	0.918 [0.921]
13		6	1250 [1258]	1205 [1219]	0.964 [0.969]
9a		7	1171 [1166]	874 [877]	0.746 [0.752]
18a		8	1043 [1041]	857 [851]	0.822 [0.817]
12		9	1015 [1009]	973 [968]	0.959 [0.959]
1		10	838 [835]	763 [761]	0.910 [0.911]
6a		11	547 [543]	531 [527]	0.971 [0.970]
20b	B_1	1	3098 [3107]	2361 [2353]	0.762 [0.757]
7b		2	3045 [3057]	2294 [2311]	0.753 [0.756]
8b		3	1559 [1557]	1523 [1526]	0.977 [0.980]
19b		4	1482 [1481]	1396 [1381]	0.942 [0.932]
3		5	1328 [1322]	1040 [1036]	0.783 [0.784]
14		6	1250 [1255]	1261 [1237]	1.009 [0.986]
15		7	1148 [1148]	837 [838]	0.729 [0.730]
18b		8	1068 [1071]	815 [812]	0.763 [0.758]
6b		9	637 [642]	610 [615]	0.958 [0.958]
9b		10	467 [483]	447 [462]	0.957 [0.956]
17a	A_2	1	950 [939]	763 [760]	0.803 [0.809]
10a		2	820 [816]	672 [639]	0.780 [0.783]
16a		3	415 [424]	365 [371]	0.879 [0.875]
5	B_2	1	964 [958]	803 [786]	0.833 [0.820]
10b		2	907 [876]	640 [633]	0.706 [0.722]
11		3	767 [760]	763 [760]	0.995 [1.000]
4		4	677 [679]	540 [545]	0.798 [0.803]
16b		5	513 [522]	447 [449]	0.871 [0.860]
17b		6	226 [238]	221 [224]	0.978 [0.941]

Modes 5B_1 and 6B_1 were assigned [1] by Gambi and Ghersetti as occurring at 1364 and 1329 cm^{-1} respectively. Mielke [13] gives 1294 cm^{-1} for the 5B_1 vibration. The calculated value in this work for mode 5B_1 is 1322 cm^{-1} and is in fact, the band that was assigned by Gambi and Ghersetti as mode 6B_1. No band was observed at 1364 cm^{-1} in the spectra of pyO obtained for this work, although there is a band at 1388 cm^{-1}, which is likely to be the combination band (10A_1 + 11A_1). Mode 5B_1 has been assigned in this work as occurring at 1328 cm^{-1} as this band appears without

major shifts in the spectra of the pyO Zeise's salt derivatives. Mode $6B_1$ is one of the N-O bond length dependent modes and is masked by the very intense $6A_1$ absorption with a high νN-O character. However, it is seen in the spectra for pyO coordination compounds as a weak intensity absorption at *ca.* 1250 cm^{-1} as will be discussed in the corresponding section. As can be seen in table 2.1.3, the calculated ν_D/ν_H ratio for this vibration is slightly lower than the experimental one, although both ratios are typical of a ring vibration. The modes correspond to Wilson mode 14 for the benzene system, which also yields a ν_D/ν_H close to unity. The strong dependence of this mode with the N-O bond length can account for the fact that it may very easily be miscalculated as either occurring before or after mode $6A_1$. The very strong intensity for mode $6A_1$ further encumbers the assignment of mode $6B_1$, which is expected to be considerably weaker than the $6A_1$ fundamental.

The A_1 fundamentals are the strongest in-plane absorptions observed in the ir spectra of pyO and py-d_5O. The strongest Raman bands observed for the pyO ligand occur at 1602 and 1020 cm^{-1} [12], and correspond to the ring stretch mode $4A_1$ and the star of David mode, $9A_1$. It is this latter mode that shows the strongest Raman band in the coordination compounds with Pt(II) for both isotopomers, as will be discussed in section 2.3.2.

A weak intensity band occurring at 1097 cm^{-1} has been ascribed to either the overtone $2 \times 11A_1$ or the difference band $4A_1 - 5B_2$.

Accidental degeneracy dependent on N-O bond length (figure 2.1.3) is observed for modes $1A_2$, $3B_2$ and $10A_1$ in the free py-d_5O system. Interestingly, this degeneracy is lost upon coordination of the ligand to Pt(II), in agreement with a variation of bond order as previously explained.

Eight vibrations are expected to occur for the py-d_5O ligand in the range 900-750 cm^{-1}. Only four well-defined bands are observed in this region, with two shoulders appearing on the bands at 857 and 815 cm^{-1}. Calculated frequency values for the $7A_1$ and $8A_1$ vibrations are 877 and 851 cm^{-1} respectively. The ir spectrum shows a medium intensity band centred at 857 cm^{-1} with a shoulder at *ca.* 874 cm^{-1}. These have been assigned as the $8A_1$ and $7A_1$ fundamentals respectively.

Mode $7B_1$ has been assigned to the weak intensity band appearing at 837 cm^{-1} while the band at 815 cm^{-1} shows a shoulder at *ca.* 805 cm^{-1}. These have been assigned as modes $8B_1$ and $1B_2$ respectively.

Three vibrations are calculated to occur at 760 cm^{-1} and only one very intense absorption is observed at 763 cm^{-1}. Modes $10A_1$, $3B_2$ and $1A_2$ are thus accidentally degenerate and have been assigned at 763 cm^{-1}. Both modes $10A_1$ and $3B_2$ are observed as intense absorptions in the ir spectrum for pyO, the first mode corresponds to the symmetric ring breathing mode while the second is the intense out-of-plane umbrella mode. Interestingly, the very intense absorption at 766 cm^{-1} in the py-d_5O Zeise's salt derivatives, shows a weak intensity band occurring at approximately 783 cm^{-1}, which has been assigned as mode $3B_2$ in $[Pt(C_2H_4)(py\text{-}d_5O)Cl_2]$, in agreement with the calculated values obtained for this compound.

Modes $10B_1$ and $5B_2$ in py-d_5O have been assigned at 447 cm^{-1}. Mode $10B_1$ is expected to occur at a higher frequency but it appears to be accidentally degenerate with the out-of-plane mode. The fact that mode $10B_1$ is the αN-O vibration accounts for its intensity in the ir spectra for pyO and py-d_5O while the out-of-plane mode $5B_2$ is a less intense band in the spectrum for pyO. The position of both modes is dependent on the N-O bond length (figure 2.1.3), and their assignment would need to be confirmed through single crystal polarization studies.

2.1.2.2. Out-of-plane vibrations

Six modes of B_2 and three of A_2 symmetry are obtained for the pyO and py-d_5O systems. The B_2 symmetry modes provide medium to strong intensity bands in the ir spectra for these compounds. The A_2 vibrations are ir forbidden and are either absent or extremely weak absorptions in the ir spectra for pyO and py-d_5O. Raman spectra for the pyO system have been previously reported [4, 7, 9, 12] but no Raman data was available for the spectrum of the py-d_5O compound. Assignments for the A_2 fundamentals are based on the Raman bands reported by Kakiuti *et al.* [4] for pyO and are in good agreement with the calculated values obtained in this work. The A_2 modes, although extremely weak absorptions, are activated in the ir spectra for the Zeise's salt derivatives, and these were used as an aid in the assignment problem. The $1A_2$ vibration for py-d_5O is calculated to occur at 760 cm^{-1}. It is accidentally degenerate with modes $10A_1$ and $3B_2$ and has been assigned at 763 cm^{-1} where only one medium intensity band is observed in the ir spectrum. This vibration is observed at 788 cm^{-1} as a weak intensity band in the spectra for $[PtA(py\text{-}d_5O)]X_2$ compounds as will be discussed in section 2.3.2. Modes $2A_2$ and $3A_2$ occur as weak intensity bands in the mid and far ir spectra for py-d_5O.

Gambi and Ghersetti assigned mode $1B_2$ as occurring at 977 cm^{-1}. Of all the modes of B_2 symmetry, it is this vibration that occurs as the weakest absorption. The calculated value for this

vibration is of 958 cm^{-1} and the 966 cm^{-1} band (also reported at 965 cm^{-1} by Kakiuti *et al.* [4]) is preferred as the $1B_2$ fundamental in this work. All other B_2 modes are in agreement with Gambi and Ghersetti's work [1].

2.1.2.3. N-O vibrations

Calculations performed on the py-^{18}O and py-d_5^{18}O systems were carried out to determine the O-18 sensitive vibrations for both the pyO and py-d_5O isotopomers. Table 2.1.4 shows the frequency values obtained for the pyO ligand and the pyO/py-^{18}O mixture obtained in the labelling studies. The calculated shifts obtained and the O-18 sensitive modes are also shown.

Table 2.1.4. Principal N-O vibrations in pyO and py-d_5O and calculated shifts upon O-18 labelling. $\Delta\nu_{calc} = \nu_{pyO} - \nu_{py\text{-}18O}$ and $\nu_{py\text{-}d5O} - \nu_{py\text{-}d5O\text{-}18}$ respectively . All values in cm^{-1}.

Mode	pyO	pyO/py-^{18}O	$\Delta\nu_{calc}$	py-d_5O	$\Delta\nu_{calc}$	Assignment
$5A_1$				1561	4	αC-D + νN-O coupled
$6A_1$	1250	1225	18	1205	16	νN-O coupled
$7A_1$	1170	1176	1	874	3	αC-H/D + νN-O coupled
$8A_1$				857	2	αC-H/D
$10A_1$	838	835/819	12	763	1	Ring breathing + νN-O coupled
$1A_2$				763	1	γC-H/D
$3B_2$	767	772	1	763	6	γC-H/D (umbrella) + γN-O coupled
$9B_1$				610	1	νring
$11A_1$	547	550/542	10	531	9	νring + γN-O coupled
$5B_2$	513	510	2	447	1	γring
$10B_1$	467	470/456	14	447	14	αN-O
$6B_2$	229	–	5	221	5	γN-O coupled

The spectra for the 880-420 cm^{-1} region of the pyO ligand and the pyO/py-^{18}O mixture obtained in this work is shown in figure 2.1.9, where splitting of some of the O-18 sensitive bands is observed for the pyO/py-^{18}O mixture. The appearance of two well defined bands is more noticeable in the spectrum of the Zeise's salt derivative [$Pt(C_2H_4)$(py-^{18}O)Br_2] and provides further evidence that supports the O-18 sensitivity of certain modes. This will be discussed further in section 2.3.2.

It must be pointed out that due to the low enrichment of the labelled ligand obtained (approximately 35 %) and its extremely hygroscopic nature, the ir spectrum shows a considerable amount of water (very strong broad absorption at 3400 cm^{-1}). Although the frequencies obtained

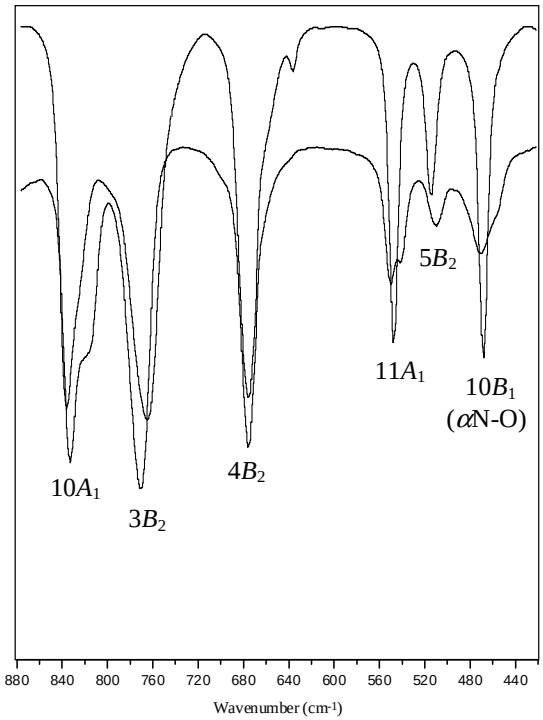

Figure 2.1.9. Spectra for pyO (top) and pyO/py-^{18}O. Two bands are observed for the O-18 sensitive modes $10A_1$ and $11A_1$ in the spectrum for the pyO/py-^{18}O mixture. A shoulder is observed for mode $10B_1$ (αN-O).

for the spectrum of the pyO/py-^{18}O mixture have been included in table 2.1.4, it is important to note that the shifts observed may be reflective of hydrogen bonding more than O-18 labelling, as many bands are solvent sensitive, particularly the mode assigned to the νN-O stretch [5, 6]. Only the appearance of two bands or shoulders is indicative of the pyO/py-^{18}O mixture, and hence it is only modes $10A_1$, $11A_1$ and $10B_1$ that can be accounted for as O-18 sensitive modes from the spectrum recorded, as is shown in figure 2.1.9.

Previous work on the pyO system [11 and references therein] has shown that the modes observed at 1250, 840, 470 and 280 cm^{-1} are N-O vibrations. They have been assigned as νN-O (coupled), νring(coupled), αN-O (pure) and γN-O (coupled) vibrations respectively. The results obtained in this work support the previous assignments of mode $6A_1$ at 1250 cm^{-1} having the highest νN-O character. Mode $10A_1$ at *ca.* 840 cm^{-1} is indeed an O-18 sensitive mode, as can be seen from the splitting of this band into two bands that account for the pyO/py-^{18}O mixture. The same can be

said for the pure αN-O mode at *ca.* 470 cm^{-1}. However, modes $10A_1$ and $11A_1$ that show equivalent O-18 sensitivity both show radial displacements in the same direction of the N and O atoms. Their O-18 sensitivity is hence not indicative of a pure νN-O stretch mode but rather indicates equivalent strong coupling to the N-O stretch, mode $6A_1$. It is perhaps mode $7A_1$ that reveals a new point of interest. It can be considered a coupled ring vibration and νN-O mode. However, this mode has a strong dependence to the N-O bond length and may become the highest character νN-O vibration for long N-O bond distances.

It is interesting to note that the calculated $\Delta\nu$ values for the out-of-plane vibrations $3B_2$ and $6B_2$ are evidential of the former mode having considerable γN-O character in py-d_5O, a situation which is not observed for the pyO system, indicative of increased deuteration coupling between the γN-O and the umbrella modes such that their assignments are reversed.

Finally, it is worth mentioning that most of the bands that are sensitive to a variation in the bond length are also sensitive to O-18 substitution, as would be expected despite the fact that the former consideration involves a change in the N-O force constant, while the latter is strictly a mass effect.

2.2. Vibrational spectra of quinoline *N*-oxide and its isotopomers

The assignment of the vibrational spectra of Zeise's salt derivatives with quinoline *N*-oxide (quinO) requires a complete understanding of the fundamental vibrations of this ligand. For that reason, the labelling studies of quinO were supported by DFT calculations of the ligands performed at the B3LYP level with the 6-31 G** basis set.

Assignments for quinoline *N*-oxide were extensively performed by Thornton and his co-workers [19, 21, 26, 27] based on the ν_D/ν_H ratios observed for quinoline-d_0, quinoline-d_7, (quinO and quin-d_7O), as well as on vibrational assignments performed on naphthalene and monosubstituted naphthalenes. As a result of these studies, Thornton and Watkins cautioned the use of extended normal modes of aromatic homocyclic systems to their heterocyclic analogues [28]. The question is then raised on whether or not a similar set of rules may be developed for substituted naphthalenes and their *N*-oxide analogues as Varsányi and Szöke established for substituted benzenes [29], and which was extended to various azine *N*-oxides [30-32].

In light of the caution in the use of the vibrational assignment of aromatic homocycles to their heterocyclic analogues [28] and following the ideas used in these assignments of quinoline *N*-oxide and its deuterated analogue, DFT calculations were performed on naphthalene, naphthalene-d_8, 1-fluoronaphthalene, quinoline, quinoline-d_7, quinoline *N*-oxide, quinoline-d_7 *N*-oxide and quinoline *N*-oxideO-18 (-d_0 and -d_7, O-18 labelled) in order to establish whether or not the normal modes obtained for molecules related to naphthalene can be extended from those of naphthalene.

A considerable amount of vibrational coupling is observed in the naphthalene molecule and an idealized representation of the normal modes of vibration for this molecule encumbers the assignment of the normal modes obtained for related molecules. From the cartesian displacement diagrams obtained in this study, a relationship to the normal modes of vibration of the naphthalene fundamentals can readily be performed for some of the normal modes obtained for the molecules studied. However, this is not the case for all the normal modes, as will be explained later.

The frequencies obtained for the molecules studied were rescaled using the values reported in the literature and those obtained experimentally in this work. In all cases a linear relationship was obtained between experimental and calculated frequencies. For some species, better fits were obtained by excluding the νC-H vibrations in the 3100-3000 cm^{-1} region and working only with the 1700-100 cm^{-1} region.

The symmetry of all modes has been determined considering that the molecules lie in the *xy* plane.

2.2.1. Naphthalene-d_0 and naphthalene-d_8

The assignment of the fundamental vibrations of naphthalene and its perdeuterated analogue has been the object of many studies [33-42] and it was only in 1980 that a less unambiguous assignment of the 48 fundamental vibrations of this molecule was made with the works of Behlen, *et al.* [41] and Sellers, *et al.* [42]. The latter group carried out *ab initio* calculations and scaled the diagonal force constants obtained for naphthalene by extension of the scale factors obtained for the benzene molecule. This allowed for the re-assignment of several of the fundamentals and perhaps remains the most complete work performed on the vibrational

assignment of the naphthalene-d_0 and naphthalene-d_8 fundamentals. The naphthalene and perdeuterated naphthalene cations have been examined [43] and, in more recent work, DFT calculations have been used in order to assign the vibrational spectrum of naphthalene-d_0 and naphthalene-d_8 in the lowest excited triplet state [44]. DFT calculations have also been recently employed to assign the vibrational spectrum of naphthalene and related annulene molecules [45] and correlations have been attempted with the normal modes of naphthalene.

The normal modes obtained for naphthalene-d_0 and naphthalene-d_8 very closely resemble those reported in the literature [35, 37, 39] and are in good agreement with the re-assignment of several of these modes performed in later work [42]. The normal modes obtained for the in-plane and out of plane vibrations for both molecules are shown in figures 2.2.1-2.2.3. Table 2.2.1 shows the experimental and calculated rescaled frequencies obtained for naphthalene-d_0 and naphthalene-d_8 by means of DFT calculations.

The assignment performed in this work is in excellent agreement with the re-assignment of the vibrational spectra of naphthalene-d_0 and naphthalene-d_8 performed by Sellers, *et al*. [42], except for the assignment of mode $5B_{1g}$ in naphthalene-d_8. The authors reported mode $5B_{1g}$ as occurring at 828 cm^{-1} having obtained the calculated value of 833 cm^{-1}, and mode 6 B_{1g} at 1027 cm^{-1} with a calculated value of 1030 cm^{-1}. No cartesian displacement diagrams for the normal modes obtained are included in their work, but it seems likely that the mode assigned by them as $5B_{1g}$ in naphthalene-d_8 is in fact mode $6B_{1g}$ (figures 2.2.1 and 2.2.2). This corrects the very low ν_D/ν_H ratio of 0.668 obtained by them for mode $5B_{1g}$, to 0.826, which is consistent with a coupled ring C-H vibration and agrees with the assignment performed previously by other authors [37, 39-41]. The ν_D/ν_H ratio for mode $6B_{1g}$ changes from 0.934 to 0.759, a value that is more consistent with the assignment of this mode to an in-plane C-H bending mode.

The normal modes of naphthalene (figures 2.2.1-2.2.3) have been included in an effort to correlate the normal modes of vibration obtained for quinoline and quinoline *N*-oxide and their deuterated analogues, to the normal modes of naphthalene.

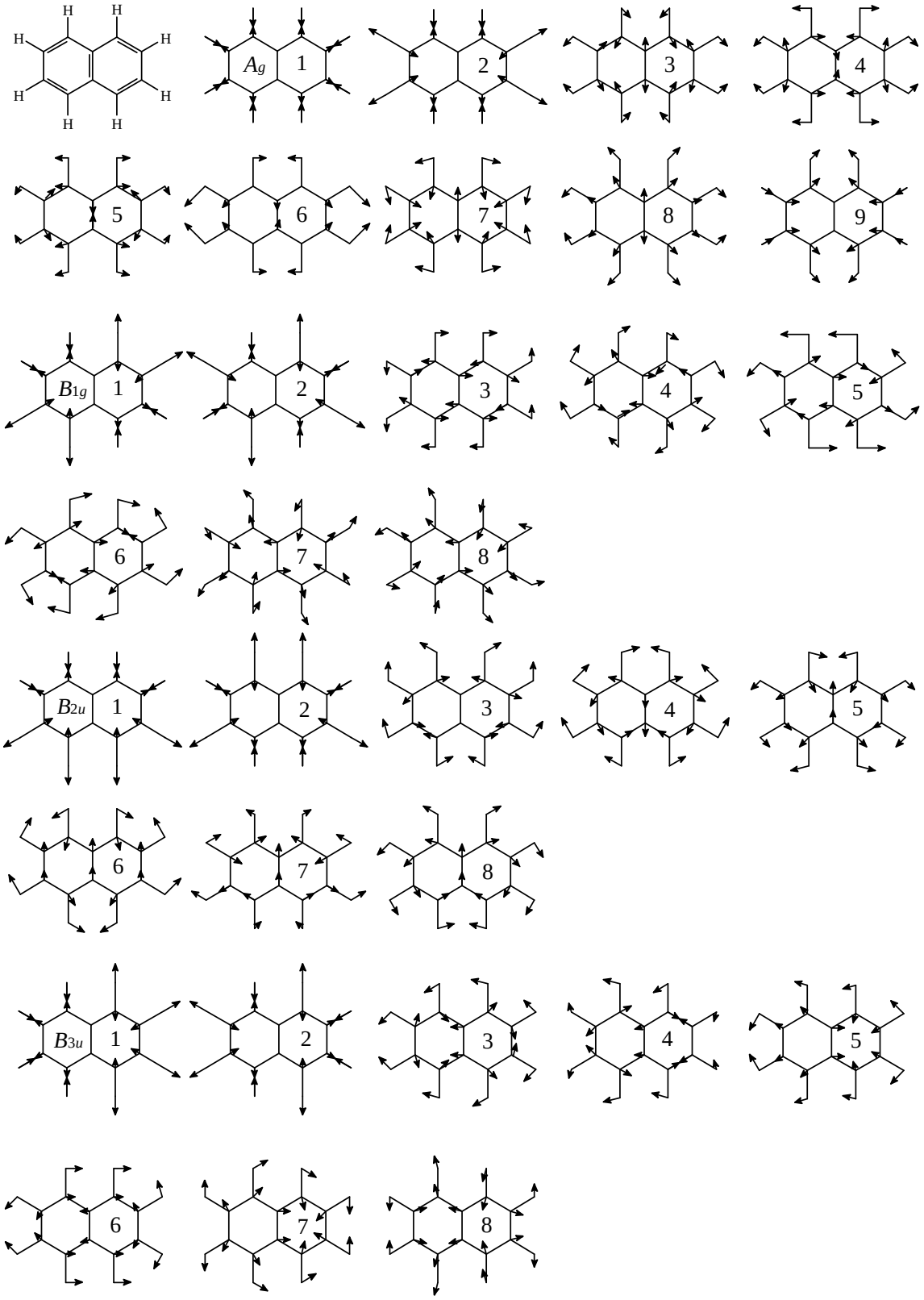

Figure 2.2.1. In-plane vibrations for naphthalene-d_0

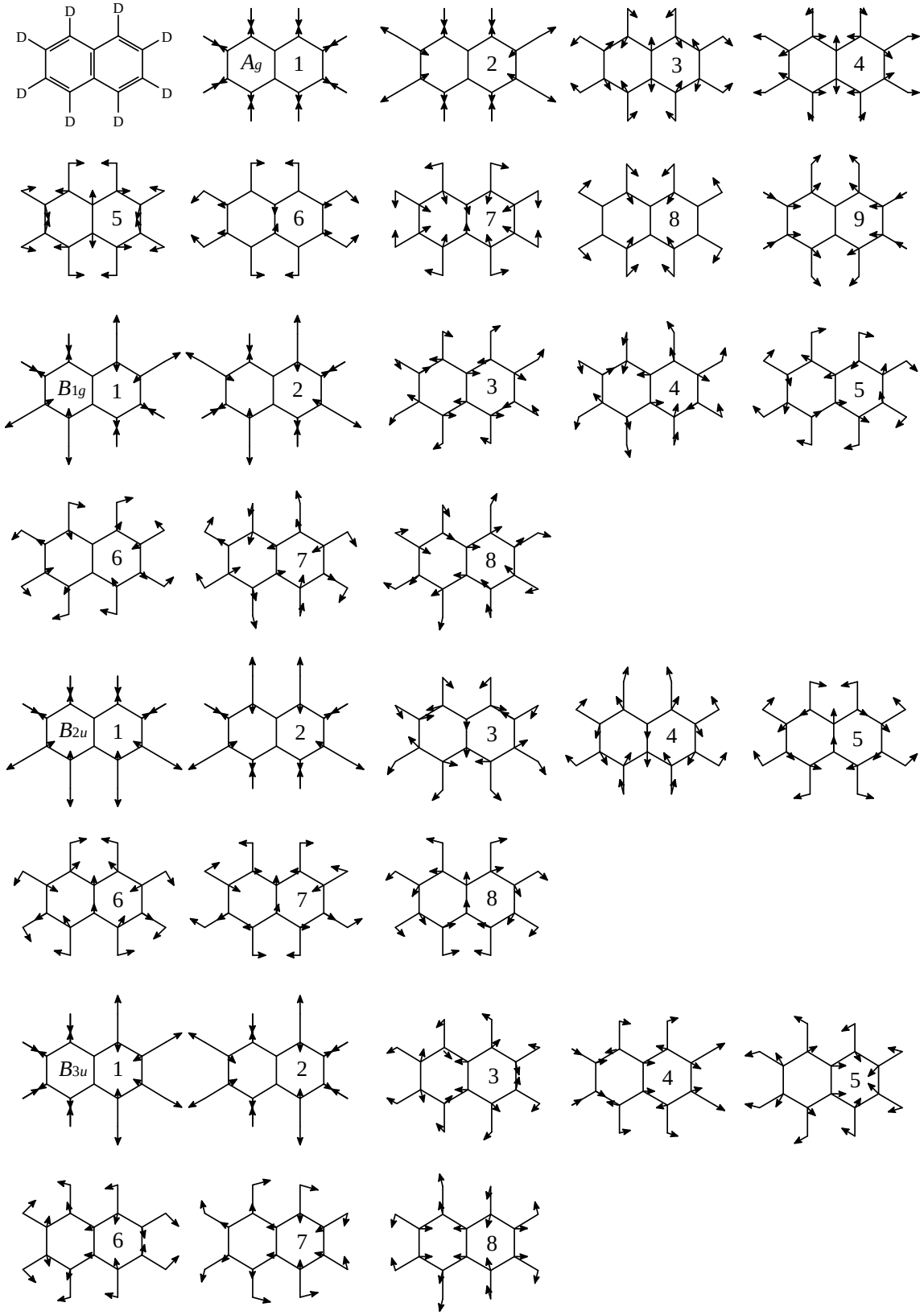

Figure 2.2.2. In-plane vibrations for naphthalene-d_8

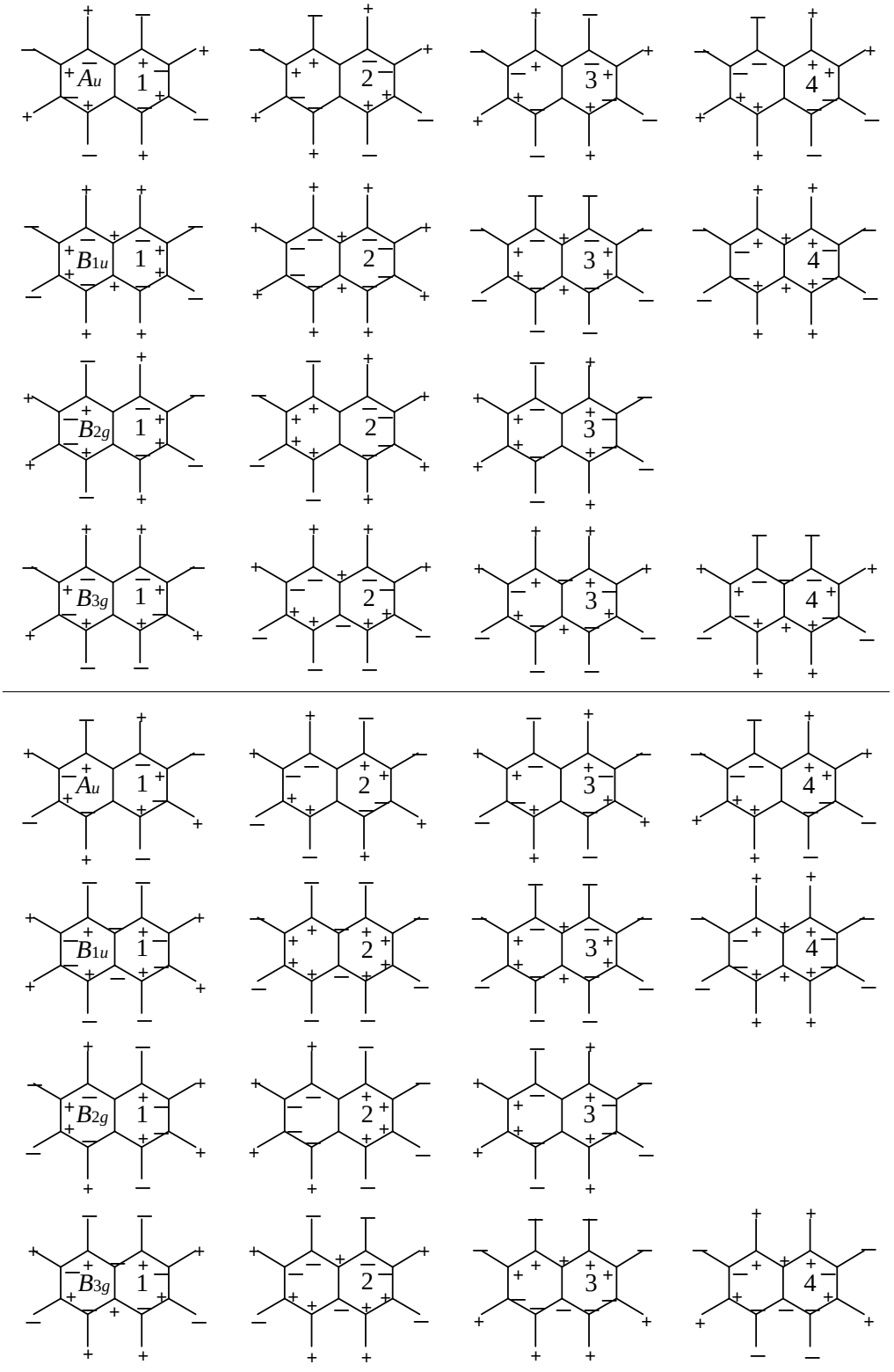

Figure 2.2.3. Out-of-plane vibrations for naphthalene-d_0 (top 15) and naphthalene-d_8 (bottom 15).

Table 2.2.1 Experimental [19, 26] and calculated rescaled frequencies (in brackets) for naphthalene-d_0 and naphthalene-d_8. All frequency values in cm^{-1}. Values for the spectroscopically inactive A_u vibrations are those estimated by Sellers, *et al.* [42]. In assigning the symmetry of the modes obtained, the naphthalene molecule lies on the *xy* plane.

In-plane frequencies of naphthalene-d_0 and naphthalene-d_8

		naphthalene-d_0	naphthalene-d_8	ν_D/ν_H			naphthalene-d_0	naphthalene-d_8	ν_D/ν_H
A_g	1	3086 [3068]	2291 [2293]	0.742 [0.747]	B_{1g}	1	3051 [3054]	2276 [2280]	0.746 [0.747]
	2	3030 [3044]	2276 [2265]	0.751 [0.744]		2	3006 [3037]	2261 [2256]	0.742 [0.743]
	3	1576 [1571]	1545 [1550]	0.980 [0.987]		3	1629 [1625]	1605 [1603]	0.985 [0.986]
	4	1464 [1452]	1298 [1291]	0.887 [0.889]		4	1458 [1450]	1353 [1361]	0.928 [0.939]
	5	1383 [1370]	1386 [1378]	1.002 [1.006]		5	1243 [1233]	1027 [1010]	0.826 [0.819]
	6	1163 [1154]	840 [833]	0.722 [0.722]		6	1158 [1143]	879 [876]	0.759 [0.766]
	7	1020 [1025]	862 [863]	0.845 [0.842]		7	936 [924]	828 [826]	0.885 [0.894]
	8	765 [762]	697 [692]	0.911 [0.908]		8	509 [515]	493 [496]	0.969 [0.963]
	9	512 [519]	494 [496]	0.965 [0.956]					
B_{2u}	1	3056 [3056]	2278 [2282]	0.745 [0.747]	B_{3u}	1	3060 [3066]	2284 [2292]	0.746 [0.747]
	2	3027 [3039]	2258 [2258]	0.746 [0.743]		2	3029 [3040]	2261 [2262]	0.746 [0.744]
	3	1601 [1611]	1552 [1556]	0.969 [0.966]		3	1508 [1508]	1445 [1448]	0.958 [0.960]
	4	1387 [1388]	1257 [1243]	0.906 [0.895]		4	1361 [1362]	1312 [1323]	0.964 [0.971]
	5	1268 [1258]	1045 [1036]	0.824 [0.823]		5	1210 [1204]	1082 [1090]	0.894 [0.905]
	6	1128 [1125]	884 [878]	0.784 [0.780]		6	1163 [1144]	857 [836]	0.737 [0.731]
	7	789 [789]	738 [734]	0.935 [0.930]		7	1010 [1016]	831 [830]	0.823 [0.817]
	8	359 [360]	328 [335]	0.914 [0.930]		8	618 [627]	590 [599]	0.955 [0.955]

Out-of-plane frequencies of naphthalene-d_0 and naphthalene-d_8

		naphthalene-d_0	naphthalene-d_8	ν_D/ν_H			naphthalene-d_0	naphthalene-d_8	ν_D/ν_H
A_u	1	981 [965]	815 [790]	0.831 [0.819]	B_{1u}	1	955 [945]	791 [778]	0.828 [0.823]
	2	825 [834]	647 [656]	0.784 [0.787]		2	780 [785]	629 [633]	0.806 [0.806]
	3	622 [622]	531 [544]	0.854 [0.875]		3	474 [482]	404 [415]	0.852 [0.861]
	4	188 [192]	169 [181]	0.899 [0.943]		4	166 [177]	153 [171]	0.922 [0.966]
B_{2g}	1	951 [929]	761 [744]	0.800 [0.801]	B_{3g}	1	983 [973]	838 [832]	0.852 [0.855]
	2	717 [720]	545 [547]	0.760 [0.760]		2	875 [878]	766 [761]	0.875 [0.867]
	3	385 [390]	348 [351]	0.904 [0.900]		3	772 [766]	646 [644]	0.837 [0.841]
						4	470 [474]	413 [426]	0.879 [0.899]

2.2.2. Quinoline-d_0 and quinoline-d_7

Based on the previous works of Chiorboli and Bertoluzza [49] and the normal coordinate analysis performed by Wait and McNerney [50], assignments for quinoline and deuterated quinoline have previously been performed by Thornton and co-workers [19, 21, 26, 46-48] for both the ligands and coordination compounds. Substituted quinolines like 8-hydroxyquinoline have also been assigned on the basis of the quinoline fundamentals [51]. In more recent work, Ferri and Bürgi have employed DFT calculations to obtain some of the quinoline vibrations as well as the frequencies obtained for the ligands adsorbed on Pt [52]. This very recent study still employs the assignments for quinoline reported by Wait and McNerney [50] and Srivastava, *et al*. [51].

DFT calculations performed on quinoline-d_0 and quinoline-d_7 yield a molecule with C_s symmetry. A total number of 45 modes of vibration of *A*' and *A*'' symmetry (in-plane and out-of plane, respectively) are obtained for the isotopomers modelled; 31 in-plane modes and 14 out-of-plane modes. Although the lowering in symmetry makes all of the in-plane vibrations of naphthalene fall into one class, (A_g, B_{1g}, B_{2u}, B_{3u}) $\rightarrow$ *A*', and all of the out-of-plane vibrations into another, (A_u, B_{1u}, B_{2g}, B_{3g}) $\rightarrow$ *A*'', almost all of the modes obtained for quinoline-d_0 and quinoline-d_7 can be identified with the normal modes of naphthalene-d_0 and naphthalene-d_8. The most significant differences are observed for the seven C-H stretching frequencies and for the out-of-plane vibrations, as will be discussed below.

The normal modes of quinoline-d_0 and quinoline-d_7 are shown in figures 2.2.4-2.2.6. Table 2.2.2 shows the experimental and calculated rescaled frequencies obtained for these molecules. The poor fit in some cases between the two molecules re-emphasizes the need for caution in basing the assignment of aromatic heterocycles on those of their homocyclic analogues. The modes have been related to the naphthalene vibrations where possible. Infrared spectra of quinoline-d_0 and quinoline-d_7 are shown in figure 2.2.7.

2.2.2.1 In-plane vibrations

From the normal modes obtained for quinoline-d_0 and quinoline-d_7, it can be seen that most can be related to the naphthalene-d_0 and naphthalene-d_8 fundamentals. Some of the variations observed will be explained in the following discussion using the labelling scheme depicted for quinoline in figure 2.2.8, in which the rings have been labelled as A and B and the hydrogen atoms have been labelled according to the numbering scheme employed for the carbon atoms.

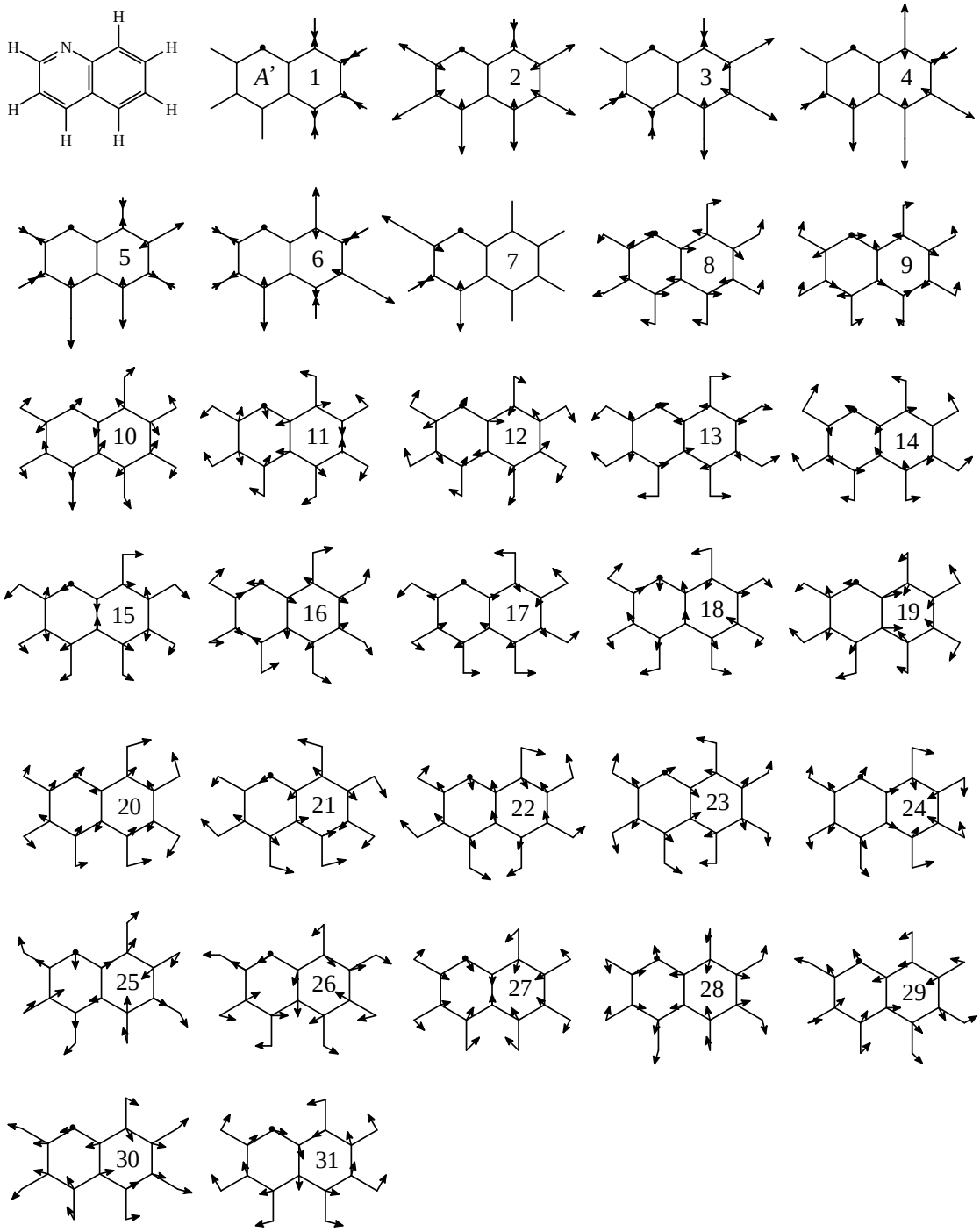

Figure 2.2.4. In-plane vibrations for quinoline-d_0

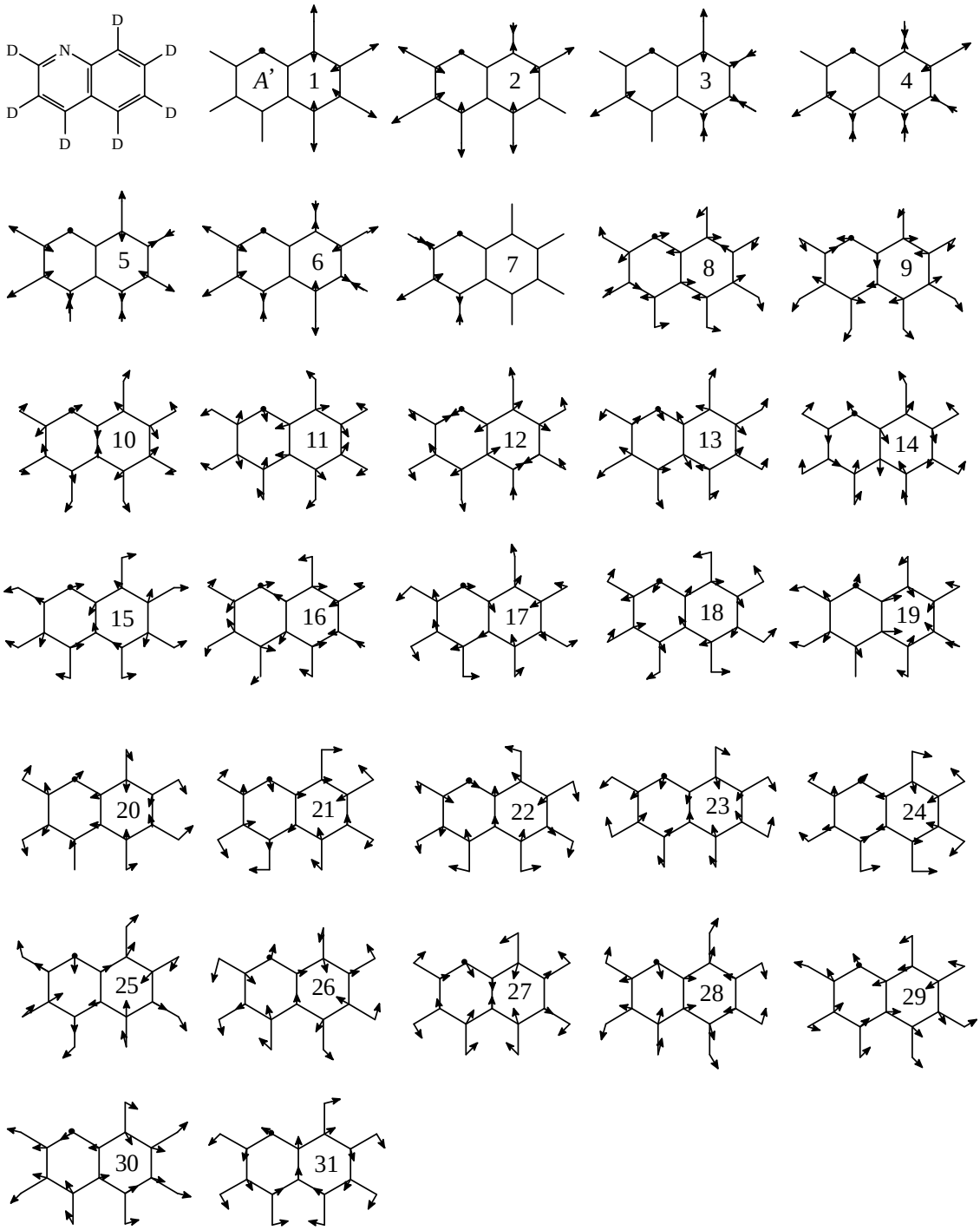

Figure 2.2.5. In-plane vibrations for quinoline-d_7

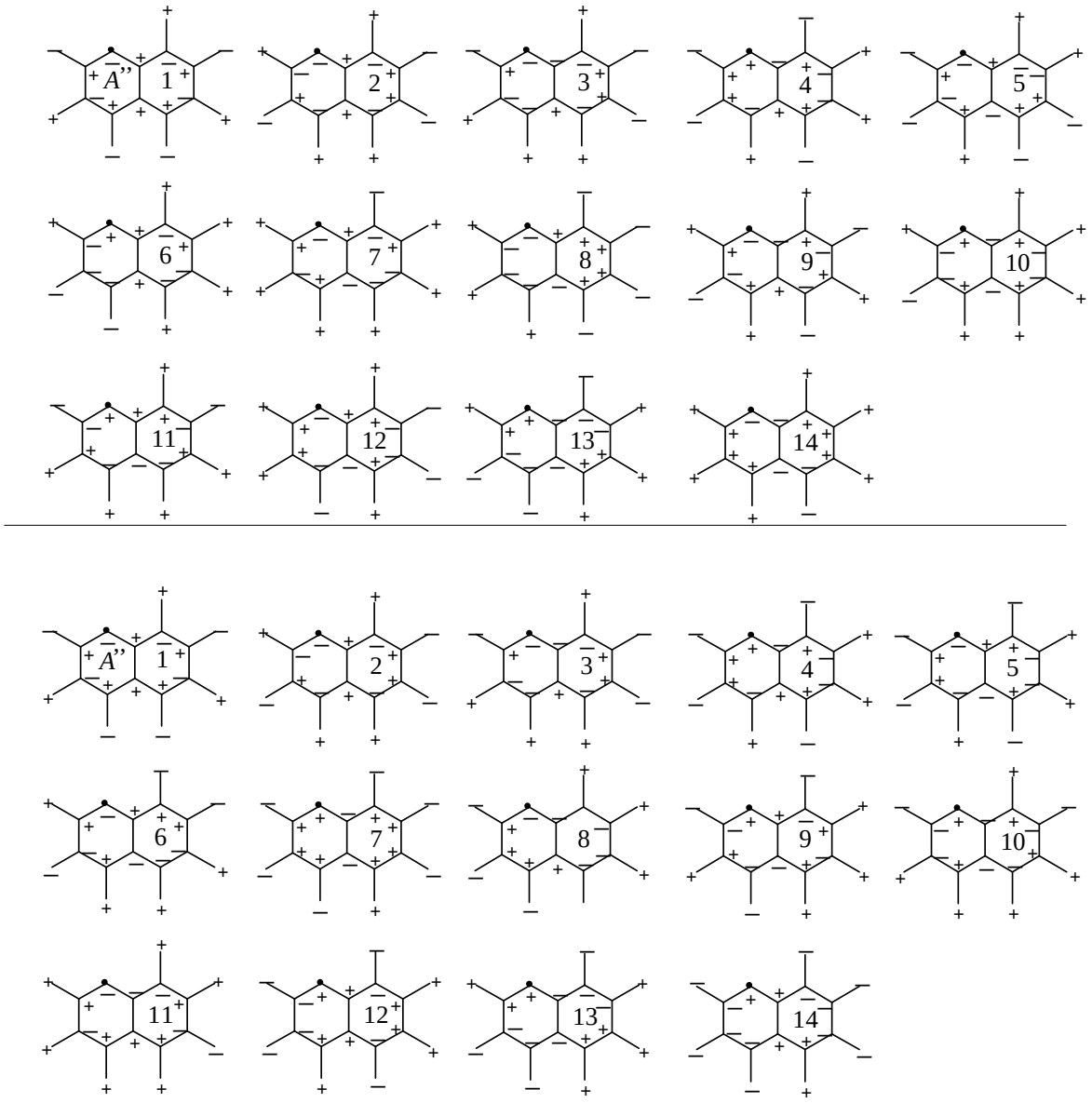

Figure 2.2.6. Out-of-plane vibrations for quinoline-d_0
(top 14) and quinoline-d_7 (bottom14).

Table 2.2.2. Experimental and calculated frequencies for quinoline-d_0 and quinoline-d_7, showing naphthalene related modes. Calculated values in brackets. All frequency values in cm^{-1}.

vibration		naphthalene mode	quinoline-d_0	quinoline-d_7	ν_D/ν_H
A'	1	$1A_g$	3078* [3082]	2287* [2296]	0.743 [0.745]
	2		3078* [3074]	2287* [2291]	0.743 [0.745]
	3		3057 [3069]	2287* [2285]	0.748 [0.744]
	4		3057 [3055]	2276 [2268]	0.744 [0.742]
	5		3037 [3047]	2254 [2262]	0.742 [0.742]
	6		3037 [3043]	2254 [2256]	0.742 [0.741]
	7	$2B_{1g}$	3014 [3022]	2243 [2244]	0.744 [0.742]
	8	$3B_{1g}$	1620 [1625]	1586 [1591]	0.979 [0.979]
	9	$3B_{2u}$	1596 [1604]	1552 [1558]	0.972 [0.971]
	10	$3A_g$	1571 [1569]	1542 [1541]	0.981 [0.982]
	11	$3B_{3u}$	1501 [1505]	1439 [1441]	0.959 [0.957]
	12	$4B_{1g}$	1470 [1465]	1384 [1384]	0.941 [0.945]
	13	$4A_g$	1432 [1433]	1368 [1363]	0.955 [0.951]
	14	$4B_{2u}$	1393 [1388]	1241 [1242]	0.891 [0.895]
	15	$5A_g$	1372 [1363]	1261 [1266]	0.919 [0.929]
	16	$4B_{3u}$	1314 [1333]	1284 [1291]	0.977 [0.968]
	17	$5B_{1g}$	1256 [1250]	1016 [1005]	0.809 [0.804]
	18	$5B_{2u}$	1232 [1230]	1038 [1025]	0.842 [0.833]
	19	$5B_{3u}$	1192 [1210]	1094 [1096]	0.918 [0.906]
	20	$6B_{3u}$	1147* [1145]	838* [835]	0.731 [0.729]
	21	$6B_{1g}$	1141 [1137]	827 [819]	0.725 [0.720]
	22	$6B_{2u}$	1118 [1115]	878 [872]	0.785 [0.782]
	23	$7A_g$	1033 [1031]	863 [854]	0.835 [0.828]
	24	$7B_{3u}$	1013 [1014]	827 [826]	0.816 [0.815]
	25	$7B_{1g}$	939 [927]	893 [883]	0.951 [0.952]
	26	$7B_{2u}$	805 [810]	752 [751]	0.934 [0.927]
	27	$8A_g$	760 [755]	698 [695]	0.918 [0.920]
	28	$8B_{3u}$	611 [612]	591 [595]	0.967 [0.972]
	29	$8B_{1g}$	522 [521]	506 [509]	0.969 [0.977]
	30	$9A_g$	522 [519]	506 [506]	0.969 [0.975]
	31	$8B_{2u}$	377 [377]	347 [353]	0.920 [0.936]
A''	1	$1B_{3g}$	980 [976]	838 [835]	0.855 [0.855]
	2	$1A_u$	971† [971]	827 [807]	0.852 [0.831]
	3	$1B_{1u}$	954 [944]	782 [774]	0.820 [0.820]
	4	$1B_{2g}$	954 [942]	752 [746]	0.788 [0.792]
	5	$2B_{3g}$	867 [866]	782 [780]	0.902 [0.901]
	6	$2B_{1u}$	805 [807]	643 [646]	0.799 [0.800]
	7	$2A_u$	786 [785]	668 [655]	0.850 [0.834]
	8	$2B_{2g}$	738 [737]	570 [573]	0.772 [0.777]
	9	$3A_u$	628 [631]	544 [550]	0.866 [0.872]
	10	$3B_{1u}$	479 [486]	419 [430]	0.875 [0.885]
	11	$4B_{3g}$	467* [475]	410 [423]	0.878 [0.890]
	12	$3B_{2g}$	392 [399]	353 [365]	0.900 [0.915]
	13	$4A_u$, $4B_{1u}$	194 [191]	174 [180]	0.897 [0.942]
	14	$4B_{1u}$, $4A_u$	181 [180]	169 [173]	0.934 [0.961]

* Shoulder

† Raman band; not observed in ir spectrum. Taken from reference 50.

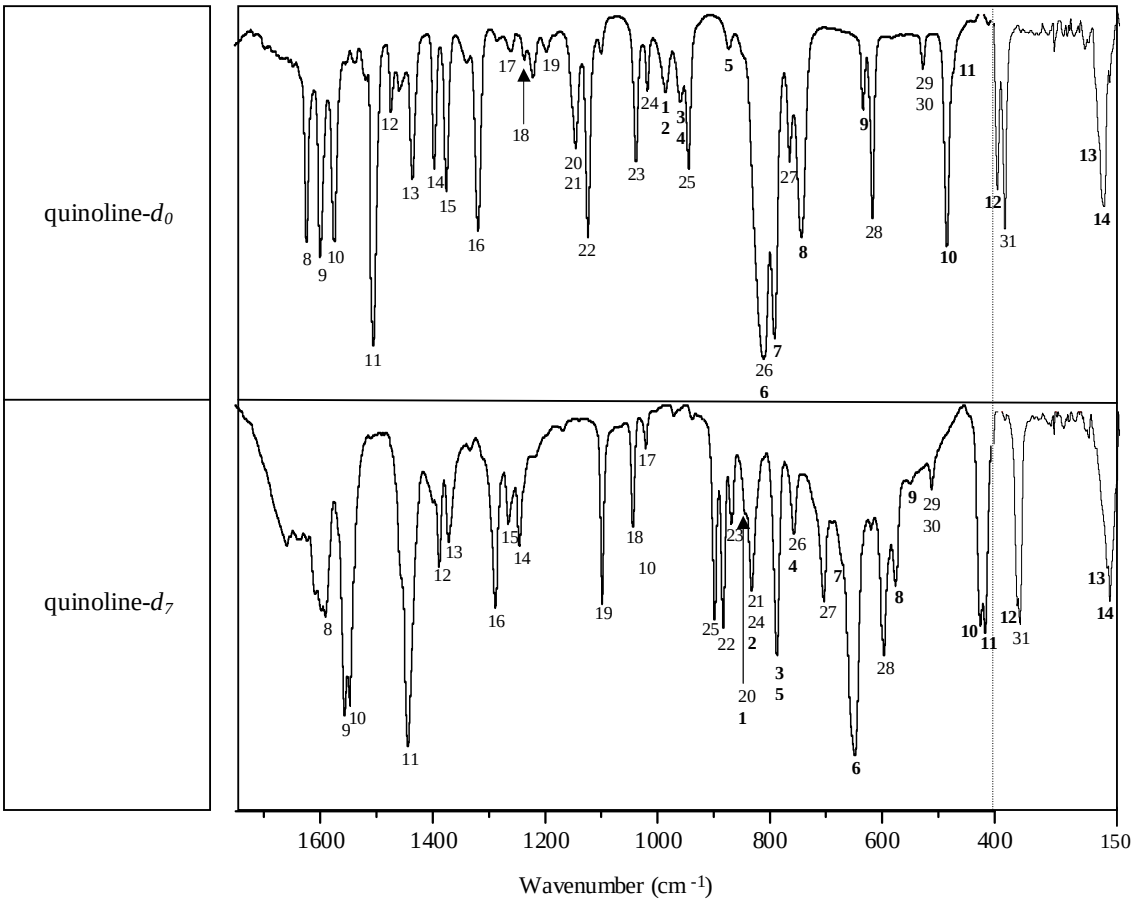

Figure 2.2.7. Mid and far ir spectra of quinoline-d_0 and quinoline-d_7 showing the in-plane and out-of-plane (bold) fundamentals

Wait and McNerney [50] carried out normal coordinate analysis calculations for the quinoline-d_0 molecule and assigned the fundamentals based on ir and Raman spectra as well as depolarization studies performed on the Raman spectrum of this compound. Out of the 31 in-plane fundamentals, twelve vibrations assigned by the authors have been re-assigned in the present work with the remaining nineteen in-plane vibrations matching the assignments previously performed. Three of the fourteen out-of-plane fundamentals have been re-assigned based on the calculated values obtained in this work. The assignment of the remaining eleven out-of-plane fundamentals matches that performed by the authors previously. The extensive suggested changes

are a reflection of the difficulty in vibrational assignment of a molecule of low symmetry, and highlight the role of molecular modelling studies in aiding such vibrational analyses.

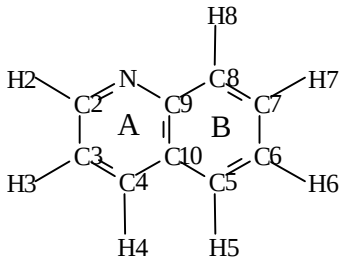

Figure 2.2.8. Labelling scheme employed for quinoline.
The molecule lies on the *xy* plane.

The carbon hydrogen stretching vibrations occur as a broad medium intensity band in the region 3100-3000 cm^{-1} for quinoline-d_0 and 2290-2240 cm^{-1} for quinoline-d_7. Very few of the normal modes obtained can be related to any of the naphthalene fundamentals, as all show displacements of different magnitudes for the hydrogen atoms and these displacements occur more noticeably in one ring than in the other. The 1*A*' vibration involves a symmetric displacement of all H atoms in the molecule and is in this way closely related to the $1A_g$ naphthalene-d_0 fundamental, although Wait and McNerney related this vibration to the $1B_{3u}$ naphthalene-d_0 fundamental. The authors show no displacement diagrams in their work, and it is unclear if this assignment has been performed on the basis of the normal mode obtained, or by comparison with the naphthalene-d_0 frequencies and the order at which they appear for that molecule. Displacements are considerably greater for the H atoms on ring A than for those on ring B, which hardly move at all. This is reversed in mode 2*A*', where the greater displacement is observed for the hydrogens on ring B than on ring A. This indicates that for the imine system, the heterocyclic ring and homocyclic ring can be considered as being independent of each other for these two vibrations. Mode 2*A*' shows a symmetric displacement of all hydrogen atoms, except H8, which contracts while all the rest expand. The rest of the normal modes, with the exception of 7*A*' which resembles the $2B_{1g}$ naphthalene vibration, can be explained as linear combinations of the naphthalene fundamentals, where the loss in symmetry allows for all of the internal coordinates to partake of any of the modes. Fewer bands than expected are obtained in the spectrum, but the calculations performed

show that certain bands should appear very close to others and they have been assigned accordingly in both isotopomers.

In light of the calculated values obtained in this work, it is likely that some combination bands were assigned as fundamentals in Wait and McNerney's work. Of the twelve in-plane modes that have been re-assigned, four are νC-H modes. The fact that bands overlap in this region makes the unambiguous assignment of these fundamentals difficult.

All of the remaining in-plane vibrations in both isotopomers can be related to the naphthalene fundamentals and the most important differences will be discussed below. Wait and McNerney assigned several of the modes associated to the naphthalene fundamentals differently. As was mentioned previously, it is unclear how these assignments were made due to the fact that no displacement diagrams are shown. Table 2.2.3 shows the experimental and calculated frequencies reported by Wait and McNerney [50] and those obtained in this work. The nomenclature employed and the relation to the naphthalene fundamentals is also shown.

Assignments for quinoline *N*-oxide performed by Watkins and co-workers [19, 21, 26, 27] assumed that the absent mode in quinoline would be present in the *N*-oxide as the one with a high αN-O character. This does not seem to be the case, as the $6A_g$ mode is necessary to explain the highly coupled modes obtained for quinO. It is in fact another vibration that couples with the αN-O in-plane bend, as will be discussed in section 2.2.3.

In order of decreasing frequencies and considering those in-plane vibrations below 1630 cm^{-1} (modes 8*A*'-31*A*'), three pairs of modes are inverted in the quinoline molecule when compared to the naphthalene vibrations. In naphthalene-d_0, mode $4A_g$ occurs before mode $4B_{1g}$, $5B_{2u}$ before $5B_{1g}$ and $9A_g$ before $8B_{1g}$, three of which involve C-H vibrations. All the remaining modes occur in the same order. The lower energy ring modes (modes 25-31*A*') are identical to the naphthalene fundamentals.

Assignments performed previously by Thornton and Watkins for quinoline and its perdeuterated analogue [26] failed to yield the proper modes due to these inversions, but more so, due to the fact that the strongest tool used in this assignment was the ν_D/ν_H ratio obtained for the naphthalene-d_0 and naphthalene-d_8 isotopomers. Hence, of the in-plane vibrations for quinoline-d_0, only modes 8, 11-13, 19, 22 and 27-31 agree with the assignment performed for

Table 2.2.3. Experimental and calculated frequencies for quinoline-d_0 vibrations, and their relation to naphthalene-d_0 modes as reported by Wait and McNerney[a] [50] and as obtained in this work[b]. All values in cm^{-1}. In relating the quinoline-d_0 fundamentals to the naphthalene-d_0 vibrations, the nomenclature employed by Wait and McNerney has been kept, in which the naphthalene molecule lies on the *yz* plane.

In-plane frequencies of quinoline-d_0								
Vibration[a]	Naphthalene mode[a]	Exp.[a]	Calc.[a]	Vibration[b]		Naphthalene mode[b]	Exp.[b]	Calc.[b]
ν_1	$1B_{2u}$	3086	3064	*A*'	1	$1A_g$	3078*	3082
ν_2	$1A_g$	3056	3058		2		3078*	3074
ν_3	$1B_{3g}$	3056	3058		3		3057	3069
ν_4	$2B_{1u}$	3036	3043		4		3057	3055
ν_5	$2A_g$	3014	3008		5		3037	3047
ν_6	$2B_{2u}$	3004	3004		6		3037	3043
ν_7	$2B_{3g}$	2979	3002		7	$2B_{3g}$	3014	3022
ν_8	$3B_{3g}$	1619	1609		8	$3B_{3g}$	1620	1625
ν_9	$3B_{1u}$	1593	1578		9	$3B_{1u}$	1596	1604
ν_{10}	$3A_g$	1571	1551		10	$3A_g$	1571	1569
ν_{11}	$3B_{2u}$	1500	1501		11	$3B_{2u}$	1501	1505
ν_{12}	$4A_g$	1469	1457		12	$4B_{3g}$	1470	1465
ν_{13}	$4B_{3g}$	1431	1427		13	$4A_g$	1432	1433
ν_{14}	$4B_{1u}$	1392	1390		14	$4B_{1u}$	1393	1388
ν_{15}	$5A_g$	1371	1377		15	$5A_g$	1372	1363
ν_{16}	$4B_{2u}$	1314	1308		16	$4B_{2u}$	1314	1333
ν_{17}	$5B_{1u}$	1256	1252		17	$5B_{3g}$	1256	1250
ν_{18}	$5B_{2u}$	1216	1213		18	$5B_{1u}$	1232	1230
ν_{19}	$5B_{3g}$	1192	1186		19	$5B_{2u}$	1192	1210
ν_{20}	$6A_g$	1140	1155		20	$6B_{2u}$	1147*	1145
ν_{21}	$6B_{1u}$	1118	1124		21	$6B_{1g}$	1141	1137
ν_{22}	$6B_{3g}$	1095	1115		22	$6B_{1u}$	1118	1115
ν_{23}	$7A_g$	1031	1008		23	$7A_g$	1033	1031
ν_{24}	$7B_{2u}$	1013	996		24	$7B_{2u}$	1013	1014
ν_{25}	$7B_{3g}$	953	927		25	$7B_{3g}$	939	927
ν_{26}	$7B_{1u}$	785	793		26	$7B_{1u}$	805	810
ν_{27}	$8A_g$	760	778		27	$8A_g$	760	755
ν_{28}	$8B_{2u}$	611	620		28	$8B_{2u}$	611	612
ν_{29}	$9A_g$	521	480		29	$8B_{3g}$	522	521
ν_{30}	$8B_{3g}$	505[c]	475		30	$9A_g$	522	519
ν_{31}	$8B_{1u}$	377	390		31	$8B_{1u}$	377	377

* Shoulder.

c Estimated wavenumber.

Table 2.2.3. (continued)

Out-of-plane frequencies of quinoline-d_0								
Vibration[a]	Naphthalene mode[a]	Exp.[a]	Calc.[a]	Vibration[b]		Naphthalene mode[b]	Exp.[b]	Calc.[b]
ν_{32}	$1B_{2g}$	980	1057	A"	1	$1B_{2g}$	980	976
ν_{33}	$1A_u$	970	1045	2		$1A_u$	971†	971
ν_{34}	$1B_{1g}$	939	940	3		$1B_{3u}$	954	944
ν_{35}	$2B_{2g}$	867	904	4		$1B_{1g}$	954	942
ν_{36}	$2A_u$	840	867	5		$2B_{2g}$	867	866
ν_{37}	$3B_{2g}$	804	755	6		$2B_{3u}$	805	807
ν_{38}	$2B_{3u}$	786	716	7		$2A_u$	786	785
ν_{39}	$2B_{1g}$	741	562	8		$2B_{1g}$	738	737
ν_{40}	$3A_u$	628	354	9		$3A_u$	628	631
ν_{41}	$3B_{3u}$	479	322	10		$3B_{3u}$	479	486
ν_{42}	$4B_{2g}$	472	287	11		$4B_{2g}$	467*	475
ν_{43}	$3B_{1g}$	392	226	12		$3B_{1g}$	392	399
ν_{44}	$4A_u$	192	140	13		$4A_u$	194	191
ν_{45}	$4B_{3u}$	178	109	14		$4B_{3u}$	181	180

† Taken from reference 50.
* Shoulder.

both isotopomers in this work. The fact that certain vibrations appear to be accidentally degenerate as obtained from the DFT calculations (modes 20*A*' and 21*A*'; 29*A*' and 30*A*'; 26*A*' and 6*A*''; 1*A*'' and 2*A*''; and 3*A*'' and 4*A*''), obviously encumbers the assignment process. In fact, Wait and McNerney's extensive vibrational study for quinoline, assigns only two vibrations as being accidentally degenerate, a problem which arises from the fact that the calculated values obtained by means of the force-field employed seem to be in some cases (especially regarding the out-of-plane vibrations) considerably less accurate than the ones obtained in the present work, as can be seen from the values shown in table 2.2.3.

The assignments for the in-plane modes 7-17, 19, 23, 24, 27, 28, 30 and 31*A*', all occurring below 1630 cm^{-1}, match those previously performed by Wait and McNerney and other authors whose work was primarily based on theirs. The remaining eight in-plane modes have been re-assigned as will be discussed below.

As can be seen from tables 2.2.1 and 2.2.2, the ν_D/ν_H ratios are quite close for quinoline-d_0 and quinoline-d_7 when compared to naphthalene-d_0 and naphthahlene-d_8. The employment of the naphthalene ν_D/ν_H ratios in the assignment problem is useful in comparing ring vibrations with those of C-H vibrations, and can highlight isotope induced coupling or decoupling, but is susceptible to errors where there is no difference in coupling between isotopomers. Consequently, it must be performed with caution, as it can easily lead to errors due to the inversion in the order of some modes.

The most important differences observed when comparing the vibrations obtained for both the naphthalene and quinoline systems, and the re-assignments proposed in this work are worth discussing further. Complex formation proves a valuable tool in the assignment of fundamental frequencies that are accidentally degenerate, and in the assignment of certain bands observed in the ir spectra as either fundamentals or combination bands.

It is worth mentioning that those modes for quinoline related to the A_g modes in naphthalene (modes 10, 13, 15, 23, 27 and 30 *A*') are quite similar to the naphthalene fundamentals. In fact, the motion of the hydrogen atoms related by the *xz* and *yz* planes is in most cases kept in direction, although not in magnitude. A change in direction is observed for one mode in quinoline-d_0 (15*A*') and one mode in quinoline-d_7 (13*A*'), where hydrogens H2, H3, H6 and H7 move in directions which resemble modes of other symmetries in naphthalene.

Mode 15*A*' can be related to mode 5A_g in naphthalene and mode 14*A*' can be related to mode 4B_{2u} in naphthalene. The large ν_D/ν_H for the 5A_g mode in naphthalene is evidence of deuteration coupling of this vibration. From the displacement diagrams obtained, modes 14*A*' and 15*A*' can be explained in terms of coupling between two of the naphthalene fundamentals (4B_{2u} and 5A_g). These occur at 1387 cm^{-1} (4B_{2u}) and 1383 cm^{-1} (5A_g) in naphthalene, and at 1393 cm^{-1} (14*A*') and 1372 cm^{-1} (15*A*') in quinoline. On those grounds, the coupling between these two modes has the net effect of increasing the frequency for mode 14*A*' and lowering it for mode 15*A*', when compared to the values obtained for the naphthalene fundamentals. It is mode 15*A*' where the most significant changes are observed, as all of the carbon atoms and hydrogens H4, H5 and H8 are displaced as in mode 5A_g, but H2, H3, H5, H6 and H7 follow the direction of mode B_{2u}. This coupling is lost for quinoline-d_7, where the modes obtained resemble the naphthalene-d_8 fundamentals and are observed at 1388 cm^{-1} (4B_{2u}) and 1370 cm^{-1} (5A_g) for naphthalene-d_8 and 1389 cm^{-1} (14*A*') and 1364 cm^{-1} (15*A*') for quinoline-d_7. The extent of coupling in the

naphthalene-d_8 and quinoline-d_7 systems is hence similar, but coupling is greater for quinoline-d_0 than naphthalene-d_0.

The region between 1290-1160 cm^{-1} is difficult to assign due to the fact that at least five weak intensity absorptions can be observed at 1281, 1256, 1232, 1217 and 1192 cm^{-1}. Previous works [19, 26] have assigned the last four of these to fundamentals. However, only the bands at 1256, 1232 and 1192 cm^{-1} have been assigned as fundamentals in the present work in agreement with the calculated values of 1250, 1230 and 1210 cm^{-1} obtained, with the next calculated frequency occurring at 1145 cm^{-1}. Coordination compounds with quinoline also show the same pattern in this region, encumbering the assignment problem, as the aforementioned bands vary in intensity in the Cu(I) compounds $\{[Cu(quin)_2I]_2\}$ and $[Cu(quin)(SCN)]_n$ [53].

Wait and McNerney assigned the bands at 1256, 1217 and 1192 cm^{-1} as the 17-19*A*' fundamentals. The assignments performed in this work agree with the frequencies assigned for the 17 and 19*A*' modes as performed by the authors, but the band at 1217 cm^{-1} can be explained as a combination band (8*A*" + 10*A*") and hence mode 18*A*' has been assigned as occurring at 1232 cm^{-1} in the present work in agreement with the calculated frequency.

In addressing the band at 1217 cm^{-1} in more detail, the out-of-plane modes 8 and 10*A*'' occur as medium to strong intensity bands at 738 and 479 cm^{-1} respectively in the spectrum of quinoline-d_0. Hence the combination band 8*A*'' + 10*A*'' of 1217 cm^{-1}, adequately accounts for the weak intensity band previously assigned as a fundamental. In the spectrum for $\{[Cu(quin)_2I_2]_2\}$ the aforementioned out-of-plane modes occur at 733 and 485 cm^{-1} respectively and a combination band would be expected at *ca*. 1218 cm^{-1}. This is indeed the case for the weak intensity band that appears at 1218 cm^{-1} in the spectrum of the Cu(I) complex. Figure 2.2.9 shows the spectrum of quinoline and $\{[Cu(quin)_2I]_2\}$ and the assignment of the fundamentals in this region. Wait and McNerney assigned the band occurring at 1232 cm^{-1} as a combination band arising from the out-of-plane modes at 840 and 392 cm^{-1}, however, no band occurring at 840 cm^{-1} was observed in the ir spectra recorded in this work except for a higher wavenumber shoulder on the very intense absorption occurring at 867 cm^{-1}. Furthermore, the calculated values yield no expected frequencies close to 840 cm^{-1} except for the calculated value of 867 cm^{-1} that has been assigned as mode 5*A*''. It must be pointed out that several combinations can yield values very close to those of the weak intensity bands observed in the spectrum of quinoline in this region. The assignment

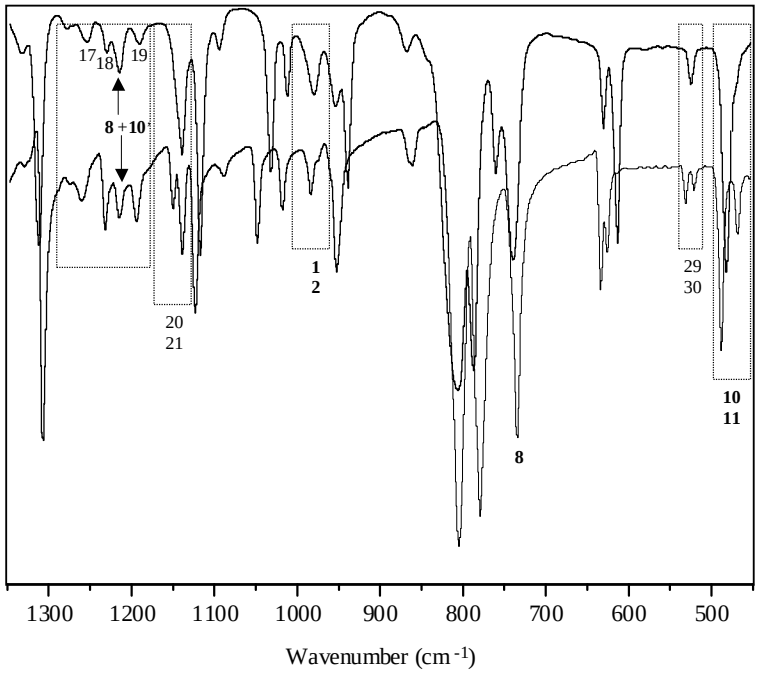

Figure 2.2.9. Spectra of quinoline (top) and $\{[Cu(quin)_2I]_2\}$ (bottom) showing the loss of accidental degeneracy of some of the fundamentals upon complexation. Out-of-plane vibrations are shown in bold numbers.

of the 1217 cm^{-1} band as a combination band has been performed on the basis of its appearance in the spectra for the ligand and the $\{[Cu(quin)_2I_2]_2\}$ complex.

Modes 20 and 21*A*' have been assigned at 1147 and 1141 cm^{-1} in the quinoline-d_0 spectrum, as the 1141 cm^{-1} band shows a shoulder at 1147 cm^{-1} (calculated frequencies of 1145 and 1137 cm^{-1}, respectively). Evidence for this assignment is supported by complex formation where two bands appear in this region in the spectrum of the dimeric $\{[Cu(quin)_2I]_2\}$ compound [53]. Wait and McNerney assigned the band at 1141 cm^{-1} as mode 20*A*' but failed to assign the shoulder occurring at 1147 cm^{-1} and hence mode 21*A*' was assigned at 1118 cm^{-1} and mode 22*A*' at 1095 cm^{-1}. The calculated values obtained in this work show no calculated value close to 1095 cm^{-1}, except for the 1115 cm^{-1} calculated value which is better assigned to mode 22*A*' occurring at 1118 cm^{-1}.

Accidental degeneracy is observed for modes 29 and 30*A*', which are observed as a weak intensity band at 522 cm^{-1} in the quinoline-d_0 spectrum. Interestingly, this is also the case for the quinoline-d_7 molecule, where modes 29 and 30*A*' are accidentally degenerate and occur at 506 cm^{-1} (this weak intensity absorption is observed as two weak intensity bands in the spectrum of $[Cu(quin\text{-}d_7)(SCN)]_n$ [53]. The $\{[Cu(quin)_2I]_2\}$ system supports the assignments performed on several of the vibrations that have been assigned as accidentally degenerate, as is shown in figure 2.2.9.

The 26*A*' in-plane mode and the 6*A*'' out-of-plane mode have been assigned to the strongest intensity band in the quinoline spectrum occurring at 805 cm^{-1}. Wait and McNerney assigned mode 26*A*' as occurring at 785 cm^{-1} and mode 6*A*'' as occurring at 805 cm^{-1} [50]. The calculated frequency values for these modes are very close and an interesting feature of the modes obtained is that, that both show displacements in and out of the *xy* plane. The 26*A*' mode shows displacements of the order of -10^{-2} in the *z* coordinate for those displacements that are of the order of $+10^{-1}$ in the *z* coordinate for the 6*A*'' mode. The 6*A*'' mode shows displacements of the order of $+10^{-2}$ and $+10^{-3}$ for the *x* and *y* coordinates which are of the order of $+10^{-1}$ and $+10^{-2}$ respectively in the 26*A*' mode. This unexpected coupling between modes of different symmetry must be due to the low symmetry of the molecule, but is not obtained for the quinoline-d_7 system, where the coupling is lost.

Wait and McNerney pointed out ambiguities in their assignment of the band at 785 cm^{-1} as the in-plane mode 26*A*' and the out-of-plane mode 7*A*''. This band has been assigned as the latter out-of-plane mode in the present work, while mode 26*A*' has been assigned as occurring at 805 cm^{-1}. The authors pointed out that two bands, one polarized and one depolarized occur at 785 cm^{-1}, and their vapour phase studies provided information for an in-plane mode and an out-of-plane mode for this band which is primarily an out-of-plane mode as observed in the vapour phase [50]. The cartesian displacements obtained for this mode show that it is an out-of-plane mode. However, minor displacements are also observed in the *xy*-plane. This mixing of in-plane and out-of-plane displacements is observed for several low energy modes calculated for the quinoline molecule in the gaseous state.

Mode 25*A*' at 939 cm^{-1} had been previously assigned to an out-of-plane, γC-H, vibration [19, 26, 50]. It has been re-assigned to an in-plane mode in this work.

2.2.2.2. Out-of-plane vibrations

The higher energy out-of-plane modes show a considerable amount of coupling in the quinoline-d_0 molecule, which is lost in the perdeuterated analogue. In fact, two pairs of out-of-plane modes are accidentally degenerate and are obtained at basically the same frequency value (1*A*'' and 2*A*'', and 3*A*'' and 4*A*''). The out-of-plane modes occur in the same order as the naphthalene-d_0 vibrations except for modes 6*A*'' and 7*A*'' (related to modes $2B_{1u}$ and $2A_u$ respectively), with mode $2A_u$ occurring before mode $2B_{1u}$ in naphthalene-d_0.

The mode that is absent when compared to the naphthalene-d_0 and naphthalene-d_8 modes is $3B_{3g}$, as pointed out previously by Watkins and his co-workers [19, 26]. However, this mode does not correspond to one of the lowest ν_D/ν_H ratios for naphthalene, as is the case with the absent in-plane mode. This is due to the fact that the $3B_{3g}$ mode in naphthalene is a coupled γC-H γring vibration for naphthalene-d_0, while as a result of deuteration decoupling it is basically a γC-H vibration for naphthalene-d_8. As is the case with the absent in-plane mode which is observed for quinoline *N*-oxide, a N-O mode related to the $3B_{3g}$ vibration is also observed for the *N*-oxide derivative as will be discussed in the corresponding section.

Less coupling is observed for the quinoline-d_7 higher energy out-of-plane modes than for quinoline-d_0. The quinoline-d_7 displacement diagrams can easily be related to the naphthalene-d_8 modes and assignments for the highly coupled quinoline-d_0 high energy out-of-plane vibrations have been performed by applying the ν_D/ν_H ratios obtained for naphthalene-d_0 and naphthalene-d_8 to the vibrations assigned for quinoline-d_7. Most lower energy out-of-plane modes can be related to the naphthalene modes with very few changes. Some differences however need to be highlighted.

The first two out-of-plane modes, 1 and 2*A*''can be distinguished for quinoline-d_7 and each ascribed to one particular naphthalene-d_8 fundamental, but there is no way to similarly assign one or the other to one particular naphthalene-d_0 fundamental for quinoline-d_0. Both vibrations are quite similar in the naphthalene system reflecting an in phase (B_{3g}) and out of phase (A_u) torsion of the two rings and both fundamentals occur very close to each other for quinoline-d_0. Furthermore, the displacements of the H atoms seem to be split between both modes, with displacements along the *z* coordinate of the order of $+10^{-1}$ for hydrogens on ring B and of $+10^{-2}$ for those on ring A in the 1*A*'' mode, with the opposite trend being observed for mode 2A''. Both out-of-plane modes are compared to the naphthalene-d_0 fundamentals in figure 2.2.10. They have

been assigned in the order obtained for quinoline-d_7. Mode 2A'' which is not observed in the present ir spectrum, has been assigned at 971 cm^{-1} from the Raman band reported by Wait and McNerney. Watkins and co-workers [19, 26] assigned the 2A'' fundamental to the previously reported frequencies at 970 cm^{-1} for quinoline-d_0 and 807 cm^{-1} for quinoline-d_7. A shoulder is indeed observed at approximately 974 cm^{-1} in the spectrum of $\{[Cu(quin)_2I]\}_2$ as can be seen in figure 2.2.9.

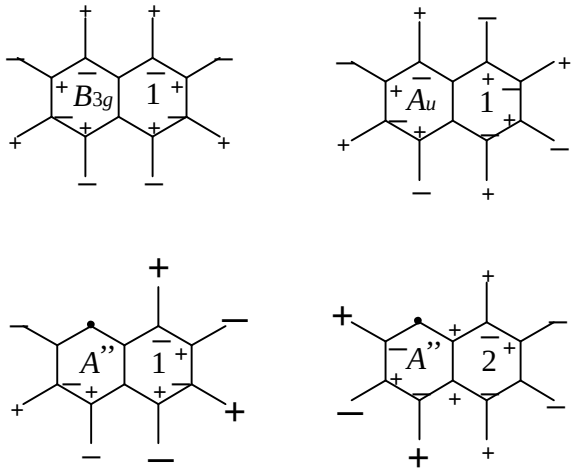

Figure 2.2.10. Out-of-plane naphthalene-d_0 modes 1B_{3g} and 1A_u related to the out-of-plane quinoline-d_0 modes 1A" and 2A". Increased + and – signs indicate larger displacements in the z coordinate.

Modes 6 and 7A'' have been assigned from the quinoline-d_7 modes as corresponding to the 2B_{1u} and 2A_u naphthalene-d_8 vibrations due to their similarity with these modes. However, it is important to note that the corresponding modes obtained for quinoline-d_0 are quite different to the naphthalene-d_0 vibrations, especially 6A''.

The lowest energy out-of-plane mode obtained, 14A", is identical for both quinoline-d_0 and quinoline-d_7. It is a vibration composed of a linear combination of the 4B_{1u} and 4A_u naphthalene-d_0 vibrations, as shown in figure 2.2.11. Consequently, mode 13A" must also be a linear combination of the aforementioned naphthalene vibrations.

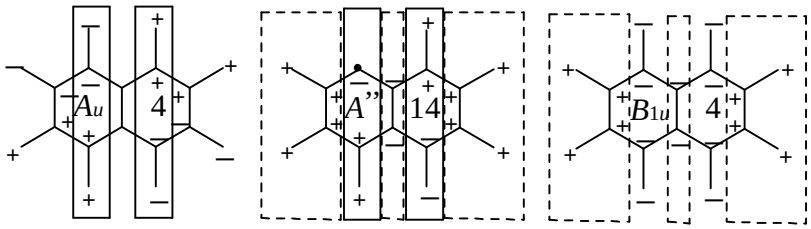

Figure 2.2.11. Linear combination of modes $4A_u$ and $4B_{1g}$ to yield the $14A''$ quinoline vibration

In summary, the most significant changes occurring in the quinoline system when compared to the naphthalene fundamentals are the displacements of carbons C9 and C10, and the hydrogen atoms where the magnitude and the direction of the displacement vary according to the vibration. This confirms the earlier caution in extending the normal modes of aromatic homocyclic systems to their heterocyclic analogues [28].

2.2.3. Quinoline *N*-oxide, O-18 labelled quinoline *N*-oxide and quinoline-d_7 *N*-oxide

Contrary to what occurs in the pyO system, where the νN-O frequency is well established, the N-O stretching frequency in the quinO system does not follow the well defined behaviour expected for a high character νN-O vibration and various assignments for this frequency place it somewhere in the 1290-1230 cm^{-1} region [5, 19, 27, 28, 54-59]. A full assignment for the infrared spectra of the quinoline *N*-oxide (quinO) ligand and its perdeuterated analogue (quin-d_7O) was previously performed by Thornton and co-workers [19, 21, 26, 27] based on ν_D/ν_H ratios and comparison with 1-fluoronaphthalene. Several re-assignments are recommended in this work aided by the calculations performed and the analysis of the normal modes obtained. The oxygen-18 labelled ligand has also been prepared but, unfortunately, due to the low enrichment of O-18 in the compound (approximately 40% quin-^{18}O), most O-18 sensitive bands are masked by the strong intensity absorptions of the prevalent quinO. However, the Raman and ir spectra for $[Pt(C_2H_4)(quin\text{-}^{18}O)Br_2]$ prove quite useful in the assignment problem, as two bands are observed where only one would be expected for those O-18 sensitive vibrations, as will be discussed in section 2.3.2. Table 2.2.4 shows the assignments performed by Thornton and Watkins [19, 26] for the ir spectra of quinO and quin-d_7O, compared to the assignments proposed in the present work.

Table 2.2.4. Assignments for quinO and quin-d_7O in-plane vibrations as reported by Watkins and Thornton [19, 26] and in this work. All frequency values in cm^{-1}.

quinO			quin-d_7O	
[19, 26]	This work	Vibration	[19, 26]	This work
3090[a]	3095	*A*' 1	2290	2276
3055[a]	3062	2	2290	2276
3050[a]	3062	3	2270	2276
3030	3052	4	2270	2242
3030	3052	5	2258	2242
3025	3052	6	2270	2242
3000	3010	7	2261	2242
1639	1656	8	1594	1596
1616	1617	9	1581	1557
1577	1568	10	1536	1530
1514	1509	11	1453	1455
1455	1450	12	1301	1372
1447	1443	13	1377	1352
1398	1398†	14	1357	1321
1377	1377†	15	1242	1305
1313	1307	16	1313	1261
1275	1266	17	1055	1169
1266	1230	18	823	1074
1230	1208	19	1147	1013
1210	1179	20	1073	1027
1179	1136	21	1011	823
1146	1091	22	835	843
1138	1057	23	879	875
1054	1047*	24	879	783
928	1014	25	924	773
878	866	26	787	741
778	795	27	742	697
743	725	28	721	681
628	582	29	564	563
557	547	30	508	528
545	491	31	497	478
365	482	32	340	457
321	317	33	307	302

* Shoulder

† Value taken from references 19 and 26. A broad band is observed at 1392 cm^{-1} in the spectrum of quinO in this work.

‡ Taken from references 19 and 26; not observed in spectra collected for this work.

a Estimated value.

Table 2.2.4 (continued). Assignments for quinO and quin-d_7O out-of-plane vibrations as reported by Watkins and Thornton [19, 26] and in this work. All frequency values in cm^{-1}.

quinO			quin-d_7O	
[19, 26]	This work	Vibration	[19, 26]	This work
997	965	*A''* 1	830	783
984	917	2	854	755‡
970	883	3	755	741
878	—	4	773	721
828*a*	828	5	646*a*	637
802	767	6	676	626
798	767	7	627	—
722	—	8	590	519
610	628	9	526	592
480	564	10	441	494
466	465	11	416	412
422	420	12	374	373
211	269	13	196	252
185	191	14	175	177
185	160	15	170	152

* Shoulder
† Value taken from references 19 and 26. A broad band is observed at 1392 cm^{-1} in the spectrum of quinO in this work.
‡ Taken from references 19 and 26; not observed in spectra collected for this work.
a Estimated value.

As was observed for the pyO system, the calculations performed on the quinO systems yield a N-O bond length which is considerably shorter than that observed from X-ray diffraction studies for quinO coordination compounds. The calculated N-O bond length obtained from the geometry optimization is of 1.2603 Å, while the bond length observed for the coordination compound $[Pt(CO)(quinO)Br_2]$ is of 1.36 Å. No crystal structure was found reported for the un-coordinated quinO ligand in a Cambridge Structural Database search performed. Although bonding via the O atom to a metal centre is expected to change the N-O bond order and the bond length as compared to the free ligand, the calculated bond distance of 1.26 Å seems too short. As a result of this, the calculated νN-O frequency occurs at higher energy values than those observed experimentally [19, 26, 54, 60]. Calculations and vibrational analyses were performed on the quinO and quin-d_7O systems constraining the bond distances to 1.2900 and 1.3200 Å. As opposed to what was observed for the pyO system where the νN-O frequencies are located exclusively in modes of A_1 symmetry, the low symmetry for the quinO system allows for a mixing of internal coordinates that makes some of the νN-O modes quite different. Figures 2.2.12 and 2.2.13 show all of the calculated frequency values obtained for the in-plane and out-of-plane modes for quinO and

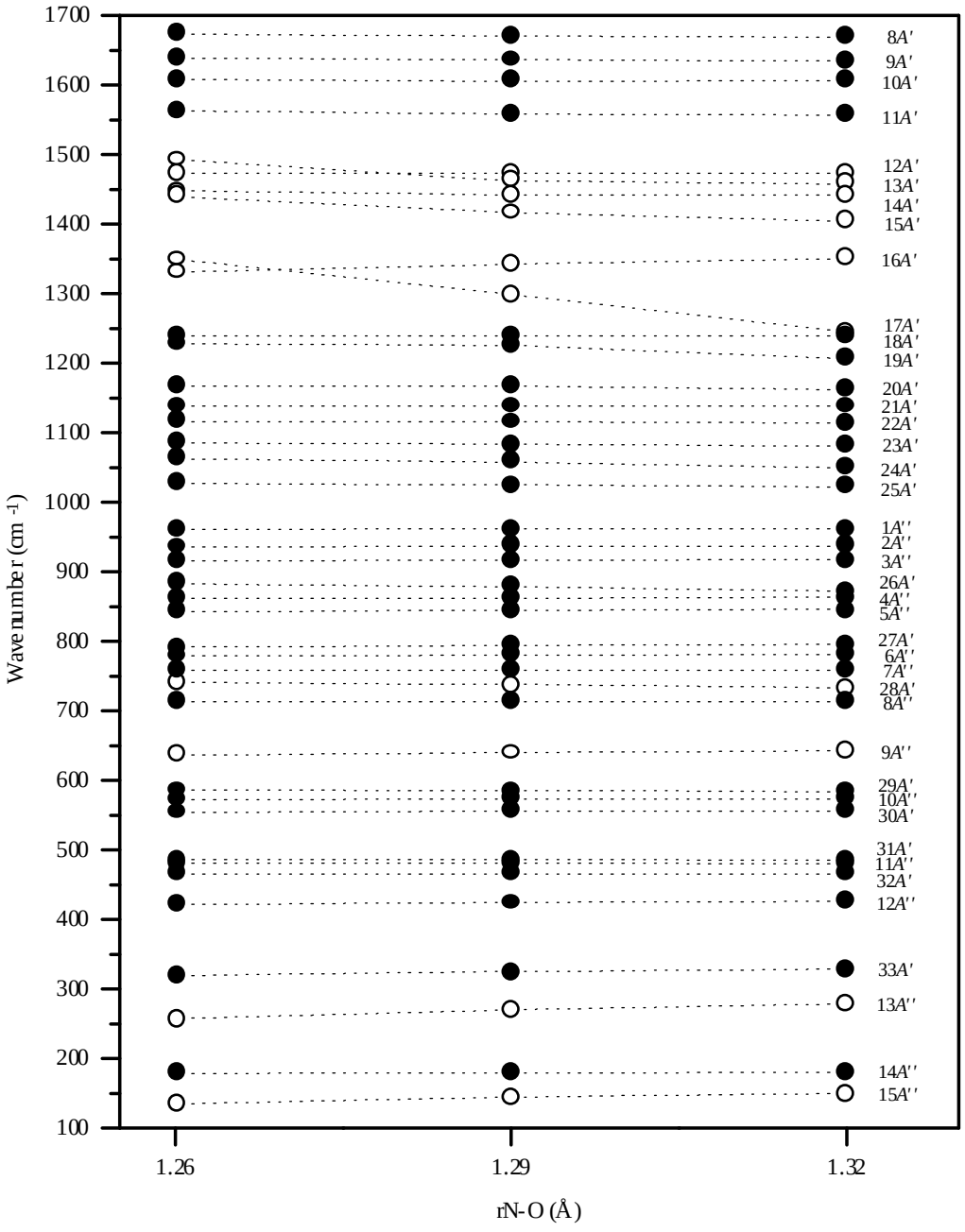

Figure 2.2.12. Calculated unscaled frequencies for the in-plane and out-of-plane modes in quinO as a function of the N-O bond length.

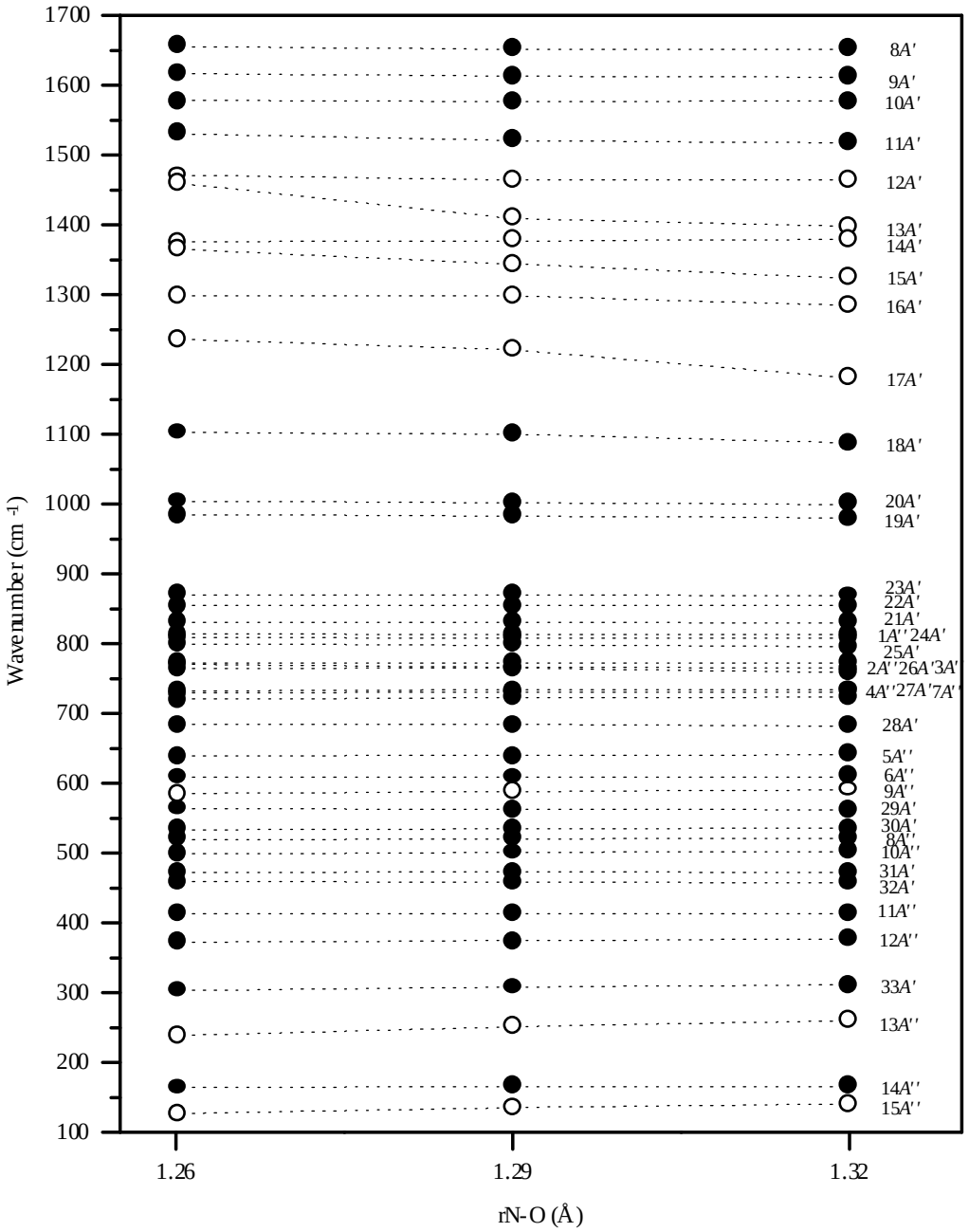

Figure 2.2.13. Calculated unscaled frequencies for the in-plane and out-of-plane modes in quin-d_7O as a function of the N-O bond length.

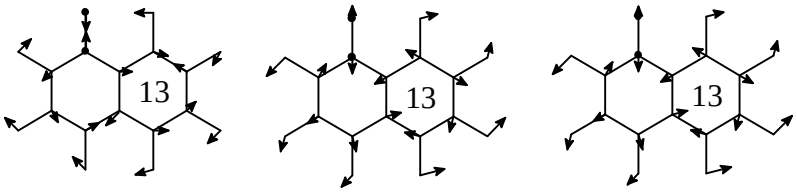

rN-O = 1.2603 Å
||rN-O|| = 0.252 Å
ν = 1493.03 cm^{-1}
$\Delta\nu$ = 11.22 cm^{-1}

rN-O = 1.2900 Å
||rN-O|| = 0.100 Å
ν = 1462.36 cm^{-1}
$\Delta\nu$ = 0.84 cm^{-1}

rN-O = 1.3200 Å
||rN-O|| = 0.056 Å
ν = 1458.10 cm^{-1}
$\Delta\nu$ = 0.13 cm^{-1}

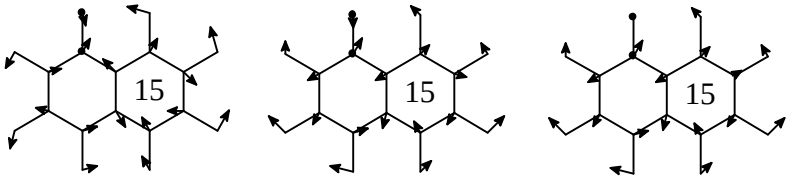

rN-O = 1.2603 Å
||rN-O|| = 0.073 Å
ν = 1439.49 cm^{-1}
$\Delta\nu$ = 2.89 cm^{-1}

rN-O = 1.2900 Å
||rN-O|| = 0.179 Å
ν = 1416.88 cm^{-1}
$\Delta\nu$ = 3.64 cm^{-1}

rN-O = 1.3200 Å
||rN-O|| = 0.135 Å
ν = 1404.34 cm^{-1}
$\Delta\nu$ = 0.75 cm^{-1}

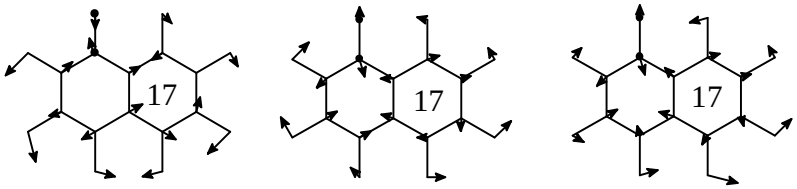

rN-O = 1.2603 Å
||rN-O|| = 0.154 Å
ν = 1348.95 cm^{-1}
$\Delta\nu$ = 9.79 cm^{-1}

rN-O = 1.2900 Å
||rN-O|| = 0.262 Å
ν = 1299.47 cm^{-1}
$\Delta\nu$ = 14.99 cm^{-1}

rN-O = 1.3200 Å
||rN-O|| = 0.174 Å
ν = 1244.89 cm^{-1}
$\Delta\nu$ = 3.06 cm^{-1}

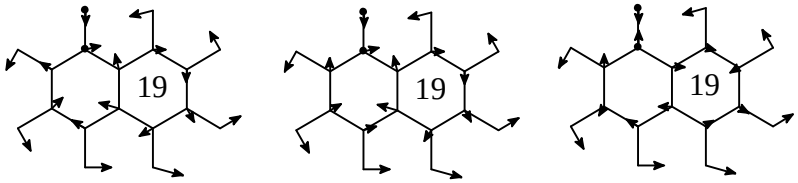

rN-O = 1.2603 Å
||rN-O|| = 0.045 Å
ν = 1228.27 cm^{-1}
$\Delta\nu$ = 0.59 cm^{-1}

rN-O = 1.2900 Å
||rN-O|| = 0.075 Å
ν = 1225.94 cm^{-1}
$\Delta\nu$ = 1.88 cm^{-1}

rN-O = 1.3200 Å
||rN-O|| = 0.213 Å
ν = 1206.79 cm^{-1}
$\Delta\nu$ = 6.80 cm^{-1}

Figure 2.2.14. Affected νN-O modes for quinO as the N-O bond length is modified. Calculated frequencies are unscaled and $\Delta\nu = \nu_{\text{quinO}} - \nu_{\text{quin-18O}}$.

quin-d_7O occurring below 1700 cm^{-1} as a function of the N-O bond distance employed. Although several modes in the 1500-1200 cm^{-1} region are sensitive to variations in the bond length, the most significant changes are observed for modes 13, 15, 16, 17 and 19*A*', with mode 17*A*' showing the greatest sensitivity. Several crossovers occur in the 1500-1400 cm^{-1} region, especially when going from a 1.26 Å N-O bond distance to 1.29 Å. Calculated frequencies for the O-18 isotopomers yield interesting results. The modes shown on figure 2.2.14 are those for which the largest calculated $\Delta\nu = \nu_{quinO} - \nu_{quin\text{-}18O}$ values are obtained for all the bond distances used in the calculations. No shifts are obtained for modes 16*A*' and 18*A*', regardless of the bond length employed.

For a distance of 1.26 Å, the νN-O frequency is shared mainly by two modes, 13*A*' (principal) and 17*A*' (secondary). Mode 17*A*' is the predominant νN-O mode for a distance of 1.29 Å, although mode 13*A*' shows some O-18 sensitivity. For a distance of 1.32 Å, mode 19*A*' is the highest character νN-O vibration obtained, although mode 17*A*' shows some sensitivity as well. This sensitivity to the N-O bond length of assigning the principal N-O stretch to either of modes 13*A*', 17*A*' or 19*A*' accounts for the two characteristic N-O frequency ranges reported for substituted quinoline *N*-oxides [28, 55, 56]. It seems likely that some of the difficulties encountered in the study of quinoline *N*-oxide and substituted derivatives could be explained in terms of the way in which slight variations in the N-O bond order affect the νN-O frequencies. Studies with substituted quinoline *N*-oxide derivatives [55, 56] have assigned the νN-O frequency in the ir spectra to several modes occurring in the 1400-1200 cm^{-1} region. It remains an interesting problem to study, aided by DFT calculations, the substituted systems so as to shed some light on the ambiguities that work in this particular field has given rise.

For the quin-d_7O species, the situation is less complicated and no crossovers are observed. Most of the modes in the νN-O region show a calculated O-18 sensitivity, except for mode 14*A*' which remains impervious to O-18 substitution for all the bond lengths explored. In the perdeuterated species, mode 13*A*' is the highest character νN-O stretching frequency for a N-O bond distance of 1.26 Å. For a N-O bond length of 1.29 Å it is mode 17*A*', and finally, for a larger bond length of 1.32 Å, the νN-O stretching frequency is shared between modes 17*A*' and 18*A*'. Interestingly, mode 18*A*' is insensitive to O-18 substitution regardless of the bond length for quinO while mode 19*A*' is insensitive in quin-d_7O, and reflects a deuteration coupling/decoupling difference within the molecule. Figure 2.2.15 shows some of the normal modes that are most affected by a change

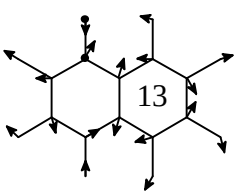

rN-O = 1.2603 Å
||rN-O|| = 0.165 Å
ν = 1459.15 cm^{-1}
$\Delta\nu$ = 10.72 cm^{-1}

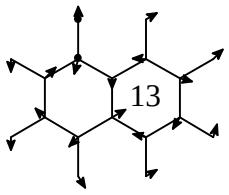

rN-O = 1.2900 Å
||rN-O|| = 0.139 Å
ν = 1408.98 cm^{-1}
$\Delta\nu$ = 4.06 cm^{-1}

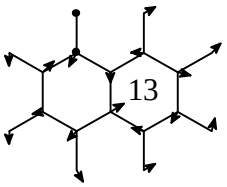

rN-O = 1.3200 Å
||rN-O|| = 0.123 Å
ν = 1397.76 cm^{-1}
$\Delta\nu$ = 0.51 cm^{-1}

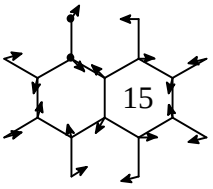

rN-O = 1.2603 Å
||rN-O|| = 0.102 Å
ν = 1364.93 cm^{-1}
$\Delta\nu$ = 3.01 cm^{-1}

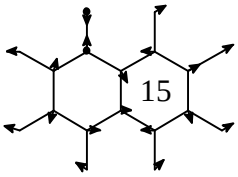

rN-O = 1.2900 Å
||rN-O|| = 0.189 Å
ν = 1343.96 cm^{-1}
$\Delta\nu$ = 5.97 cm^{-1}

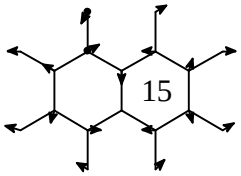

rN-O = 1.3200 Å
||rN-O|| = 0.141 Å
ν = 1323.36 cm^{-1}
$\Delta\nu$ = 1.06 cm^{-1}

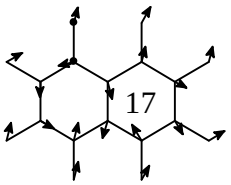

rN-O = 1.2603 Å
||rN-O|| = 0.106 Å
ν = 1235.68 cm^{-1}
$\Delta\nu$ = 4.48 cm^{-1}

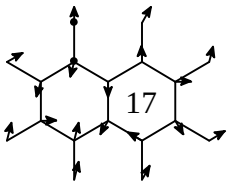

rN-O = 1.2900 Å
||rN-O|| = 0.159 Å
ν = 1220.92 cm^{-1}
$\Delta\nu$ = 9.19 cm^{-1}

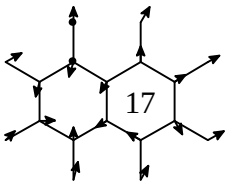

rN-O = 1.3200 Å
||rN-O|| = 0.226 Å
ν = 1180.07 cm^{-1}
$\Delta\nu$ = 9.45 cm^{-1}

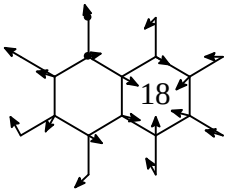

rN-O = 1.2603 Å
||rN-O|| = 0.054 Å
ν = 1102.67 cm^{-1}
$\Delta\nu$ = 2.16 cm^{-1}

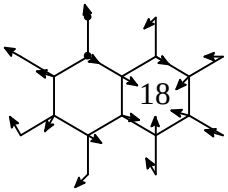

rN-O = 1.2900 Å
||rN-O|| = 0.083 Å
ν = 1099.92 cm^{-1}
$\Delta\nu$ = 3.51 cm^{-1}

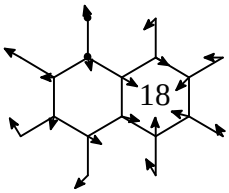

rN-O = 1.3200 Å
||rN-O|| = 0.151 Å
ν = 1087.51 cm^{-1}
$\Delta\nu$ = 7.06 cm^{-1}

Figure 2.2.15. Affected νN-O modes for quin-d_7O as the N-O bond length is modified. Calculated frequencies are unscaled and $\Delta\nu = \nu_{\text{quin-}d7\text{O}} - \nu_{\text{quin-}d7,18\text{O}}$.

in bond length in quin-d_7O.

Two of the out-of-plane modes in the low energy region, modes 13*A*" and 15*A*", show a slight increase to higher energy as the N-O bond length increases for both isotopomers, while mode 14*A*" is insensitive to N-O bond length.

Employment of the values obtained from the geometry optimization yield extremely high calculated νN-O frequencies which do not satisfactorily explain the experimental observations. The pyO molecule that yielded the best-calculated fit to observed values was that for which the N-O bond length was approximately 0.03 Å greater than the value obtained from the geometry optimization. Based on this, the value of 1.2900 Å (0.03 Å larger than that obtained) was chosen for the vibrational analyses of quinO and quin-d_7O. With this N-O bond length, the highest character νN-O frequencies fall in the range where this vibration is expected to occur [19, 26, 55, 56].

The calculations provide a molecule with C_s symmetry and a total of 48 normal modes of vibration; 33 in-plane modes of *A*' symmetry and 15 out-of-plane modes of *A*'' symmetry. Some of the in-plane modes can be readily identified with the naphthalene-d_0 and naphthalene-d_7 vibrations, especially the ring modes at high and low energy. However, a significant amount of coupling is observed for those modes that display a high C-H bend character. Many of these can be obtained by means of linear combinations of the naphthalene-d_0 and naphthalene-d_7 modes.

The normal modes of quinO and quin-d_7O are shown in figures 2.2.16-2.2.18. Table 2.2.5 shows the experimental and calculated rescaled frequencies obtained for these molecules. The spectra of quinO, quin-^{18}O and quin-d_7O are shown in figure 2.2.19.

2.2.3.1. In-plane vibrations

The C-H stretch vibrations occur as a medium intensity band in the mid ir spectra of quinO and quin-d_7O. Figure 2.2.20 shows the labelling scheme adopted for this molecule, which will be used during the discussion of the modes. The spectra of both quinO and quin-d_7O show a broad band with shoulders in the 3100-3000 and 2300-2220 cm^{-1} regions respectively. The calculated frequencies are very close to each other, and the assignments for these frequencies have been performed on the basis of the calculated results. These vibrations largely occur independently in either of the rings of quinO. Vibrations 1 and 5*A*' occur exclusively in ring A while vibrations 4,

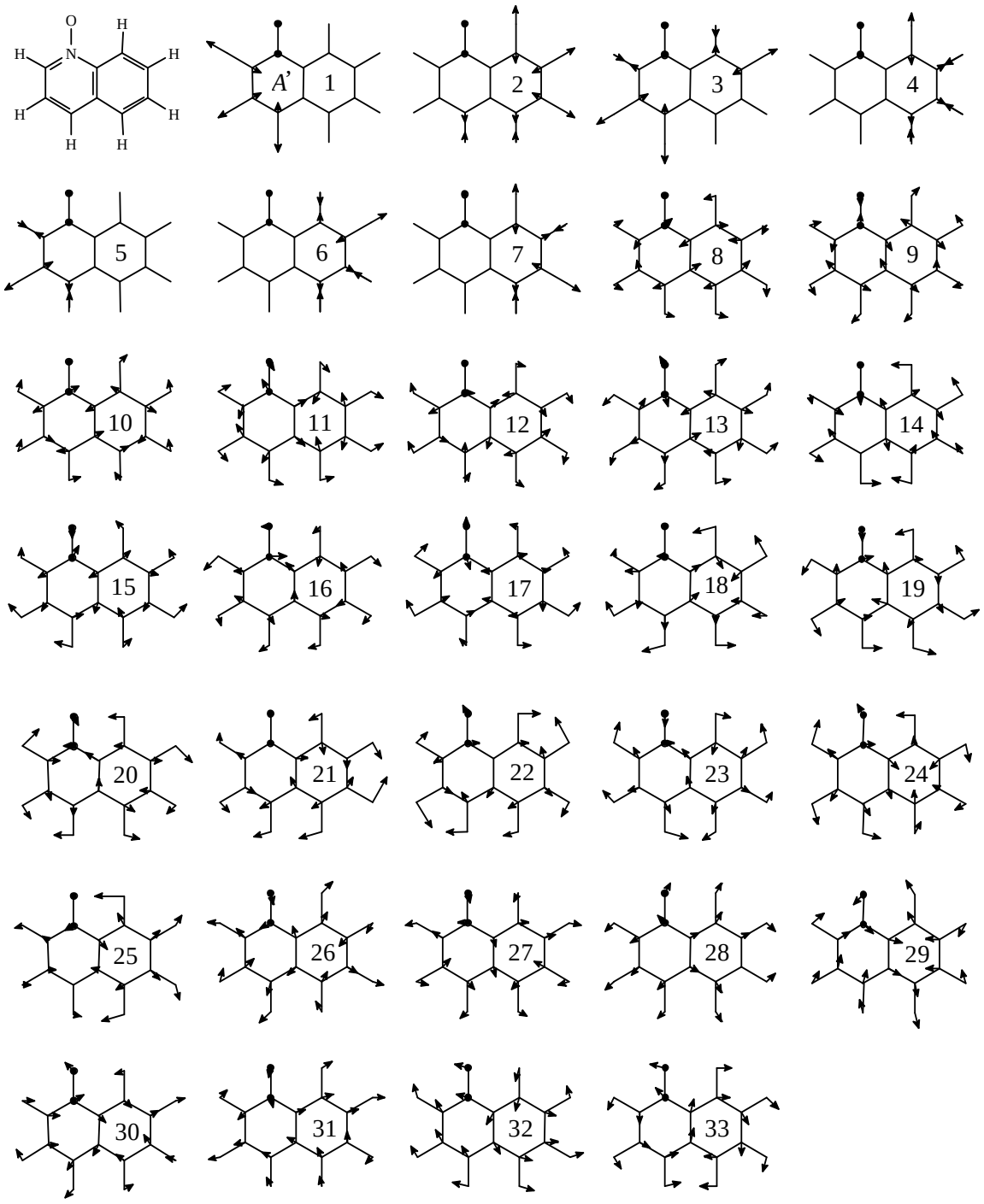

Figure 2.2.16. In-plane vibrations for quinO

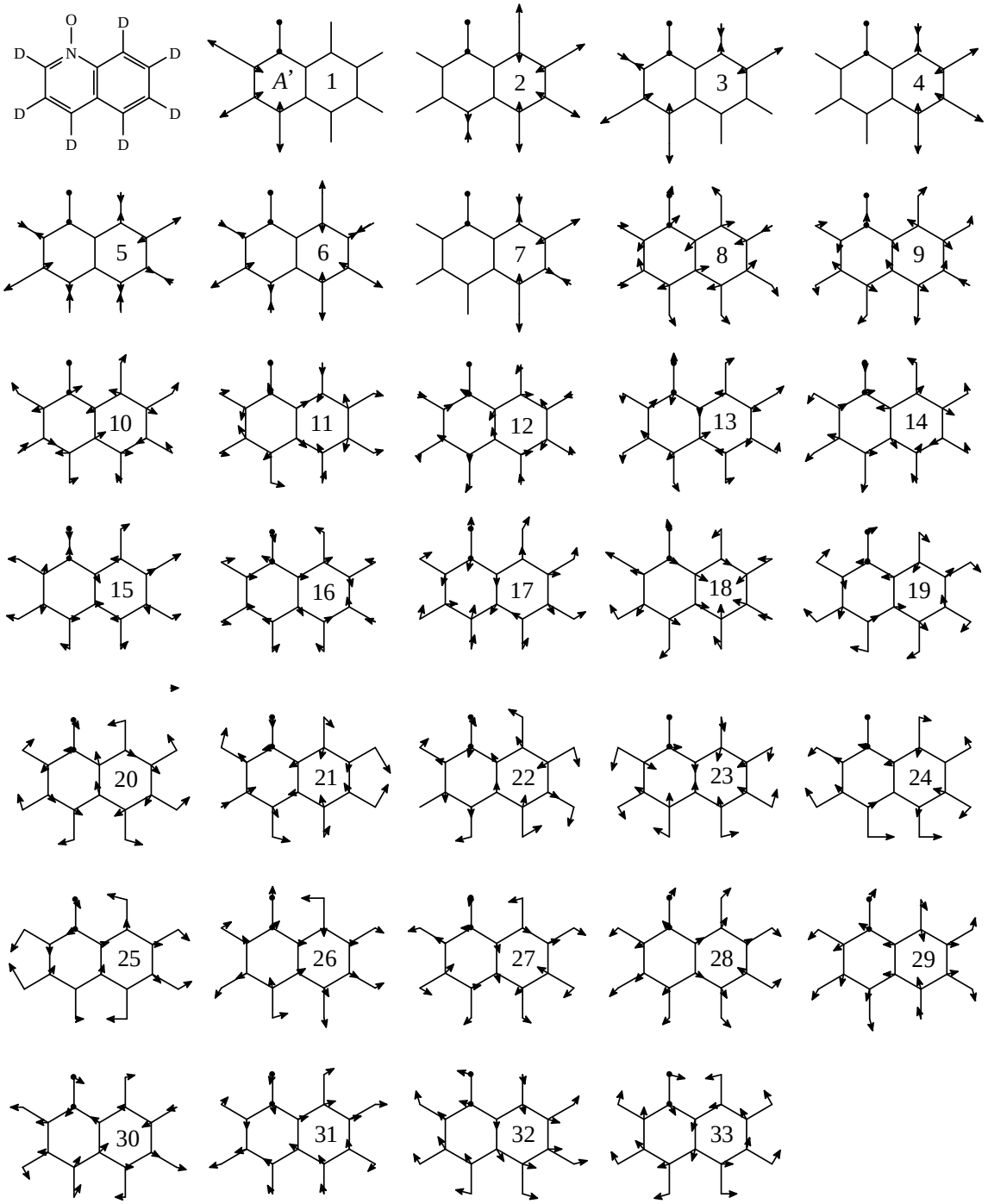

Figure 2.2.17. In-plane vibrations for quin-d_7O.

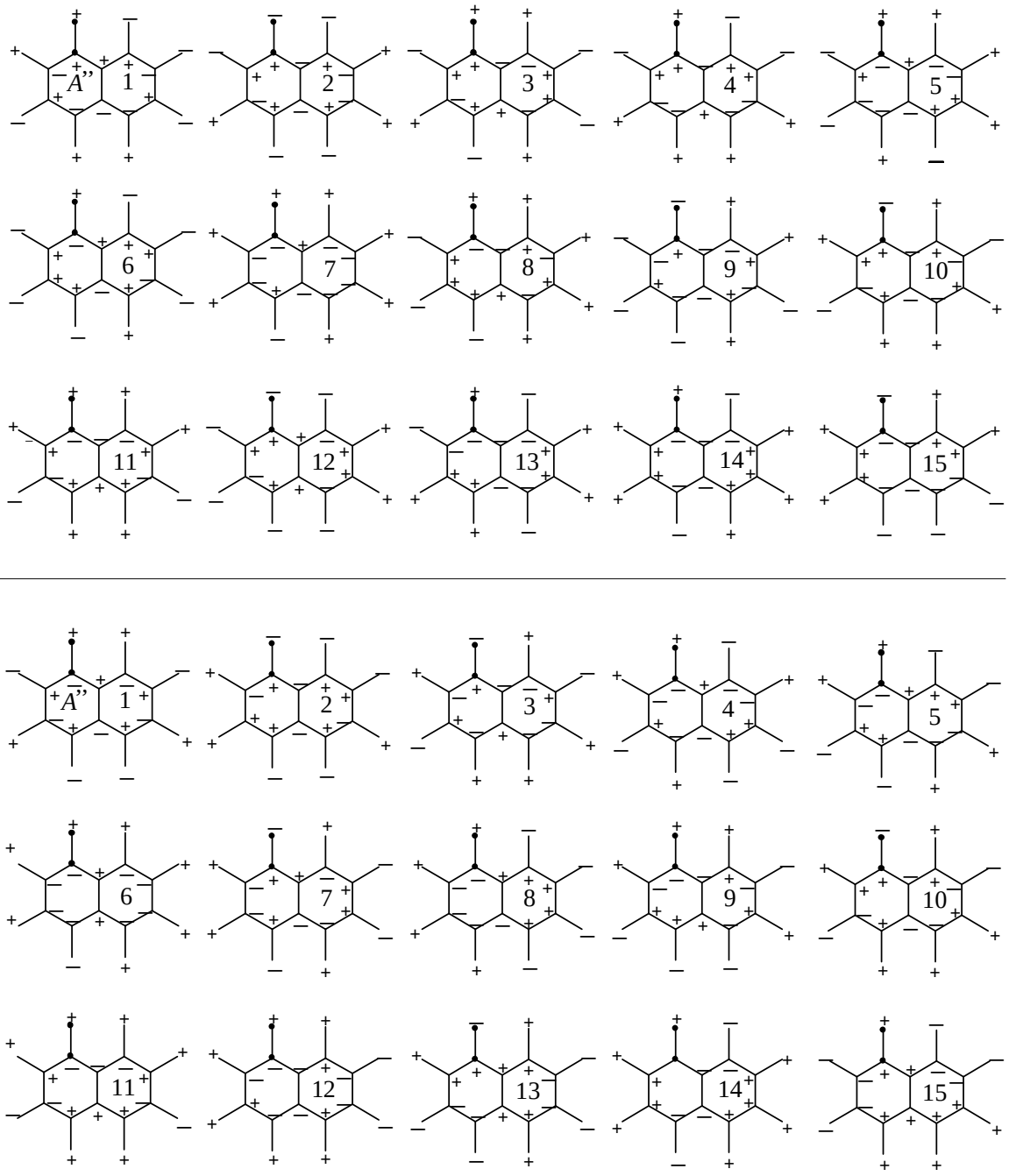

Figure 2.2.18. Out-of-plane vibrations for quinO
(top 15) and quin-*d*$_7$O (bottom 15).

Table 2.2.5. Experimental and calculated rescaled frequencies (in brackets) for quinO and quin-d_7O, showing naphthalene-d_o and naphthalene-d_8 related modes. All frequencies in cm^{-1}.

Vibration		quinO		naphthalene-d_0 mode(s)	quin-d_7O		naphthalene-d_8 mode(s)	ν_D/ν_H
A'	1	3095	[3098]		2276	[2279]		0.735 [0.736]
	2	3062	[3068]		2276	[2259]		0.743 [0.736]
	3	3062	[3064]		2276	[2256]		0.743 [0.736]
	4	3052	[3056]		2242	[2248]		0.735 [0.736]
	5	3052	[3050]		2242	[2235]		0.735 [0.733]
	6	3052	[3044]		2242	[2235]		0.735 [0.734]
	7	3010	[3033]		2242	[2221]		0.745 [0.732]
	8	1656	[1639]	$3B_{1g}$	1596	[1588]	$3B_{1g}$	0.964 [0.969]
	9	1617	[1605]	$3A_g$	1557	[1552]	$3A_g$	0.963 [0.967]
	10	1568	[1576]	$3B_{2u}$	1530	[1517]	$3B_{2u}$	0.976 [0.962]
	11	1509	[1530]	$3B_{3u}$	1455	[1464]	$3B_{3u}$	0.964 [0.957]
	12	1450	[1447]	$4B_{1g}$ $5A_g$ $4B_{3u}$	1372	[1411]	$3B_{3u}$ $5A_g$ $4B_{3u}$ $4A_g$	0.946 [0.975]
	13	1443	[1436]	$3B_{3u}$ $4A_g$ $4B_{1g}$	1352	[1358]	$3B_{3u}$ $5A_g$ $4B_{1g}$	0.937 [0.946]
	14	1398†	[1416]	$4A_g$ $4B_{1g}$	1321	[1327]	$5A_g$ $4B_{1g}$	0.945 [0.937]
	15	1377†	[1391]	$4B_{1g}$ $4B_{2u}$ $5A_g$	1305	[1296]	$4A_g$ $4B_{3u}$ $4B_{2u}$	0.945 [0.932]
	16	1307	[1319]	$4B_{2u}$ $4B_{3u}$ $5B_{2u}$	1261	[1253]	$4A_g$ $4B_{3u}$	0.965 [0.950]
	17	1266	[1277]	$4B_{2u}$ $5A_g$ $4B_{3u}$	1169	[1179]	$4B_{2u}$	0.923 [0.923]
	18	1230	[1218]	$5B_{2u}$ $5B_{3u}$	1074	[1065]	$5B_{3u}$	0.873 [0.874]
	19	1208	[1205]	$5B_{1g}$ $5B_{3u}$	1013	[953]	$5B_{1g}$	0.839 [0.791]
	20	1179	[1148]	$5B_{2u}$ $5B_{1g}$ $5B_{3u}$	1027	[972]	$5B_{2u}$	0.871 [0.847]
	21	1136	[1120]	$6B_{3u}$ $6A_g$ $6B_{1g}$	823	[809]	$6B_{1g}$ $7A_g$ $6B_{3u}$	0.724 [0.722]
	22	1091	[1098]	$6A_g$ $6B_{1g}$	843	[832]	$6B_{2u}$ $6B_{1g}$	0.773 [0.758]
	23	1057	[1067]	$6B_{2u}$ $7A_g$	875	[846]	$6B_{2u}$ $6B_{1g}$ $7A_g$	0.828 [0.793]
	24	1047*	[1042]	$6B_{2u}$ $7B_{3u}$ $7A_g$	783	[788]	$6B_{3u}$ $7B_{3u}$ $7B_{1g}$	0.748 [0.756]
	25	1014	[1010]	$7A_g$ $7B_{3u}$	773	[778]	$6A_g$ $7B_{3u}$	0.762 [0.770]
	26	866	[867]	$7B_{1g}$	741	[747]	$6B_{1g}$ $7A_g$ $6B_{3u}$ $7B_{1g}$ $7B_{2u}$	0.856 [0.861]
	27	795	[784]	$7B_{2u}$	697	[713]	$7B_{2u}$	0.877 [0.909]
	28	725	[730]	$8A_g$	681	[670]	$8A_g$	0.939 [0.918]
	29	582	[581]	$8B_{3u}$	563	[555]	$8B_{3u}$	0.967 [0.955]
	30	547	[552]	$8B_{1g}$	528	[528]	$8B_{1g}$	0.965 [0.956]
	31	491	[484]	$8B_{1g}$	478	[469]	$8B_{1g}$	0.973 [0.969]
	32	482	[479]	$9A_g$	457	[456]	$9A_g$	0.948 [0.952]
	33	317	[327]	$8B_{2u}$	302	[313]	$8B_{2u}$	0.953 [0.957]

* Shoulder.
† Value taken from references 19 and 26. A broad band is observed at 1392 cm^{-1} in the spectrum of quinO in this work.
‡ Taken from references 19 and 26; not observed in spectra collected for this work.
a Values taken from spectra for [PtA(quinO)X_2] and [PtA(quin-d_7O)X_2] derivatives, A = C_2H_4, CO; X = Cl, Br.

Table 2.2.5. (cont.)

Vibration		quinO	naphthalene-d_0 mode(s)	quin-d_7O	naphthalene-d_8 mode(s)	ν_D/ν_H
A''	1	965 [947]	$1B_{3g}$	783 [792]	$1B_{3g}$	0.828 [0.836]
	2	917 [923]	$1B_{1u}$	755‡ [754]	$1B_{1u}$	0.811 [0.817]
	3	883 [904]	$1B_{2g}$	741 [741]	$1B_{2g}$ $2B_{3g}$	0.839 [0.820]
	4	868[a] [851]	$2B_{3g}$	721 [717]	$2B_{3g}$	0.831 [0.843]
	5	828 [834]	$2A_u$	637 [628]	$2A_u$ $3B_{3g}$	0.769 [0.753]
	6	767 [771]	$2B_{1u}$	626 [598]	$2B_{1u}$	0.816 [0.776]
	7	767 [749]	$3B_{3g}$ $2B_{1u}$	748[a] [706]	$3B_{3g}$ $2A_u$ $2B_{1u}$	0.975 [0.942]
	8	740[a] [705]	$2B_{2g}$	519 [514]	$2B_{2g}$ $3A_u$	0.701 [0.729]
	9	628 [634]	$3A_u$	592 [579]	$2B_{2g}$ $3A_u$	0.943 [0.913]
	10	564 [569]	$3B_{1u}$ $4B_{3g}$	494 [496]	$3B_{1u}$	0.876 [0.872]
	11	465 [464]	$4B_{3g}$	412 [413]	$4B_{3g}$	0.886 [0.890]
	12	420 [424]	$3B_{2g}$	373 [376]	$3B_{2g}$	0.888 [0.887]
	13	269 [273]	$3B_{2g}$	252 [259]	$3B_{2g}$	0.937 [0.949]
	14	191 [185]	$4A_u$ $4B_{1u}$	177 [177]	$4A_u$ $4B_{1u}$	0.927 [0.957]
	15	160 [151]	$4B_{1u}$ $4A_u$	152 [149]	$4B_{1u}$ $4A_u$	0.950 [0.987]

* Shoulder.
† Value taken from references 19 and 26. A broad band is observed at 1392 cm^{-1} in the spectrum of quinO in this work.
‡ Taken from references 19 and 26; not observed in spectra collected for this work.
a Values taken from spectra for [PtA(quinO)X_2] and [PtA(quin-d_7O)X_2] derivatives, A = C_2H_4, CO; X = Cl, Br.

6 and 7*A*' occur exclusively in ring B, with vibrations 2 and 3*A*' occurring in both rings. There is greater interaction between the two rings in the deuterated isotopomer as can be seen in figures 2.2.16 and 2.2.17. Consequently, the modes obtained hold no relation to the naphthalene modes or the quinoline modes, as in these latter molecules the C-H vibrations are shared between the H atoms on both rings A and B. An attempt at expressing these vibrations in terms of linear combinations of the naphthalene fundamentals has not been done. This has been done, however, for the fundamentals below 2000 cm^{-1}.

The high-energy ring vibrations, 8-11*A*', can be readily identified to the normal modes obtained for naphthalene-d_0 and naphthalene-d_8. However, they are coupled vibrations and slight variations in the direction of the displacements are noticed. Modes $3B_{2u}$ and $3A_g$ are close together in energy in naphthalene-d_0 and in naphthalene-d_8, and strong coupling between the two modes is observed for the quinO and the quin-d_7O vibrations on the lowering of symmetry. The displacement diagrams for quinO and quin-d_7O show that these modes occur predominantly as the 9*A*' and 10*A*' modes, with 9*A*' more closely related to the $3A_g$ mode and 10*A*' to the $3B_{2u}$ mode. This inversion in the energy values for these modes was also observed for the quinoline-d_0 and quinoline-d_7 systems.

Modes 12-27*A*' are extremely coupled, as can be seen from the displacement diagrams shown in figures 2.2.16 and 2.2.17 compared with figures 2.2.1 and 2.2.2. However, all of these modes can be approximated by linear combinations of the naphthalene-d_0 and naphthalene-d_8 in-plane vibrations. The lowering of symmetry from D_{2h} in naphthalene to C_s in quinO allows for a mixing of all internal coordinates to yield the in-plane modes, provided that these are close in energy. However, an additional problem is posed by the fact that the nature of the quinO molecule is such, that there is a decrease in energy for the fundamental vibrations in this molecule when

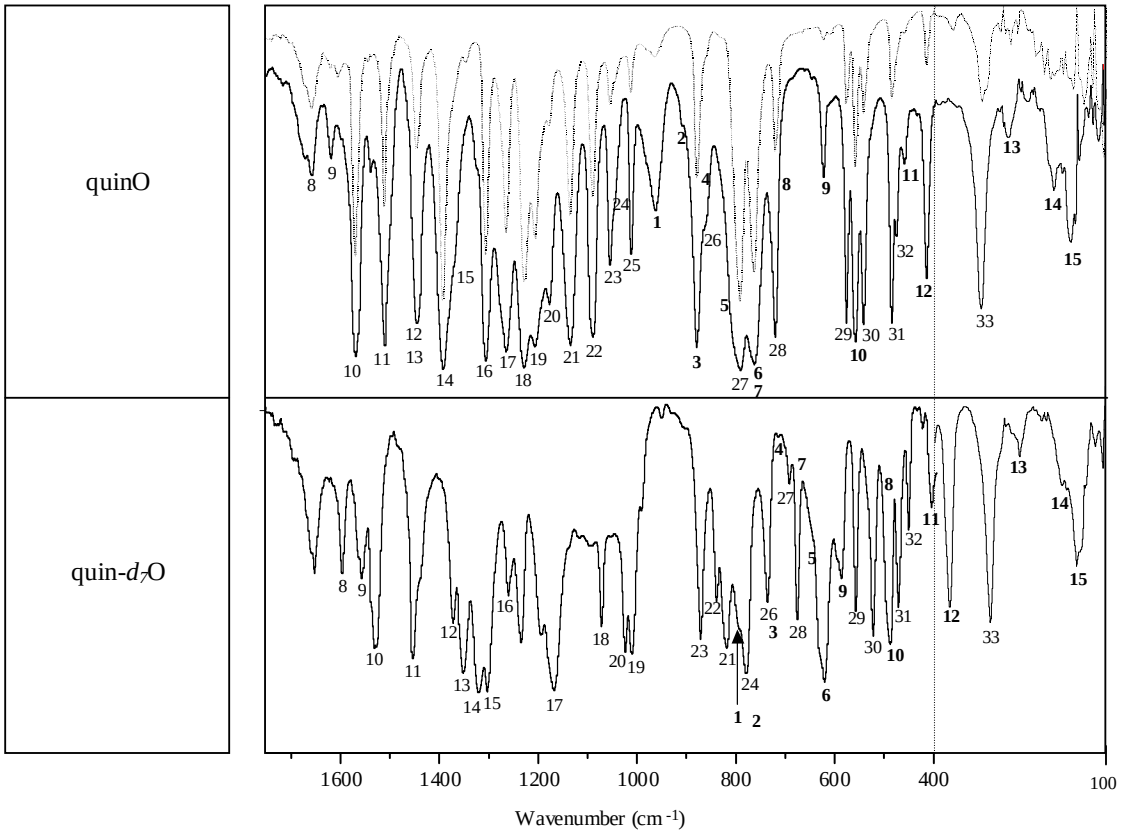

Figure 2.2.19. Mid and far ir spectra of quinO, quin-^{18}O (dotted line) and quin-d_7O showing the in-plane and out-of-plane (bold) fundamentals. Out-of-plane modes 4*A*" and 8*A*" in quinO, and 7*A*" in quin-d_7O, are shown in the spectra according to the calculated values obtained.

compared to the naphthalene fundamentals. This can easily be seen from the values obtained for the ring vibrations at high and low energy, which are in general, lower than those obtained for naphthalene-d_0 and naphthalene-d_8. As opposed to the normal modes obtained for quinoline-d_0 and quinoline-d_7, where all of the in-plane fundamentals can be related to naphthalene vibrations,

the analysis of the quinO and quin-d_7O modes is highly complicated due to the fact that not all naphthalene fundamentals occur in the same order for both isotopomers. Hence, coupling between different modes provide quinO and quin-d_7O vibrations that may be related by some, but not all of the naphthalene fundamentals occurring in a particular energy region for naphthalene-d_0 and naphthalene-d_8. Such is the case for the 4, 5, 6 and 7A_g modes, which couple to other vibrations occurring close together in energy. This suggests significant deuteration decoupling on isotope labelling.

Where possible, the modes in quinO and quin-d_7O have been assigned on the basis of the highest number of naphthalene modes of similar symmetry that couple to provide a given mode.

The coupling involves naphthalene vibrations with the two rings vibrating in phase (A_{1g}, B_{2u}) or out of phase (B_{1g}, B_{3u}), hence linear combinations result in various out of phase vibrations for the quinO and quin-d_7O systems, with the exception of high energy and low energy modes, such as 10*A*' and 27*A*'. The out of phase motion of the atoms in the highly coupled vibrations greatly encumbers the assignment problem when compared to the naphthalene-d_0 and naphthalene-d_8 vibrations.

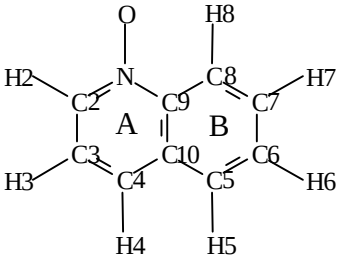

Figure 2.2.20. Labelling scheme employed for quinO.

Table 2.2.5 shows the naphthalene fundamentals related to the quinO and quin-d_7O vibrations. Linear combinations of these modes provide modes that greatly resemble those of quinO and quin-d_7O. Modes at high and low energy are very close to the naphthalene vibrations. However, a certain degree of coupling is also observed for these vibrations.

Needless to say, the amount of coupling experienced in the quinO and quin-d_7O systems will generate considerable differences in the ν_D/ν_H ratios obtained compared with naphthalene and

quinoline, and assignment of fundamentals on the basis of the ratios obtained for the frequencies in related molecules would render rather futile results.

As can be seen from the values shown on table 2.2.5, some frequencies are either under- or over-estimated in the calculations. This is particularly the case for modes 20 and 21*A*' in quinO and for modes 12, 19 and 20*A*' in quin-d_7O. Although the proximity of the frequency values is satisfactorily calculated, mode 12*A*' is over-estimated while 19 and 20*A*' are expected to occur at a much lower energy than the one observed. This under-estimation of the two latter modes occurs consistently regardless of the bond length employed, as can be seen from figure 2.2.13. Interestingly, calculations performed on the [Pt(CO)(quinO)Br_2] system and its isotopomers provide very accurate results for the frequencies observed for the coordinated quinO and quin-d_7O molecules, and prove very useful to confirm the assignments here.

Modes 19 and 20*A*' in quin-d_7O were left out of the linear regression analysis as a much better fit of all the remaining experimental to calculated values was obtained. The rest of the experimental values are in good agreement with the calculated values, although larger differences are observed for the quinoline-*N* oxide systems than the ones observed for naphthalene and quinoline.

Modes 12 and 13*A*' occur as one broad band centred at 1445 cm^{-1} for quinO. However, in dilute samples of the compound the band is resolved into two bands occurring at 1450 and 1443 cm^{-1}. The same appears to be the case for modes 14 and 15*A*' which occur as one single broad band centred at 1392 cm^{-1}. Thornton and Watkins [19, 26] report two values for this band at 1398 and 1377 cm^{-1}, which have been used in this work. Zeise's salt derivatives [PtA(quinO)X_2] (A = C_2H_4, CO and X = Cl, Br) show two strong absorptions in this region, confirming the existence of two fundamentals that are close together in energy.

Mode 24*A*' has been assigned as a shoulder of the medium intensity absorption occurring at 1057 cm^{-1} (mode 23*A*'). The calculated frequency for mode 24*A*' is 1042 cm^{-1} and is hence in good agreement with the shoulder *ca*. 1047 cm^{-1}. Calculations performed on the [Pt(CO)(quinO)Br_2] system, show that mode 23*A*' increases in energy while mode 24*A*' remains unchanged. Furthermore, the spectrum for quinO between 1180 and 1010 cm^{-1} shows five well defined absorptions whereas six (modes 20-25*A*') are observed in the spectrum for the coordination compound. This supports the fact that there are two fundamentals in the free ligand that occur

very close to each other, which shift in energy and become well defined by changes brought upon by coordination to a metal centre.

Mode 27*A*' has been assigned to the very intense absorption occurring at 795 cm^{-1} in quinO and the weak aborption at 697 cm^{-1} in quin-d_7O. Examining the displacement diagram for mode 27A' of both isotopomers shows that the oxygen and nitrogen atoms are displaced in opposite directions for quinO but in the same direction for quin-d_7O. This slight shift in motion would account for a larger variation of the dipole moment in quinO but quite a small one in quin-d_7O. Figure 2.2.21 shows the calculated magnitude for the dipole moment, μ, during both vibrations. It is on the basis of the calculated values and the analysis of the dipole moment that this vibration has been assigned. However, it must be borne in mind that a change in the dipole moment is not the only factor to affect the intensity of an ir absorption [61].

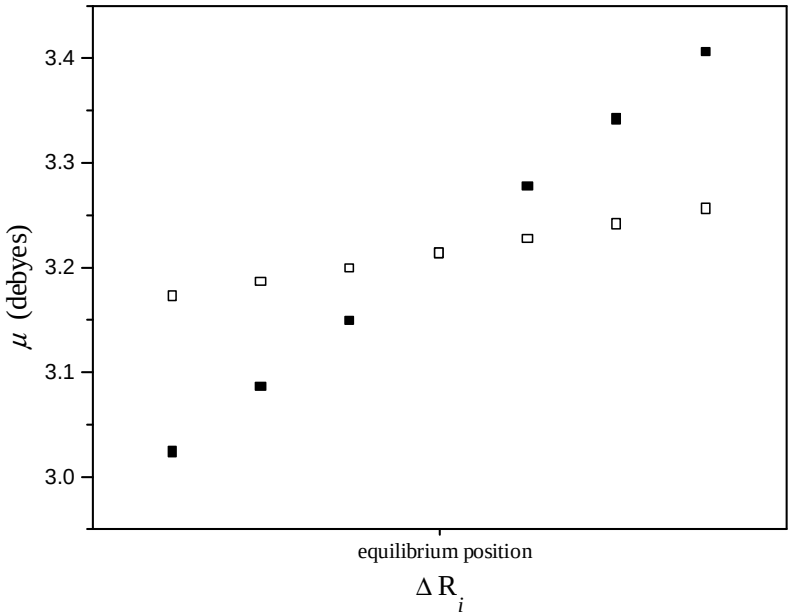

Figure 2.2.21. Change in magnitude of the dipole moment, μ, during the 27*A*' vibration in quinO (solid squares) and quin-d_7O (open squares).

In attempting to ascribe a single fundamental to either the N-O stretch or in plane bend, as was pointed out earlier, there is no single vibration from naphthalene-d_0 or naphthalene-d_8 which being absent in the quinoline systems can be so identified in the *N*-oxide systems. In fact, all naphthalene fundamentals need to be employed in order to explain the quinO vibrations.

2.2.3.2. Out of plane vibrations

The out-of-plane modes for quinO and quin-d_7O are shown in figure 2.2.18. Assignments for these modes and the relationship they hold to naphthalene vibrations is shown in table 2.2.5. Out of the fifteen out-of-plane modes obtained for quinO and quin-d_7O, seven are almost identical for both molecules. Modes 1*A*'' and 10-15*A*'' have been assigned on the basis of their similarity for both molecules. The remaining modes experience a certain amount of coupling, especially in the quin-d_7O system.

Most of the quinO modes can be easily related to the out-of-plane modes for naphthalene-d_0 with subtle differences in the motion of certain atoms arising from the change in the centre of mass of the molecule. The assignment of the modes for quin-d_7O is slightly more complicated, indicative of increased coupling.

Neither of the quinO and quin-d_7O out-of-plane modes has been related to the $1A_u$ vibration in naphthalene. This mode extensively couples to so many that it cannot be identified as the primary source of any one in particular.

With only three exceptions (modes 9, 10 and 12*A*''), all of the *A*'' vibrations for quinO are observed to occur at a lower energy than the corresponding naphthalene-d_0 vibrations that they are related to. The situation is slightly similar for quin-d_7O, except for the fact that the naphthalene-d_8 vibrations are much closer together in energy than the naphthalene-d_0 vibrations, and hence greater coupling is observed for the quin-d_7O vibrations.

Analysis of the modes obtained for quinO shows that there are two normal modes, 6 and 7*A*'', which resemble the umbrella vibration $2B_{1u}$ in naphthalene-d_0. Both modes in quinO are expected to occur close to each other and have been assigned to the very intense absorption at 767 cm^{-1}. The corresponding umbrella mode, 6*A*'', for quin-d_7O, has been assigned to the intense absorption at 625 cm^{-1}, although the calculated value for this vibration is slightly lower. Mode 5*A*'' in the perdeuterated analogue is observed as a shoulder occurring at *ca*. 640 cm^{-1}

Three bands have been left unassigned in the mid ir spectrum for quin-d_7O. These occur at 1650, 1237 and 1195 cm^{-1}. The first one is more than likely the δOH vibration from H_2O in the compound, and the latter two vibrations can be explained as combination bands. The combination

bands 24*A*' + 32*A*', 3*A*" + 10*A*" and 4*A*" + 8*A*" yield values close to 1237 cm^{-1} while 26*A*' + 32*A*' and 1*A*" + 11*A*" yield values close to 1195 cm^{-1}.

Not all of the out-of-plane modes have been assigned, as these are either very weak intensity absorptions or occur close to other intense ones that mask them. The situation changes with coordination compounds where a better definition of the bands is observed. These results will be discussed in the corresponding chapter.

2.2.3.3. N-O vibrations

Calculated frequencies for the molecules quin-^{18}O and quin-d_7-^{18}O were compared to those obtained for quinO and quin-d_7O in order to establish which normal modes have the largest shifts upon O-18 labelling. The results obtained are shown in table 2.2.6, and are indicative of the N-O vibrations, νN-O, αN-O and, to a lesser extent, the γN-O vibration, being highly coupled to several modes. The calculations and displacement diagrams suggest a need to revise the previous assignment of all three vibrations. Unfortunately, many of the bands in the spectrum of the

Table 2.2.6. Principal N-O vibrations in quinO, quinO/quin-^{18}O and quin-d_7O , from their experimental ir spectra and experimental and calculated shifts upon O-18 labelling. $\Delta\nu = \nu_{quinO} - \nu_{quinO\text{-}18}$ and $\nu_{quin\text{-}d7O} - \nu_{quin\text{-}d7,18\text{-}O}$. All values in cm^{-1}.

Mode	quinO	quinO/quin-^{18}O	$\Delta\nu_{exp}$	$\Delta\nu_{calc}$	quin-d_7O	$\Delta\nu_{calc}$	N-O vibration
13*A*'	1443	1445	-2	1	1352	4	αC-D + νN-O coupled
15*A*'	1377	1377	0	3	1305	6	αC-H/D + νN-O coupled
16*A*'	1307	1306	1	0	1261	3	νring + αC-D + νN-O coupled
17*A*'	1266	1265	1	15	1169	9	νN-O coupled
18*A*'	1230	1228	2	0	1074	3	αC-H/D + νN-O coupled
19*A*'	1208	1207	1	2	1013	1	αC-H/D + νN-O coupled
24*A*'	1047	1047	0	2	783	0	νring + αC-H + αN-O coupled
26*A*'	866	866	0	3	741	1	νring + νN-O coupled
28*A*'	725	724	1	5	650	3	νring + νN-O coupled
29*A*'	582	581	1	5	563	4	νring + αN-O coupled
30*A*'	547	547/541*	6	6	528	6	αN-O coupled
31*A*'	491	492/486*	6	4	478	4	νring + αC-H/D + αN-O coupled
32*A*'	482	482	0	4	457	5	νring + αC-H/D
33*A*'	317	317/309*	8	7	302	6	νring
13*A*''	269	266	3	3	252	3	γN-O coupled
14*A*"	191	192	-1	0	177	0	γring
15*A*''	160	158	2	2	152	2	γring (butterfly mode)

* Shoulder.

quinO/quin-^{18}O mixture show small shifts of *ca.* 1 cm^{-1}. The richness of the vibrational spectrum and the mixed isotopomers possibly masks the appearance of a second band that could be attributed to the O-18 sensitivity necessary in determining the three principal N-O vibrations.This is regrettable since other spectroscopic evidence has previously been argued to suggest alternate identification of the principle N-O stretch [55, 62, 63] in the range 1220 to 1260 cm^{-1} and in the range 1300-1340 cm^{-1}.

The νN-O vibration is observed to occur in the 1250 cm^{-1} region in pyridine *N*-oxide (pyO) as was discussed previously. It is a very coupled mode in quinO and quin-d_7O, but calculations indicate it occurs predominantly as mode 17*A*' for both isotopomers. Identifying the νN-O vibration to the band at 1230 cm^{-1} (mode 18*A*'), and based on the protonation sensitivity of quinO and quin-d_7O reported by Ghersetti *et al.* [62, 63], Thornton and Watkins [26] postulated that the N-O stretch would be a more pure vibration for the -d_7 isotopomer. The present assignment and calculation indicate otherwise.

Experimental observations and calculated shifts upon O-18 labelling for quin-d_7O are in agreement with mode 17*A*' as the highest character νN-O vibration observed for this molecule, but this is not the case for quinO. Mode 18*A*' (a coupled ring/C-H bend according to the assignment carried out in this work) occurring at *ca.* 1230 cm^{-1} in quinO and mode 17*A*' occurring at 1169 cm^{-1} in quin-d_7O have been previously considered [19, 26] as coupled νN-O vibrations on account of the shifts induced by hydrogen bonding. However, mode 18*A*' is one of the calculated O-18 insensitive vibrations in quinO, regardless of the bond lengths explored. As can be seen from table 2.2.6, the $\Delta\nu$ experimental values obtained for the quinO/quin-^{18}O mixture are too small to allow for unambiguously attributing these to lower energy shifts produced by isotopic labelling. More so, due to the fact that a mixture was obtained, it seems reasonable to assume that only those bands where splitting or the appearance of shoulders is observed can be treated as O-18 sensitive vibrations, such as the lower energy modes 30, 31 and 33*A*'. Evidence is hence lacking in order to render the calculations and/or bond length utilized as inadequate. The possibility exists as well that proton and metal binding studies bring about a change of coupling within the molecule that would hence limit their applicability to the assignment problem for the free ligand. It is possible that modes 17 and 18*A*' are inverted in the assignment performed for quinO. If the trend towards lower energy observed for mode 17*A*' as a function of increasing N-O bond length is maintained, then it can easily be seen from figure 2.2.12 that a crossover is expected to occur changing the order of the assignments for these bands.

Mode 33*A*' occurring at *ca*. 320 cm^{-1} for quinO had been previously assigned to the αN-O vibration on the basis of its shift upon H-bond formation [19, 26]. The band is indeed O-18 sensitive as a shoulder occurring at 309 cm^{-1} is observed in the far ir spectrum of the O-16/O-18 quinO mixture as can be seen in figure 2.2.19. However, although the calculations indicate a large shift upon O-18 labelling, analysis of the normal modes obtained reveals that the motion of the N and O atoms in this vibration occurs in the same direction (the same occurs for mode 32*A*' which is also O-18 sensitive) indicative of an in-plane bend. Based on the displacement diagram, the αN-O vibration is calculated to occur at a higher frequency, and has been assigned principally to mode 30*A*' in both quinO and quin-d_7O. Mode 29*A*' shows O-18 sensitivity as well, but less than mode 30*A*'. The latter mode has a large degree of $8B_{1g}$ character from naphthalene, and this is present in a lower frequency mode, 31*A*', for both quinO and quin-d_7O, indicating extensive coupling of the in-plane N-O bend.

The γN-O vibration, had been previously assigned [19, 26] to the low energy out-of-plane mode occurring in the 170 cm^{-1} region. Although the band shows O-18 sensitivity, mode 15*A*'' shows that both the O and N atoms are displaced in the same direction, and is thus a better description of the butterfly mode of quinO. Modes 13 and 14*A*'' show a displacement of the N and O atoms in different directions, but the shift upon O-18 labelling is negligible for the latter mode and 3 cm^{-1} for the former. Mode 13*A*'' has hence been assigned as the principal γN-O vibration. It occurs as a very weak intensity band in the far ir spectrum of quinO and no clear differences are observed in the spectrum for the O-16/O-18 quinO mixture.

The present calculations suggest that in large fused ring systems of low symmetry, the use of isotope labelling studies needs to be interpreted judiciously. In a highly coupled system the largest isotopic shift may not indicate the principal pure vibration of interest, but might rather represent an associated vibration, as reflected in the behaviour of butterfly mode 15*A*" at 170 cm^{-1}. In addition, it appears that neither the homocyclic parent not the heterocyclic analogue of fused ring systems represent a suitable basis to interpret the spectrum of the substituted system.

2.2.4. Naphthalene related molecules

Regarding the question raised as to whether a set of rules can be developed for substituted naphthalenes as that developed by Varsányi and Szöke for substituted benzenes [29], calculations were performed on quinoline *N*-oxide's isoelectronic analogue 1-fluoronaphthalene. An analysis of the displacement diagrams obtained showed that the modes obtained are very similar to those

obtained for quinO and so are not presented here. It remains to be seen what differences occur when in a series of substituted naphthalenes, $C_{10}H_7X$, where X = F, Cl, Br, I, the substituent increases in mass and electrons. The results obtained in this work, show that future such assignments must proceed with extreme caution, as the vibrations for each of the systems may be extremely different due to the extent of coupling inherent to the system.

Vibrations for 1-substituted naphthalene molecules, $C_{10}H_7X$, where X = F, NH_2, OH, CH_3, are expected to be quite similar to those obtained for the quinO systems and are worth exploring further.

As regards the assignments performed on the 8-hydroxyquinoline molecule by Srivastava *et al.* [51], these were done by direct comparison to the quinoline fundamentals. It seems extremely likely that the vibrations obtained for the 8-hydroxyquinoline compound will be more related to those obtained for quinO or for 1-fluoronaphthalene, than those obtained for quinoline, which very much resemble the naphthalene system.

2.3. Zeise's salt derivatives

Olefin and carbonyl compounds with Pt(II) have been extensively studied ever since Zeise's salt, $K[Pt(C_2H_4)Cl_3]$, was obtained in 1825 [64]. Coordination of ethylene, olefins, and CO to Pt(II) has allowed for a large number of derivatives to be prepared with many different ligands [14, 65-74].

Zeise's salt derivatives $[Pt(C_2H_4)LX_2]$ form a wide variety of compounds depending on the nature of L. The following discussion will focus mainly on those ligands L which bind monodentately to the Pt(II) atom, as those are the object of the present study. These compounds, in which η^2-C_2H_4 coordination is observed, are usually considered as square planar tetra-coordinated but can also be viewed as exhibiting a trigonal bipyramidal geometry if the ethylene unit is considered to bind via both carbon atoms. As such, the ethylene carbons and the donor atom from the L ligand constitute the equatorial plane while the X atoms are axially bound.

Bonding in these compounds has been described by Chatt in terms of a σ-type bond from the olefin filled π orbital to the vacant orbitals in the metal, in conjunction with π-backbonding from the metal to the π^* antibonding orbital in the olefin [61]. The extent of π-backbonding is dependent on the oxidation state of the metal, and becomes significant for lower oxidation states

as would be expected due to an increase in electron density in the metal atom. In Zeise's salt derivatives, the σ-bonding scheme is widely accepted to be predominant [61].

Substitution of ethylene by CO yields in most cases the tetra-coordinated $[Pt(CO)LX_2]$ derivatives, where a square planar geometry is observed. A schematic representation of these compounds is shown in figure 2.3.1.

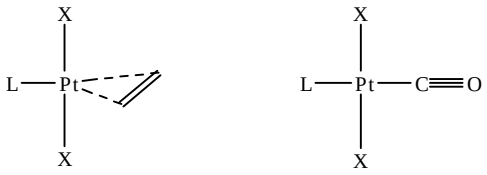

Figure 2.3.1. Zeise's salt derivatives, *trans*-$[PtALX_2]$, where A = C_2H_4, CO.

η^2-C_2H_4 derivatives with L = substituted pyridines have previously been prepared and characterized by single crystal XRD studies. The compounds $[Pt(C_2H_4)LCl_2]$ where L = 4-methylpyridne, 4-cyanopyridine [75] and 2,4,6-trimethylpyridine [76] all show Pt-N and Pt-C_2H_4 bond lengths which are equal within levels of accuracy. Bonding of the ligand L in these compounds has been explained in terms of both σ and π-bonding due to the fact that the pyridine systems are good π-acid ligands which can accept electron density from the metal centre [75-77].

A study of compounds of the type $[Pt(C_2H_4)(4\text{-R-py})X_2]$ performed on a series of eleven compounds with different R substituents, yielded no differences in the νC=C stretching frequency or the Pt-C_2H_4 bonds as observed from spectroscopic data [75, 77, 78]. This apparent independence of the νC=C stretching frequency to the nature of substituted L ligands has also been observed in substituted pyO Zeise's salt derivatives [20]. This apparent independence is due to the extensive vibrational coupling between νC=C and δCH_2 of the ethylene system and led to the use of the summed percentage shifts of the νC=C and δCH_2 as a rough estimate of double bond character [77, 78].

In the compounds where L = 4-CH_3-pyridine, 4-CN-pyridine and X = Cl [75] changes are observed for the νPt-N stretching frequencies, with a lower frequency observed for the electron

withdrawing 4-CN group, as would be expected. These studies have been extended to other systems to allow for a better understanding of the bonding occurring in the Zeise's salt derivatives.

For a given series of [Pt(olefin)LCl_2] compounds where the donor atom in the ligand L was varied, it could be established that the *trans* influence increases in the order O < Cl^- < N, with a lowering in the mean frequency value of the ν_aPt-C_2 and ν_sPt-C_2 observed for increasing basicity of the donor atoms in L [77].

Meester, *et al*. studied the ^{13}C nmr shifts of C_2H_4 and CO shifts for compounds of the type [$PtALX_2$], where A = C_2H_4, CO; L = 4-R-py and X = Cl, Br [78]. They were able to find a correlation between the Hammett σ_p parameters for the R substituents on the pyridine systems and both the $\delta^{13}C(C_2H_4)$ and the $\delta^{1}H(C_2H_4)$.

For the carbonyl derivatives, it was observed that the νCO stretch and $\delta^{13}C$(CO) are R-dependent. The more electron-withdrawing the R substituents become, the νCO stretching frequency increases and a larger upfield shift is observed. These results have been explained in terms of an increase in the π-bonding ability of the 4-R-py ligands as R becomes more electron-withdrawing, which in turn debilitates the π-Pt$\rightarrow$CO backbond producing a higher νCO stretching frequency and a larger $\delta^{13}C$(CO) upfield shift [78].

In a study of fifteen substituted Zeise's salt aniline derivatives, [$Pt(C_2H_4)$(R-an)Cl_2] performed by Thornton and co-workers [73], an increase in ν_aPt-C_2, ν_sPt-C_2, νC=C and νPt-N was observed for electron-releasing groups whereas a marked lowering of the frequency values was obtained for electron-withdrawing groups. The properties of the R substituent are transferred to the N donor atom in the aniline system and contribute to better π-Pt-C_2H_4 backbonding and Pt-N σ-bonding the more electron enriched the Pt atom is.

Further studies on [PtA(R-an)Br_2] (A = C_2H_4, CO) systems performed by Thornton's group [79] confirmed the trends observed previously (with the exception of νC=C which seems impervious to a change in R). For the carbonyl derivatives, an increase in the νPt-CO frequency and a well defined, albeit subtle, trend towards lower frequencies for νCO was observed as the substituents vary from electron-withdrawing to electron-releasing.

The *trans* effect that the π-acid donors have on the Pt(II)-halide moiety allows for coordination of donor atoms that will not bind to the Pt(II) atom otherwise. In this way, it was observed that *N*-oxide coordination to Pt(II) did not occur when an aqueous solution of $K_2[PtCl_4]$ was stirred with pyridine *N*-oxide (pyO). However, *trans* coordination of this ligand is observed immediately when the ligand is stirred with $K[Pt(C_2H_4)Cl_3]$ due to the labilizing effect that η^2-C_2H_4 coordination has on the halide that is *trans* to it [20].

The structure of the η^2-C_2H_4 and CO Zeise's salt derivatives with aromatic *N*-oxide ligands is shown in figure 2.3.2. The fact that in these compounds, the Pt-O-N angles are very close to 120° allows for the Pt-O bond to be considered a σ-bond with very little π-backbonding character as is the case with the aniline derivatives of Zeise's salt [20]. The angle of 120° is accepted as evidence of sp^2 hybridization of the oxygen (the two lone pairs, one of which forms the dative covalent bond to the platinum, plus the bonding pair, with the third lone pair in a *p*-orbital for π-interaction with the pyridine ring). However, for metal to ligand backbonding to occur the planes of the M-O-N and pyridine ring should be coincident [80].

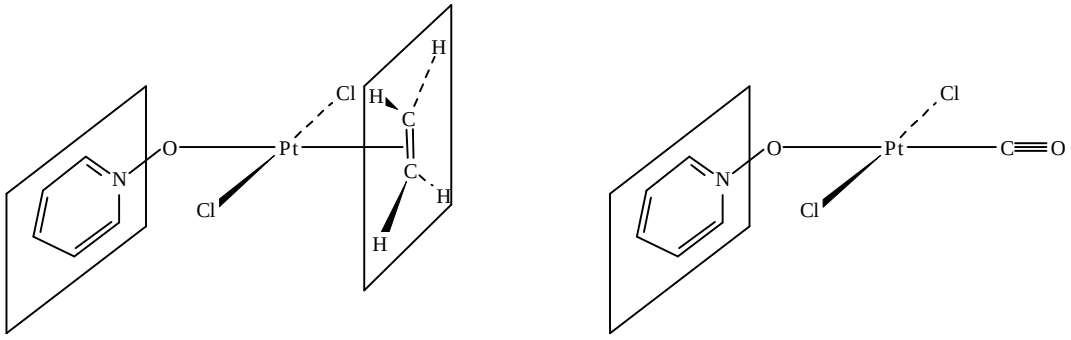

Figure 2.3.2. Structure for Zeise's salt derivatives, $[PtALX_2]$,
where A = C_2H_4, CO and L = aromatic *N*-oxide ligand.

Studies performed on Zeise's salt derivatives with substituted *N*-oxide ligands, show very little R sensitivity on the spectroscopic properties of the compounds. Decomposition temperatures vary, and there is no trend that can be related to the electronic properties of the substituents employed [20]. As is the case with most of the η^2-C_2H_4 compounds prepared, the νC=C frequency is impervious to substituents in the *N*-oxide systems [20]. This is not the case for carbonyl

derivatives, where a very marked trend to lower frequencies is observed for the νCO stretching frequency for electron-releasing subtituents on the substituted pyO systems, as is also the case with the substituted aniline systems [73, 79].

No conclusions have been drawn as regards the νPt-O frequency for these substituted derivatives as the frequency for this vibration has not been established with certainty. It has been assigned by several authors [19, 20] as a weak shoulder occurring *ca.* 323 cm^{-1}, but this band has been shown to be insensitive to R-substitution in the pyO systems. Other assignments have mistakenly identified pyO low energy ring vibrations for the νPt-O frequency [19, 21]. The assignment confusion has been compounded by the wide acceptance of Shindo's characteristic N-O frequencies, which have been shown to be erroneous [11].

2.3.1. Crystal structures of *N*-oxide Zeise's salt derivatives

Despite the fact that [PtALX$_2$] (A = C_2H_4, CO; L = *N*-oxide; X = Cl, Br) systems have been studied extensively, very little information is known regarding their crystal structure. In fact, a search performed on the CSD up to June 2003 shows no crystal structures for Zeise's salt derivatives with *N*-oxide ligands. The crystal structure of the carbonyl compound [Pt(CO)(4-CH_3O-pyO)Cl_2] has been reported [20] previously.

Table 2.3.1. Crystallographic data for [Pt(C_2H_4)(pyO)Cl_2] and [Pt(CO)(quinO)Br_2]

	trans-[Pt(C_2H_4)(pyO)Cl_2]	*trans*-[Pt(CO)(quinO)Br_2]
empirical formula	$C_7H_9Cl_2NOPt$	$C_{10}H_7Br_2NO_2Pt$
Fw	389.13	528.08
crystal system	monoclinic	triclinic
space group	C2/*m* (no.5)	P-1 (no.2)
a (Å)	18.391(4)	8.2115(16)
b (Å)	6.7850(14)	8.3089(17)
c (Å)	8.5432(17)	9.4738(19)
α (deg)	90.000	85.140(3)
β (deg)	112.460(3)	74.010(3)
γ (deg)	90.000	81.900(3)
V ($Å^3$)	985.2(4)	614.5(2)
Z	4	2
ρ_{calcd} (gcm^{-3})	2.6235(11)	2.8539(9)
temp (K)	193(2)	193(2)
λ (Mo Kα) (Å)	0.71073	0.71073
μ (Mo Kα) (cm^{-1})	147.36	179.02
min-max 2θ (deg)	7.68-56.58	6.74-56.56
R	0.0243	0.0287
W*R*	0.0541	0.0623

The crystal structures of the compounds $[Pt(C_2H_4)(pyO)Cl_2]$ and $[Pt(CO)(quinO)Br_2]$ have been obtained in this work and will be discussed in the following section. Crystal structure parameters, bond lengths and angles, and average isotropic displacement parameters for both compounds are shown in appendices 1 and 2. Crystallographic data for the compounds obtained is shown in table 2.3.1.

2.3.1.1.Crystal structure of $[Pt(C_2H_4)(pyO)Cl_2]$

The structure and labelling scheme for the $[Pt(C_2H_4)(pyO)Cl_2]$ compound is shown in figure 2.3.3 and packing in the unit cell is shown in figure 2.3.4. Selected bond lengths and angles for the compound are shown in table 2.3.2.

The compound forms discrete molecules in which 4-coordination to the Pt(II) atom is observed. The structure is better described as having a trigonal bipyramidal geometry where the trigonal plane is defined by the η^2-bound C_2H_4 molecule and the oxygen atom from the pyO ligand and the Cl atoms are axially bound to the metal centre. The Pt(II) atom lies –0.0764 Å below the plane defined by C(6), O(1) and C(7). The Pt-C distances are of 2.1117 and 2.1150 Å respectively for the Pt(1)-C(6) and Pt(1)-C(7) bonds with the shortest distance of 2.0178 Å from the Pt(II)

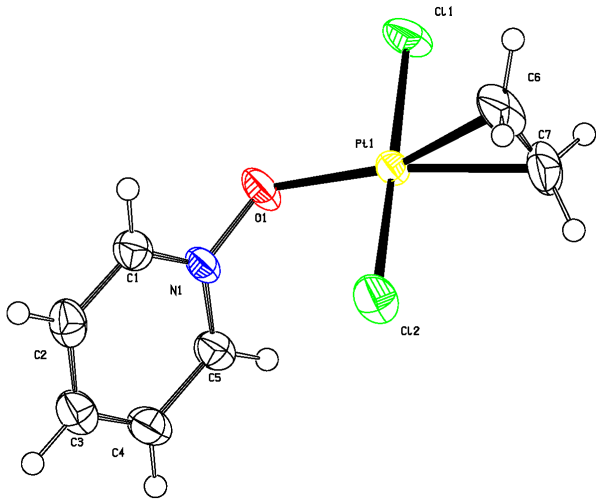

Figure 2.3.3. PLATON [81] drawing of $[Pt(C_2H_4)(pyO)Cl_2]$ showing the labelling scheme employed for the atoms.

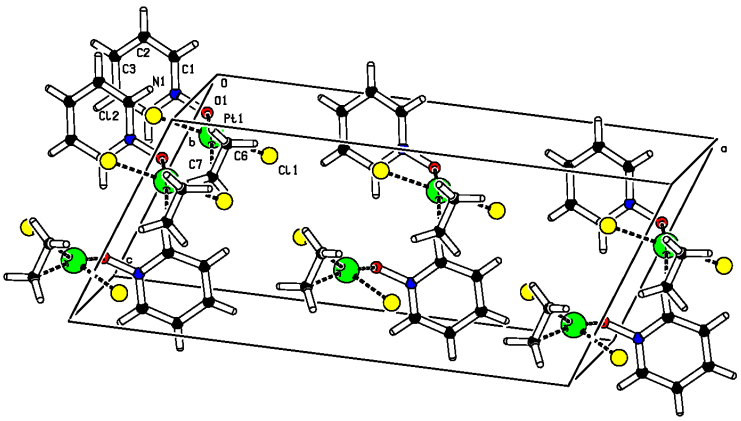

Figure 2.3.4. PLATON [81] drawing of the packing of $[Pt(C_2H_4)(pyO)Cl_2]$ molecules in the unit cell.

Table 2.3.2. Selected bond lengths (Å) and bond angles (degrees) for $[Pt(C_2H_4)(pyO)Cl_2]$. Relative error in distances 0.0002 Å, absolute angle error 0.03 degrees.

Pt(1)-C(6)	2.1117	Cl(1)-Pt(1)-Cl(2)	178.95
Pt(1)-C(7)	2.1150	Pt(1)-O(1)-N(1)	120.52
Pt(1)-Cl(1)	2.2914	Cl(1)-Pt(1)-O(1)	85.15
Pt(1)-Cl(2)	2.2835	Cl(2)-Pt(1)-O(1)	93.88
Pt(1)-O(1)	2.0474	Cl(1)-Pt(1)-C(6)	90.93
C(6)-C(7)	1.3910	Cl(1)-Pt(1)-C(7)	90.01
O(1)-N(1)	1.3672	Cl(2)-Pt(1)-C(6)	90.12
C(6)-Pt(1)-C(7)	38.43	Cl(2)-Pt(1)-C(7)	90.75
Pt(1)-C(6)-C(7)	70.92	C(6)-Pt(1)-O(1)	161.00
Pt(1)-C(7)-C(6)	70.66	C(7)-Pt(1)-O(1)	159.64

atom to the double bond, which would reflect the η bond length . As can be seen from table 2.3.3, the Pt-C bond distances in the pyO compound are slightly shorter than those observed for Zeise's salt and other η^2-C_2H_4 derivatives.

The Cl atoms are axially bound to the Pt(II) atom and are at basically 90° angles to the trigonal plane defined by the ethylene moiety and the oxygen atom.

The O(1) - Pt(1) - N(1) bond angle of 120.52° is in good agreement with other *N*-oxide structures [20] obtained, and the angle between the pyridine ring system and the trigonal plane of the molecule defined by C(6), O(1) and C(7) is 59.34°. If the compound is described as square planar, then the angle between the pyridine ring system and the plane defined by Cl(1), O(1) and Cl(2) is close to 90° (83.42°), similar to that observed in the carbonyl derivative with 4-methoxypyridine *N*-oxide (87.5°) [20].

Table 2.3.3. Selected bond lengths (Å) and angles (degrees) for *trans*-[PtALCl$_2$] compounds. Values in brackets for the compound with A = C_2H_4 and L = pyO are the calculated values for the optimized geometry arrived at by DFT calculations (section 2.3.1.3).

Bond distance/ Angle	A =C_2H_4 L = Cl [64]	A = C_2H_4 L =4-Me-py [75]	A = C_2H_4 L = 4-CN-py [75]	A = CO L = 4-MeO-pyO [20]	[a] A = C_2H_4 L = pyO
Pt-C1	2.14(2)	2.16(2)	2.13(4)	1.74(4)	2.1117 [2.1399]
Pt-C2	2.16(2)	2.14(2)	2.19(3)		2.1150 [2.1383]
Pt-X1	2.296(3)	2.290(5)	2.302(7)	2.26(3)	2.2835 [2.3909]
Pt-X2	2.296(3)	2.295(4)	2.302(7)	2.25(3)	2.2914 [2.3650]
Pt-L	2.335(6)	2.05(1)	2.06(2)	1.99(2)	2.0474 [2.1182]
N-O				1.35(3)	1.3672 [1.3357]
C1-C2	1.37(3)	1.32(3)	1.35(4)		1.3910 [1.4071]
C1-Pt-C2	37.2(8)	35.6(7)	36.4(12)		38.43 [38.40]
X1-Pt-X2	178.5(2)	180(14)	180(21)	178.1(3)	178.95 [178.48]
Pt-O-N				120(1)	120.52 [119.35]

a Relative error in distances 0.0002 Å, absolute angle error 0.03 degrees.

The observed Pt-O bond of 2.0474 Å is slightly longer than that of 1.99(2) Å for the CO derivative with the 4-MeO-pyO derivative. Within experimental error, N-O bond distances in both systems are similar as is shown in table 2.3.3.

2.3.1.2. Crystal structure of [Pt(CO)(quinO)Br$_2$]

The structure and labelling scheme for the [Pt(CO)(quinO)Br$_2$] compound is shown in figure 2.3.5, and packing in the unit cell is shown in figure 2.3.6. Selected bond lengths and angles are shown in table 2.3.4. The compound has a square planar geometry with the Pt(II) atom lying 0.0236 Å below the plane defined by the Br(1), Br(2) and O(1) atoms. The CO ligand is bound to

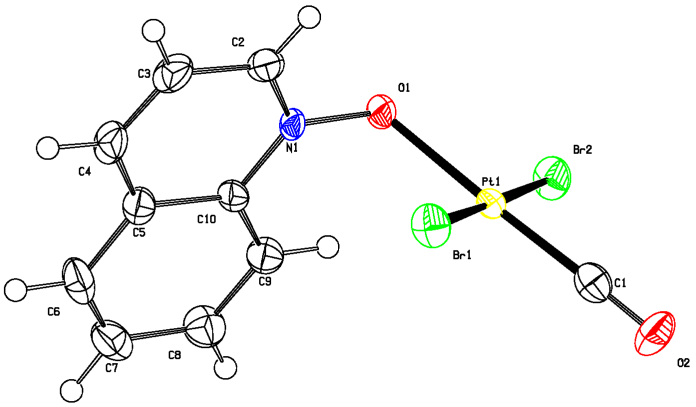

Figure 2.3.5. PLATON [81] drawing of [Pt(CO)(quinO)Br_2] showing the labelling scheme employed for the atoms.

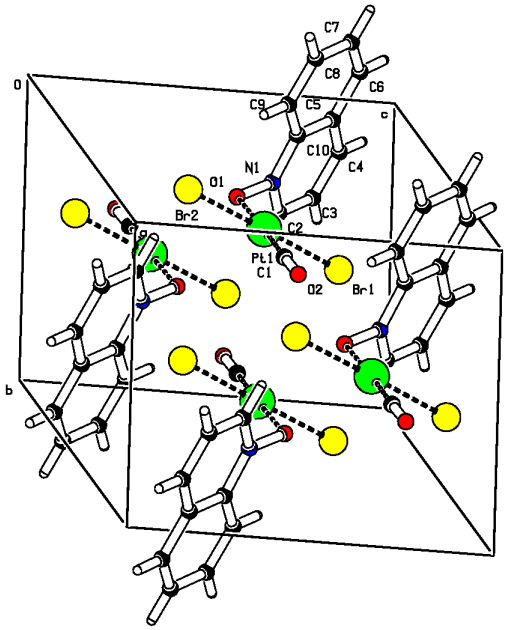

Figure 2.3.6. PLATON [81] drawing of the packing of [Pt(CO)(quinO)Br_2] molecules in the unit cell.

Table 2.3.4. Selected bond lengths (Å) and bond angles (degrees) for $[Pt(CO)(quinO)Br_2]$.

Pt(1)-C(1)	1.823(5)	O(1)-Pt(1)-C(1)	176.53(16)
Pt(1)-Br(1)	2.4240(7)	Pt(1)-O(1)-N(1)	118.5 (2)
Pt(1)-Br(2)	2.4242(7)	Br(1)-Pt(1)-Br(2)	178.83(3)
Pt(1)-O(1)	2.045(3)	O(1)-Pt(1)-Br(1)	93.94(9)
C(1)-O(2)	1.131(6)	O(1)-Pt(1)-Br(2)	85.71(9)
O(1)-N(1)	1.361(4)	Br(1)-Pt(1)-C(1)	89.34(14)
Pt(1)-C(1)-O(2)	178.2(4)	Br(2)-Pt(1)-C(1)	90.99(14)

the Pt(II) atom at a distance of 1.823(5) Å with a Pt(1)-C(1)-O(2) bond angle of 178.2(4), and is slightly below the plane formed by Br(1), Br(2) and O(1) with the C(1) and O(2) atoms lying 0.0106 and 0.0262 Å below the plane, respectively. The Pt-CO bond is basically at 90 degrees to the coordinated bromide atoms.

The Pt-O bond distance of 2.045(3) is slightly longer than that observed in the $[Pt(CO)(L)X_2]$ compound with L = 4MeO-pyO and X = Cl [20], but similar to that of $[Pt(C_2H_4)(pyO)Cl_2]$ obtained here. The N-O bond distance for the quinO system of 1.361(4) Å is similar to the pyO system. The Pt(1)-O(1)-N(1) angle is of 118.5(2) and the angle between the quinoline ring system and the plane of the molecule is of 87.40 degrees, with the aforementioned planes defined by C(2)-N(1)-C(10) and Br(1)-O(2)-Br(2).

Table 2.3.5. Selected bond lengths (Å) and angles (degrees) for $[Pt(CO)LX_2]$ compounds. Values in brackets for the compound with A = CO, L = quinO and X = Br, are the calculated values for the optimized geometry of the stable structure arrived at by DFT calculations (section 2.3.1.3).

Bond distance/ angle	$[Pt(CO)Cl_3]^-$ L = Cl [72]	*cis*-$[PtA_2X_2]$ A = L = CO X = SO_3F [82]	*cis*-$[PtALCl_2]$ A = CO L = PPh3 [82]	*cis*-$[PtA_2X_2]$* A = L = CO X = Br [83]	*trans*-$[Pt(CO)LBr_2]$ L = quinO
Pt-C	1.82(1)	1.897(13)[a]	1.858(7)	1.86(4)[a], 1.88(3)[a]	1.823(5) [1.8459]
Pt-L	2.289(3)	1.868(13)	2.282(2)	1.96(6), 1.89(5)	2.045(3) [2.1075]
Pt-X1	2.294(4)	2.024(9)	2.343(2)	2.417(4), 2.416(4)	2.4240(7) [2.5223]
Pt-X2	2.290(4)	2.022(9)[a]	2.276(1)[b]	2.411(4)[a], 2.417(4)[a]	2.4242(7) [2.5391]
C-O	1.12(2)	1.103(16) 1.130(17)	1.114(8)	1.12(4), 1.12(4) 1.06(5), 1.17(5)	1.131(6) [1.1447]
Pt-C-O	178(2)	178.3(11) 176.6(12)	175.6(7)	177(4), 179 (3) 178(4), 176 (3)	178.2(4) [177.95]

* Two crystallographically independent units are observed in the unit cell for the compound.
a CO and X atoms *trans* to each other.
b Cl atom *trans* to CO.

From tables 2.3.3 and 2.3.5, bond distances and angles for $[Pt(C_2H_4)(pyO)Cl_2]$ and $[Pt(CO)(quinO)Br_2]$, are typical of those observed for related compounds. It is interesting to note, in the carbonyl compound with L = 4-MeO-pyO, the Pt-O bond distance is slightly shorter than those for compounds with pyO and quinO, reported here. However, this difference is very small, and must be related to the presence of the electron-releasing substituent (4-MeO) on the pyridine ring. This would contribute a greater electron density in the system, favouring a stronger σ-bond between oxygen and Pt(II). The 4-MeO-pyO compound exhibits the shortest observed Pt-CO bond length at 1.74(4) Å.

2.3.1.3. Molecular modelling

Attempts to model the $[PtALX_2]$ systems (where A = C_2H_4, CO; L = pyO, quinO; X = Cl, Br) by means of molecular mechanics using semi-empirical methods were performed using Cerius2 and the universal force field (UFF). However, although the results obtained in the vibrational analyses for the *N*-oxide ligands coordinated to the Pt(II) centre are reliable, this is not the case for the vibrations for the A ligands (especially the C_2H_4 system) nor for the Pt-A, Pt-L and Pt-X vibrations. All of the latter vibrations are overestimated in their wavenumbers, by up to 100 cm^{-1} in some cases, and attempts at matching the calculated and observed frequencies proved redundant.

DFT calculations performed on the $[PtALX_2]$ systems were carried out at the B3LYP level by use of a pseudopotential employing the basis set LACVP** for Pt(II) and 6-31G** for the remaining atoms. Geometry optimizations of the molecules studied do not always yield the geometry that has been established for these compounds by means of X-ray diffraction studies. However, several geometries explored yield stable molecules in which vibrational analyses provide all real frequency values. Such is the case for the $[Pt(C_2H_4)(pyO)Cl_2]$ and $[Pt(CO)(quinO)Br_2]$ systems, which are shown in figures 2.3.7 and 2.3.8 respectively. Knowledge of the crystal structure for these compounds allows for modelling of these systems by constraining the distance between two atoms and allowing for a geometry optimization in order to arrive at calculated structures that resemble those observed by XRD studies (structure I for both compounds modelled). This was done for the aforementioned systems by constraining the distance between one of the X atoms and one of C atoms from the aromatic *N*-oxide ring systems. Using the labelling scheme shown in figures 2.3.3 and 2.3.5, the $[Pt(C_2H_4)(pyO)Cl_2]$ was optimized subject to the constraint of a 3.52 Å distance between the Cl(2) atom and the C(5) atom in the pyO ring system, while the constraint of a 4.44 Å bond distance between the Br(1) atom and the C(9) atom in the quinO ring system

was used for [Pt(CO)(quinO)Br_2]. Both distances were calculated from the coordinates obtained by the crystal structure studies performed. Interestingly, both of the calculated [Pt(C_2H_4)(pyO)Cl_2] structures yield all real frequency values, while this was not the case for the quinO system. A vibrational analysis performed on structure I for [Pt(CO)(quinO)Br_2] subject to the constraint yielded one imaginary frequency value, while the geometry for structure II yielded

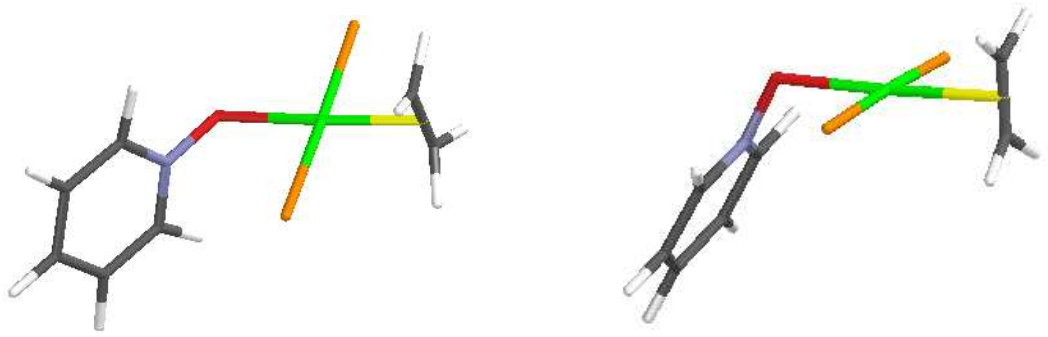

Structure I Structure II

Figure 2.3.7. Stable conformers obtained by DFT calculations for [Pt(C_2H_4)(pyO)Cl_2]. Both structures yield vibrational analyses with all real frequency values. Structure I resembles the one obtained by means of XRD studies and was obtained by means of one distance constraint.

Structure I Structure II

Figure 2.3.8. Stable conformers obtained by DFT calculations for [Pt(CO)(quinO)Br_2]. Both structures yield vibrational analyses with all real frequency values. Structure I was obtained by means of geometry optimization subject to one distance constraint followed by another geometry optimization removing the constraint, and resembles that obtained by means of XRD studies.

all real frequency values. Removal of the constraint for structure I subject to an additional geometry optimization yielded a stable structure with all real frequency values. A comparison of bond distances obtained between structures I and II for the $[Pt(CO)(quinO)Br_2]$ compound, showed small variations in bond lengths and angles. However, the different geometries for the compounds yield noticeably different vibrational analyses, especially in the low energy region.

The problem posed by the existence of several local minima in the potential energy surface for both the $[Pt(C_2H_4)(pyO)Cl_2]$ and $[Pt(CO)(quinO)Br_2]$ compounds can be easily overcome with structural evidence from crystallographic studies.

Comparison between the experimental and calculated bond distances and angles in the $[Pt(C_2H_4)(pyO)Cl_2]$ and $[Pt(CO)(quinO)Br_2]$ compounds and the standard deviation between observed and calculated values is shown in figures 2.3.9-2.3.12. Selected calculated bond lengths and angles are included in tables 2.3.2 and 2.3.4. The calculated bond lengths and angles obtained for structures I of the $[Pt(C_2H_4)(pyO)Cl_2]$ and $[Pt(CO)(quinO)Br_2]$ compounds were used in the comparison of the experimental bond lengths obtained by XRD studies.

As can be seen from figures 2.3.9-2.3.12 and as was discussed in the previous chapter, the N-O bond length is consistently under-estimated in both the calculations for the ligands and the coordination compounds. For both compounds modelled, the bond distances between the Pt(II) atom and coordinated ligands are slightly over-estimated, with the largest differences observed for the Pt-X and Pt-O bonds. The trend to over-estimate M-L bond lengths, has been previously reported for calculations performed at the B3LYP level. However, they are a significant improvement to calculations performed by Hartree-Fock methods, where differences of 0.1-0.3 Å between experimental and observed bond lengths are usually obtained [84].

The over-estimation in the Pt-L, Pt-A and Pt-X bonds and the under-estimation of the N-O bond length in the ring systems has an important effect in the calculated vibrational frequencies. This is particularly noticeable in the νPt-X vibrations, which are calculated at lower energies as will be discussed in section 2.3.2.8.

Attempts at modelling the $[Pt(CO)(pyO)Cl_2]$ system by substituting the CO ligand for the C_2H_4 ligand, and allowing for a geometry optimization yielded, in all cases explored, optimized

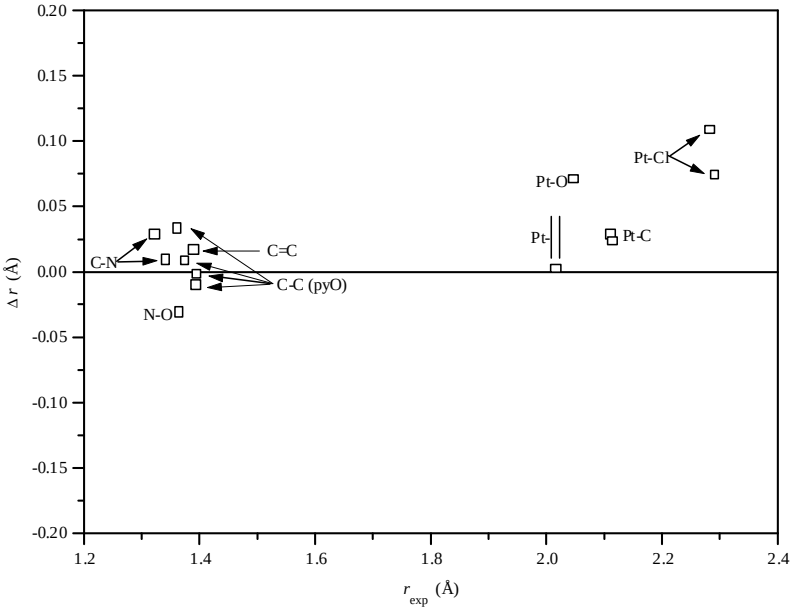

Figure 2.3.9. Comparison between calculated and observed bond lengths for $[Pt(C_2H_4)(pyO)Cl_2]$; $\Delta r = r_{calc} - r_{exp}$. Standard deviation between experimental and calculated values is 0.0277 Å.

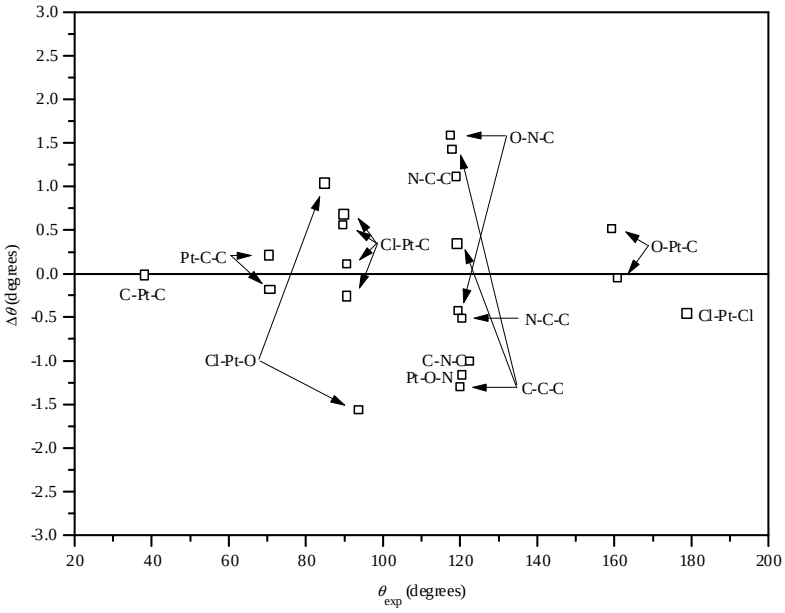

Figure 2.3.10. Comparison between calculated and observed bond angles for $[Pt(C_2H_4)(pyO)Cl_2]$; $\Delta \theta = \theta_{calc} - \theta_{exp}$. Standard deviation between experimental and calculated values is 0.8948°.

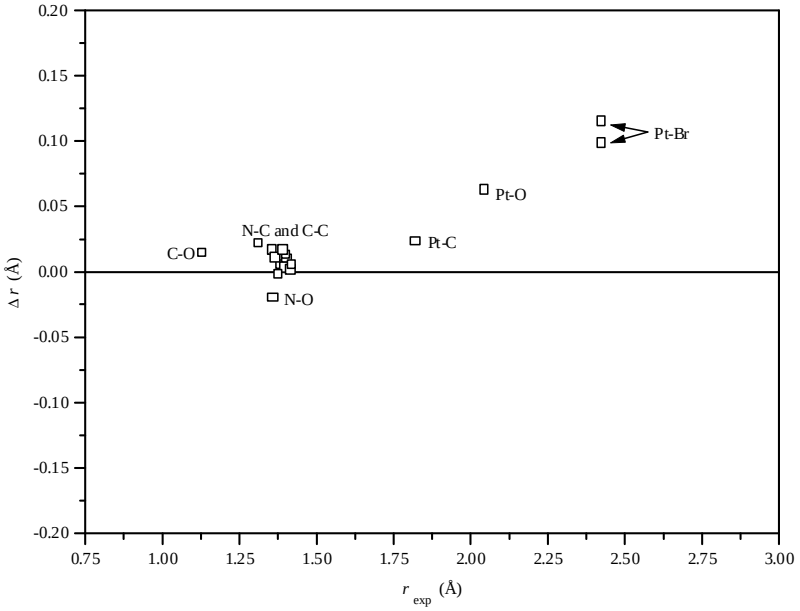

Figure 2.3.11. Comparison between calculated and observed bond lengths for [Pt(CO)(quinO)Br_2]; $\Delta r = r_{calc} - r_{exp}$. Standard deviation between experimental and calculated values is 0.0143 Å.

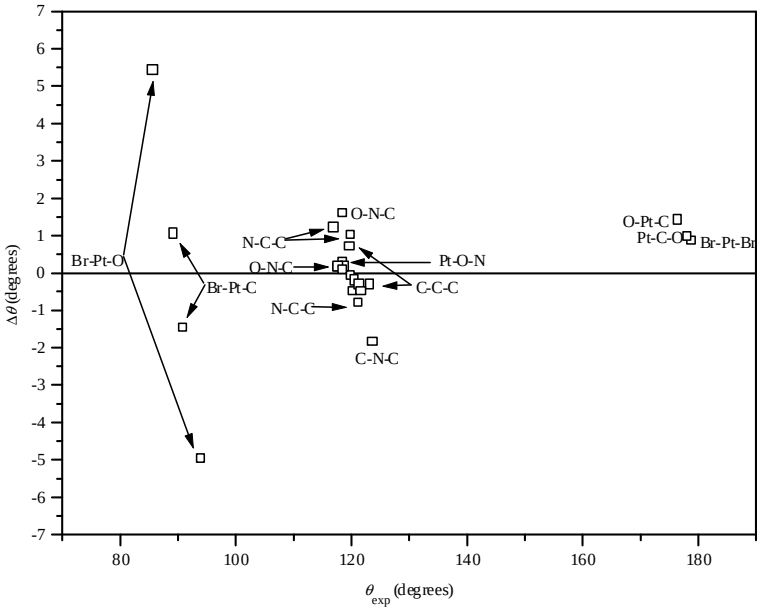

Figure 2.3.12. Comparison between calculated and observed bond angles for [Pt(CO)(quinO)Br_2]; $\Delta \theta = \theta_{calc} - \theta_{exp}$. Standard deviation between experimental and calculated values is 1.785°.

geometries with at least one imaginary frequency value. This was observed whether distances were constrained or not, when using both the optimized geometries obtained for the calculated and stable (all real frequency values) $[Pt(C_2H_4)(pyO)Cl_2]$ compounds. The results obtained are interesting in that, of all Zeise's salt derivatives prepared in this work, it is the pyO carbonyl derivatives that are the less stable and undergo very fast decomposition to platinum oxide. More so, chloride derivatives seem to be less stable than the bromide ones. The quinO carbonyl systems are considerably more stable, and it is worth mentioning that both geometries explored for the $[Pt(CO)(quinO)Br_2]$ compound, provide vibrational analyses with all real frequency values.

Geometries for the other Zeise's salt derivatives modelled are expected to be quite similar to those obtained by the XRD studies performed and calculated by means of the use of constraints. Hence, geometry optimizations for the compounds where no crystal structure information is available, were performed by substituting the X atoms or the A ligands in the stable structures obtained by means of one constrained distance, and removing the constraint and allowing for a geometry optimization. The results obtained show that the optimized geometries resemble those obtained for the constrained compounds, and these were used in the vibrational analyses for these compounds. The fact that a band to band correspondence is obtained for the mid and far ir spectra for all the $[Pt(C_2H_4)LX_2]$ and $[Pt(CO)LX_2]$ compounds, further supports the assumption that the compounds are isostructural for a given L and X = Cl or Br.

Previous knowledge of the crystal structure allows for a positioning of the ring systems such that they resemble the compound studied in the solid state. The importance of structural information obtained from XRD studies cannot be over-stated, especially when performing a vibrational study where slight variations in geometry lead to significant changes in the low frequency region, as will be discussed in the following section.

2.3.2. Vibrational spectra of Zeise's salt derivatives

Vibrational spectra of Zeise's salt derivatives, $[PtALX_2]$, where A = C_2H_4, CO; L = *N*-oxide ligand and X = Cl, Br; have been extensively studied in the past [14, 19-21, 77, 85]. Perhaps the most detailed studies on these systems have been carried out by Thornton and co-workers, where studies were systematically accompanied by deuteration labelling of the *N*-oxide systems [14, 19, 21, 85]. A revision [19] of the previous assignments performed on the pyO derivatives [14, 85]

shows that many of the fundamentals in this system have been incorrectly assigned, as they have been based on the assignments for the N-O vibrations given by Shindo [5, 59], which have been shown to be in error [11]. Furthermore, although there exist several works that have assigned the νPt-O stretching vibration in the low energy region, the frequency for this vibration has not been absolutely established, and the possibility of significant coupling for this mode has been suggested [19, 21].

The current aim of this study is to provide extensive labelling of the Zeise's salt derivatives [PtALX$_2$] where A = C_2H_4, C_2D_4, CO and ^{13}CO; L = pyO, py-d_5O, py-^{18}O, quinO, quin-d_7O and quin-^{18}O; and X = Cl and Br. Mid and far ir spectra and Raman spectra have been recorded for all the compounds prepared (with the exception of [Pt(C_2H_4)(py-^{18}O)Br$_2$] where only ir spectra were recorded). The labelling studies and the DFT calculations performed on the ligands and the coordination compounds and their isotopomers, allow for a much better understanding of these systems.

2.3.2.1. Calculated frequencies

Vibrational analyses were performed for the geometries obtained by means of DFT calculations as has been mentioned previously. The fact that two stable geometries are obtained for both [Pt(C_2H_4)(pyO)Cl$_2$] and [Pt(CO)(quino)Br$_2$] is worth discussing further, as regards the information provided by the vibrational analyses performed.

A comparison between the frequency values obtained for both pairs of structures shown in figures 2.3.7 and 2.3.8 shows that the ring vibrations are calculated at similar values for both systems with only minor differences observed in the 1600-600 cm^{-1} region. Important changes that are geometry dependent are observed in the low energy region, where coupling is observed for different ring modes and Pt-A, Pt-L and Pt-X vibrations as will be discussed below.

2.3.2.2. [PtA(pyO)X$_2$] systems

The compounds modelled have C_1 symmetry and vibrational analyses for the [Pt(C_2H_4)(pyO)X$_2$] compounds and their isotopomers yield real frequency values for all 57 fundamental vibrations obtained. Although most of the ring vibrations appear in the same order for the different geometries obtained in the optimization process, some crossovers are observed which are geometry dependent.

The low energy region is strongly geometry dependent as would be expected, and changes in the geometry of the compounds produce noticeable changes in the extent of coupling observed for the Pt-A and Pt-L vibrations. For structure II shown in figure 2.3.7, the ν_sPt-C_2H_4 and νPt-O vibrations are calculated as extremely coupled vibrations in the [Pt(C_2H_4)(pyO)Cl_2] and [Pt(C_2H_4)(py-^{18}O)Cl_2] isotopomers, with the higher frequency vibration having more ν_sPt-C_2H_4 character and the lower one having more νPt-O character. Calculated frequencies for the [Pt(C_2D_4)(pyO)Cl_2] isotopomer show that this coupling is lost and the frequencies are inverted, with the lower frequency predominant in νPt-O character vibration increasing in energy while ν_sPt-C_2H_4 decreases. The coupling is similarly lost for the [Pt(C_2H_4)(py-d_5O)Cl_2] isotopomer and the ν_sPt-C_2H_4 occurs at a lower value than that calculated for [Pt(C_2H_4)(pyO)Cl_2] and [Pt(C_2H_4)(py-^{18}O)Cl_2], and the νPt-O vibration also occurs at a lower frequency as an effect of perdeuteration.

The significant coupling calculated for the low energy Pt-A and Pt-L modes for structure II provides different values for ν_sPt-C_2H_4 and νPt-O for each of the isotopomers. This situation does not explain the experimentally observed trend, where the ν_sPt-C_2H_4 vibration is seen to occur at the same frequency value for the [Pt(C_2H_4)LX_2] compounds and is shifted to lower energy upon C_2D_4 labelling without a noticeable difference occurring for the other vibrations observed in this range. However, the experimentally observed results are in excellent agreement with the `vibrational analyses performed for the isotopomers for structure I as shown in figure 2.3.7. The ν_sPt-C_2H_4 and νPt-O vibrations are calculated as uncoupled modes for all isotopomers, and match the experimental values satisfactorily. The choice of an adequate geometry seems to play a fundamental role when performing vibrational analyses for those modes occurring in the low energy region, and isotopic labelling and crystal structure information are an invaluable tool in the assignment problem, as well as in the evaluation of the performance of the calculations.

For reasons stated previously, the calculated frequency values employed were those for the structures obtained that resemble those shown in figure 2.3.2 (structure I; figures 2.3.7 and 2.3.8), as XRD studies for the compounds are consistent with these geometries. More so, due to the fact that the carbonyl derivatives are prepared by substitution of C_2H_4 by CO, it seems reasonable to assume that minor changes will be observed for the carbonyl compounds as regards their geometry.

Optimized geometries for [Pt(CO)(pyO)X_2] compounds yield vibrational analyses with at least one imaginary frequency for X = Cl. The symmetry for the compounds explored is C_1 and 45 fundamental vibrations were obtained. The calculated frequency values for the pyO and Pt-X, Pt-L vibrations are consistent with those obtained for the ethylene system and have been used as an aid in the vibrational assignment for these compounds.

2.3.2.3. [PtA(quinO)Br_2] systems

Geometry optimizations and vibrational analyses performed on the [Pt(C_2H_4)LBr_2] Zeise's salt derivatives provide stable molecules with C_1 symmetry and a total number of 75 fundamental vibrations with all real frequency values. The assignment for the quinO derivatives is based on the calculated frequencies obtained for the modelled stable [PtA(quinO)Br_2] (A = C_2H_4, CO) compounds and their isotopomers.

Both structures obtained (where A = CO) have C_1 symmetry and a total number of 63 fundamental vibrations. An interesting inversion in the order of the quinO vibrations, perhaps the most noticeable of all changes brought upon by a change in geometry, occurs in the high energy νC-H region, where modes 1-7*A*' (as previously assigned for the quinO system) are obtained in the same order as the ligand for structure I, but not for structure II (figure 2.3.8). Calculated νC-H frequency values for structure II order them as occurring in the sequence 2, 1, 4, 3, 6, 5 and 7*A*'. This order inverts the νC-H vibrations observed predominantly for ring A in the quinO ligand (modes 1, 3 and 5*A*' as shown in figure 2.2.16), with those that occur predominantly on ring B (modes 2, 4 and 6*A*') for the stable [Pt(CO)(quinO)Br_2] system modelled (structure II, figure 2.3.8). This inversion is not observed for structure I.

It is also worth mentioning that the νC-H displacements are observed to occur in both rings, although the trend in the coordination compounds is for larger displacements to be predominant in one ring over the other, in line with that observed for the free ligand.

Coordination also brings about changes in coupling within the ligand that affects some of the modes obtained in the very sensitive region in which the N-O vibrations occur, as is to be expected from the considerations in the previous section regarding variations in the N-O bond length.

The pyO and quinO vibrations have been classified according to the nomenclature used in the previous sections. Discrepancies to this nomenclature will be discussed in detail below.

The observed and calculated frequencies obtained for the [PtALX$_2$] (where A = C_2H_4, CO; L = pyO, quinO and X = Cl, Br) systems and the corresponding assignments are shown in tables 2.3.6-2.3.12. Due to their relative instability, the Raman spectra for the some of the carbonyl derivatives (particularly for the pyO derivatives) show fluorescence and the quality of the spectra was not always good. The frequencies listed as Raman bands are those that could definitely be interpreted as such.

2.3.2.4. C_2H_4 vibrations

The assignment for the C_2H_4/C_2D_4 vibrations follows that used by Watkins and his co-workers [19, 21] that were based on the normal coordinate analysis performed on Zeise's salt, as cited therein. The following discussion will focus mainly on the pyO derivatives, for which the C_2H_4 bands are more easily observed than in the quinO systems. One difference between the previous assignments and those determined in the present work is the reversal of the assignment of ν_4 and ν_8.

The νC-H frequencies are weak intensity bands in the ir spectra for the ethylene derivatives and overlap with the νC-H(pyO/quinO) bands. The only band that is absent in the νC-H stretch region for the C_2D_4 derivative is at 3014 cm^{-1} (ν_1) and it is observed in both the ir and Raman spectra for the [Pt(C_2H_4)(py-d_5O)X$_2$] derivatives.

Two weak intensity bands at *ca.* 3100 and 3080 cm^{-1} are observed in the Raman spectrum for the [Pt(C_2H_4)(py-d_5O)X$_2$] derivatives. They appear in the ir spectrum for the compound as extremely weak absorptions as well. These have been assigned as ν_5 and ν_9 respectively according to the calculated values and are in agreement with the values observed for Zeise's salt [19, 21]. In the spectra for the pyO compounds, both absorptions are masked by the very intense νC-H(pyO) absorptions at 3106 cm^{-1} ($1A_1$) and 3082 cm^{-1} ($2A_1$).

The most intense νC-D Raman band for the C_2D_4 derivatives is observed at 2226 cm^{-1} (ν_1), as would be expected for a symmetric C-D stretch.

Table 2.3.6. Experimental and calculated rescaled frequencies for [PtALCl$_2$] compounds (A = C_2H_4, C_2D_4; L = pyO, py-d_5O. Raman values are shown in parenthesis. Values in square brackets are calculated shifts to lower energy expected upon O-18 labelling of pyO in the coordination compound. All frequency values in cm^{-1}.

A = C_2H_4 L = pyO		A = C_2D_4 L = pyO		A = C_2H_4 L = py-d_5O		Assignment[□]
exp.	calc.	exp.	calc.	exp.	calc.	
3106*	3109	2334[‡] (2335)[‡]	2318	3097 (3097)	3117	νC-H/D (ν_5)
3106	3106	3106 (3105)	3101	2317 (2317)	2322	1A_1 (20a)
3082 (3083)	3107	3082 (3084)	3100	2317 (2317)	2319	1B_1 (20b)
3082 (3083)*	3090	2287 (2281)	2312	3083 (3081)	3101	νC-H/D (ν_9)
3082 (3083)	3077	3082 (3084)	3069	2307	2297	2A_1 (2)
3062 (3061)	3071	3062	3063	2307	2288	2B_1 (7b)
3051 (3049)	3060	3051 (3050)	3052	2297 (2296)	2275	3A_1 (7a)
3036 (3034)		3036 (3036)		3036 (3035)		not assigned
3014 (3013)	3009	2226 (2226)	2208	3014 (3014)	3020	νC-H/D (ν_1)
(2990)	3007	2195 (2196)	2179	(2990)	3017	νC-H/D (ν_{11})
1613 (1612)	1620	1613 (1611)	1619	1571 (1569)	1571	4A_1 (8a)
(1599)		(1600)				comb. band
(1580)	1577	1576 (1578)	1576	1545 (1546)	1538	3B_1 (8b)
1503 (1504)	1512	953 (952)	962	1505 (1504)	1504	δCH$_2$/D$_2$ (ν_2)
(1495)	1473	(1494)	1472	1384 (1382)	1356	4B_1 (19b)
1471	1468	1471 (1471)	1467	1349 (1349)	1341	5A_1 (19a)
1414 (1414)	1431	1056	1067	1414 (1414)	1424	δCH$_2$/D$_2$ (ν_{12})
1327	1325	1327 (1323)	1324	1038	1034	5B_1 (3)
1258	1275	1257 (1257)	1275	1249 (1249)	1259	6B_1 (14)
1232 (1232)	1227	1340 (1340)	1334	1232 (1232)	1221	νC=C (ν_3)
1192*	1205	953 (952)	970	1189	1199	ρCH$_2$/D$_2$ (ν_6)
1192 (1192)[•]	1203 [9]	1192 (1192)[•]	1203	1140 (1137)	1160 [13]	6A_1 (13)
1168 (1172)	1167 [5]	1168 (1172)	1166	870 (871)	875 [3]	7A_1 (9a)
(1156)	1155	(1157)	1154	845 (846)	845	7B_1 (15)
1095		1096				comb. band
1072	1082	1072	1082	830	820	8B_1 (18b)
1049 (1047)	1051	1049[•] (1049)	1051	855	856 [3]	8A_1 (18a)
	1030	756 (754)	771	1010 (1010)	1026	ωCH$_2$/D$_2$ (ν_7)
1027 (1029)	1026	1028 (1029)	1026	987 (986)	982	9A_1 (12)
1010 (1009)	1024	804 (805)	818	1010 (1010)	1020	ωCH$_2$/D$_2$ (ν_8)
1010 (1009)[†]	987	1010 (1010)	987	818	817	1B_2 (5)
979	978		707	978	974	τCH$_2$/D$_2$ (ν_4)
966	955		955	801 (801)	780	1A_2 (17a)
944	924	944 (944)[•]	923	653 (654)	654	2B_2 (10b)
826 (825)	838 [16]	826 (826)	838	763 (763)	771 [12]	10A_1 (1)
	836		836	674	658	2A_2 (10a)
815[•] (817)[•]	831	(620)	614	818* (823)	828	ρCH$_2$/D$_2$ (ν_{10})
781	779	781 (781)	779	783 (782)	782	3B_2 (11)
727 (729)	765	523 (523)	567	727 (729)	762	τCH$_2$/D$_2$ (ν_{13})
679 (678)	676	679 (679)	676	547 (549)	550 [3]	4B_2 (4)
639 (641)	652	640 (641)	652	613 (614)	624	9B_1 (6b)
574 (574)	577 [12]	574 (575)	577	562 (562)	562 [10]	11A_1 (6a)
(559)	557	(562)	550	511 (510)[†]	499 [8]	5B_2 (16b)
(542)		(547)				comb. band
510 (511)	496	467 (469)	462	511* (510)	496	ν_aPt-C$_2$H$_4$/D$_2$ (*tilt*)
451	456 [13]	452	453	428[†]	439 [13]	10B_1 (9b)

Table 2.3.6. (cont.)

A = C_2H_4 L = pyO		A = C_2D_4 L = pyO		A = C_2H_4 L = py-d_5O		Assignment□
exp.	calc.	exp.	calc.	exp.	calc.	
427 (427)	424	399† (408)	408	428 (427)	426	ν_sPt-C_2H_4/D_2
421	422	423	422		371	$3A_2$ (16a)
400	402 [12]	400	402	381 (382)	386 [9]	νPt-O
346 (345)	335	344 (344)	335	346 (344)	336	ν_aPt-Cl
338 (335)	315	335 (335)	316	339 (334)	317	ν_sPt-Cl
326		326		326		comb. band
227 (220)	222 [1]	215 (219)	221	203 (204)	206	$6B_2$ (17b)
(213)	209	196 (199)	199	215 (215)	218	δPt-C_2H_4/D_2
196	193		167	202	196	τPt-C_2H_4/D_2
172 (169)	176	171 (169)	177	169 (169)	178	δCl-Pt-Cl
150 (151)	154	150 (151)	153	(148)	156	πCl-Pt-Cl
144	148	141	148	142	149	δCl-Pt-O
121 (120)	114	121 (121)	113	121 (117)	116	πO-Pt-C_2
84	88	89	89	92	90	coupled δ and π
	53	54	53		56	skeletal vibrations
	33		34		36	

* Masked by pyO absorption
† Masked by C_2H_4 absorption
‡ Band overlaps with pyO overtone or combination band.
• Shoulder
□ Wilson mode and ethylene mode in parenthesis.

A weak intensity absorption at 2990 cm^{-1}, absent in the ir spectra, is observed in the Raman spectra for the [Pt(C_2H_4)LX_2] (L = pyO, py-d_5O; X = Cl, Br) compounds. This band is absent in the spectra for the C_2D_4 isotopomers and appears as a weak intensity absorption at 2196 cm^{-1} in both the ir and Raman spectra. It has been assigned to mode ν_{11}. The ethylene modes ν_1 and ν_{11} correspond to the $\nu_s CH_2/D_2$ (Raman active) and $\nu_a CH_2/D_2$ (ir active) modes respectively in Zeise's salt. Although both absorptions are weak, the relative intensity of ν_1 in the Raman spectra for the C_2D_4 isotopomers is noticeably greater than that for ν_{11}. The situation is reversed in the ir spectra for these compounds, supporting the assignments made.

The $\delta_s CH_2$ (ν_2) absorption is a weak intensity band occurring at 1505 cm^{-1} in the ir spectra of the [Pt(C_2H_4)LCl_2] compounds, where L = pyO, py-d_5O. As has been pointed out previously [19, 61], this scissors mode couples significantly to the νC=C (ν_3) mode and the vibrations obtained by means of the calculations performed show that the lower energy frequency (ν_3) band in the C_2H_4

Table 2.3.7. Experimental frequencies for [PtALBr$_2$] (A = C_2H_4, C_2D_4; L = pyO, pyO/py-^{18}O, py-d_5O) compounds. Raman values are shown in parenthesis. All frequency values in cm^{-1}.

A = C_2H_4 L = pyO	A = C_2H_4 L = pyO/py-^{18}O	A = C_2D_4 L = pyO	A = C_2H_4 L = py-d_5O	Assignment
3103	3103	3103 (3102)	2315 (2316)	$1A_1$ (20a)
3103*	3103	(2330)	3090 (3091)	νC-H/D (ν_5)
3079 (3080)	3079	3079 (3080)	2315 (2316)	$1B_1$ (20b)
3079 (3080)*	3079	(2274)	3076 (3075)	νC-H/D (ν_9)
3079 (3080)	3079	3079 (3080)	2304	$2A_1$ (2)
3059	3061	3059	2304	$2B_1$ (7b)
(3047)		(3047)	2293 (2293)	$3A_1$ (7a)
3036 (3034)	3033	3034 (3023)	3033 (3032)	not assigned
3010 (3010)	3009	2222 (2222)	3010 (3009)	νC-H/D (ν_1)
(2987)		2192 (2192)	(2987)	νC-H/D (ν_{11})
1612 (1610)	1611	1611 (1610)	1568 (1568)	$4A_1$ (8a)
(1598)		(1598)		comb. band
1575 (1577)	1575	1577 (1577)	1544 (1546)	$3B_1$ (8b)
1504 (1502)	1505	939 (935)	1505 (1502)	δCH$_2$/D$_2$ (ν_2)
1495 (1495)	1497	(1495)	1382 (1381)	$4B_1$ (19b)
1470	1468	1470 (1472)	1348 (1350)	$5A_1$ (19a)
1413 (1413)	1413	1055	1413 (1413)	δCH$_2$/D$_2$ (ν_{12})
1325 (1328)	1325	1325 (1321)	1038	$5B_1$ (3)
1257	1259	1257	1248	$6B_1$ (14)
1230 (1230)	1229	1338 (1338)	1229 (1230)	νC=C (ν_3)
1190*	1189*	953 (951)	1188 (1187)	ρCH$_2$/D$_2$ (ν_6)
1190 (1183)	1189	1189 (1183)•	1134 (1133)	$6A_1$ (13)
1164 (1168)	1165	1164 (1168)	871 (871)	$7A_1$ (9a)
	1156			$7A_1$ (9a) -^{18}O
(1155)		(1155)	842 (844)	$7B_1$ (15)
1093	1093	1093 (1097)		comb. band
1068	1068	1068 (1072)	831 (833)	$8B_1$ (18b)
1048 (1048)	1048	1047• (1047)	853	$8A_1$ (18a)
		753 (752)		ωCH$_2$/D$_2$ (ν_7)
1026 (1029)	1026	1026 (1029)	986 (986)	$9A_1$ (12)
1008 (1009)	1008	802 (803)	1010 (1010)	ωCH$_2$/D$_2$ (ν_8)
1008† (1009)	1008†	1007 (1009)	817 (818)	$1B_2$ (5)
(981)		(691)	978	τCH$_2$/D$_2$ (ν_4)
951			789 (791)	$1A_2$ (17a)
939 (935)	939	939 (935)	651 (652)	$2B_2$ (10b)
824 (824)	823	824 (824)	762 (763)	$10A_1$ (1)
	802			$10A_1$ (1) -^{18}O
		849 (849)	672	$2A_2$ (10a)
			817* (818)	ρCH$_2$/D$_2$ (ν_{10})
778 (777)	776	778 (780)	778 (777)	$3B_2$ (11)
726 (729)	726	521 (521)	726 (728)	τCH$_2$/D$_2$ (ν_{13})
676 (678)	676	676 (675)	559 (560)	$4B_2$ (4)
640 (640)	639	640 (640)	610 (613)	$9B_1$ (6b)
			586 (588)	not assigned
572 (574)	572	572 (572)	546 (549)	$11A_1$ (6a)
	559			$11A_1$ (6a) -^{18}O
(558)		(560)	506 (506)	$5B_2$ (16b)
507 (506)	505	460 (465)	507* (506)	ν_aPt-C_2H_4/D$_2$ (*tilt*)
444	436	447	424†	$10B_1$ (9b)
424 (427)	423	(405)	424 (424)	ν_sPt-C_2H_4/D$_2$

Table 2.3.7.(cont.)

A = C_2H_4 L = pyO	A = C_2H_4 L = pyO/py-^{18}O	A = C_2D_4 L = pyO	A = C_2H_4 L = py-d_5O	Assignment□
			(394)	$3A_2$ (16a)
396	396[b]	396	376 (376)	νPt-^{16}O
	388[b]			νPt-^{18}O
	330	329		comb. band
	280			comb. band
252 (254)	251	250 (250)	252 (254)	ν_aPt-Br
216 (221)[a]	217	(220)[a]	215 (214)[a]	$6B_2$ (17b)
(221)	217	(220)	215 (214)	ν_sPt-Br
201	200	203 (206)	203	δPt-C_2H_4/D_2
		187 (188)	167	πPt-C_2H_4/D_2
140 (140)	141	142 (140)	143 (137)	δBr-Pt-Br
116 (116)	117	(114)	117 (117)	δBr-Pt-O
(84)	91	90 (84)	(84)	πBr-Pt-Br
(70)	80	79		
	74	73		

* Masked by pyO absorption
† Masked by C_2H_4 absorption
a Masked by Pt-Br intense absorption.
b Broad band centred at 391 cm^{-1}. The values given are for the beginning and end of the peak observed.
• Shoulder.
□ Wilson mode and ethylene mode in parenthesis.

derivative contains more νC=C character while the high energy mode is a coupled $\delta_s CH_2$ + νC=C mode. The νC=C (ν_3) mode occurs at 1340 cm^{-1} in both the ir and Raman spectra for the [Pt(C_2D_4)(pyO)X_2] derivatives as a very weak ir absorption and a medium intensity absorption in the Raman spectra and is only slightly coupled to the $\delta_s CD_2$ mode, indicating some deuteration decoupling. The corresponding $\delta_s CD_2$ vibration (ν_2) is observed at 953 cm^{-1} for the C_2D_4 compounds as a strong intensity absorption in the Raman spectra.

The asymmetric scissoring mode, $\delta_a CH_2$ (ν_{12}), is a medium intensity band in the ir spectra for the C_2H_4 compounds occurring at 1414 cm^{-1} and extremely weak in the Raman spectra. It shifts to 1056 cm^{-1} in the ir spectra for the C_2D_4 isotopomers and is absent in the Raman spectra for these compounds.

Table 2.3.8. Experimental and calculated rescaled frequencies for [PtACl$_2$] compounds (A = CO, ^{13}CO; L = pyO, py-d_5O). Raman values are shown in parenthesis. Values in square brackets are calculated shifts to lower energy expected upon O-18 labelling of pyO in the coordination compound. The calculated values are for the transition state geometry obtained with one imaginary frequency value. All frequency values in cm^{-1}.

A = CO L = pyO			A = ^{13}CO L = pyO			A = CO L = py-d_5O			Assignment[a]
exp.		calc.	exp.		calc.	exp.		calc.	
3135		3117	3134		3101	2337	(2336)	2326	1A_1 (20a)
3110	(3102)	3116	3109		3100	2337	(2336)	2322	1B_1 (20b)
3084	(3083)	3085	3084	(3083)	3069	2310	(2310)	2300	2A_1 (2)
3067		3080	3067		3063	2300	(2297)	2291	2B_1 (7b)
3056	(3054)	3068	3055	(3050)	3052	2275	(2272)	2278	3A_1 (7a)
2109		2102	2107			2110	(2100)	2101	νCO
2056			2059		2058	2056			ν^{13}CO
			2009						$\nu^{13}C^{18}O$
1614	(1613)	1614	1614		1618	1571	(1569)	1573	4A_1 (8a)
1561		1573	1558		1577	1548	(1548)	1541	3B_1 (8b)
		1467		(1495)	1471	1386		1357	4B_1 (19b)
1474		1464	1473		1470	1353	(1353)	1346 [1]	5A_1 (19a)
1329		1321	1329		1324	1040	(1037)	1035	5B_1 (3)
1246	(1242)	1273	1246		1275	1248		1263	6B_1 (14)
1187	(1186)	1204 [10]	1191		1207	1144	(1142)	1166 [14]	6A_1 (13)
1173	(1173)	1166 [4]	1172	(1171)	1169	875	(875)	877 [3]	7A_1 (9a)
1155	(1155)	1152	1155	(1155)	1155	843	(843)	846	7B_1 (15)
1095			1094						comb. band
1069		1079	1069		1081	830	(830)	822	8B_1 (18b)
1053	(1046)	1049	1053		1052	859	(859)	859 [3]	8A_1 (18a)
1026	(1027)	1023	1026	(1027)	1026	989	(988)	984	9A_1 (12)
1004		987	1003		990	818	(820)	820	1B_2 (5)
965		955	965		958	788		784	1A_2 (17a)
935	(936)	926	935		929	657	(657)	657 [2]	2B_2 (10b)
830	(832)	839 [16]	830		841	765	(766)	775 [10]	10A_1 (1)
		837			839	677		661	2A_2 (10a)
777		779	777		781	782	(784)	785	3B_2 (11)
669	(678)	676	669		677		(560)	561 [4]	4B_2 (4)
640	(641)	650	641	(640)	652	613	(614)	625	9B_1 (6b)
599	(599)	582 [9]	597		583	575	(576)	570 [10]	11A_1 (6a)
580		579 [11]	575		577	507	(503)	497 [6]	5B_2 (16b)
523	(519)	531			525	517	(517)	517	νPt-CO
523	(519)	520 [1]	512		510	532	(534)	538$^+$	δPt-CO + 5B_2
508	(505)	507 [2]	493		495	507	(503)	509	πPt-CO
438		447 [11]	437		447	416	(420)	431 [12]	10B_1 (9b)
		421	418		422	369		371	3A_2 (16a)
412	(407)	411 [11]	412		412	392	(388)	394 [8]	νPt-O
353		342	353	(344)	343	352		343	ν_aPt-Cl
340	(340)	318		(339)	319	335	(339)	319	ν_sPt-Cl
224	(224)	224	224	(223)	225	210	(209)	215	6B_2 (17b)
	(196)			(192)					not assigned
162	(162)	169		(162)	169	158	(162)	169	δCl-Pt-Cl
153	(153)	148	151	(154)	149	150	(152)	148	δCl-Pt-C
132		140	131		141	131		141	πCl-Pt-Cl
121	(117)	123	121	(119)	124	128		125	δCl-Pt-O
106		106 [1]	104		107	106	(113)	107	skeletal

Table 2.3.8. (cont.)

A = CO L = pyO		A = ^{13}CO L = pyO		A = CO L = py-d_5O		Assignment
exp.	calc.	exp.	calc.	exp.	calc.	
84	84	84	84	81	84	coupled δ and π skeletal vibrations
47	43		43	54	50	
	13[i]		13[i]	41	43[i]	

* Masked by pyO absorption
† Masked by CO absorption
‡ Band overlaps with pyO overtone or combination band.
• Shoulder
+ δPt-CO + 4B_2 for py-d_5O derivative.
i Rescaled imaginary frequency.
 Wilson mode in parenthesis.

Two CH_2 rocking vibrations, ρCH_2 (ν_6 and ν_{10}), are calculated for the coordinated ethylene molecule. A weak intensity absorption (ν_6) is observed at 1189 cm^{-1} in the ir spectra for the [Pt(C_2H_4)(py-d_5O)X_2] compounds. This absorption is masked in the both the ir and Raman spectra for the [Pt(C_2H_4)(pyO)X_2] compounds by pyO absorptions occurring in the 1150-1200 cm^{-1} region. A weak intensity absorption, absent in the spectra for the C_2H_4 compounds, is observed at 952 cm^{-1} in both the ir and Raman spectra for the C_2D_4 isotopomers. It has been assigned to ν_6 in the C_2D_4 derivatives.

The second rocking vibration, ν_{10}, occurs at 817 cm^{-1} as a weak intensity absorption in both the ir and Raman spectra for the [Pt(C_2H_4)(py-d_5O)X_2] compounds. It is masked in the pyO derivatives by the intense pyO absorption at 826 cm^{-1} (10A_1). It is observed as an extremely weak absorption occurring at 620 cm^{-1} in the Raman spectra for the C_2D_4 derivatives.

Two out-of-plane wagging vibrations, ωCH_2 (ν_7 and ν_8), are calculated as coupled vibrations for the C_2H_4 derivatives. One (ν_7) is calculated as occurring lower than the 9A_1 (star of David) pyO absorption and the other one (ν_8) as occurring higher. No band was observed lower than the 9A_1 absorption in either the Raman or ir spectra for the C_2H_4 compounds. The medium intensity band in the ir spectra at 1010 cm^{-1} which shifts upon C_2D_4 substituion to 804 cm^{-1} has been assigned to the ν_8 wagging mode which is ir active in the free ligand. Both absorptions are observed in the

Table 2.3.9. Experimental frequencies for [PtALBr$_2$] (A = CO, ^{13}CO; L = pyO, py-d_5O) compounds. Raman values are shown in parenthesis. All frequency values in cm^{-1}.

A = CO L = pyO	A = ^{13}CO L = pyO	A = CO L = py-d_5O	Assignment
3127	3126	2323	1A_1 (20a)
3107	3108	2323	1B_1 (20b)
3080	3080	2312	2A_1 (2)
3066	3065	2295	2B_1 (7b)
3054	3053	2274	3A_1 (7a)
2102	2101	2100	νCO
2050	2052	2052	ν^{13}CO
	2004		$\nu^{13}C^{18}O$
1614	1612	1568	4A_1 (8a)
1558	1561	1546	3B_1 (8b)
		1385	4B_1 (19b)
1473	1473	1351	5A_1 (19a)
1328	1329	1040	5B_1 (3)
1257	1258	1249	6B_1 (14)
1189	1191	1150,1143	6A_1 (13)
1170	1170	875	7A_1 (9a)
1154	1155	841	7B_1 (15)
1092	1093		comb. band
1066	1067	831	8B_1 (18b)
1052	1054	858	8A_1 (18a)
1026	1026	989 (988)	9A_1 (12)
1000	1000	820 (825)	1B_2 (5)
964	966	787	1A_2 (17a)
932	932	652	2B_2 (10b)
829	829	765	10A_1 (1)
		673	2A_2 (10a)
773	773	779	3B_2 (11)
667	668	562•	4B_2 (4)
640	641	613	9B_1 (6b)
594	591	569	11A_1 (6a)
577	572	495	5B_2 (16b)
520	517•	517	νPt-CO
520	508	535	δPt-CO + 5B_2^+
510	495	524 (522)	πPt-CO
437	436	416	10B_1 (9b)
418	422		3A_2 (16a)
408, 400	407,399	382	νPt-O
256	256	257	ν_aPt-Br
228	225	214	6B_2 (17b)
212		214 (216)	ν_sPt-Br
133	135	133 (138)	δBr-Pt-Br
122	122	122 (120)	δBr-Pt-O
103	103	98	πBr-Pt-Br

• Shoulder

+δPt-CO + 4B_2 for py-d_5O derivative.

 Wilson mode in parenthesis.

Table 2.3.10. Experimental frequencies for [PtALCl$_2$] (A = C_2H_4, C_2D_4; L = quinO, quin-d_7O) compounds. Raman values are shown in parenthesis. All frequency values in cm^{-1}.

A = C_2H_4 L = quinO	A = C_2D_4 L = quinO	A = C_2H_4 L = quin-d_7O	Assignment[□]
		2335 (2335)	1*A*’
3083[*] (3088)[*]	2335 (2333)	3084 (3084)	νC-H/D (ν_5)
3109 (3112)	3110 (3112)	2316 (2318)	3*A*’
3067	2322 (2322)	3064 (3063)	νC-H/D (ν_9)
3109 (3112)	3110 (3112)	2316 (2301)	2*A*’
3092 (3088)	3084 (3090)	2300 (2292)	4*A*’
3067	3060 (3060)	2290 (2270)	5*A*’
3067	3060 (3060)	2293 (2283)	6*A*’
(3061)	(3060)	2266 (2270)	7*A*’
(3015)	(2218)	3034 (3044)	νC-H/D (ν_1)
3007 (3003)	2185 (2185)	3003 (3010)	νC-H/D (ν_{11})
1621 (1621)	1621 (1621)	1601 (1601)	8*A*’
1607 (1604)	(1602)	1560 (1563)	9*A*’
1515 (1516)	1515 (1516)	1460 (1460)	11*A*’
1588 (1586)	1588 (1586)	1543	10*A*’
(1516)	952 (950)	1509 (1495)	δCH$_2$/D$_2$ (ν_2)
1457 (1458)	1457 (1458)	1310	14A’
1451 (1444)	1451 (1444)	1363 (1364)	13A’
1417 (1416)	1058 (1057)	1417 (1415)	δCH$_2$/D$_2$ (ν_{12})
1397 (1397)	1397	1307 (1306)	15*A*’
1379 (1380)	1379 (1380)	1383 (1383)	12*A*’
1325 (1325)	1325 (1325)	1263 (1263)	16*A*’
1271 (1271)	1270 (1272)	1132 (1133)	17*A*’
1226 (1225)	(1222)	1224 (1224)	νC=C (ν_3)
1225 (1225)[†]	1227 (1228)	1009 (1009)	19*A*’
1211 (1213)	1211	1071 (1070)	18*A*’
(1190)	(950)	1199	ρCH$_2$/D$_2$ (ν_6)
1170 (1171)	1170 (1171)	1021 (1022)[†]	20*A*’
1148 (1149)	1148 (1149)	844 (845)	21*A*’
1148 (1149)	1148 (1149)	876 (876)	22*A*’
1088 (1091)	1088 (1090)	876 (876)	23*A*’
1046 (1040)	1046 (1044)	832 (833)	24*A*’
(1040)[*]	805[‡] (804)	1027 (1037)	ωCH$_2$/D$_2$ (ν_7)
1027	768[‡] (767)	1021 (1022)	ωCH$_2$/D$_2$ (ν_8)
1013[†] (1018)	1016 (1017)	832 (833)	25*A*’
996 (992)	995 (992)	812 (814)	1*A*”
(984)[*]	703	(971)	τCH$_2$/D$_2$ (ν_4)
(984)	990 (982)	789 (789)	3*A*”
963 (962)	964 (962)[•]	770 (771)	2*A*”
937 (936)	937	654 (658)	5*A*”
876 (876)	876 (876)	789 (789)	26*A*’
876 (876)	876 (876)	758 (757)	4*A*”
(824)		812 (814)	ρCH$_2$/D$_2$ (ν_{10})
805 (804)	805 (804)	629 (631)	6*A*”
805 (804)	805 (804)	723 (724)	27*A*’
769 (773)	768 (767)	749 (750)	7*A*”
(751)	540 (543)	(750)	τCH$_2$/D$_2$ (ν_{13})
(751)[†]		541 (548)	8*A*”
724 (723)	724 (724)	682 (682)	28*A*’
627 (631)	626 (632)	609 (611)	9*A*”
589 (590)	589 (589)	571 (571)	29*A*’
575 (573)	575 (573)	513 (515)	10*A*”
547 (544)	547 (543)	528 (526)	30*A*’
504 (507)	505 (506)	490 (490)	31*A*’
461			11*A*”
517 (515)	475 (471)	513[*] (515)	ν_aPt-C_2H_4/D_4

Table 2.3.10. (cont.)

A = C_2H_4 L = quinO	A = C_2D_4 L = quinO	A = C_2H_4 L = quin-d_7O	Assignment□
476 (478)	475 (481)	449 (452)	32*A*’
454 (455)	454 (454)	408	12*A*”
431 (428)	415 (410)	430 (428)	ν_sPt-C_2H_4/D_4
390 (391)	389 (390)•	359 (361)	νPt-O
346	346	345	ν_aPt-Cl
(340)	(341)	(339)	ν_sPt-Cl
319 (319)•	319 (319)	305 (307)	33*A*’
249 (253)	248 (253)	234 (234)	13*A*”
210 (210)	200	209 (210)	δPt-C_2H_4/D_4
195 (195)	195 (195)	183 (180)	14*A*”
195* (195)*	195* (195)*		πPt-C_2H_4/D_4
(178)	171 (171)	168 (167)	δCl-Pt-Cl
151 (151)	151 (151)	151 (148)	πCl-Pt-Cl
151 (151)	151 (151)	138 (140)	15*A*”
141	140	132	δCl-Pt-O
130	126	121	πO-Pt-C_2
98	100	105	coupled δ and π
72		71	skeletal vibrations
		53	

* Masked by quinO absorption
† Masked by C_2H_4 band
• Shoulder
□ Ethylene mode in parenthesis

C_2D_4 analogue as two weak intensity bands in both the ir and Raman spectra of the $[Pt(C_2D_4)(pyO)X_2]$ compounds at 804 cm^{-1} (ν_8) and 756 cm^{-1} (ν_7). The ν_7 absorption could not be seen in the spectra of the C_2H_4 derivatives, as is also the case for Zeise's salt [19]. The calculated value obtained in this work (~1030 cm^{-1}) places it very close to the value obtained by Jobic's inelastic neutron scattering (nis) studies (1020 cm^{-1}).

The coordinated ethylene torsional mode ν_4 appears in the ir spectra for the C_2H_4 derivatives as an extremely weak absorption at 980 cm^{-1}. It is observed as an extremely weak absorption in both the ir and Raman spectra for $[Pt(C_2D_4)(pyO)Br_2]$ at *ca*. 690 cm^{-1}.

A weak intensity absorption at 729 cm^{-1} in both the ir and Raman spectra for $[Pt(C_2H_4)(pyO)Cl_2]$ and which is absent in the C_2D_4 analogues has been assigned to the C_2H_4 torsional mode ν_{13}, which shifts to 523 cm^{-1} for the C_2D_4 analogues.

The Pt-C_2H_4 vibrations will be discussed in the Pt-L section.

Table 2.3.11. Experimental and calculated rescaled frequencies for [PtALBr$_2$] (A = C_2H_4, C_2D_4; L = quinO, quinO/quin-^{18}O, quin-d_7O) compounds. Raman values are shown in parenthesis. Values in brackets are calculated shifts to lower energy expected upon O-18 labelling of quinO in the coordination compound. All frequency values in cm^{-1}.

A = C_2H_4 L = quinO			A = C_2H_4 L = quinO/ quin-^{18}O		A = C_2D_4 L = quinO			A = C_2H_4 L = quin-d_7O			Assignment[□]
exp.		calc.	exp.		exp.		calc.	exp.		calc.	
		3149	3140				3149		(2331)	2339	1*A*’
3086[*]	(3086)[*]	3134	3084		2343	(2343)	2340	3086	(3085)	3136	νC-H/D (ν_5)
3106	(3106)	3101	3106			(3106)	3102	2307	(2306)	2306	3*A*’
	(3070)[*]	3117		(3071)	2329	(2327)	2334	3072	(3070)	3120	νC-H/D (ν_9)
3106	(3106)	3103	3106		3103	(3106)	3103	2307	(2306)	2305	2*A*’
3086	(3086)	3086	3084	(3085)		(3085)	3086	2295	(2292)	2294	4*A*’
3077		3074	3077		3079		3075	2273	(2273)	2276	5*A*’
	(3070)	3070		(3071)		(3071)	3071	2279	(2280)	2279	6*A*’
	(3062)	3063		(3062)		(3062)	3064	2273	(2273)	2267	7*A*’
		3035			2222	(2219)	2228	3034	(3037)	3037	νC-H/D (ν_1)
3008	(3007)	3033	3008		2192	(2187)	2199	3008	(3007)	3036	νC-H/D (ν_{11})
1622	(1621)	1619 [3]	1621	(1621)	1620	(1621)	1619	1600	(1599)	1591	8*A*’
1602	(1600)	1589	1604	(1603)	1602	(1601)	1588	1565	(1563)	1556	9*A*’
1588	(1586)	1583	1587	(1586)	1588	(1586)	1582	1543	(1540)	1544	10*A*’
1516	(1515)	1517	1516	(1511)	1516	(1516)	1516	1460	(1460)	1457	11*A*’
	(1515)	1511		(1511)	956	(956)	958	1509	(1510)	1509	δCH$_2$/D$_2$ (ν_2)
1458	(1459)	1452	1458	(1459)	1458	(1459)	1451	1310		1312 [1]	14*A*’
1442	(1443)	1444	1449	(1445)	1445	(1443)	1444	1363	(1364)	1356	13*A*’
1420	(1420)	1436	1419	(1420)	1060	(1061)	1068	1420	(1419)	1434	δCH$_2$/D$_2$ (ν_{12})
1394		1392	1393		1393		1398	1305	(1304)	1299	15*A*’
1380	(1381)	1375	1380	(1381)	1380	(1381)	1375	1384	(1383)	1377	12*A*’
1322	(1322)	1325	1321	(1321)	1323	(1322)	1325	1261	(1261)	1254 [1]	16*A*’
1270	(1271)	1265	1268	(1272)	1270	(1270)	1265	1133	(1133)	1143 [9]	17*A*’
			1263	(1265)							17*A*’ -^{18}O
1230[•]	(1233)	1229	1230[•]	(1233)	1339	(1339)	1337	1233	(1232)	1226	νC=C (ν_3)
1215	(1217)	1222	1214	(1217)	1215	(1217)	1222	1008	(1007)	1003 [1]	19*A*’
1193		1207 [3]	1192		1193		1207	1073	(1071)	1072 [4]	18*A*’
1192		1201	1192			(967)	967	1195		1199	ρCH$_2$/D$_2$ (ν_6)
1167	(1165)	1174 [5]	1166		1167	(1165)	1174	1021	(1021)[†]	1017 [2]	20*A*’
1151		1154	1150		1150		1154	848	(849)	843	21*A*’
			1143								21*A*’ -^{18}O
	(1145)	1146		(1144)		(1145)	1145	876	(876)	874	22*A*’
1089	(1089)	1089 [2]	1086	(1089)	1087	(1089)	1089	881		875	23*A*’
1045	(1041)	1050 [5]	1044		1045	(1041)	1050	831	(832)[•]	835	24*A*’
			1039[•]	(1039)							24*A*’ -^{18}O
		1037			810[*]	(808)	815			1034	ωCH$_2$/D$_2$ (ν_7)
1021	(1020)	1027		(1020)	771[*]	(759)	769	1021	(1021)	1024	ωCH$_2$/D$_2$ (ν_8)
1021[†]	(1020)	1026		(1020)	1018	(1020)	1026	825	(826)	830	25*A*’
1001	(1001)	996		(1001)	1000	(999)	996	814	(814)[•]	827	1*A*”
		980			696		708	972	(973)	977	τCH$_2$/D$_2$ (ν_4)
989		969	990	(985)	989	(989)	969	787	(802)	801	3*A*”
967	(969)	957		(967)	969	(967)	956	770	(771)	783	2*A*”
939	(938)	907		(937)	938	(938)	907	653	(653)	660	5*A*”
876	(876)	876 [1]	876	(876)	876	(876)	876	787	(787)	789 [5]	26*A*’
868		873 [4]	869	(869)	868		874	757	(757)	759	4*A*”
	(819)	833		(830)		(599)	606		(826)	820	ρCH$_2$/D$_2$ (ν_{10})
811		804	810	(812)	810		804	632	(637)	630	6*A*”
802	(801)	798	801	(800)	802	(802)	799	723	(723)	744	27*A*’
771	(776)	773	770	(776)	771	(775)	773	745		746	7*A*”
741	(739)	756	742	(738)	531	(533)	548	737	(739)	753	τCH$_2$/D$_2$ (ν_{13})
738	(739)[†]	735		(738)[†]	739	(743)	736	546	(549)	545 [2]	8*A*”

Table 2.3.11. (cont.)

A = C_2H_4 L = quinO			A = C_2H_4 L = quinO/ quin-^{18}O		A = C_2D_4 L = quinO			A = C_2H_4 L = quin-d_7O			Assignment□
Exp.		calc.	exp.		exp.		calc.	exp.		calc.	
724	(724)	726 [6]	723	(723)	724	(724)	726	682	(681)	682 [4]	28*A*’
			717	(716)							28*A*’ -^{18}O
630	(629)	637	629	(629)	630	(630)	638	609	(609)	605 [2]	9*A*”
591	(591)	590 [6]	590	(590)	590	(590)	590	573	(572)	571 [6]	29*A*’
			582								29*A*’ -^{18}O
575	(574)	578 [3]	574	(574)	576	(575)	578	515	(514)	513 [3]	10*A*”
547	(546)	550 [4]	547	(543)	547	(545)	549	528	(526)	528 [3]	30*A*’
507	(507)	507 [5]	506		507	(507)	507	490	(491)	491 [4]	31*A*’
			504	(504)							31*A*’ -^{18}O
		485 [1]					485			425	11*A*”
499	(499)•	481		(499)•	462	(460)	443	501	(499)	477	ν_aPt-C_2H_4/D_4
475	(477)	478 [2]	474	(476)	476	(477)	480	450	(451)	454 [6]	32*A*’
452	(452)	450 [4]		(451)‡	452	(452)•	453	409		406 [6]	12*A*”
				(447)‡							12*A*” -^{18}O
419	(417)	404	417	(417)	399	(399)	389	419	(416)	401	ν_sPt-C_2H_4/D_4
390	(390)•	384 [10]	390	(390)‡	389	(389)•	384	360	(360)	361 [7]	νPt-^{16}O
			382	(383)‡							νPt-^{18}O
316	(318)	321 [9]	316		315	(319)	321	302	(305)	306 [8]	33*A*’
			305*b*								33*A*’ -^{18}O
	(253)	252 [1]		(252)		(253)	253	233	(237)	234 [1]	13*A*”
250		234	250		248		233	251	(250)	230	ν_aPt-Br
208	(209)	204	209•	(209)	205	(209)	197	207	(207)	194	ν_sPt-Br
200	(197)•	203	199	(199)•	192		205	179	(182)	187	14*A*”
200		197	199		184	(184)	191	198	(196)	203	δPt-C_2H_4/D_4
		192					166			190	πPt-C_2H_4/D_4
155	(151)	150	151	(150)	152	(153)	150	139	(143)	141	15*A*”
127	(131)	130	130	(131)	127	(131)	130	125	(123)	123	δBr-Pt-O
122	(120)	123	122	(119)	121	(118)	122	121	(123)	120	πO-Pt-C_2
103	(98)	120	105		98	(97)	119	100	(110)	116	δBr-Pt-O
81	(84)	86	87	(84)	89	(84)	85	89	(84)	83	δBr-Pt-Br
74		75	76				76	74		70	πBr-Pt-Br
56		54	55		54		54	56		51	coupled
47		43	47				43	47		40	skeletal

* Masked by quinO absorption

† Masked by C_2H_4 band

• Shoulder

‡ Broad table-top band in Raman spectrum. Values quoted correspond to the beginning and end of the absorption.

b Band observed to broaden in far ir spectrum

□ Ethylene mode in parenthesis

Table 2.3.12. Experimental frequencies for $[PtALX_2]$ (A = CO, ^{13}CO; L = quinO, quin-d_7O) compounds. Raman values are shown in parenthesis. All frequency values in cm^{-1}.

A = CO L = quinO				A = ^{13}CO L = quinO				A = CO L = quin-d_7O				Assignment
X = Cl		X = Br		X = Cl		X = Br		X = Cl		X = Br		
3112		3110		3112	(3112)	3110		2316		2313	(2312)	1*A*’
3094	(3093)	3091	(3089)	3094	(3093)	3091	(3089)	2298		2295		2*A*’
3094	(3093)	3091	(3089)	3094	(3093)	3091	(3090)				(2280)	3*A*’
3083		3080		3083		3080					(2280)	4*A*’
3083		3080		3083		3080					(2280)	5*A*’
3060	(3060)		(3057)	3060	(3060)		(3058)	2266		2264	(2264)	6*A*’
	(3024)		(3022)		(3024)		(3023)	2266		2264	(2264)	7*A*’
2118	(2104)	2111	(2097)	2113		2106		2118	(2104)	2111	(2097)	νCO
2061		2054		2067	(2055)	2060	(2048)	2061		2054		ν^{13}CO
				2036								$\nu^{13}C^{17}O$
				2014	(2013)	2007	(2008)					$\nu^{13}C^{18}O$
1622	(1623)	1622	(1622)	1622	(1622)	1622	(1622)	1600	(1601)	1600	(1599)	8*A*’
	(1607)		(1604)	1607•	(1607)		(1605)	1567	(1564)	1566	(1564)	9*A*’
1587	(1588)	1587	(1587)	1587	(1587)	1587	(1587)	1543	(1543)	1543	(1543)	10*A*’
1517	(1517)	1516	(1516)	1516	(1516)	1515	(1516)	1462	(1462)	1462	(1462)	11*A*’
1455	(1458)	1459	(1460)	1456	(1459)	1459	(1460)	1312		1312		14*A*’
1448	(1447)	1448	(1447)	1446	(1446)	1448	(1447)	1363	(1365)	1363	(1364)	13*A*’
1398	(1398)	1397	(1396)	1398		1397	(1397)	1306	(1306)	1306	(1305)	15*A*’
1381	(1382)	1380	(1381)	1381	(1381)	1380	(1381)	1384	(1384)	1384	(1383)	12*A*’
1323	(1322)	1321	(1321)	1323	(1322)	1321	(1321)	1260	(1261)	1259	(1259)	16*A*’
1276	(1276)	1275	(1273)	1277	(1274)	1275	(1274)	1138	(1138)	1137	(1137)	17*A*’
1229	(1230)	1229	(1229)	1230	(1230)	1229	(1229)	1010	(1010)	1010	(1009)	19*A*’
1216	(1218)	1216	(1217)	1217	(1218)	1216	(1218)	1073	(1072)	1073	(1071)	18*A*’
1168	(1171)	1167	(1171)	1168	(1170)	1167	(1170)	1021		1021		20*A*’
1158	(1155)•	1157	(1155)•	1158	(1155)•	1157	(1155)•	847	(850)	847	(848)	21*A*’
1144	(1147)	1143	(1146)	1144	(1147)	1143	(1146)	876	(878)	876	(877)	22*A*’
1086	(1092)	1087	(1092)	1087	(1092)	1087	(1092)	880•	(878)	880		23*A*’
1047	(1045)	1047	(1045)	1048	(1045)	1047	(1044)	835	(835)	834	(834)	24*A*’
1021	(1022)	1021	(1021)	1021	(1021)	1021	(1021)	835	(835)	830	(834)	25*A*’
1002	(998)		(1005)	1002	(1001)	997	(996)	818	(820)	814	(816)	1*A*”
988	(982)	981	(984)	987	(983)	981	(981)	796	(795)	795	(794)	3*A*”
967	(971)	964	(965)	967		964	(966)	773	(773)	771	(771)	2*A*”
952	(953)	947	(951)	952		947	(938)	656		653	(656)	5*A*”
880	(878)	879	(877)	880	(878)	879	(878)	790	(794)	788	(794)•	26*A*’
868		865		867		865		761	(762)	758	(759)	4*A*”
809		807		809		807		630		630	(628)	6*A*”
804•	(803)	807	(803)		(803)	807	(802)	726	(725)	717	(723)	27*A*’
772	(774)	770	(774)	772		769	(772)	748	(748)	747	(747)	7*A*”
740		737		740	(748)	737		540	(540)	538		8*A*”
726	(727)	726	(726)	726	(727)	726	(726)	685	(686)	685	(685)	28*A*’
638	(646)	635	(643)	637	(642)	635	(642)	617	(621)	614	(615)	9*A*”
597	(598)	596	(597)	597	(597)	596	(597)	578	(574)	578	(576)	29*A*’
585	(587)	582	(585)	582	(574)	580	(576)	520	(519)	517	(525)¤	10*A*”
	(543)	547•	(544)	547	(543)	547	(544)	529•	(526)	527¤	(525)¤	30*A*’
541		539	(539)	528	(526)	526	(525)•	540	(540)	538	(538)	δPt-CO
522	(520)	526	(524)	514	(514)	518	(517)	520	(526)	527	(525)	νPt-CO
504	(509)	506	(509)	494	(499)	494	(500)	498	(501)	500	(501)	πPt-CO
504	(509)	506	(509)	508		508	(507)•	487	(489)	487	(488)	31*A*’
	(493)	485	(492)	494		494¤		422	(423)	420	(416)	11*A*”
470	(472)	470	(473)	467	(469)	467	(469)	446	(449)	445	(448)	32*A*’
448	(448)	459		445	(445)	459		408	(406)	406		12*A*”
396	(397)	390	(393)	395	(396)	390	(392)	360•	(365)	356	(360)	νPt-O
316	(319)	313		316	(317)	314	(314)	303		303	(302)	33*A*’
353	(350)•	255	(255)*	353	(350)•	255	(255)*	352	(350)	255	(255)	ν_aPt-X
339•	(339)	210	(210)	339•	(339)	210	(210)		(339)	211	(210)	ν_sPt-X

Table 2.3.12. (cont.)

A = CO L = quinO				A = $C^{13}O$ L = quinO				A = CO L = quin-d_7O				Assignment
X = Cl		X = Br		X = Cl		X = Br		X = Cl		X = Br		
255	(260)	255[a]	(259)	257	(259)	255[a]	(259)	237	(241)	236	(238)	13*A*”
196	(191)	194	(189)	196	(190)	194	(189)	179	(178)	178	(174)	14*A*”
	(162)	156	(156)	169	(161)		(156)	140		144	(148)	15*A*”
151								155				δCl-Pt-Cl
140	(147)			131	(146)			140				πCl-Pt-Cl
		130	(134)			127	(134)			125	(128)	δBr-Pt-O
125	(119)	121	(119)	122	(119)	120	(118)	125	(119)	119	(119)	skeletal
		109				109				111		skeletal
		104				103				102		δBr-Pt-Br
		88				89				84		πBr-Pt-Br
		70				72						skeletal

* Masked by quinO absorption
¤ Masked by Pt-CO absorption
a Masked by Pt-X band
• Shoulder

2.3.2.5. CO vibrations

The νCO stretch occurs at approximately 2100 cm^{-1} as a very intense ir absorption for all of the derivatives studied. The ν^{13}CO and $\nu^{13}C^{18}O$ bands have been observed in the labelling studies and are in good agreement with the calculated values for these bands by use of the simple harmonic diatomic oscillator approximation. A weak intensity band is observed at 2036 cm^{-1} in the mid ir spectrum for [Pt(^{13}CO)(quinO)Cl_2]. This is the only species for which this band is observed and it has been assigned to the $\nu^{13}C^{17}O$ stretch in agreement with the calculated value obtained by means of the simple harmonic diatomic oscillator approximation. The spectrum for this compound in the νCO region is shown in figure 2.3.13.

The Pt-CO stretch, νPt-CO, and the in-plane and out-of-plane Pt-CO bending modes, δPt-CO and πPt-CO respectively, show a considerable amount of coupling according to the calculated vibrations for the Zeise’s salt derivatives modelled. This has also been observed for the K[Pt(CO)X_3] compounds [19, 21 and references therein, 86]. The in-plane bending mode is calculated to occur before the out-of-plane bending mode, consistent with previous observations. These vibrations will be discussed further in the Pt-L section.

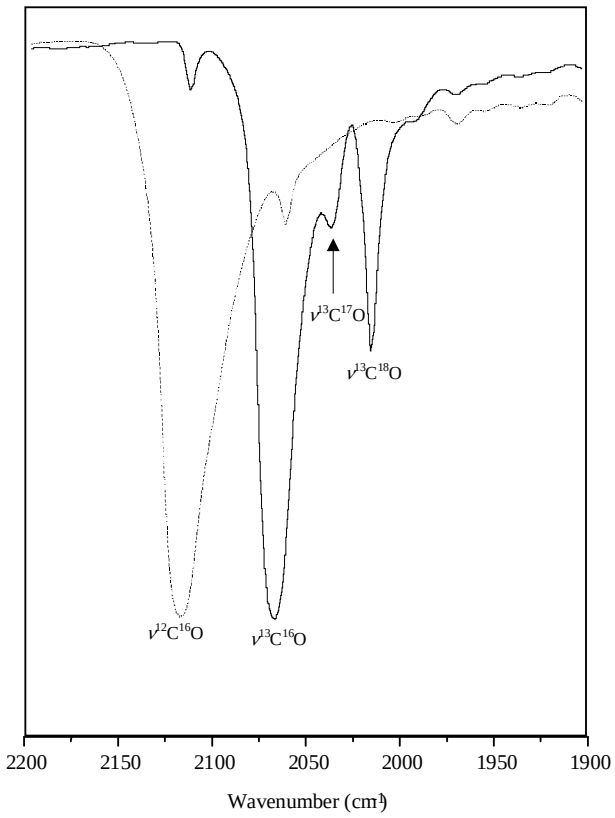

Figure 2.3.13. Spectra for [Pt(CO)(quinO)Cl_2] (dotted line) and [Pt(^{13}CO)(quinO)Cl_2] (solid line) in the νCO stretch region. Assignments are shown for the [Pt(^{13}CO)(quinO)Cl_2] compound.

2.3.2.6. pyO vibrations

The most intense absorption observed in the high frequency region in the Raman spectra of the [PtA(pyO)X_2] compounds occurs at 3084 cm^{-1}. It has been assigned to the $2A_1$ mode in pyO due to its appearance in the spectra for both the ethylene and ethylene-d_4 compounds. The remaining νC-H vibrations in the pyO and py-d_5O derivatives have been assigned according to their calculated values. Much better definition is observed for these bands in the ir spectra for the CO derivatives, where all five νC-H frequencies can be observed as individual absorptions. This is not the case for the ethylene derivatives, where vibrations $1B_1$ (Wilson mode 20b) and $2A_1$ (Wilson mode 2) have been assigned in the experimental spectra as accidentally degenerate. In the [Pt(CO)(py-d_5O)X_2] compounds, modes $1A_1$ (Wilson mode 20a) and $1B_1$ have been assigned as accidentally degenerate, in agreement with the calculated values obtained.

In the 1650-400 cm^{-1} region, the Raman spectra for the pyO/py-d_5O derivatives show two very intense absorptions that have been assigned to the ring modes $4A_1$ and $9A_1$.

The very weak ir absorption at 1612 cm^{-1} gives rise to a very strong Raman band in the pyO complexes. In the samples with py-d_5O, the very weak ir absorption at 1571 cm^{-1} is a very intense Raman band at 1569 cm^{-1}. The aforementioned frequencies have been assigned to the ring stretch mode $4A_1$ (Wilson mode 8a) which, together with the star of David mode $9A_1$ (Wilson mode 12), are the strongest intensity absorptions in the Raman spectra of pyO as described in the assignment of the ligand spectra (section 2.1.2.1).

In the py-d_5O derivatives, mode $3B_1$ (Wilson mode 8b) occurs as a weak intensity band at 1545 cm^{-1}, very similar in intensity in the ir to mode $4A_1$ (8a) occurring at 1575 cm^{-1}. However, Raman spectra of the py-d_5O compounds show a very strong absorption at 1575 cm^{-1} and a weak one at 1545 cm^{-1}. Both bands had been previously assigned [85] in py-d_5O compounds as being ascribed to the ring mode at 1613 cm^{-1} in the pyO compounds, which split into two bands in the py-d_5O analogue. In the present work, the Raman spectra for the compounds and the calculated values obtained for the free ligand and the coordination compounds suggest rather the assignment of the band at 1545 cm^{-1} as mode $3B_1$ and the one at 1575 cm^{-1} as mode $4A_1$.

The second most intense absorption observed in the Raman spectra of the $[Pt(CO)(pyO)X_2]$ and $[Pt(C_2H_4)(pyO)X_2]$ compounds occurs at 1027 cm^{-1} and 990 cm^{-1} for the py-d_5O derivative. It has been unambiguously assigned as the highly symmetrical star of David ring breathing mode, $9A_1$ (Wilson mode 12). Two very weak Raman bands occur higher and lower than the very intense ring breathing mode at 1027 cm^{-1}. These occur at 1047 and 1010 cm^{-1} and are observed as very well defined bands in the ir spectra of the $[Pt(CO)(pyO)X_2]$ compounds. The 1010 cm^{-1} pyO band in the C_2H_4 derivative is masked by the very intense ωCH_2 (ν_8) mode with which it is accidentally degenerate. However, it is observed at 1010 cm^{-1} in the ir spectrum of the C_2D_4 derivative and has been assigned as the out-of-plane mode $1B_2$ (Wilson mode 5). The remaining bands in the range 1650-1100 cm^{-1} have been assigned according to their calculated values (tables 2.3.6-2.3.9). The Raman band band at 1600 cm^{-1} is ascribed to a combination band –possibly ($10B_1 + 7B_1$); ($5B_2 + 8A_1$); ($11A_1 + 9A_1$); ($9B_1 + 1A_2$) or ($3B_2 + 10A_1$). It is worth mentioning that complexation brings about an enhanced definition of all of the pyO and py-d_5O fundamentals, which is clearly noticeable in the spectra for the carbonyl derivatives.

The 1100-700 cm^{-1} region shows more bands than expected for the pyO derivatives (figures 2.3.14 and 2.3.15). This is particularly clear in the $[PtA(pyO)X_2]$ (A = CO and ^{13}CO) compounds and while they are also seen in the C_2H_4 and C_2D_4 analogues, to some extent the C_2H_4 1010 cm^{-1} and C_2D_4 1056 cm^{-1} absorptions mask them. One particularly prominent band occurring at 1096 cm^{-1} can be traced back to the free ligand where it occurs at 1097 cm^{-1}. This absorption is not mentioned in any of the previous references cited for the pyO assignment [1-4, 12, 13]. However, it is definitely a ligand band that can be explained as being either an overtone or one of several combination bands in the free ligand. It may be ascribed as either ($9B_1 + 10B_1$) or more likely as ($4B_2 + 3A_2$).

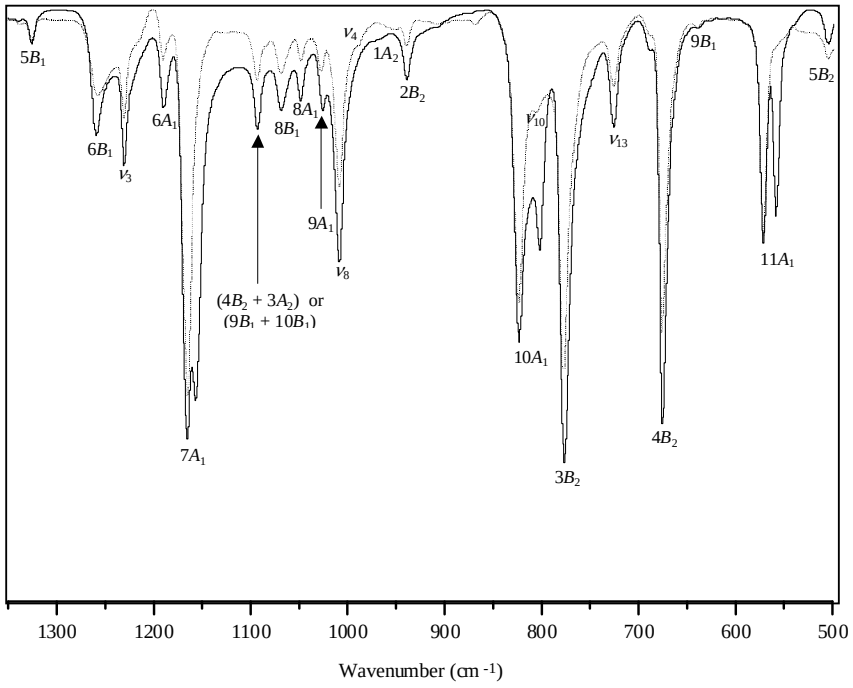

Figure 2.3.14. Mid ir spectra for $[Pt(C_2H_4)(pyO)Br_2]$ (dotted line) and $[Pt(C_2H_4)(pyO/py\text{-}^{18}O)Br_2]$ (solid line) showing the O-18 sensitive vibrations $7A_1$, $10A_1$ and $11A_1$ where two bands are observed on O-18 enrichment where only one is observed for the pyO derivative.

A very weak intensity absorption occurring at 966 cm^{-1} in the ir spectra of the $[Pt(C_2H_4)(pyO)Cl_2]$ compound has been assigned to mode $1A_2$ in good agreement with its calculated value. This very weak intensity absorption occurs in the ir spectrum of the $[Pt(CO)(pyO)Cl_2]$ compound, but is absent from the $[Pt(CO)(py\text{-}d_5O)Cl_2]$ compound further supporting the assignment performed. The band is not observed in the Raman spectra of the compounds mentioned. All of the vibrations

of A_2 symmetry are either extremely weak, or not present in the spectra for the compounds prepared. They have been assigned to weak intensity bands that are slightly more noticeable in the spectra of the py-d_5O derivatives and occur very close to the calculated values, as can be seen in tables 2.3.6-2.3.9.

The N-O vibrations are strongly dependent on the bond length and bond order of the coordinated *N*-oxide ligand, as has been previously noted when discussing the free ligand. The changes are more noticeable with the νN-O stretching frequency, than with the in-plane and out-of-plane N-O modes. The information provided by the ir spectra for the $[Pt(C_2H_4)(pyO/py\text{-}^{18}O)Br_2]$ allows for a much better understanding of the vibrational spectra of pyO coordination compounds and clarifies several ambiguities and misassignments that have been performed in previous works [14, 20, 85]. The ir spectra from 1350-500 cm^{-1} for the $[Pt(C_2H_4)LBr_2]$ (L = pyO, pyO/py-^{18}O) are shown in figure 2.3.14.

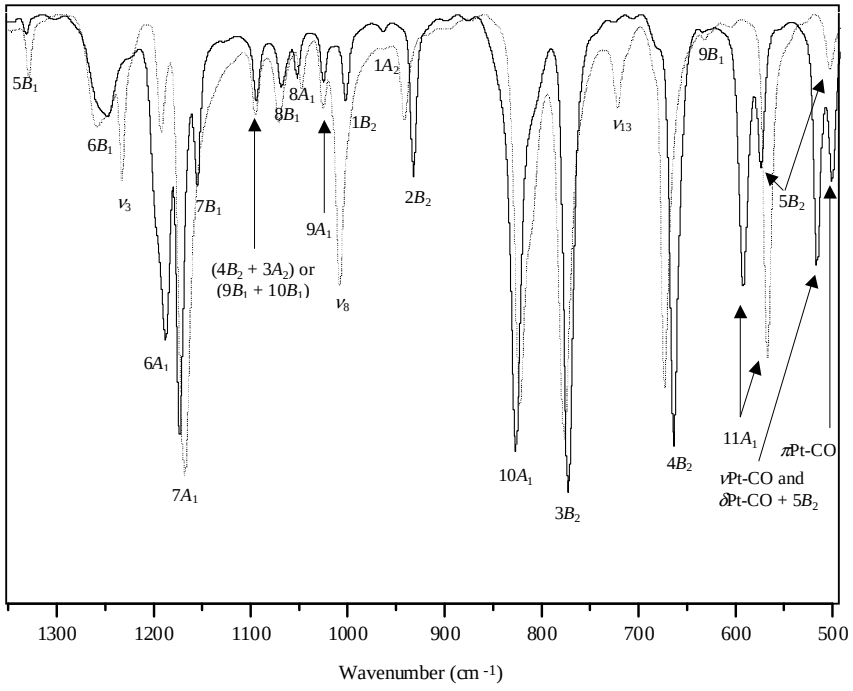

Figure 2.3.15. Mid ir spectra for $[Pt(C_2H_4)(pyO)Cl_2]$ (dotted line) and $[Pt(CO)(pyO)Cl_2]$ (solid line).

The very intense ir absorption at 1170 cm^{-1} has been assigned to the $7A_1$ pyO mode. The Raman spectra of $[Pt(C_2H_4)(pyO)X_2]$ compounds show an intense absorption at 1172 cm^{-1} and a medium

intensity absorption at 1157 cm^{-1} which is masked in the ir spectra by the $7A_1$ absorption, although it is seen for all the $[Pt(CO)(pyO)X_2]$ compounds. The lower energy band has been assigned as mode $7B_1$, in agreement with the calculated values obtained for the ligand and for the coordination compounds, and previous assignments performed on the pyO ligand.

The νN-O vibration is calculated to occur mainly in mode $6A_1$ in the pyO systems according to the calculated shifts of approximately 9 cm^{-1} to lower energy upon O-18 substitution in the pyO ligand. However, this band remains unaffected in the spectrum of the $[Pt(C_2H_4)(pyO/py\text{-}^{18}O)Br_2]$ mixture. This is not the case for the following band which splits into two bands occurring at 1165 and 1156 cm^{-1} respectively (figure 2.3.14), which is consistent with the shift expected for the pyO/py-^{18}O mixture, and which is assigned to mode $7A_1$. The fact that it occurs as mode $7A_1$ and not mode $6A_1$, would indicate that the calculations underestimate the N-O bond length, which is indeed the case, as discussed previously. Furthermore, calculations on the pyO system subject to bond length constraints are consistent with the fact that for longer bond lengths mode $7A_1$ becomes the predominant νN-O mode.

Mode $7B_1$ is not observed in the the ir spectra of any of the $[PtA(pyO)X_2]$ (A = C_2H_4, C_2D_4) derivatives, although it is seen as a Raman band at 1156 cm^{-1}. The appearance of a second band at 1156 cm^{-1} observed only in the ir spectra for $[Pt(C_2H_4)(pyO/py\text{-}^{18}O)Br_2]$, together with the fact that the νN-O vibration is expected to occur in this range and is bond distance dependent, allows for the assignment of the band occurring at 1168 cm^{-1} to be identified as the main νN-O vibration.

Thornton and co-workers had previously assigned a weak intensity band occurring *ca*. 1254 cm^{-1} in the ir spectra for pyO derivatives [14, 85] to the νN-O vibration. The calculations for the free ligand and for the coordination compounds place mode $6B_1$ as occurring at this frequency value. It is overlapped by the very intense $6A_1$ absorption in the free ligand, which is the principal νN-O mode and accounts for the earlier misassignment.

As can be seen in figure 2.3.14, the $10A_1$(1) and $11A_1$(6a) O-18 sensitive modes which were shown in figure 2.3.9 in the free ligand section, show the same O-18 sensitivity in the $[Pt(C_2H_4)(pyO/py\text{-}^{18}O)Br_2]$ compound and become better defined as two separate absorptions on complexation. These vibrations have previously been recognized as strongly coupled with the N-O stretch [11, 19].

An interesting difference in the 1350-500 cm^{-1} region is observed between the C_2H_4 and the CO derivatives. While mode $7A_1$ overlaps with the less intense mode $7B_1$, which is visible in the Raman spectra for the ethylene derivatives, this band (mode $7B_1$) is observed at *ca.* 1155 cm^{-1} for all of the [PtA(pyO)X_2] (A = CO, ^{13}CO) compounds prepared. Furthermore, the shape of the higher energy band assigned as mode $6A_1$ for both compounds is noticeably different, as can be seen in figure 2.3.15. It is possible that differences in the electronic distribution in these systems produce a stronger N-O bond for the CO derivatives and a weaker one for the C_2H_4 derivatives, which would hence contribute to mode $6A_1$ having more νN-O character.

The [PtA(py-d_5O)X_2] compounds show the principal νN-O vibration (mode $6A_1$) as occurring at 1140 cm^{-1} for A = C_2H_4 and 1145 cm^{-1} for A = CO. The fact that this mode is the principal νN-O vibration in the py-d_5O ligand, as was shown previously, suggests that this subtle difference may indeed be attributable to a stronger N-O bond in the carbonyl derivatives than in the ethylene derivatives. N-O bond lengths are indeed different for the compounds [Pt(C_2H_4)(pyO)Cl_2] and [Pt(CO)(4-MeO-pyO)Cl_2] (table 2.3.3), with the latter compound having a shorter N-O bond length. However, this would be expected on account of the electron releasing substituent.

The differences observed in the free ligand for the νN-O vibrations do not satisfactorily explain all of the trends obtained in the coordination compounds. If the N-O bond in the CO derivatives is indeed stronger, then the expected νN-O frequencies for the [PtA(pyO)X_2] compounds should be higher for the A = CO than for A = C_2H_4. This is not the case, as modes $6A_1$ and $7A_1$ occur at 1192 and 1168 cm^{-1} for A = C_2H_4, and 1187 and 1173 cm^{-1} for A = CO. Although the frequency for mode $7A_1$ follows the same trend observed in the py-d_5O compounds, this is not the case for mode $6A_1$ which, on the basis of the N-O bond distance studies in the free ligand, is expected to be higher. Unfortunately, no stable structures could be obtained for the [Pt(CO)(pyO)X_2] compounds and computational costs involved in the calculation of the systems under study is very high. A similar study where bond lengths in the coordination compounds were to be varied, could perhaps allow for a better understanding of these systems.

It is interesting to note that the in-plane modes sensitive to variations in bond length and to O-18 substitution ($7A_1$, $10A_1$, $11A_1$) with the exception of mode $6A_1$, are obtained at a higher frequency value in the experimental spectra for the CO derivatives, than for the C_2H_4 derivatives, as is shown in figure 2.3.15. This subtle difference is what would be expected for a stronger N-O bond

in the CO complex, following the results obtained for the variation of the N-O bond length in the pyO ligand.

The same trend in the N-O bond length sensitive vibrations is observed for the [PtA(py-d_5O)X_2] compounds with the exception that $6A_1$ is also shifted to a higher frequency in the complex. The spectra in the mid ir region for the chloride derivatives are shown in figure 2.3.16.

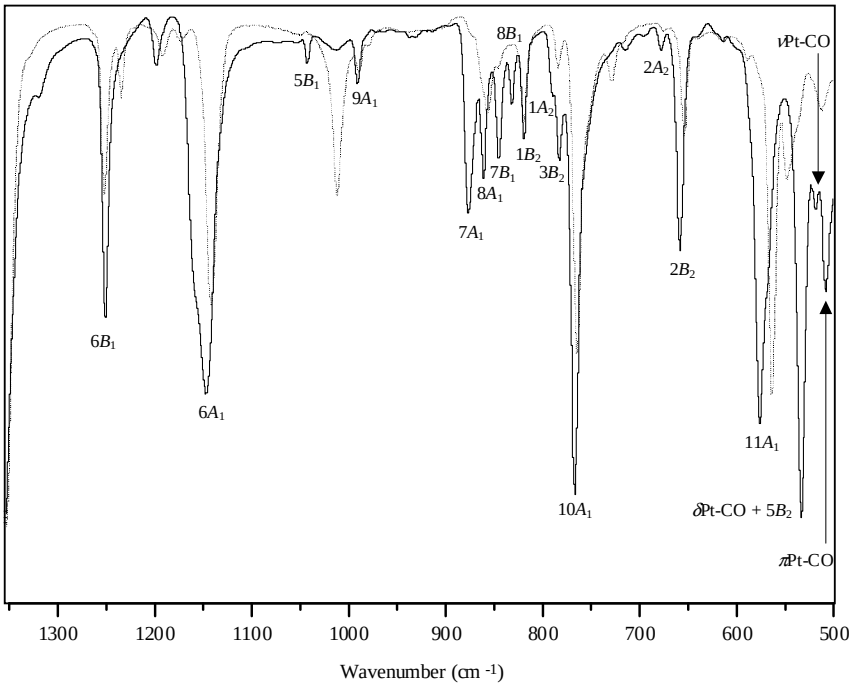

Figure 2.3.16. Mid ir spectra for [Pt(C_2H_4)(py-d_5O)Cl_2] (dotted line) and [Pt(CO)(py-d_5O)Cl_2] (solid line). The assignments shown on the spectra for the compounds are for the CO derivative.

The αN-O vibration, mode $10B_1$(9b), is the only mode of B_1 symmetry in the free ligand that gives rise to an intense band in the ir spectra. It is considerably shifted to lower frequencies upon coordination and decreases noticeably in intensity. It is observed in the far ir spectra for the compounds studied at *ca*. 450 cm^{-1} and on O-18 labelling shifts to 436 cm^{-1} with a broadening of the band. The calculated frequencies and shifts expected upon O-18 labelling are in good agreement with the observed results.

The Raman band observed at approximately 545 cm^{-1} in the C_2H_4 and C_2D_4 complexes is ascribed to an A_2 difference band of either ($5B_1 - 3B_2$) or, less likely, ($1A_1 - 3A_2$).

The low energy region of the Raman spectra of the compounds is extremely useful in assigning the pyO fundamentals of the Zeise's salt derivatives, as poor quality of the high resolution far ir spectra encumbers the assignment of the fundamental frequencies. The low energy out-of-plane coupled γN-O mode, $6B_2$(17b) is observed as a very weak intensity band in the far ir spectra for the carbonyl derivatives. Raman spectra in this region are extremely useful in locating the position of this absorption at 224 cm^{-1} for the $[PtA(pyO)Cl_2]$ (A = CO, ^{13}CO) systems and at 209 cm^{-1} for $[Pt(CO)(py\text{-}d_5O)Cl_2]$. This mode appears at 220 and 219 cm^{-1} for $[Pt(C_2H_4)(pyO)Cl_2]$ and $[Pt(C_2D_4)(pyO)Cl_2]$ respectively and at 204 cm^{-1} for $[Pt(C_2H_4)(py\text{-}d_5O)Cl_2]$.

2.3.2.7. quinO vibrations

Several crossovers are observed for some of the fundamentals in the quinO coordination compounds when compared to the order obtained for the free ligand. The assignments of the modes obtained for these compounds follows that made for the fundamental vibrations of the free quinO and quin-d_7O ligands. The order of the quinO fundamentals in both the C_2H_4 and CO derivatives has been assigned according to the calculated values obtained for the stable $[Pt(C_2H_4)(quinO)Br_2]$ compound modelled.

The most affected modes for the $[PtA(quinO)X_2]$ compounds are those observed to occur in the 1500 to 1150 cm^{-1} region. Several crossovers are noted and some of the modes are slightly affected by coordination to the Pt(II) atom, as would be expected due to the decrease in bond order experienced in the ligand on complexation. This is not the case for the $[PtA(quin\text{-}d_7O)X_2]$ compounds, where the aforementioned region shows all modes in the free ligand occurring in the same order for the coordination compounds and with no significant changes in atomic displacement. This suggests there is extensive vibrational coupling in the -d_0 isotopomer that is particularly sensitive to complexation.

The most affected modes for the $[Pt(C_2H_4)(quinO)Br_2]$ compound are modes 12-14*A*'. Mode 12*A*' occurring at 1450 cm^{-1} in the free ligand, is calculated to occur at 1375 cm^{-1} in the Zeise's salt derivative and is observed at 1381 cm^{-1}. Mode 12*A*' is calculated to occur at 1377 cm^{-1} for the quin-d_7O derivative and is observed at 1384 cm^{-1}. The fact that the mode assigned as 12*A*' in both compounds is the strongest intensity absorption in the Raman spectra for the quinO and quin-d_7O derivatives further supports the assignment presented based on the vibrational analyses for these compounds. This is similarly the most intense Raman band observed in the mid ir region for the carbonyl derivatives (L = quinO, quin-d_7O) as is shown in figure 2.3.17.

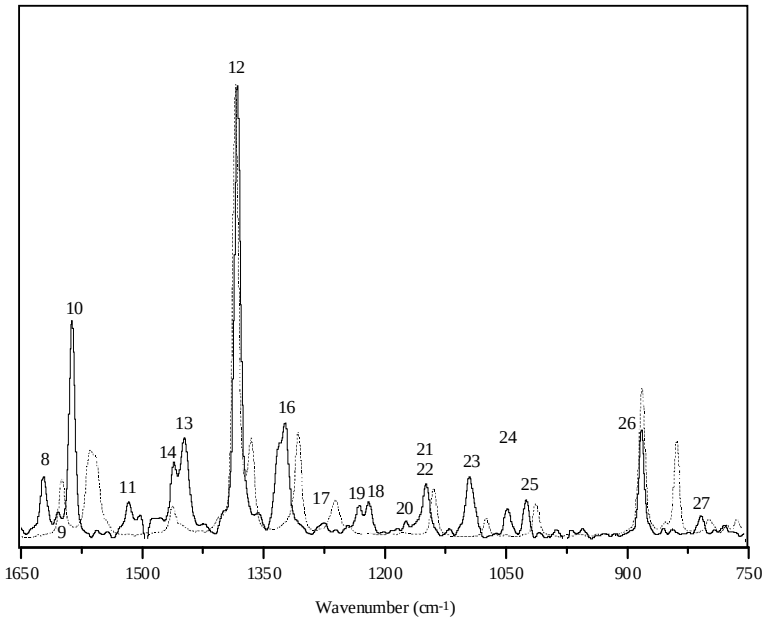

Figure 2.3.17. Raman spectra for [Pt(CO)LBr$_2$] compounds; L = quinO (solid line), L = quin-d_7O (broken line). Assignments shown are for the L = quinO (solid line) in-plane (*A*') vibrations. The most intense Raman band occurs at *ca*. 1385 cm^{-1} (mode 12*A*') for both the L = quinO, quin-d_7O derivatives.

Mode 12*A*' is insensitive to coordination in the [PtA(quin-d_7O)X$_2$] compounds, and appears at the same frequency value of 1372 cm^{-1} observed in the free quin-d_7O ligand. In the -d_0 isotopomer it is a metal sensitive mode reflecting significant coupling. It occurs at 1450 cm^{-1} for the free quinO ligand and shifts to 1380 cm^{-1} in the [PtA(quinO)X$_2$] compounds.

Although modes 12, 13 and 15*A*' experience a certain degree of coupling in the coordination compounds when compared to the modes for the free quinO ligand, it is only mode 14*A*' in the coordination compound for which the displacement diagram does not resemble mode 14*A*' in the free quinO ligand. This identifies mode 14*A*' as experiencing the greatest coupling of these four modes.

For both the quinO and quin-d_7O Zeise's salt derivatives, important differences are observed close to the region in which the first out-of-plane modes are calculated to occur. The 1000-600 cm^{-1} and the 850-600 cm^{-1} regions are the most affected for the quinO and quin-d_7O compounds respectively. Both the [PtA(quinO)X$_2$] and [PtA(quin-d_7O)X$_2$] compounds, show an inversion in

the out-of-plane modes 2 and 3*A*''. The order of other modes is also affected as can be seen from the values shown in the corresponding tables for both the quinO and quin-d_7O ligands and their Zeise's salt derivatives. Although it is usually agreed that the order of the fundamentals in coordination compounds will follow the order observed for the free ligand, the results obtained here for the quinO and quin-d_7O coordination compounds show this to be definitely not the case when the ligand employed has very low symmetry.

The two in-plane modes 19 and 20*A*' which were under-estimated in the calculations for the free quin-d_7O ligand (observed frequencies of 1013 and 1027 cm^{-1}; calculated frequencies of 953 and 972 cm^{-1} respectively) are calculated to occur at 1007 and 1021 cm^{-1} in the [Pt(C_2H_4)(quin-d_7O)Br_2] compound, in excellent agreement with the observed values of 1008 and 1021 cm^{-1} respectively.

As was pointed out when discussing the assignment of the free ligand, several bands show accidental degeneracy that is lifted on complexation. Such is the case for pairs of modes 12 and 13*A*', and 14 and 15*A*' which are observed as individual absorptions due to a much better resolution of these bands in the coordination compounds. However, as has been previously noted, these modes cross over and do not occur in the order observed for the free ligand.

The bands assigned as modes 21 and 22*A*' overlap in the ir spectra for the [PtA(quinO)X_2] compounds (A = C_2H_4, C_2D_4), although the lower energy mode 22*A*' can be identified as a moderate band in the Raman spectra for these compounds. Much better resolution is observed in the ir spectra for the [PtA(quinO)X_2] compounds (A = CO, ^{13}CO) where two distinct bands are observed occurring at *ca*. 1150 and 1145 cm^{-1} as is shown in figure 2.3.18. These two modes had been previously assigned [19, 21] as a single fundamental observed to split into two bands in the spectra for Zeise's salt derivatives. The calculated values obtained point to the fact that there are actually two fundamentals that occur very close in energy. The ir spectra in this region for the [PtA(quinO)Br_2] compounds where A = C_2H_4, CO are shown in figure 2.3.18.

The principal νN-O frequencies are calculated to occur in modes 20 and 24*A*' for the [Pt(C_2H_4)(quinO)Br_2] compound and in modes 17 and 18*A*' for the [Pt(C_2H_4)(quin-d_7O)Br_2] compound. The largest calculated O-18 induced shift for the νN-O frequency is of 5 cm^{-1} for both modes 20 and 24*A*' for [Pt(C_2H_4)(quinO)Br_2] as compared to 9 cm^{-1} for mode 17*A*' obtained for

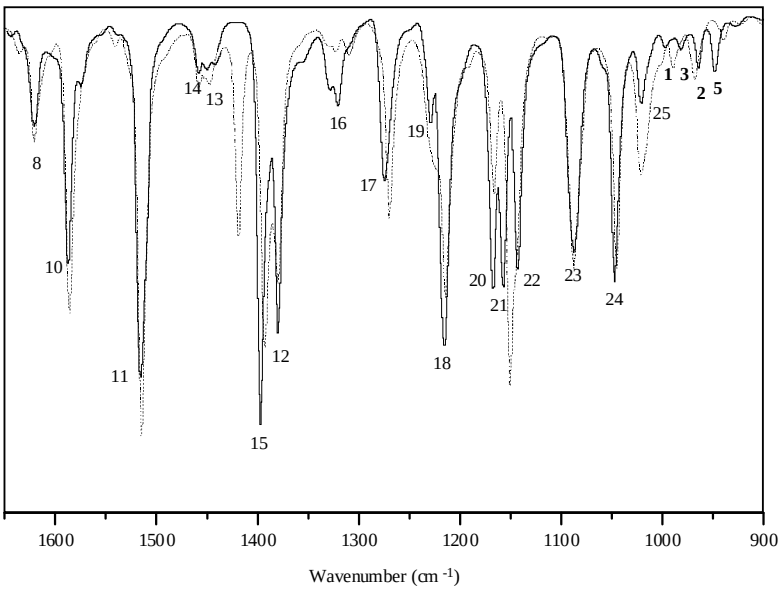

Figure 2.3.18. Infrared spectra for [PtA(quinO)Br_2] compounds; A = C_2H_4 (broken line), CO (solid line). Assignments shown are for the A = CO compound (solid line). Out-of-plane vibrations in bold numbering.

[Pt(C_2H_4)(quin-d_7O)Br_2]. As was calculated for the free quin-d_7O ligand, the highest character νN-O vibration is obtained for the quin-d_7O derivative. A comparison with the calculated shifts obtained for the pyO and py-d_5O Zeise's salt derivatives is consistent with the fact that the νN-O stretching frequency is a highly coupled mode in quinO and less coupled in its perdeuterated analogue. In fact, larger shifts are expected for several modes in the [Pt(C_2H_4)(quinO)Br_2] derivatives, than for those that involve the νN-O mode. This is the case for modes 28, 29 and 33*A*', which are all in-plane modes that involve the motion of the oxygen atom in the molecule, although they are not representative of a νN-O stretch as can be seen from the displacement diagrams shown in the previous chapter. The fact that these lower energy modes are identical to the ones obtained for the free quinO ligand, indicates that the most sensitive O-18 vibrations are not necessarily those that pertain to the νN-O, αN-O and γN-O vibrations in a system of low symmetry as quinO, but rather to those modes that experience a lower degree of coupling. The smaller calculated shifts on O-18 labelling of the N-O stretch in the quinO compound are a consequence of the extensive isotope dilution resulting from the high degree of vibrational coupling due to the low symmetry.

Figure 2.3.19 shows the infrared spectra for the [Pt(C_2H_4)LBr_2] compounds where L = quinO, quinO/quin-^{18}O and the splitting observed for the modes that have been discussed above. In the

mid ir region where the νN-O stretch is expected to occur, two bands are observed to split and one to broaden in the spectrum for the [Pt(C_2H_4)(quinO/quin-^{18}O)Br_2] compound. The former two have been assigned as modes 17 and 21*A*' and the latter as mode 24*A*'. The first band observed to split (mode 17*A*'), has a negligible calculated shift to lower energy upon O-18 labelling in the [Pt(C_2H_4)(quin-^{18}O)Br_2] isotopomer. More so, no shifts to lower energy are expected to occur upon labelling of the ligand in the coordination compound until the occurrence of mode 18*A*' which is observed at 1193 cm^{-1} and calculated to occur at 1207 cm^{-1}. The results obtained experimentally are consistent with the results calculated for the free quinO ligand, where the highest O-18 sensitivity is calculated for mode 17*A*'. However, they contradict the theoretical results in that no O-18 sensitivity is calculated for mode 17*A*' in the coordination compound. No alternate satisfactory explanation can be given for the splitting observed for this band, which raises a caution over the model defined here.

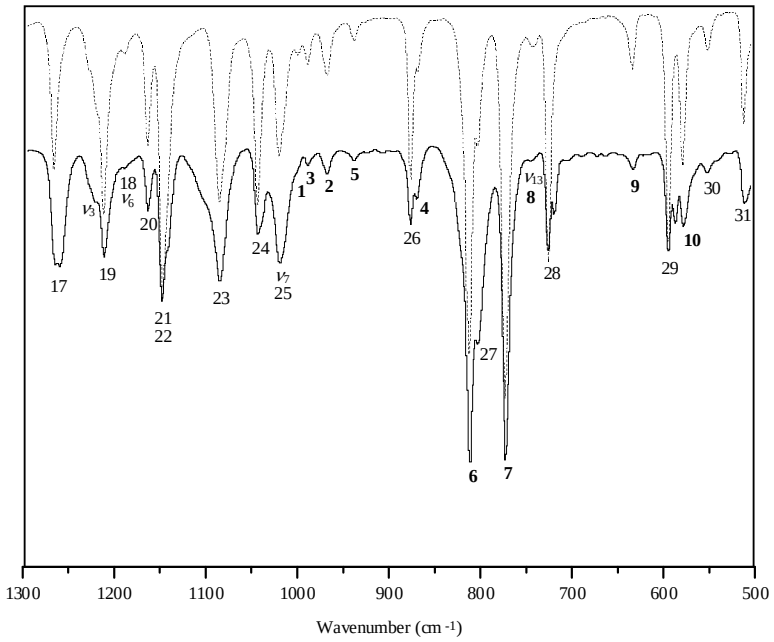

Figure 2.3.19. Mid ir spectra for [Pt(C_2H_4)LBr_2] where L = quinO (broken line) and L = quinO/quin-^{18}O (solid line) showing the splitting of some of the O-18 sensitive vibrations. Out-of-plane vibrations in bold numbering.

The other band observed to split in the spectrum for the quinO/quin-^{18}O compound has been assigned as mode 21*A*'. This band occurs at 1151 cm^{-1} in the spectrum for [Pt(C_2H_4)(quinO)Br_2] and at 1150 cm^{-1} with a distinct shoulder at 1143 cm^{-1} for the O-18 compound. Although no O-18

sensitivity is calculated for this mode, it occurs directly after mode 20*A*' which is calculated to have high O-18 sensitivity. No splitting is observed for mode 20*A*' in the spectrum of $[Pt(C_2H_4)(quinO/quin\text{-}^{18}O)Br_2]$, but the fact that the mode that follows shows splitting might be explained in terms of the calculated bond length for this compound being underestimated in the coordination compounds, as was explained previously for the $[Pt(C_2H_4)(pyO/py\text{-}^{18}O)Br_2]$ compound.

The band that is observed to broaden slightly has been assigned as mode 24*A*'. It occurs at 1044 cm^{-1} and clearly shows broadening when superimposed on the spectrum for the unlabelled $[Pt(C_2H_4)(quinO)Br_2]$ compound with a poorly defined shoulder at *ca*. 1039 cm^{-1} (figure 2.3.19). The calculations performed on the free ligand show that this is indeed an O-18 and bond length sensitive mode, although it is not a νN-O mode for the free ligand but a coupled αN-O mode. For the N-O bond length used in the assignment for the quinO ligand discussed previously, a shift of 5 cm^{-1} to lower energy is expected upon O-18 labelling of quinO for mode 24*A*' which is in good agreement with that found here.

Splitting into two distinct bands is observed for the in-plane modes 28, 29, 31 and 33*A*'. All the modes involve the motion of the oxygen atom but they are considered as neither the principal νN-O nor the principal αN-O vibration. The calculated shifts obtained for the corresponding frequencies are in good agreement with those obtained experimentally.

The αN-O vibration is calculated to be a highly coupled vibration distributed between modes 30 and 32*A*'. However, no splitting is observed for either of the bands in the far ir or Raman spectra for the labelled compounds.

Mode 12*A*'' is the only out of plane mode observed to broaden in the Raman spectrum for $[Pt(C_2H_4)(quinO/quin\text{-}^{18}O)Br_2]$. The corresponding absorption is a weak intensity absorption with a distinct table-top when superimposed on the Raman spectrum for the $[Pt(C_2H_4)(quinO)Br_2]$ species, with the beginning of the absorption at 451 cm^{-1} and the end at 447 cm^{-1}.

Both modes 12 and 13*A*'' show displacement of the N-O atoms in different directions as was observed for the free quinO ligand. However, in the coordination compound, a 4 cm^{-1} shift to lower energy on O-18 labelling is expected for mode 12*A*'' and one of only 1 cm^{-1} to lower energy for mode 13*A*''. Mode 12*A*'' has hence been assigned as the principal γN-O vibration in

the [PtA(quinO)X_2] compounds in lieu of mode 13*A*'' so assigned for the free ligand. This is in agreement with the calculated shifts obtained for this band and the splitting observed in the far ir spectrum of [Pt(C_2H_4)(quinO/quin-^{18}O)Br_2].

The most O-18 sensitive mode for the [Pt(C_2H_4)(quin-d_7O)Br_2] compound is mode 17*A*' which undergoes a calculated shift of 9 cm^{-1} for the O-18 labelled species. This mode displays the largest N-O displacement in both the free ligand and the coordination compounds and is consistent with this mode being ascribed the purest νN-O mode for quin-d_7O. As is the case with free ligand, several other modes in the coordination compounds show O-18 sensitivity from the calculations performed and these have been pointed out in table 2.3.11.

2.3.2.8. Pt-L vibrations

To assist the discussion of the Pt-L vibrations, the far ir spectra for the [PtALBr$_2$] compounds where A = C_2H_4, C_2D_4; L = pyO, py-d_5O and pyO/py-^{18}O are shown in figure 2.3.20, and in

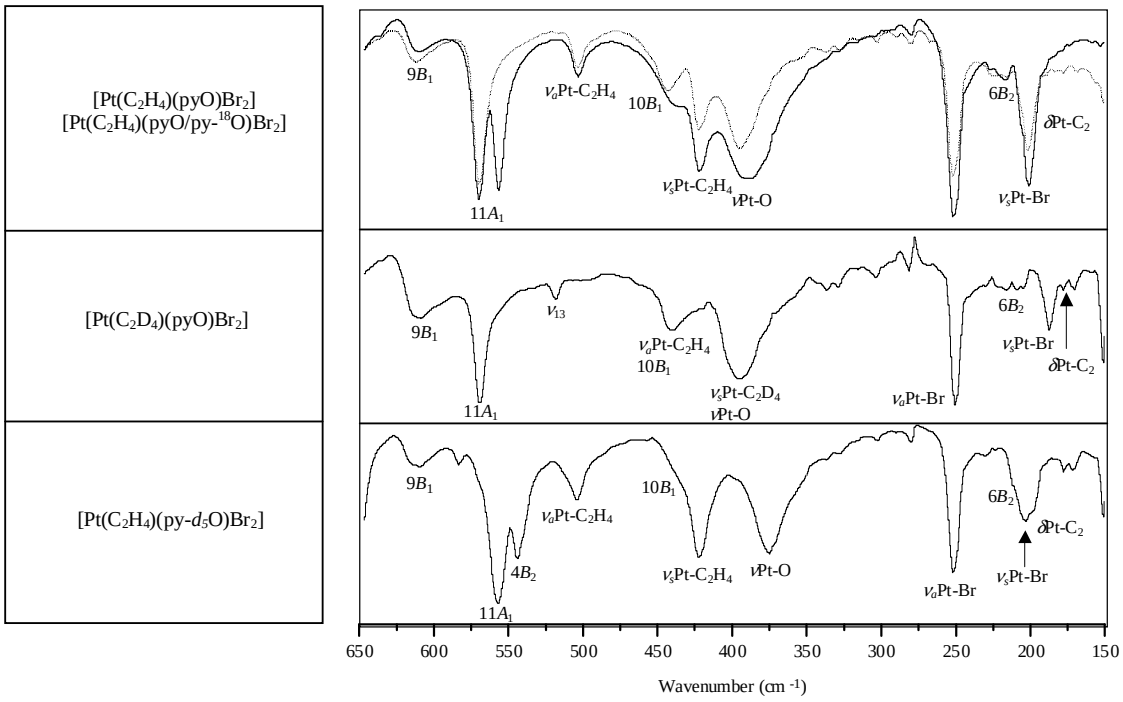

Figure 2.3.20. Far ir spectra for the [PtALBr$_2$] compounds, A = C_2H_4, C_2D_4; L = pyO, pyO/py-^{18}O, py-d_5O. The spectra on the top box are for [Pt(C_2H_4)(pyO)Br_2] (dotted line) and for [Pt(C_2H_4)(pyO/py-^{18}O)Br_2] (solid line).

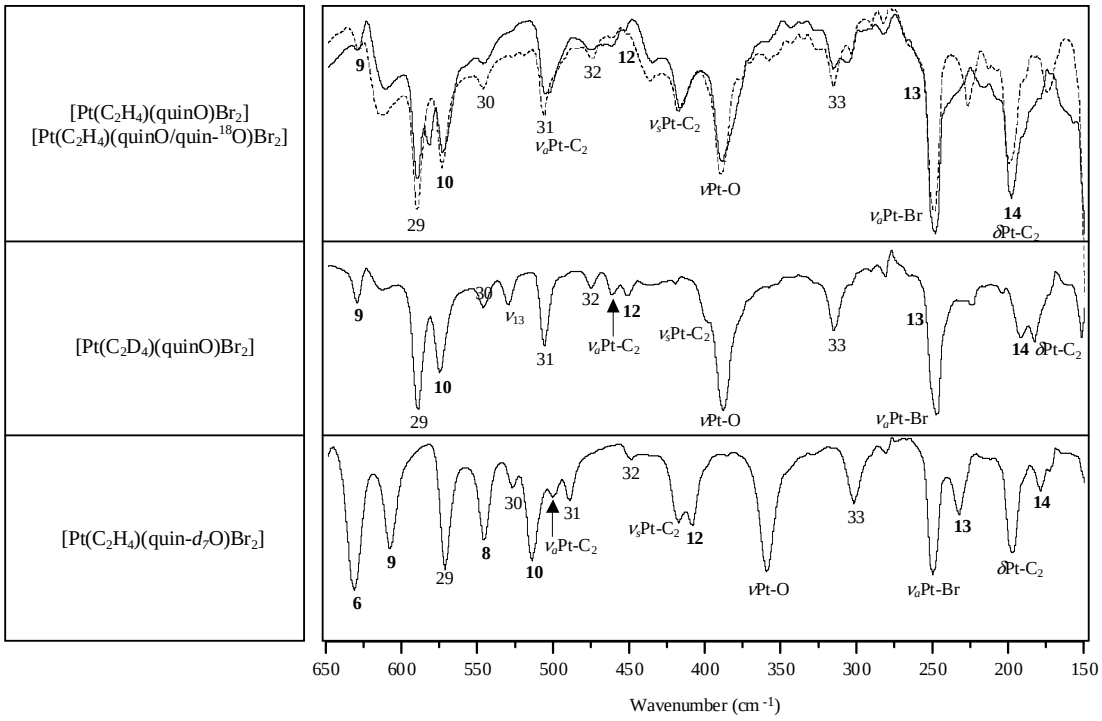

Figure 2.3.21. Far ir spectra for the [PtALBr$_2$] compounds, A = C_2H_4, C_2D_4; L = quinO, quinO/quin-^{18}O, quin-d_7O. The spectra on the top box are for [Pt(C_2H_4)(quinO)Br$_2$] (dotted line) and for [Pt(C_2H_4)(quinO/quin-^{18}O)Br$_2$] (solid line). Out-of-plane fundamentals in bold numbering.

figure 2.3.21 for A = C_2H_4, C_2D_4; L = quinO, quin-d_7O and quinO/quin-^{18}O. Raman spectra in the low energy region for the [PtALX$_2$] compounds where A = C_2H_4, C_2D_4; L = pyO, py-d_5O; X = Br, Cl are shown in figure 2.3.22, and in figure 2.3.23 for A = C_2H_4, C_2D_4; L = quinO, quin-d_7O; X = Br, Cl.

The Pt-C_2H_4 asymmetric and symmetric stretching frequencies have been previously assigned for several compounds [10, 14, 19-21, 61, 73, 74, 79]. In Zeise's salt, they appear at 501 and 408 cm^{-1} respectively [10]. They occur at *ca*. 510 and 427 cm^{-1} in the pyO derivatives and are observed in both the ir and Raman spectra of the compounds. The asymmetric stretch is a weak intensity band while the symmetric stretch is slightly stronger in both the ir and Raman spectra. The higher values obtained when compared to the values observed for Zeise's salt seem

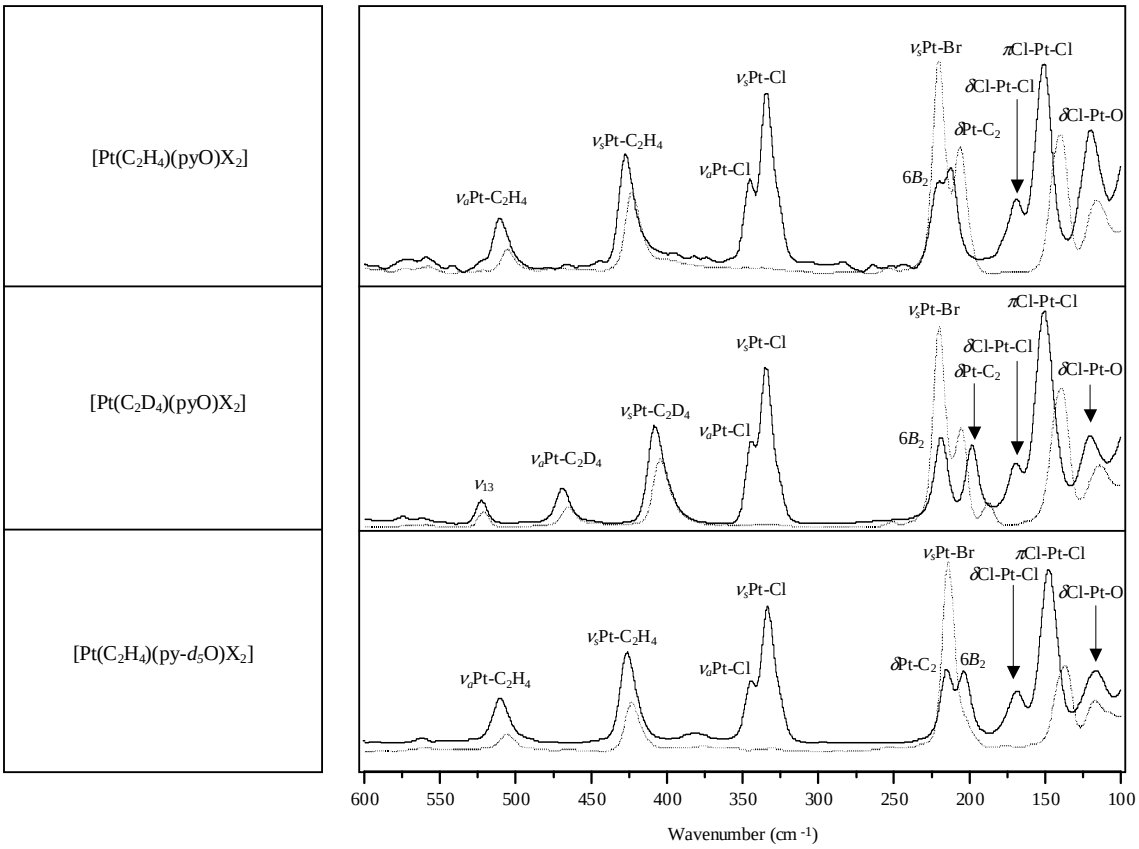

Figure 2.3.22. Raman spectra for $[PtALX_2]$ compounds, A = C_2H_4, C_2D_4; L = pyO, py-d_5O; X = Cl (solid line), Br (broken line). Assignments below 200 cm^{-1} are given for the X = Cl compounds (solid line) as coupling is observed for the X = Br derivatives.

indicative of a stronger Pt-C_2H_4 bond by the presence of a *trans*-Pt-O bond. The results are expected, as the *trans*-influence of chloride is more significant than that of the O atom in the *N*-oxide ligands. The asymmetric stretch at *ca*. 500 cm^{-1} is masked in some of the quinO derivatives but the symmetric stretch occurs at 417 cm^{-1}. This shift to lower energy is also expected due to the fact that the Pt-O bond formed with quinO is expected to be a stronger bond on account of the oxygen atom in quinO being a better σ-donor than in pyO [87], hence weakening the Pt-C_2H_4 bond.

The δPt-C_2H_4 band is a very well defined weak intensity band in the Raman spectra occurring at *ca*. 213 and 199 cm^{-1} for the ethylene-d_0 and ethylene-d_4 analogues respectively. The observed

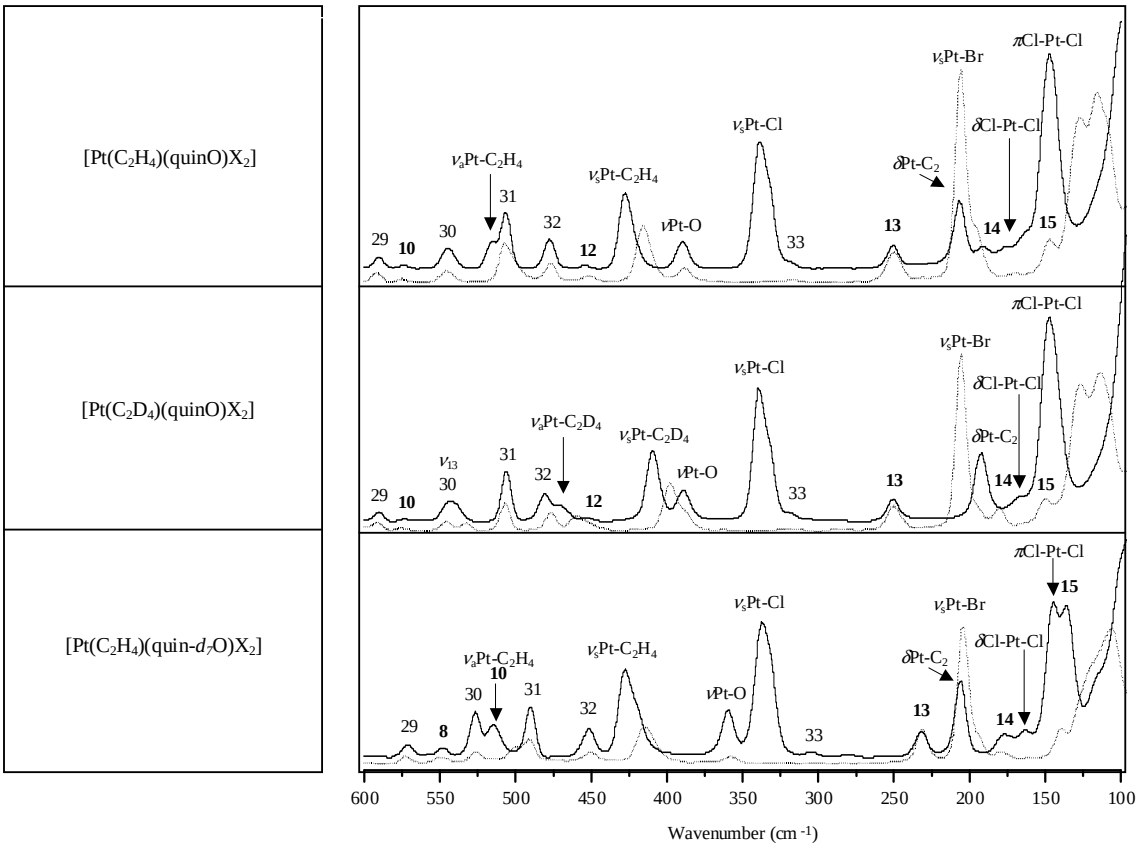

Figure 2.3.23. Raman spectra for $[PtALX_2]$ compounds, A = C_2H_4, C_2D_4; L = quinO, quin-d_7O; X = Cl (solid line), Br (broken line). Assignments below 200 cm^{-1} are given for the X = Cl compounds (solid line).

frequencies for the Pt-C_2H_4 bend are in very good agreement with the calculated ones, as can be seen in the corresponding tables.

The in-plane and out-of-plane Pt-CO vibrations are extremely coupled modes as has been discussed in previous works [19, 21, 86]. Coupling is extensive in the systems as observed from the shifts obtained for the experimental values shown in tables 2.3.8, 2.3.9 and 2.3.12. However, the δPt-CO vibration is expected to occur at higher frequencies than the πPt-CO vibration with the νPt-CO being found in between them [86]. Coupling of the Pt-CO vibrations with low energy ligand modes has been obtained in the calculations for the transition state geometries as mentioned previously. The experimental results obtained seem to be in agreement with the calculations performed, despite the fact that the geometry is not that of the stable

[Pt(CO)(pyO)Cl_2]. The coupled $5B_2$ + δPt-CO mode is calculated to occur at higher frequency than νPt-CO, followed by the δPt-CO + $5B_2$ vibration and finally by the out-of-plane πPt-CO vibration. According to the vibrational analysis performed for the [Pt(CO)(pyO)Cl_2] compound, the in-plane δPt-CO mode couples to the out-of-plane pyO mode $5B_2$. It is calculated to contribute to vibrations higher and lower than the νPt-CO vibration, with the higher frequency band having more pyO character and the lower frequency band more δPt-CO character. In the py-d_5O derivative, a similar extensive coupling is calculated to occur between the δPt-CO and $4B_2$ py-d_5O out-of-plane vibration. The carbonyl compounds with quinO fit the sequence δPt-CO > νPt-CO > πPt-CO previously described [86] as they are less extensively coupled.

The νPt-O vibration occurs as a broad and intense absorption in the far ir spectra for the pyO derivatives. Interestingly, the shape of the band resembles in detail the description for other M(II) pyO compounds [10, 16-18, 87-89] and the frequency obtained falls in the range described for other transition metal compounds. From the calculated modes obtained, it is a pure νPt-O vibration that is not coupled to other Pt-L vibrations. Furthermore, although it involves the motion of the pyO ring, especially of the H atom on position 4 of the heterocycle, the vibration obtained is not one of the low energy out-of-plane ligand vibrations but a new vibration that requires the out-of-plane displacement of the 4-H atom as the oxygen atom is displaced. The νPt-O vibrations obtained by means of the calculations are shown in figure 2.3.24. Thornton and co-workers previously assigned two possible frequencies for the νPt-O stretch in their work with pyO Zeise's salt derivatives [14, 85] on the basis of the shifts obtained by deuteration of the ring

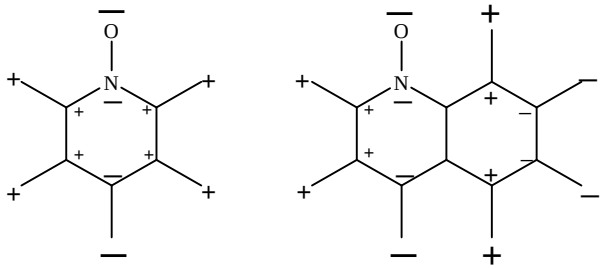

Figure 2.3.24. Displacement diagrams for the νPt-O vibration. The Pt-O bond lies beneath the plane of the molecules and is displaced towards the O atoms in the pyO and quinO ligands.

system. The lower frequency band is indeed the νPt-O stretch, while the higher frequency band is the αN-O vibration $10B_1$(9b), which undergoes a –20 cm^{-1} frequency shift from the observed frequency for the free ligand, and a noticeable change in the shape of the band which is a strong sharp band in the ir spectra for the free ligands, but broadens and decreases in intensity upon coordination as has been mentioned previously. Both the αN-O and νPt-O vibrations are observed in the ir spectra for the compounds but are absent in the Raman spectra. Both vibrations would bring about a change in the dipole moment, consistent with the above observations.

Other authors [20] had also assigned the Pt-O stretch to a weak intensity band that was insensitive to substitution in the pyO ring system, occurring at *ca.* 323 cm^{-1}. Furthermore, this vibration was expected to be a strong absorption, whereas in fact it is quite the opposite. Meester *et al*. [90] identify this as a combination band, as in the present work. However, their assignment of νPt-O at 296 cm^{-1} [90] is similarly here considered as a combination band. Watkins [19] pointed out the need to perform O-18 substitution studies in order to arrive at an unambiguous assignment for these vibrations. He correctly identified the high frequency band that Thornton *et al*. had assigned as a possible νPt-O candidate as the αN-O vibration, but the assignment of the band at *ca*. 400 cm^{-1} was still uncertain, and Watkins noted that it could be ascribed alternatively to the pyO ring mode $3A_2$(16a). The calculated frequency value for this vibration is expected to be *ca.* 420 cm^{-1} but no band could be assigned to this fundamental and it is more than likely masked by other bands, or absent in the ir spectra for the derivatives as is the case for several of the pyO vibrations of A_2 symmetry. The calculations in the present work strongly support the assignment of this band to νPt-O.

A final note on the sensitivity of the νPt-O vibration in 4-substituted pyO systems can be made on the basis of the νPt-O vibrations shown in figure 2.3.24. The motion of the atom in position 4 of the pyO molecule cannot be ignored, and mass effects of substituents in this position may play a significant role in the frequency value at which this vibration occurs.

The shifts obtained upon O-18 labelling and deuteration of the pyO ligand are in very good agreement with the calculated expected values as can be seen from tables 2.3.6 and 2.3.7. Although the O-18 labelled compound is a mixture of pyO/py-^{18}O, the band occurring at 396 cm^{-1} in $[Pt(C_2H_4)(pyO)Br_2]$ is quite a sharp well-defined band which broadens noticeably in the spectrum for the $[Pt(C_2H_4)(pyO/py\text{-}^{18}O)Br_2]$ compound. The far ir spectra for this compound were run several times and the shape of the band was consistently obtained. The broadening can

therefore be explained in terms of the O-18 sensitivity expected for the Pt-O stretch and is the result of the overlapping of the νPt-O (*ca*. 396 cm^{-1}) and ν Pt-^{18}O (*ca*. 386 cm^{-1}) stretching vibrations, and confirms its assignment. The far ir spectra for the $[Pt(C_2H_4)(pyO)Br_2]$ isotopomers are shown in figure 2.3.20.

In the far ir spectrum for $[Pt(C_2H_4)(quinO/quin\text{-}^{18}O)Br_2]$ the band occurring at 390 cm^{-1} is observed to broaden in a similar way to that described for the $[Pt(C_2H_4)(pyO/py\text{-}^{18}O)Br_2]$ compound. It is this mode that is calculated as the νPt-O mode that involves a similar atomic displacement of the atoms as that observed for pyO and which is shown in figure 2.3.24. As is the case with the pyO systems, the vibration is not one of the out-of-plane quinO modes but rather the νPt-O vibration that involves atomic displacement of the ring system in order to counterbalance the change in the centre of mass during the vibration. The absorption begins at 390 cm^{-1} and ends at *ca*. 383 cm^{-1} when the far ir spectra for $[Pt(C_2H_4)(quinO)Br_2]$ and $[Pt(C_2H_4)(quinO/quin\text{-}^{18}O)Br_2]$ are superimposed. The calculated shift of 10 cm^{-1} to lower energy accounts for the broadening of this band in the far ir spectrum for the L = quinO/quin-^{18}O mixture of compounds as was also observed for $[Pt(C_2H_4)(pyO/py\text{-}^{18}O)Br_2]$. The far ir spectra for the quinO isotopomers are shown in figure 2.3.21. Watkins and co-workers [19, 21] had previously assigned the band occurring at 390 cm^{-1} to a ring mode and a weak intensity band occurring at *ca*. 340 cm^{-1} as a possible candidate for the νPt-O vibration. No calculated values are obtained *ca*. 340 cm^{-1}, and the band observed is more than likely a combination band appearing in the far ir region.

The present work has therefore clearly established the νPt-O assignment in Zeise's salt derivative systems for aromatic *N*-oxide by utilizing both isotope studies and modelling studies.

The Pt-X asymmetric stretch vibrations, ν_aPt-X, are observed as a strong absorption in the far ir spectra for the compounds. They occur at *ca*. 350 cm^{-1} for X = Cl and *ca*. 250 cm^{-1} for X = Br. The symmetric stretch, ν_sPt-X, is observed in the Raman spectra for the compounds as a very strong absorption at *ca*. 335 cm^{-1} (X = Cl) and 220 cm^{-1} (X = Br). Calculated frequencies for these vibrations are slightly lower than observed. However, the calculations overestimate the Pt-X bond lengths as was previously mentioned, and hence a lower frequency was calculated.

Watkins and co-workers [19, 21] assigned the shoulder at 335 cm^{-1} in the infrared spectra of the X = Cl derivatives of Zeise's salt as the ν_aPt-^{37}Cl stretch due to the high natural abundance of this

isotope. The ν_aPt-^{37}Cl/ν_aPt-^{35}Cl ratio does indeed yield the ν_aPt-^{37}Cl stretch at that precise value. However, the fact that both the symmetric and asymmetric νPt-Cl are ir and Raman active suggests an alternate assignment of the higher energy absorption as the asymmetric stretch, while the low frequency absorption is the symmetric stretch which is observed as a strong absorption in the Raman spectra. This is also reflected in the appearance of both vibrations in the Br analogues.

δPt-X and πPt-X vibrations have been assigned on the basis of their calculated values and previous assignments [19, 21, 61, 86]. It must be pointed out that the low energy modes, especially the out-of-plane X-Pt-X vibrations, are extremely coupled to the out-of-plane modes involving displacements of both the atoms in the A and L ligands.

2.4. References

1. Gambi, A.; Ghersetti, S.; *Spectrosc. Letters*; **8**, 1977, 627–632.
2. Pujari, P.R.; Bist, H.D.; *J. Raman Spectrosc.*; **1**, 1973, 255–258.
3. Katritzky, A.R.; Hands, A.R.; *J. Chem. Soc. Part 2*; 1958, 2195–2198.
4. Kakiuti, Y.; Saito, H.; Akiyama, M.; *J. Mol. Spectrosc.*; **35**, 1970, 66–72.
5. Shindo, H.; *Bull. Chem. Pharm.*; **4**, 1956, 460–469.
6. Shindo, H.; *Bull. Chem. Pharm.*; **6**, 1958, 117–129.
7. Bist, H.D.; Parihar, J.S.; Brand, J.C.D.; *J. Mol. Spectrosc.*; **64**, 1977, 211–216.
8. Mielke, Z.; *J. Phys. Chem.*; **88**, 1984, 3288–3292.
9. Bist, H.D.; Parihar, J.S.; *Chem. Phys. Lett.*; **32**, 1975, 244–246.
10. Kakiuti, Y.; Kida, S.; Quagliano, J.V.; *Spectrochim. Acta*; **19**, 1963, 201–211.
11. Thornton, D.A.; Watkins, G.M.; *Spectrosc. Lett.*; **25**, 1992, 1023–1036.
12. Dollish, F.R.; Fateley, W.G.; Bentley, F.F.; *Characteristic Raman Frequencies of Organic Compounds*; John Wiley & Sons, New York, 1974, pp. 263–272.
13. Mielke, Z.; *Spectrochim. Acta*; **39**, 1983, 141–144.
14. Auf der Heyde, T.P.E.; Foulds, G.A.; Thornton, D.A.; *J. Mol. Struct.*; **98**, 1983, 11–18.
15. Hall, P.S.; Thornton, D.A.; Foulds, G.A.; *Polyhedron*, **6**, 1987, 85–94.
16. Hutton, A.T.; Thornton, D.A.; *Spectrosc. Letters*; **10**, 1977, 57–65.
17. Hutton, A.T.; Thornton, D.A.; *J. Mol. Struct.*; **39**, 1977, 33–38.
18. Auf der Heyde, T.P.E.; Green, C.S.; Needham, D.E.; Thornton, D.A.; Watkins, G.M.; *J. Mol. Struct.*; **70**, 1981, 121–126.
19. Watkins, G.M.; *Ligand Isotope Vibrational Studies of Metal (II) ComplexesWith Particular Reference to Heterocyclic N-oxides*, PhD Thesis, University of Cape Town, 1988.
20. Orchin, M.; Schmidt, P.J.; *Coord. Chem. Rev.*; **3**, 1968, 345–373.
21. Foulds, G.A.; Thornton, D.A.; Watkins, G.M.; *Spectrochim. Acta*; **48A**, 1992, 577–604.
22. La Lau, C.; Snyder, R.G.; *Spectrochim. Acta*; **27A**, 1971, 2073–2088.
23. Draeger, J.A.; *Spectrochim. Acta*; **39A**, 1983, 809–825.
24. Miller, F.A.; *J. Chem. Phys.*; **24**, 1956, 996–1001.
25. Ülkü, D.; Huddle, B.P.; Morrow, J.C.; *Acta Cryst.*; **B27**, 1971, 432–436.
26. Thornton, D.A.; Watkins, G.M.; *Bull. Soc. Chim. Belg.*; **100**, 1991, 235–245.
27. Thornton, D.A.; Watkins, G.M.; *J. Coord. Chem.*; **29**, 1993, 45–56.
28. Thornton, D.A.; Watkins, G.M.; *Spectrosc. Letters*; **26**, 1993, 887–895.

29. Várs anyi, G.; Szöke, S.; *Vibrational Spectra of Benzene Derivatives*, Academic Press, New York; 1969.
30. Thornton, D.A.; Verhoeven, P.F.M.; Watkins, G.M.; Desseyn, H.O.; Van der Veken, B.J.; *Spectrochim. Acta*; **46A**, 1990, 1439–1451.
31. Thornton, D.A.; Watkins, G.M.; *Bull. Soc. Chim. Belg.*; **100**, 1991, 221–233.
32. Thornton, D.A.; Verhoeven, P.F.M.; Watkins, G.M.; Desseyn, H.O.; Van der Veken, B.J.; *Bull. Soc. Chim. Belg.*; **100**, 1991, 211–220.
33. Person, W.B.; Pimentel, G.C.; Schnepp, O.; *J. Chem. Phys.*; **23**, 1955, 230–233.
34. Pimentel, G.C.; McClellan, A.L.; Person, W.B.; Schnepp, O.; *J. Chem. Phys.*; **23**, 1955, 234–237.
35. Lippincott, E.R.; O'Reilly, Jr., E.J.; *J. Chem. Phys.*; **23**, 1955, 238–244.
36. McClellan, A.L.; Pimentel, G.C.; *J. Chem. Phys.*; **23**, 1955, 245–248.
37. Freeman, D.E.; Ross, I.G.; *Spectrochim. Acta*; **16**, 1960, 1393–1408.
38. Scully, D.B.; Whiffen, D.H.; *Spectrochim. Acta*; **16**, 1960, 1409–1415.
39. Scherer, J.R.; *J. Chem. Phys.*; **36**, 1962, 3308–3321.
40. Neto, N.; Scrocco, M.; Califano, S.; *Spectrochim. Acta*; **22**, 1966, 1981–1998.
41. Behlen, F.M.; McDonald, D.B.; Sethuraman, V.; Rice, S.A.; *J. Chem. Phys.*, **75**, 1981, 5685–5693.
42. Sellers, H.; Pulay, P.; Boggs, J.E.; *J. Am. Chem. Soc.*; **107**, 1985, 6487–6494.
43. Hudgins, D.M.; Sandford, S.A.; Allamandola, L.J.; *J. Phys. Chem.*; **98**, 1994, 4243–4253.
44. Nakata, M.; Kudoh, S.; Takayanagi, M.; Ishibashi, T.; Kato, C.; *J. Phys. Chem. A*; **104**, 2000, 11304–11309.
45. Gellini, C.; Salvi, P.R.; Vogel, E.; *J. Phys. Chem. A*; **104**, 2000, 3110–3116.
46. Foulds, G.A.; Hodgson, A.T.; Hutton, A.T.; Niven, M.L.; Percy, G.C.; Rutherford, P.E.; Thornton, D.A.; *Spectrosc. Letters*; **12**, 1979, 25–32.
47. Niven, M.L.; Thornton, D.A.; *S. Afr. J. Chem.*; **32**, 1979, 250–251.
48. Niven, M.L.; Thornton, D.A.; *J. Mol. Struct.*; **53**, 1979, 157–163.
49. Chiorboli, P.; Bertoluzza, A.; *Ann. Chim. Rome*; **49**, 1959, 245–265. (As cited in references 19 and 46).
50. Wait Jr., S.C.; McNerney, J.C.; *J. Mol. Spectrosc.*; **34**, 1970, 56–77.
51. Srivastava, S.L.; Prasad, M.; Rohitashava; *Spectrochim. Acta*; **40A**, 1984, 681–685.
52. Ferri, D.; Bürgi, T.; *J. Am. Chem. Soc.*; **123**, 2001, 12074–12084.
53. Unpublished results.
54. MacDougall, J.J.; Nathan, L.C.; Nelson, J.H.; *Inorg. Chim. Acta*; **17**, 1976, 243–246.

55. Shindo, H.; *Bull. Chem. Pharm.*; **8**, 1960, 845–855.
56. Nelson, J.H.; Nathan, L.C.; Ragsdale, R.O.; *Inorg. Chem.*; **7**, 1968, 1840–1845.
57. Nelson, J.H.; Ragsdale, R.O.; *Inorg. Chim. Acta*; **2**, 1968, 230–232
58. Nelson, J.H.; Ragsdale, R.O.; *Inorg. Chim. Acta*; **3**, 1969, 473–477.
59. Shindo, H.; *Bull. Chem. Pharm.*; **5**, 1957, 472–481.
60. Karayannis, N.M.; Pytlewski, L.L.; Mikulski, C.M.; *Coord. Chem. Rev.*; **11**, 1973, 93–159.
61. Nakamoto, K.; *Infrared and Raman Spectra of Inorganic and Coordination Compounds. Parts A and B: Theory and Applications in Inorganic Chemistry*. 5th edition; John Wiley & Sons, 1997, New York, USA, pp. 91–97 (Part A) and pp. 276–279 (Part B).
62. Ghersetti, S.; Giorgianni, S.; Minari, M.; Spunta, G.; *Spectrosc. Letters*; **6**, 1973, 167–176.
63. Ghersetti, S.; Giorgianni, S.; Minari, M.; Spunta, G.; *Spectrochim. Acta*, **31A**, 1975, 445–449.
64. Eller, P.G.; Ryan, R.R.; Schaeffer, R.O.; *Cryst. Struct. Comm.*; **6**, 1977, 163–166.
65. Maresca, L.; Natile, G.; *Inorg. Chim. Acta*; **38**, 1980, 53–57.
66. De Renzi, A.; Panunzi, A.; Saporito, A.; Vitagliano, A.; *Gazetta Chim. Ital.*; **107**, 1977, 549–553.
67. Fanizzi, F.P.; Maresca, L.; Natile, G.; Lanfranchi, M.; Tiripicchio, A.; Pacchioni, G.; *J. Chem. Soc. Chem. Comm.*; 1992, 333–335.
68. Bartolucci, S.; Carpinelli, P.; De Felice, V.; Giovannitti, B.; De Renzi, A.; *Inorg. Chim. Acta*,; **197**, 1992, 51–57.
69. Manojlovic-Muir, L.; Muir, K.W.; Solomun, T.; *J. Organometal. Chem.*; **142**; 1977, 265–280.
70. Manojlovic-Muir, L.; Muir, K.W.; Walker, R.; *J. Chem. Soc., Dalton*; 1976, 1270–1281.
71. Albano, V.G.; Demartin, F.; De Renzi, A.; Morelli, G.; Saporito, A.; *Inorg. Chem.*; **24**, 1985, 2032–2039.
72. Russell, D.R.; Tucker, P.A.; Wilson, S.; *J. Organometal. Chem.*; **104**; 1976, 387–392.
73. Foulds, G.A.; Thornton, D.A.; *J. Mol. Struct.*; **98**, 1983, 309–314.
74. Foulds, G.A.; Thornton, D.A.; Yates, J.; *J. Mol. Struct.*; **98**, 1983, 315–321.
75. Meester, M.A.M.; Olie,K.; Sint, L.; Schenk, H.; *Cryst. Struct. Comm.*; **4**, 1975, 725–730.
76. Caruso, F.; Spagna, R.; Zambonelli, L.; *J. Cryst. Mol. Struct.*; **8**, 1978, 47–57.
77. Meester, M.A.M.; Stufkens, D.J.; Vrieze, K.; *Inorg. Chim. Acta*; **21**, 1977, 251–258.
78. Meester, M.A.M.; Stufkens, D.J.; Vrieze, K.; *Inorg. Chim. Acta*; **15**, 1975, 137–147.
79. Foulds, G.A.; Hall, P.S.; Thornton, D.A.; *J. Mol. Struct.*; **117**, 1984, 95–101.
80. Ng, S.W.; Barnes, C.L.; van der Helm, D.; Zuckerman, J.J.; *Organomet.*; 1983, 600–608.

81. A.L.Spek (2003) PLATON, A Multipurpose Crystallographic Tool, Utrecht University, Utrecht, The Netherlands.
82. Von Ahsen, B.; Wartchow, R.; Willner, H.; Jonas, V.; Aubke, F.; *Inorg. Chem.*; **39**, 2000, 4424–4432.
83. Bagnoli, F.; Belli Dell'Amico, D.; Calderazzo, F.; Englert, U.; Marchetti, F.; Merigo, A.; Ramello, S.; *J. Organometal. Chem.*; **622**, 2001, 180–189.
84. Koch, W.; Holthausen, M.C.; *A Chemist's Guide to Density Functional Theory*, 2nd edition, Wiley-VCH, Weinheim, Federal Republic of Germany, 2000.
85. Hall, P.S.; Thornton, D.A.; Foulds, G.A.; *Polyhedron*, **6**, 1987, 85–94.
86. Goggin, P.L.; Norton, M.G.; *Inorg. Chim. Acta*; **26**, 1978, 125–128.
87. Aitken, G.B.; McQuillan, G.P.; *J. Chem. Soc. Dalton*; 1973, 2637–2640.
88. Auf der Heyde, T.P.E.; Green, C.S.; Hutton, A.T.; Thornton, D.A.; *Spectrosc. Lett.*; **13**, 1980, 31–38.
89. Nathan, L.C.; Ragsdale, R.O.; *Inorg. Chim. Acta*; **3**, 1969, 473–477.
90. Meester, M.A.M.; Stufkens, D.J.; Vrieze, K.; *Inorg. Chim. Acta*; **16**, 1976, 191–198.

3. Cu(I) carbonyl compounds

3.1. Introduction

Cu(I) has for a very long time been known to interact with CO, with the first account of volatility of copper in gas streams containing CO dating back to 1916, while reports of the absorption of CO by solutions containing CuX (X = Cl, Br) go as far back as 1850 [1]. However, it was not until 1969 that the first stable Cu(I) carbonyl with trifluoroacetate was well characterized. In the last 30 years Cu(I) carbonyl chemistry has grown at a fast rate, with the discovery of a large number of ligands that stabilize the Cu(I) oxidation state and due to an increased interest in the catalytic role of Cu(I) centres in a wide variety of chemical and biochemical processes [2].

It is generally agreed that three main factors contribute to the stabilization of Cu(I) carbonyls: the nature of the donor atoms bound to the Cu(I) ion, the macrocyclic structure of the ligand employed, and the nature of the counter-ion in charged carbonyl Cu(I) complex ions [3].

A search performed on the Cambridge Structural Database (CSD) reveals that as of February 2003, a total number of 49 different Cu(I) carbonyl compounds have been characterized by means of X-ray diffraction studies in which the CO ligand is unidentately bound to the Cu(I) centre. Most of these compounds existing in the species [Cu(CO)L] contain N donor atoms in the ligand L. Geometries vary from trigonal planar to square pyramidal, with the largest number of compounds obtained in an approximate tetrahedral geometry. Only 3 of the 49 compounds contain more than one CO ligand bound to the Cu(I) atom and 24 of the 49 are mononuclear species, with the remaining compounds being either polynuclear or polymeric species. Most compounds, whether mononuclear or polynuclear, are cationic moieties or neutral species. Only one anionic Cu(I) carbonyl compound has been isolated [4]. Ten of the 49 compounds contain the tetraphenylborate anion as counter-ion. Figure 3.1.1 shows a graph of the different Cu(I) carbonyl compounds that have been characterized by XRD together with the observed geometry and the nature of the donor atoms (other than the CO ligand) bound to the Cu(I) system.

Several compounds deserve special mention, as they either had previously been considered only at a hypothetical level or they exist as extremely stable species when bound to certain ligands. Within the former is the tetrahedral tetracarbonyl species $[Cu(CO)_4][1\text{-Et-}CB_{11}F_{11}]$ [5] where employment of the superweak functionalized undecafluorocarborane anion, $1\text{-R-}CB_{11}F_{11}$ (R = benzyl, ethyl), allows for the preparation of Cu(I) species that bind more than one CO ligand. The

solid state ir spectrum (run under ~ 5 atm of CO) of the $[Cu(CO)_4]^+$ compound shows the νCO frequency at 2184 cm^{-1}. This species extends the known series of isoelectronic $3d^{10}$ metal tetracarbonyls $Cr(CO)_4^{4-}$, $Mn(CO)_4^{3-}$, $Fe(CO)_4^{2-}$, $Co(CO)_4^{-}$, $Ni(CO)_4$; with $Cu(CO)_4^{+}$ being the only cationic species in the series and the only one to exhibit a CO stretching frequency greater than 2143 cm^{-1}. The compound shows minor distortions from an ideal T_d symmetry and decarbonylates if not under a positive CO pressure.

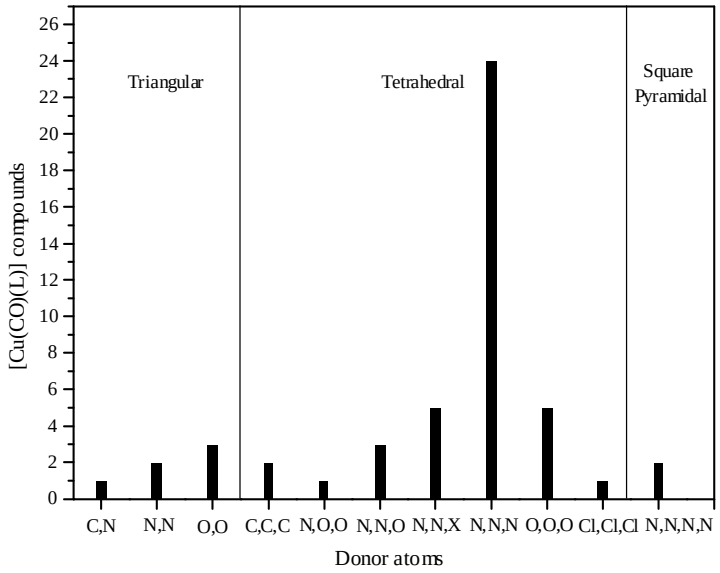

Figure 3.1.1. Graph of [Cu(CO)L] compounds (X = Cl, Br) showing the nature of the donor atoms bound to the Cu(I) centre other than CO.

Two ligands have been explored somewhat exhaustively due to the enhanced stabilization of the Cu(I) carbonyl species. The 2,2'-pyridylamine ligand, $NHpy_2$, and the hydrotris(1–pyrazolyl)borate ligand, $HB(pz)_3$, and functionalized derivatives, allow for the binding of CO and olefins to yield very stable Cu(I) species.

Compounds with the 2,2'-dipyridylamine ligand and coordinated CO, C_2H_2 and C_2H_4 (figure 3.1.2) have been prepared and characterized by means of XRD studies [6-8]. The ligand is of particular interest as it allows for the study of the proposed role of Cu(I) in the binding of the plant hormone ethylene to its receptor site [7, 8].

Compounds with the hydrotris(1-pyrazoyl)borate ligand and functionalized derivatives [9-13] (figure 3.1.3) allow for the synthesis of a wide variety of carbonyl and η^2-ethylene compounds. Of the 49 crystal structures reported for Cu(I) carbonyls, 10 correspond to ligands from this group, while of the 9 published crystal structures for coordinated ethylene compounds, 3 contain ligands that are derivatives of $HB(pz)_3$. The ethylene compounds are indefinitely stable under nitrogen and are stable towards the loss of ethylene when dissolved in olefin-free solvents, a feature not observed for most Cu(I) ethylene compounds [8]. They also prove to be interesting candidates in the modelling of the receptor site of the plant hormone ethylene. Table 3.1.1 shows Cu-CO and CO distances and νCO frequencies for some of the compounds mentioned as possible plant hormone ethylene models.

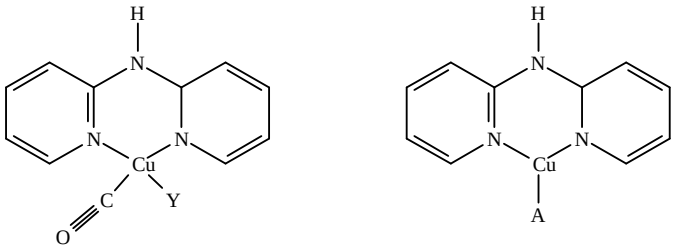

(a) (b)

Figure 3.1.2. (a) $[Cu(CO)(NHpy_2)Y]$ compounds, Y = Cl, ClO_4 and (b) $[CuA(NHpy_2)]^+$ compounds, A = C_2H_4, C_2H_2.

Table 3.1.1. Cu-CO and CO distances in Å and νCO frequencies in cm^{-1} for some Cu(I) carbonyl compounds.

Compound	Cu–CO	CO	νCO	Reference
$[Cu(CO)_4][1\text{-Et-}CB_{11}F_{11}]$	1.965*	1.111‡	2184	5
$[Cu(CO)_2][1\text{-Bn-}CB_{11}F_{11}]$	1.916*	1.112‡	2166, 2184	5
$[Cu(CO)(NHpy_2)Cl]$	1.807	1.106	2069	6
$[Cu(CO)(NHpy_2)Br]^a$	—	—	2069	6
$[Cu(CO)(NHpy_2)I]^a$	—	—	2067	6
$[Cu(CO)(NHpy_2)ClO_4]$	1.808	1.054	2110	8
$[Cu(CO)(HBpz_3)]$	1.755; 1.775†	1.120, 1.120	2083	10, 11
$\{[Cu(CO)[HB(Me,4\text{-}t\text{-Bu-}C6H_4\text{-}pz)_3]\}$	1.752	1.120	2078	9
$\{Cu(CO)[HB(Me,t\text{-Bu-}pz)_3]\}$	1.789, 1.805†	1.113, 1.106	2059	11
$\{Cu(CO)[HB(i\text{-Pr},i\text{-Pr-}pz)_3]\}$	1.769	1.118	2056	12
$\{Cu(CO)[HB(Ph,Ph\text{-}pz)_3]\}$	1.78	1.08	2080	11
$\{Cu(CO)[HB(CF_3,CF_3\text{-}pz)_3]\}$	1.808	1.110	2137	13

* Average Cu-CO distance.
† Two different molecular units in crystal structure.
‡ Average CO distance.
a No crystal structure available for these compounds.

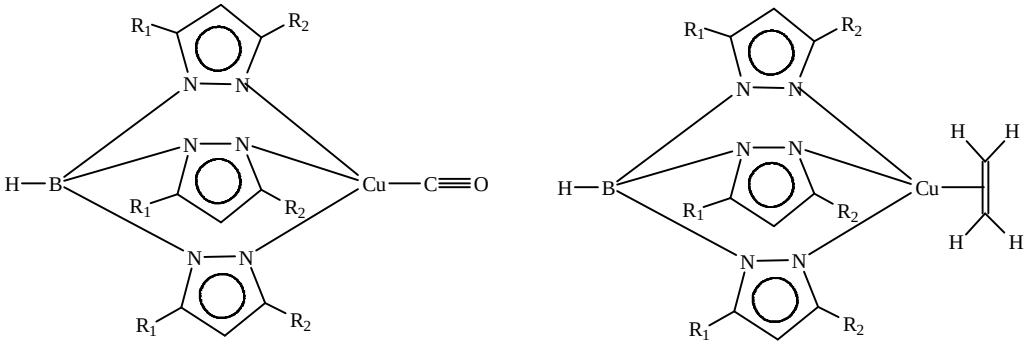

(a) (b)

Figure 3.1.3. (a) {Cu(CO)[BH(R_1,R_2-pz)$_3$]} compounds, $R_1 = R_2$ = H, CH_3, Ph, *i*-Pr, *t*-Bu, CF_3; R_1 = H and R_2 = CF_3, CF_2-CF_3, CF_2-CF_2-CF_3; R_1 = CH_3 and R_2 = 4-*t*-Bu-C_6H_4, *t*-Bu and (b) {Cu(C_2H_4)[BH(R_1,R_2-pz)$_3$]} compounds, R_1 = H, CF_3, Ph and R_2 = CF_3.

It is only very recently that proof of the important role of Cu(I) in ethylene binding activity in biological systems has been obtained [14 and references therein]. It has also been pointed out that the aminoacids histidine and cysteine play a significant role in the binding of ethylene to the receptors, as alteration of either of the residues leads to a total elimination of ethylene binding. Although Cu(I)-η^2-C_2H_4 systems have been prepared previously [7, 8, 15], it was only in 2001 that the first sulfur-ligated Cu(I)-η^2-C_2H_4 compound was reported with the macrocyclic ligand 1,4,7-trithiacyclononane, 9S3 [14]. The Cu(I)-9S3 series of compounds bind MeCN, CO and ethylene and are remarkably stable species to oxidation or loss of the ligands in the solid state. Other macrocyclic ligands have reportedly been prepared in an effort to extend the existing knowledge in this field. The 1,4,7-triazacyclonane ligand, 9N3, and its *N*-methylated derivative, 9NMe3, show an enhanced ability to bind CO, ethylene, and other ligands [15]. The macrocyclic ligands mentioned will be discussed further in section 3.2.

Cu(I) complexes have also been prepared as model compounds to study the mechanisms of copper monooxygenases, by which atmospheric O_2 is used to hydroxylate hydrocarbons both regio- and stereoselectively [16]. Cu(I) systems with the ligands α,α'-bis(4,7-diisopropyl-1,4,7-triazacyclonan-1-yl)-*p*-xylene and its -*m*-xylene analogue have been studied in their reactivity towards dioxygen. The ligands employed both stabilize the Cu(I)-carbonyl species and the stable dinuclear dicarbonyl species has been obtained with the *m*-xylene derivative which is shown in figure 3.1.4.

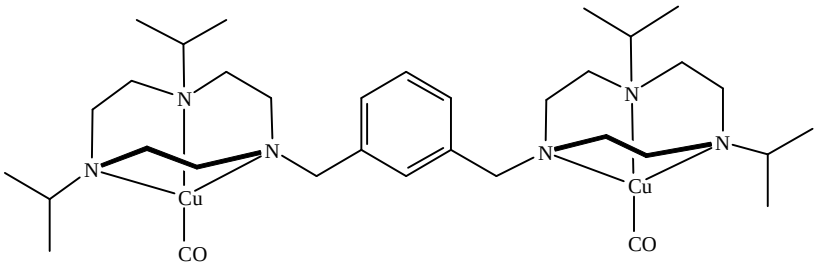

Figure 3.1.4. Structure for the dinuclear dicationic carbonyl compound with the α,α'-bis(4,7-diisopropyl-1,4,7-triazacyclonan-1-yl)-*m*-xylene ligand.

Synthetic models for the study of deoxyhemocyanin and carbon monoxyhemocyanin have previously been prepared with ligands containing benzimidazole units [17]. Such ligands bind Cu(I) to form dinuclear compounds that are employed to model the binding site in Cu(I) proteins like that of *Panulirus interruptus* hemocyanin, in which three histidines are coordinated to the dinucelar Cu(I) atoms [17]. Other model compounds obtained include histamine ligands (figure 3.1.5), which form dinuclear Cu(I) compounds that bind CO [18]. Table 3.1.2 shows Cu-CO and CO bond distances and νCO frequencies for some of the CO bound model compounds mentioned.

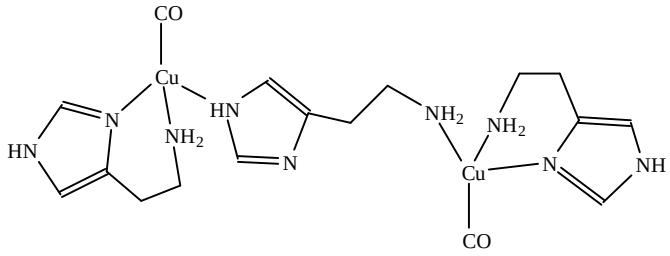

Figure 3.1.5. Structure of the dicationic dinuclear moiety $[Cu(CO)_2(histamine)_3]^{2+}$.

Blue copper proteins in which the Cu(I) coordination sphere has been determined to consist of three strongly binding ligands (His, His, Cys) and a weak interaction to methionine [17, 19-21] show only mononuclear coordination of Cu(I). The coordination geometry around the Cu(I) centre has been described as a distorted tetrahedron approximating an elongated trigonal bipyramid (figure 3.1.6). In this regard several ligands containing S, N and O atoms have previously been prepared to model the site of Cu(I) in blue proteins so as to investigate the Cu(I)/Cu(II) redox potentials dependence both on the coordination geometry and the nature of the donor atoms [2, 22-32].

Table 3.1.2. Cu-CO and CO distances in Å and νCO frequencies in cm^{-1} for some Cu(I) carbonyl model compounds.

Compound	Cu–CO	CO	νCO	Reference
$[(m\text{-}XYL^{iPr4})Cu_2(CO)_2]X_2$ [a]	1.773(6)	1.125(7)	2079	16
	1.783(6)	1.119(7)		
$[Cu_2(hm)_3(CO)_2](BPh_4)_2$	1.80(2)	1.12(3)	2066, 2055	18
	1.79(2)	1.13(3)		

a Bond distances shown are for the compound $[(m\text{-}XYL^{iPr4})Cu_2(CO)_2](CF_3SO_3)_2 \cdot 2CH_2Cl_2$; νCO frequency shown is for the compound with X = ClO_4, for which only one CO stretching frequency is reported.

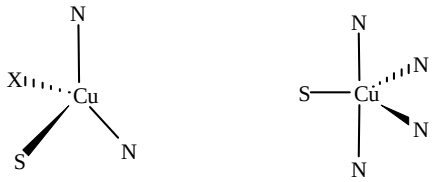

(a) (b)

Figure 3.1.6. Basic structural models for the blue type I active site. In both models two of the coordinated N atoms are from imidazole groups of histidine residues and the S atom from a cysteinate group. For structure (a) X = N, S or O [24].

The need to determine the effects of the different ligands on the Cu(I) site aimed at rationalizing their probable role in the activity of the Cu(I) systems is the main purpose of the following sections, where DFT modelling, calculation of HSAB parameters and labelling studies allow for a better understanding of these systems.

3.2. A theoretical study of 1,4,7-trisubstituted cyclononane Cu(I) carbonyl systems

Cu(I) systems with macrocyclic tridentate ligands have been previously prepared (figure 3.2.1)

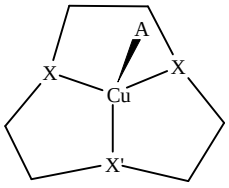

Figure 3.2.1. Structure of $[CuA(9X2X')]^+$ compunds where A = CO, C_2H_4; X = X' = S, NH, NMe; X = S and X' = NH or X = NH and X' = S.

and are remarkably stable species when bound to CO and C_2H_4 [14, 15]. The macrocyclic ligands 1,4,7-triazacyclononane, its *N*-methyl derivative and the 1,4,7-trithiacyclononane ligand, together with the mixed donor atom ligands 1,4-dithia-7-azacyclononane and 1-thia-4,7-diazacyclonane, are the main aim of the current theoretical study. The ligands all form cyclic nine membered rings with three heteroatoms and three ethylene units; they will be referred to as 9X3 (X = N, S, NMe) or 9X2X' (X, X' = N or S) in the present discussion.

Carbonyl and η^2–ethylene complexes have been prepared for the 9N3, 9NMe3 [15] and 9S3 ligands [14]. Several compounds have been prepared with the mixed macrocyclic ligands, but almost all are Cu(II) species [33-36] and in some cases the macrocyclic ligands have been functionalized further to allow for pentacoordination to the metal centre.

Küppers, *et al*. [37] attempted the preparation of the [Cu(CO)(9S3)]Y compound but were unsuccessful. They reported that at T = 293 K no CO was bound to the Cu(I) moiety. Instead, they were able to obtain the compound with coordinated iodide, [Cu(9S3)I], which is one of the few monomeric Cu(I) compounds with this ligand to have been characterized by means of X-ray diffraction. The other monomeric compounds that have been determined by this technique are $[Cu(AsPh_3)(9S3)]ClO_4$ [38] and species involving the 9S3 ligand binding in both a tridentate chelating and unidentate or bridging unidentate fashion to yield tetrahedral geometry [22, 23, 39] in the mononuclear or binuclear Cu(I) species.

Hirsch *et al*. [14] were able to prepare the carbonyl and η^2-ethylene derivatives by carrying out the reaction at 195 K and obtained the compounds [CuA(9S3)]Y; where A = CO, ^{13}CO, C_2H_4, C_2D_4 and Y = PF_6 and BF_4. The authors pointed out that at room temperature, displacement of MeCN from the starting material $[Cu(MeCN)(9S3)]PF_6$, in the presence of CO does not occur.
On the other hand, triamine macrocyclic Cu(I) carbonyl and η^2-ethylene complexes can be readily prepared at room temperature [15] and form a wide variety of $[CuA(9N3)]BPh_4$ and $[CuA(9NMe3)]BPh_4$ compounds where A = CO, C_2H_4, cyclohexene, cyclooctene, cyclohexyl isocyanide, 1,5-cyclooctadiene, norbornadiene and diphenylacetylene. The carbonyl compounds are stable to the loss of CO in the solid state and in solution and NMR analysis of these compounds could be performed, whereas fast exchange with the solvent is observed for the 9S3 compounds.

Several interesting questions arise from these observations and they will be answered by means of the results arrived at from DFT calculations for these systems.

3.2.1. Computational details

Calculations were carried out using Spartan02 DFT at the B3LYP level for the compounds $[Cu(CO)(9X3)]^+$ where X = S, N and NMe, for [CuY(9S3)] (Y = Br and I) and for $[CuA(9S3)]^+$ (A = CO, MeCN, Me_2CO) and $[Cu(CO)(9X2X')]^+$ (X = S, X' = N and X = N, X' = S). The basis set used for all calculations was 6-31G**. For the compound with iodide, pseudopotentials were used at the same level since the 6-31G** basis set has no basis for the iodine atom. Geometry optimizations were performed and vibration frequencies were calculated for all molecules and fragments obtained by removal of one of the coordinated A or Y ligands. Ionization potentials, electron affinities and other parameters were calculated as described previously in section 1.6. Mulliken population analyses were performed on all species. The optimized geometry for [Cu(9S3)Br] rendered a significantly distorted tetrahedral geometry. The calculations were performed again by taking the $[Cu(9S3)]^+$ fragment obtained from the optimized geometry for the $[Cu(MeCN)(9S3)]^+$ species, replacing the MeCN ligand by Br and allowing for a geometry optimization from this initial geometry. A much better fit was obtained (with lower energy) which may point out the existence of several local minima for the latter compound. The same can be said for fragments containing X, X' = NH, where local minima were obtained with different orientations of the N-H bond. In all cases the lower energies obtained were those for the fragments where the N-H bond is directed out of and above the plane that joins the three heteroatoms in the macrocyclic coordinated system.

For the compounds modelled to study the reaction pathway, geometry optimizations were performed at the same level and single point energy calculations were carried out with the optimized geometry. Vibrational analyses were then carried out in order to establish the transition state geometries.

Calculated parameters (ionization potential, I; electron affinities, A; electronegativities, χ; hardness, η, softness, S) and HOMO and LUMO values are shown in table 3.2.1. Fukui function values for nucleophilic and electrophilic attacks by the donor atoms in the macrocyclic ligands and in the A, Y species (CO, MeCN, Br) as well as the Cu(I) atom are shown in table 3.2.2.

Table 3.2.1. Calculated parameters for $[CuA(9X2,X')]^+$ (A = MeCN, CO) and [Cu(9X2,X')Y] (Y = Br, I) species and fragments obtained by removal of the A and Y ligands. All values in eV.

Compound	I	A	χ	η	S	HOMO	LUMO
CO(exp)*	14.0	–1.8	6.1	7.9	0.063		
MeCN(exp)*	12.2	–2.8	4.7	7.5	0.067		
[Cu(9S3)I]	6.93	1.22	4.08	2.86	0.175	2.9815	2.9828
[Cu(9S3)Br]	6.17	1.42	3.79	2.37	0.211	–4.46	–0.19
[a][Cu(9S3)]$^+$	11.21	–3.92	3.64	7.56	0.066	–8.94	–5.63
[b][Cu(9S3)]$^+$	11.28	–3.72	3.78	7.50	0.067	–9.20	–5.40
[c][Cu(9S3)]$^+$	11.26	–3.63	3.82	7.45	0.067	–9.18	–5.31
[d][Cu(9S3)]$^+$	11.23	–3.70	3.77	7.46	0.067	–9.15	–5.37
[d][Cu(9S2N)]$^+$	11.09	–3.60	3.75	7.35	0.068	–8.75	–5.30
[d][Cu(9N2S)]$^+$	10.80	–3.50	3.65	7.15	0.070	–8.39	–5.23
[d][Cu(9N3)]$^+$	10.56	–3.37	3.60	6.96	0.072	–8.01	–5.13
[d][Cu(9NMe3)]$^+$	10.15	–3.29	3.43	6.72	0.074	–7.85	–5.01
[Cu(MeCN)(9S3)]$^+$	10.49	–1.87	4.31	6.18	0.081	–8.80	–3.37
[Cu(CO)(9S3)]$^+$	11.94	–3.02	4.46	7.48	0.067	–10.21	–4.78
[Cu(CO)(9S2N)]$^+$	11.88	–2.77	4.55	7.33	0.068	–10.11	–4.63
[Cu(CO)(9N2S)]$^+$	11.76	–2.61	4.57	7.19	0.070	–9.92	–4.54
[Cu(CO)(9N3)]$^+$	11.72	–2.34	4.68	7.03	0.071	–9.81	–4.38
[Cu(CO)(9NMe3)]$^+$	11.25	–2.31	4.47	6.78	0.074	–9.54	–4.36

*From reference 40.
a Fragment obtained from [Cu(9S3)I] with the frozen optimized geometry obtained for PP, 6-31G** basis set.
b Fragment obtained from [Cu(9S3)Br].
c Fragment obtained from [Cu(MeCN)(9S3)]$^+$.
d Fragments obtained from [Cu(CO)(9X3)]$^+$ and [Cu(CO)(9X2,X')]$^+$.

Table 3.2.2. Fukui function values for the atoms in the $[CuA(9X2X')]^+$ (A = MeCN, CO) and [Cu(9X2X')Y] (Y = Br, I) compounds (right columns) and $[Cu(9X2X')]^+$ fragments (left columns) obtained by removal of the A ligand.

Compound	Atom	f^+	f^+	f^-	f^-
[Cu(9S3)I]	S_1	0.009	–0.026	0.139	–0.031
	S_2	0.009	–0.028	0.084	–0.002
	S_3	0.009	–0.044	0.139	0.048
	Cu	0.656	1.335	0.267	–1.855
	I		0.055		–0.076
[Cu(9S3)Br]	S_1	0.007	0.110	0.138	0.089
	S_2	0.007	0.191	0.083	0.085
	S_3	0.006	0.148	0.148	0.064
	Cu	0.629	0.075	0.241	0.137
	Br		0.094		0.290
$[Cu(MeCN)(9S3)]^+$	S_1	0.007	0.081	0.142	0.124
	S_2	0.007	0.067	0.144	0.126
	S_3	0.007	0.144	0.085	0.068
	Cu	0.630	0.186	0.243	0.201
	N		–0.003		–0.062
	C		0.091		0.096

Table 3.2.2. (cont.).

Compound	Atom	f^+	f^+	f^-	f^-
	S_1	0.014	0.024	0.106	0.086
	S_2	0.001	0.096	0.099	0.105
$[Cu(CO)(9S3)]^+$	S_3	0.013	0.078	0.160	0.171
	Cu	0.622	0.287	0.244	0.138
	C		0.099		0.045
	O		0.103		0.093
	S_1	0.019	0.049	0.131	0.150
	S_2	0.017	0.080	0.158	0.151
$[Cu(CO)(9S2N)]^+$	N_1	–0.044	–0.034	–0.032	–0.024
	Cu	0.654	0.366	0.297	0.170
	C		0.103		0.050
	O		0.110		0.097
	S_1	0.027	0.085	0.150	0.190
	N_1	–0.042	–0.048	–0.018	–0.007
$[Cu(CO)(9N2S)]^+$	N_2	–0.049	–0.024	–0.034	–0.025
	Cu	0.695	0.413	0.369	0.211
	C		0.108		0.058
	O		0.114		0.106
	N_1	–0.042	–0.043	–0.023	–0.003
	N_2	–0.041	–0.043	–0.011	0.017
$[Cu(CO)(9N3)]^+$	N_3	–0.047	–0.031	–0.034	–0.024
	Cu	0.718	0.517	0.435	0.262
	C		0.112		0.068
	O		0.122		0.118
	N_1	–0.031	–0.026	–0.030	–0.016
	N_2	–0.032	–0.027	–0.029	–0.009
$[Cu(CO)(9NMe3)]^+$	N_3	–0.030	–0.034	–0.011	0.020
	Cu	0.695	0.461	0.376	0.210
	C		0.132		0.058
	O		0.131		0.105

The pseudopotential calculations provide anomalous Mulliken charge values for the atoms in the [Cu(9S3)I] compound and hence parameters calculated seem highly unreliable. For that reason, only the geometry obtained will be discussed in the following section.

3.2.2. Geometry of [Cu(9S3)I] and calculated geometries of $[CuA(9S3)]^+$ (A = MeCN, CO) and [Cu(9S3)Y] (Y = I, Br)

Küpers *et al*. obtained the [Cu(9S3)I] species by reaction of a methanolic CuI suspension with the 9S3 ligand [37]. The white powder obtained was then was recrystallized from MeCN. The [Cu(9S3)I] compound proved to be extremely stable towards oxygen both in solution and in the solid state.

Geometry optimizations were performed for the [Cu(9S3)Y] (Y = Br, I) and other $[CuA(9S3)]^+$ species (A = MeCN, CO). The geometries obtained for the compounds modelled were compared to the structure obtained by means of X-ray diffraction [37, 41].

The numbering scheme for the [Cu(9S3)I] compound from its ORTEP diagram [41] is shown in figure 3.2.2. Selected bond lengths and angles are shown in table 3.2.3 and plots of $r_{calc} - r_{exp}$ *vs.* r_{exp} as well as $\theta_{calc} - \theta_{exp}$ *vs.* θ_{exp} are shown in figures 3.2.3 and 3.2.4.

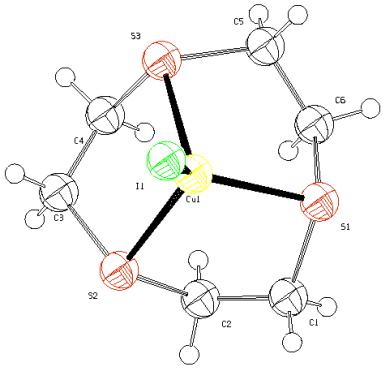

Figure 3.2.2. ORTEP drawing of [Cu(9S3)I] [37, 41]

Table 3.2.3. Selected bond lengths (Å) and angles (degrees) for [Cu(9S3)I] and calculated species $[CuA(9S3)]^+$ (A = CO, MeCN) and [Cu(9S3)Y] (Y = Br, I).

Bond length/angle	Observed [Cu(9S3)I]	Calculated			
		[Cu(9S3)I]	†[Cu(9S3)Br]	†$[Cu(CO)(9S3)]^+$	†$[Cu(MeCN)(9S3)]^+$
Cu1-L*	2.4900	2.5301	2.3033	1.7999	1.8528
Cu1-S1	2.3309	2.5174	2.3505	2.3535	2.3506
Cu1-S2	2.3430	2.5174	2.3517	2.3269	2.3495
Cu1-S3	2.3292	2.5174	2.3530	2.3920	2.3504
L*-Cu1-S1	128.64	126.62	123.82	124.49	123.07
L*-Cu1-S2	121.34	126.62	123.99	124.11	122.86
L*-Cu1-S3	118.70	126.62	123.54	121.84	122.68
S1-Cu1-S2	92.64	88.07	91.97	93.00	93.34
S1-Cu1-S3	93.09	88.07	92.14	91.03	93.29
S2-Cu1-S3	93.94	88.07	92.11	93.38	93.37

* L = I, Br in the neutral species and C and N respectively in the cationic species with CO and MeCN.
† Orientation of the [Cu(9S3)Y] or the $[CuA(9S3)]^+$ moiety was the one that yielded the best R values for θ_{calc} *vs.* θ_{exp} linear regression analyses (see text).
R values for r_{calc} *vs.* r_{exp} and θ_{calc} *vs.* θ_{exp} respectively were 0.99324, 0.94874 (Y = I); 0.9942, 0.95304 (Y = Br); 0.99808, 0.97194 (A = CO); 0.99937, 0.9608 (A = MeCN). Cu-L (L = Br, CO, MeCN) bond distance values not included in linear regression analyses.

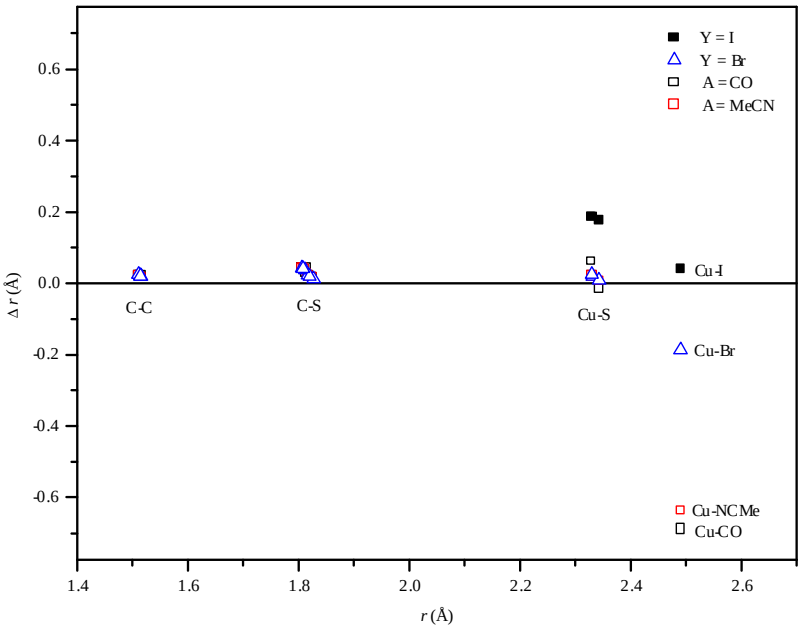

Figure 3.2.3. Comparison between calculated and observed bond lengths for [CuA(9S3)] (A = CO, MeCN) and [Cu(9S3)Y] (Y = Br, I) compounds; $\Delta r = r_{calc} - r_{exp}$.

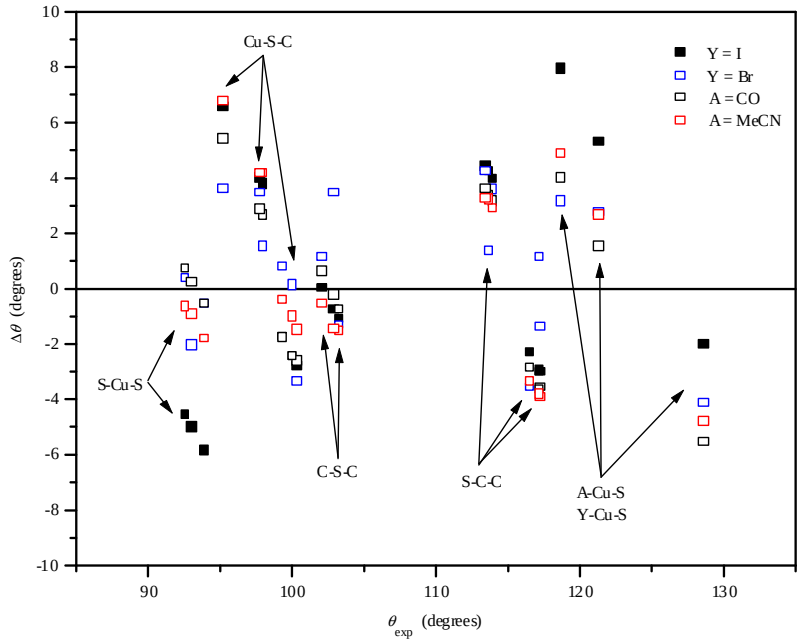

Figure 3.2.4. Comparison between calculated and observed bond angles for [CuA(9S3)] (A = CO, MeCN) and [Cu(9S3)Y] (Y = Br, I) compounds; $\Delta\theta = \theta_{calc} - \theta_{exp}$.

The pseudopotential calculations performed for the [Cu(9S3)I] compound yield the poorest fit to the experimental values, with R values of 0.99324 and 0.94874 respectively for the r_{calc} *vs.* r_{exp} and θ_{calc} *vs.* θ_{exp} linear regression analyses. This calculation also provides a molecule with C_3 symmetry and consequently all bond angles and bond lengths to similar atoms that fall within a C_3 symmetry operation are equal. This oversimplification in the calculation procedure does not occur in the calculations performed where there is no need for application of a pseudopotential. In the case of the $[CuA(9S3)]^+$ (A = CO, MeCN) and [Cu(9S3)Br] species, the symmetry for the complex cations is C_1 and a better match to experimental values is obtained. In comparing the optimized structures obtained in the calculations to the experimental values for [Cu(9S3)I] [41] three possible orientations of the calculated molecules are possible. Regression analyses performed on each of the orientations show that bond angles appear to be a better measure of the model than bond lengths, which vary only slightly. The chosen orientation of the calculated molecule was that for which the best values of the correlation coefficient were obtained for the θ_{calc} *vs.* θ_{exp} regression analyses.

Fairly good matches are obtained for all experimental bond lengths and angles and calculated values, especially for the cationic moieties. The calculations consistently provide values of bond lengths and angles which are slightly greater than those observed, with negative Δr values for the Cu-A, Cu-Y bond (A = CO, MeCN; Y = Br) as would be expected in terms of the difference in the radii of the coordinated atoms with that of the I atom with which the value is compared (the Cu-A bond distances were not considered in the bond length regression analyses).

Table 3.2.4 shows average bond distances and angles for Cu(I) compounds with chelating 9S3. It can be seen that despite the different coordination environment in these compounds, the bond

Table 3.2.4. Average bond distances (Å) and angles (degrees) for Cu(I) compounds containing the 9S3 ligand. Cu-L is the distance to the coordinated donor atom in ligand L in [CuL(9S3)].

Compound	‡Cu-S	Cu-L	‡S-Cu-S	‡S-Cu-L
[Cu(9S3)I]	2.33	2.49	93.22	122.89
$[Cu(AsPh_3)(9S3)]$ [38]	2.30	2.32	94.48	122.03
$[Cu(9S3)(9S2S{=}O)]PF_6$ [23]*	2.30	2.21	93.65	122.54
$[Cu(9S3)_2]PF_6$ [22]†	2.32, 2.31	2.22, 2.25	93.43, 94.03	122.53, 122.37
$\{Cu_2(9S3)_2[(S_2(CH_2)_4]\}(PF_6)_2$ [23]*	2.32	2.22	94.28	122.10
$[Cu_2(9S3)_3](BF_4)_2{\cdot}H_2O$ [39]	2.320	2.24	94.21	122.11

‡ Average values.
* Distances and angles from CSD.dat file for each structure.
† Unit cell contains two different molecular units

distances and angles vary only slightly, and hence the comparison with the modelled systems seems justified.

3.2.3.Interaction energies for species $[Cu(9X2X')]^+$ reacting with a ligand B.

To understand the reactivity of these systems, the $[Cu(9X2X')]^+$ fragments can be assumed to react with another B ligand in a first approximation. The fragments obtained by removal of the A ligand in the $[CuA(9X2X')]^+$ (X = X' = S, N, NMe and X = S, X' = N or X = N, X' = S) species can hypothetically be considered to react according to the following equation

$$[Cu(9X2X')]^+ + B \rightarrow [CuB(9X2X')]^+.$$

The interaction energy using the local softness approach, between two species A = $[Cu(9X2X']^+$ and B can be approximated by equation (62), described in chapter 1, section 1.4.,

$$\left(\Delta E_{\text{int}}\right)_{Ak} \approx -\frac{1}{2}\frac{\left(\mu_A - \mu_B\right)^2}{S_A f_{Ak} + S_B} S_B S_A f_{Ak} - \frac{1}{2}\frac{\lambda}{S_A f_{Ak} + S_B} \qquad (1)$$

where μ_A and μ_B are the electronic chemical potentials ($\mu_A = -\chi_A$ and $\mu_B = -\chi_B$) of species $[Cu(9X2X')]^+$ and B; S_A and S_B are the global softness values, and f_{Ak} is the condensed Fukui function for the kth atom in the A species, namely the copper atom in the $[Cu(9X2X')]^+$ fragment. The value used for the condensed Fukui function is the f^+_{Cu} for nucleophilic attack, as in both cases the Cu atom reacts with the nucleophiles CO and MeCN [42]. The first term in equation 1 corresponds to a charge transfer process at constant external potential ι(r) (yielding ΔE_ι), whereas the second term corresponds to a reshuffling of charge distribution which takes place at constant chemical potential μ (yielding ΔE_μ) and is strongly related to the hardness principle. The value of the constant λ has been obtained as described by Chandrakumar and Pal using the reacting atom approximation [43] *i.e.*, $\lambda \approx N_{Cu}[Cu(CO)(9X2X')]^+ - N_{Cu}[Cu(9X2X')]^+$, where N_{Cu} is the number of electrons on the Cu atom obtained as described in section 3.2.4. Values for λ and $(\Delta E_{\text{int}})_{Cu}$ for all of the $[Cu(9X2X')]^+$ species modelled are shown in table 3.2.5. As can be seen, ΔE_{int} values between the different fragments and CO species are larger (more negative) as the number of S atoms in the macrocycle increases. For the N systems, the interaction seems to be favoured with better σ-donor atoms. The ΔE_ι values obtained show that the charge transfer process is favoured the more N enriched the macrocycles, as would be

expected from the chemical potential values obtained for the fragments, the observed trend being established by $\Delta\mu$. However, the charge redistribution term follows the inverse trend, with major stabilization being attained the more S atoms on the macrocyles.

Table 3.2.5. Interaction energies for $[Cu(9X2X')]^+$ fragments and CO and MeCN. All values in kcal/mol except λ in a.u.

Compound	λ	ΔE_v	ΔE_μ	$(\Delta E_{int})_{Cu}$
$[Cu(CO)(9S3)]^+$	0.284	–1.74	–31.20	–32.94
$[Cu(CO)(9S2N)]^+$	0.239	–1.66	–25.57	–27.23
$[Cu(CO)(9N2S)]^+$	0.183	–1.90	–18.85	–20.75
$[Cu(CO)(9N3)]^+$	0.140	–2.45	–14.04	–16.49
$[Cu(CO)(9NMe3)]^+$	0.150	–2.56	–15.08	–17.64
$[Cu(MeCN)(9S3)]^+$	0.121	–0.23	–12.81	–13.04

As can be seen from table 3.2.5, the values of λ for the interaction between $[Cu(9S3)]^+$ and MeCN and CO are quite different, which warns against the use of interaction energies at a qualitative level (*i.e.*, using a constant λ value [44]) in these reactions.

There seems to be no reason for the compounds [Cu(CO)(9S2N)]Y and [Cu(CO)(9N2S)]Y (Y = PF_6, BF_4 or BPh_4) not to be prepared successfully, as their interaction energies fall bewteen those obtained for the 9S3 and 9N3 ligands. Reaction conditions utilized in the preparation of [Cu(CO)(9S3)]Y, (Y = PF_6, BF_4) should suffice.

3.2.4. σ-bonding and π-backbonding in $[Cu(CO)(9X2X')]^+$ compounds

The [Cu(CO)(9X3)] (X = S, N and NMe) cationic moieties show νCO frequency values that vary significantly: 2123 cm^{-1} for 9S3 [14] and 2030 and 2020 cm^{-1} respectively for 9N3 and 9NMe3 [15]. Experimental and calculated values are shown in table 3.2.6 and optimized structures are shown in figure 3.2.5. Unfortunately, the carbonyl complexes with the mixed ligands 9S2N and 9N2S have not been prepared and a comparison with the calculated values cannot be done. Hirsch *et al.* [14] assigned a small intensity band at 334 cm^{-1} in the Raman spectrum of [Cu(CO)(9S3)]PF6 to the νCu-CO frequency due to its lower energy shift upon substitution with ^{13}CO. νCu-CO frequencies have not been assigned for the triaza compounds so it remains to be seen if the calculations performed accurately represent the systems in the solid state. The CO stretching frequencies decrease the more N atoms in the ligand, *i.e.*, in the order 9S3 > 9S2N > 9N2S > 9N3, hence Cu-CO backbonding is expected to increase in the same order. For the triaza ligands, the CO stretch depends on the donor properties of the coordinated amine: the better σ-

Table 3.2.6. Observed and calculated νCO and νCu-CO stretching frequencies (cm^{-1}) in $[Cu(CO)(9X2,X')]^+$ compounds.

Compound	νCO_{exp}	νCO_{calc} †	νCO_{calc} ‡	νCu-CO_{exp}	νCu-CO_{calc} †
[a][Cu(CO)(9S3)]$^+$	2123	2205	2122	334[c]	457
[Cu(CO)(9S2N)]$^+$	—	2196	2090	—	472
[Cu(CO)(9N2S)]$^+$	—	2188	2061	—	484, 506
[b][Cu(CO)(9N3)]$^+$	2030	2182	2040	—	485, 519
[b][Cu(CO)(9NMe3)]$^+$	2020	2174	2011	—	492, 508

† Calculated values are for the [Cu(CO)(9X2X')] cationic species.
‡ Rescaled values from regression analysis for νCO_{exp} and νCO_{calc} (R = 0.98674)
a Experimental value for $[Cu(CO)(9S3)]PF_6$ compound [14].
b Experimental value for $[Cu(CO)(9N3)]BPh_4$ and $[Cu(CO)(9NMe3)]BPh_4$ [15].
c Raman intensity [14] observed at 334 cm^{-1} for compound with CO and lower energy shift in ^{13}CO isotopomer.

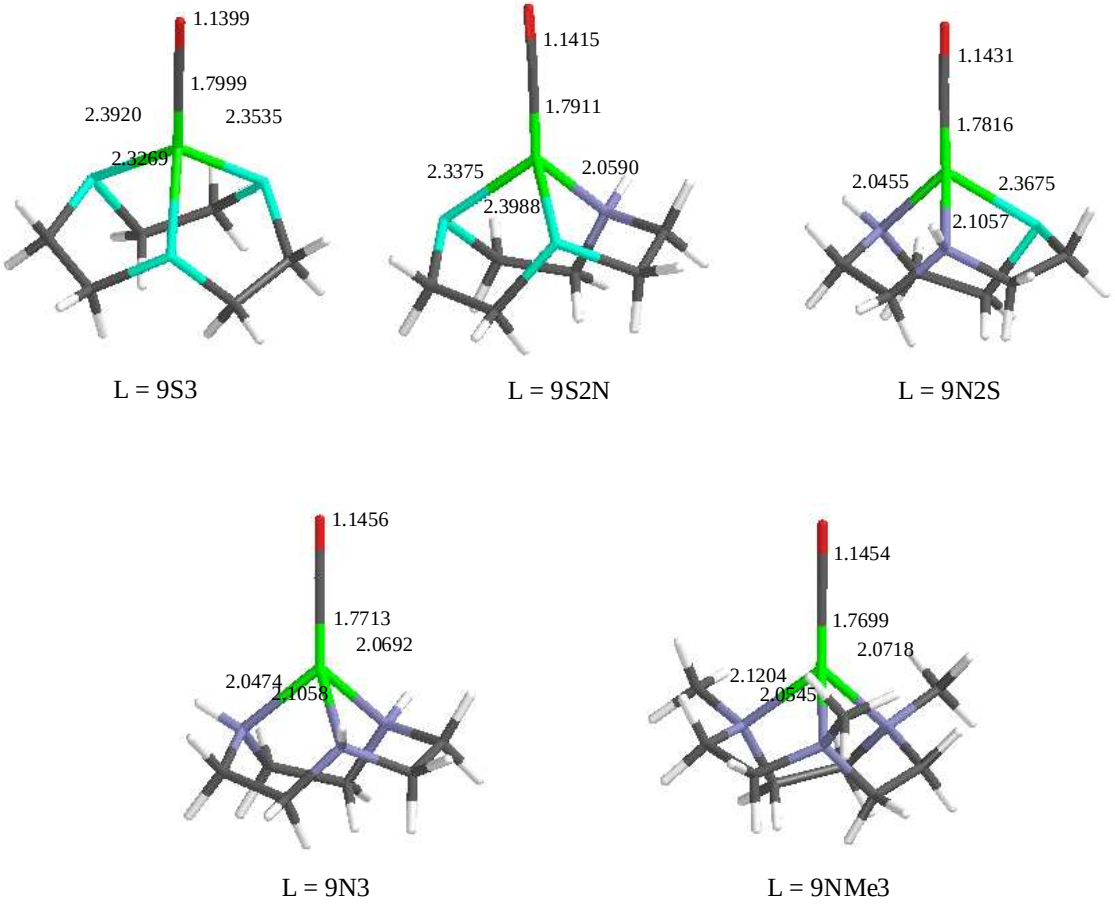

L = 9S3 L = 9S2N L = 9N2S

L = 9N3 L = 9NMe3

Figure 3.2.5. Optimized geometries for the $[Cu(CO)L]^+$ compounds modelled showing Cu-L and CO distances. All bond distances in Å.

donor 9NMe3 produces a shift to lower energy of the CO stretch which is consistent with more backbonding from the Cu ion to the CO ligand. This trend has been observed in this work (section 3.3.4.) for the triamine compounds $[Cu(CO)(n,m\text{N3})]^+$ where the lower CO stretching frequencies are obtained for the more basic amines coordinated to Cu(I).

The CO frequencies for the cyclic triamines have low values of 2030–2020 cm^{-1} when compared to the compounds obtained with the linear triamine systems which fall in the range 2080–2060 cm^{-1}. Compounds with the triamine ligands $H_2N(CH_2)_nNH(CH_2)_mNH_2$, where n = 2, 3 and m = 2, 3, 4 (n,mN3) [45] show values of CO frequencies that fall within the range mentioned, the highest value observed for the less basic 2,2N3 triamine [45]. Basicity of the triaza macrocycles is greater than that of the linear triamines studied and the enhanced σ-donor ability may account for the lower CO stretching frequencies.

As a first approximation [40, 46, 47] to elucidate the bonding in these systems, the number of electrons transferred from the metal to the CO ligand can be calculated as

$$\frac{\Delta N}{n} = \frac{\chi_{CO} - \chi_M}{2(\eta_{CO} + n\eta_M)}$$

where n is the number of CO ligands bound to the metal center, η describes global hardness and χ describes electronegativity. This equation has been shown to correlate well with the mean bond energy (D_e) in metal carbonyls [46]. It is important to point out that this is only an approximation that considers the hardness of the species involved as a constant. It must be mentioned as well, that the chemical potential ($\mu = -\chi$) is a function of external fields, and hence will vary with the distance. Despite these shortcomings, the equation can be used and has been used to explain the binding of CO to metal centres. Interestingly, the use of this equation relies on the fact that electron transfer will occur from the species with a small electronegativity value to the species with a larger value. For all of the species calculated, the metal-9X2X' fragments have a smaller χ value than the CO ligand, hence ΔN measures the number of electrons transferred from Cu to the CO ligand acting a π–acid acceptor.

Alternatively, the ΔN equation can be expressed in terms of the local parameters for the interacting Cu(I) species with the CO ligand yielding

$$\Delta N' = \frac{\chi_{CO} - \chi_{Cu}}{S_{CO} + s_{Cu}^{+}} S_{CO} s_{Cu}^{+}$$

where S_{CO} is the global softness for CO and $s_{Cu}^{+} = S_{Cu} f_{Cu}^{+}$ is the condensed local softness for the Cu(I) atom in the $[Cu(9X2X')]^{+}$ fragment. The $\Delta N'$ values obtained by means of this equation are smaller than the ΔN values obtained by use of the global properties but follow the same trend. However, an excellent correlation is observed between $\Delta N'$ and νCO and by means of the regression analysis for νCO *vs*. $\Delta N'$ the νCO frequencies have been calculated for the species that have not yet been prepared. It must be pointed out that the difference in electronegativities is indicative of the extent of an electron transfer from the Cu atom to the CO ligand while the local softness value calculated for the Cu atom makes use of the condensed Fukui function for nucleophilic attack which may seem a contradiction, as electrons will flow from Cu to CO according to the electronegativity equalization principle. The results obtained would indicate that the π-interaction measured is weighted by the σ-interaction for these systems, which corresponds to the local softness used for the Cu atom in its interaction with CO as a base. It is well known that π-bonding and σ-bonding have an inverse relation, so it seems justified to use this equation to calculate the number of electrons transferred in the πCu→CO interaction.

The values obtained by use of both equations, together with other values obtained from the Mulliken population analysis for these compounds, are shown in table 3.2.7. Figure 3.2.6 shows a graph of νCO *vs*. $\Delta N'$.

Table 3.2.7. ΔN, $\Delta N'$, N_{CO}, N_{Cu} and N_{Di} values for $[Cu(CO)(9X2X')]^{+}$ compounds. νCO_{exp} and νCO_{calc} values in cm^{-1}. νCO_{calc} values obtained from linear regression analysis of νCO_{exp} *vs*. $\Delta N'$.

Compound	ΔN	$\Delta N'$	N_{CO}	N_{Cu}	N_{Di}.	νCO_{exp}	νCO_{calc}
$[Cu(CO)(9S3)]^{+}$	0.076	0.059	0.142	0.284	–0.153	2123	2123
$[Cu(CO)(9S2N)]^{+}$	0.077	0.061	0.121	0.239	–0.104	—	2109
$[Cu(CO)(9N2S)]^{+}$	0.081	0.067	0.100	0.183	–0.052	—	2080
$[Cu(CO)(9N3)]^{+}$	0.084	0.078	0.083	0.140	–0.010	2030	2031
$[Cu(CO)(9NMe3)]^{+}$	0.091	0.080	0.079	0.150	0.000	2020	2019

From the ΔN values obtained, π–back-bonding is greater for the triaza compound than for the trithia compound and, within the triaza compounds, the N–methyl derivative shows more M→

CO electron transfer which is consistent with the experimental values obtained and what would be expected in terms of increasing σ-donor strength. It is generally agreed that π-backbonding debilitates the CO bond and reduces the value of the force constant F_{CO} for the CO bond [46]. There is also an inverse relation between σ–bonding and π–backbonding, and σ–bonding would hence be more important in the trithia compounds than in the triaza derivatives. In terms of σ–bonding it is the CO ligand that acts as a base and the metal centre that would act as an acid. Unfortunately, values of νCu–CO have not been reported for the compounds prepared except for the trithia derivative, and no conclusions can be drawn through experimental evidence. Calculated νCu-CO frequencies support the idea that the Cu-CO bond strength increases in the inverse order to the νCO stretching frequency.

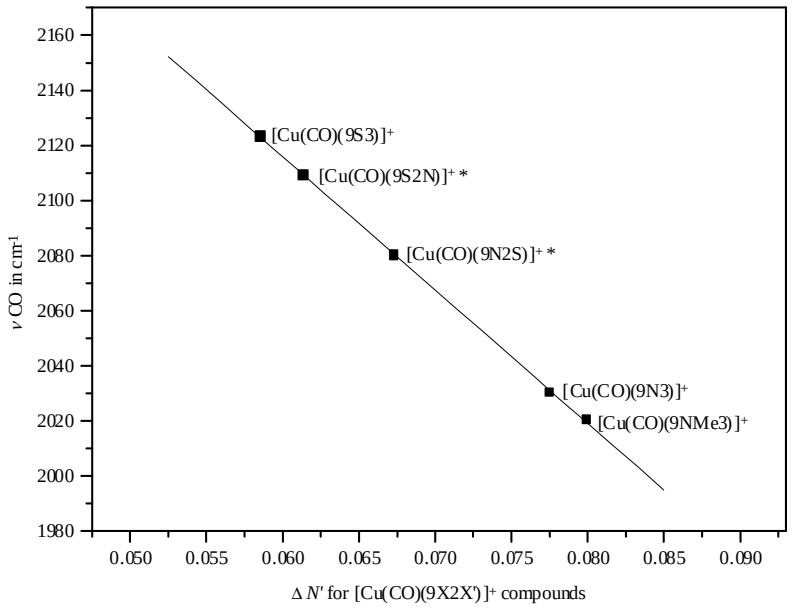

Figure 3.2.6. Graph of νCO *vs.* $\Delta N'$. Values with * were obtained by regression analysis of νCO_{exp} *vs.* $\Delta N'$ (R = -0.9999).

Mulliken population analyses for AO occupancy were used in order to determine the total number of electrons transferred from the CO ligand, N_{CO}, after binding to the $[Cu(9X2X')]^+$ species. In all cases $N_{CO} = 14 - (N_C + N_O)$, where $N_C + N_O$ is the sum of the orbital occupations for C and O in the $[Cu(CO)(9X2X')]^+$ species, yields a positive number. On the basis of the possibility of both σ and π–bonding in these systems, this value can only be taken as one that basically represents the overall number of electrons transferred from CO to the Cu(I) atom via σ–bonding. However, M

$\rightarrow$ CO π–backbonding in these systems would increase the number of electrons in the coordinated CO ligand decreasing the difference $N_{CO} = 14 - (N_C + N_O)$. σ–bonding would hence play a significant role in the trithia compound that would have very little contribution from π–backbonding, whereas the inverse effect is expected the more N enriched the macrocyle and the more basic the N atoms on the macrocycle. This indeed seems to be the case, for the lowest νCO frequency occurs for the NMe derivative while the highest is obtained for the trithia derivative.

The νCO frequency occurs at 2143 cm^{-1} in the free ligand. In the linear molecule Cl-Cu-CO obtained by co-condensation of CuCl and CO in an argon matrix [48], the νCO stretching frequency was observed at 2157 cm^{-1} and the bands at 362 cm^{-1} and 356 cm^{-1} were assigned to the highly coupled ν^{35}Cl-Cu-CO and ν^{37}Cl-Cu-CO stretching frequencies. Isotopic labelling with ^{13}CO and C^{18}O and ab initio calculations further confirmed these assignments. The authors described the Cu-C bond as mainly of the σ type with little Cu-C π-backbonding and determined by means of a Mulliken population analysis that the Cu$\leftarrow$CO transfer of electrons in the σ space was about 0.4 while Cu$\rightarrow$CO π–backbonding amounted only to about 0.2 electrons. In the polymeric tetrahedrally coordinated [Cu(CO)Cl] compound [49] the νCO frequency occurs at 2127 cm^{-1} and, although the νCu-CO frequency was not determined, it would be expected to occur at a lower value than that for Cl–Cu–CO due to the increase in coordination number for this compound. However, the fact that the νCO frequency obtained is lower, accounts for more Cu$\rightarrow$CO π–backbonding that would increase the relative Cu-CO bond strength. Although the νCO frequency is similar to the value obtained for the trithia species, the compounds are remarkably different in that the polymeric [Cu(CO)Cl] quickly undergoes decarbonylation while [Cu(CO)(9S3)]PF_6 is a remarkably stable species in the solid state.

The values of N_{CO} obtained by means of the Mulliken population analyses (λ values employed in section 3.2.3.) are consistent with the aforementioned values obtained for the linear Cl-Cu-CO species in that σ–bonding must be significantly smaller for the macrocyclic compounds on the basis of their νCO frequencies. ΔN values for the Cu$\rightarrow$CO interaction and N_{CO} values for the Cu$\leftarrow$CO interaction follow the expected trend.

From the calculated frequencies, it is apparent that the Cu-CO bond becomes stronger the more N enriched the macrocycle and the more basic the N donor atom in the macrocycle. The νCu-CO

frequencies appear at higher values in some of the triamine systems studied in this work as will be discussed later.

Analysis of the electronic AO occupancy for the Cu(I) atom and the donor atoms in these systems yields interesting results. The number of electrons on the Cu atom due to its interaction with CO was calculated as $N_{Cu} = N_{Cu}[Cu(CO)(9X2X')]^+ - N_{Cu}[Cu(9X2X')]^+$ and the number of electrons on the donor atoms that are transferred due to the interaction of the $[Cu(9X2X')]^+$ system with CO was calculated as $N_{Di} = \Sigma(N_{Di}[Cu(9X2X')]^+ - N_{Di}[Cu(CO)(9X2X')]^+)$. The values obtained are shown in table 3.2.7. From these values it can be seen that the number of electrons on the Cu atom increases in the following order 9N3 < 9NMe3 < 9N2S < 9S2N < 9S3, hence lowering the positive charge of the Cu(I) atom in the carbonyl compound in the same order. N_{Di} values decrease (become more negative) in the order 9NMe3 > 9N3 > 9N2S > 9S2N > 9S3, and account for strong S←Cu interactions in the carbonyl derivatives and a better reshuffling of charge on the S enriched compounds due to interaction with CO, as would be expected in terms of the possibility of orbital interaction between the Cu ion and the S atom. It is interesting to note that the number of electrons on the N atoms from the NMe derivative, is negligible ($N_{Di} = -0.00047$). Although it seems to be an apparent contradiction for the ability of a better σ–donor to enrich the electron density on the Cu(I) atom, the inductive effect of the methyl groups has to be taken into account. It is expected that the number of electrons on the C atoms from the methyl groups decreases from the $[Cu(9NMe3)]^+$ species to the $[Cu(CO)(9NMe3)]^+$ species, hence increasing the number of electrons on the N atom, which are then transferred to the Cu(I) atom, as would seem apparent from the fact that N_{Cu} is larger for the 9NMe3 compound than for the 9N3 compound.

3.2.5. The HSAB approach

A low value for the ionization potential *I* is usually associated to a large polarizability (*i.e.*, a softer species) whereas a high value of *I* to a low polarizability (a harder species) [50, 51]. It follows from the calculations performed and the theoretical parameters obtained, that within the 9S3 species the softest one would be the neutral molecule with the coordinated bromide ion. It is this one that has the lowest value of hardness obtained for all other species. Within the cationic derivatives with the 9S3 ligand the MeCN species is softer than the CO species. The values obtained for *I* of these species are consistent with the hardness parameters obtained. The fact that interaction of MeCN with the $[Cu(9S3)]^+$ is favoured, is in agreement with Jørgensen's symbiotic principle [51] as MeCN is a slightly softer species than CO.

In the cationic species with the CO ligand, $[Cu(CO)(9X2X')]^+$ (X = X'= S, N, NMe; X = S, X' = N and X = N, X' = S), *I* and η values obtained decrease as the number of N donor atoms in the macrocyclic ligand increase, the lowest value being for the 9NMe3 derivative. This trend is maintained in the fragments obtained by removal of the CO ligand. The hardest species would hence be $[Cu(CO)(9S3)]^+$. Pearson's maximum hardness principle [52-54] states "there seems to be a rule of nature that molecules arrange themselves so as to be as hard as possible" [54]. It can be seen from the hardness values in table 3.2.1, that interaction with CO for all the fragments studied (except the 9S3 fragment) increases the hardness of the resulting carbonyl species.

Mulliken has stated that covalent bonding will be strong if the electron affinity *A* of the electron acceptor is large and the *I* of the electron donor is low [50, 55-57]. In this regard, the Cu(I) atom in the different fragments would form more covalent bonds the more similar the electronegativities of the species involved. Although the χ values are by no means similar, the one that is closest to the CO value is the χ value for the 9S3 fragment. It is this fragment as well that has the largest value for electron affinity, *i.e.*, for $|A|$. However, the $\Delta\chi$ values are sufficiently large to consider that ionic bonding or ion-dipole bonding play a significant role, especially for the species that have a larger $\Delta\chi$ value.

In view of the results obtained, it is likely that the presence of soft sulfur atoms in the macrocycle ligands reduces the charge on the Cu(I) by an increased donation of electron density from the CO ligand to the metal centre and an efficient reshuffling of charge in the system. This in turn has an effect on the charge on the metal centre. This effect decreases with increasing number of N donor atoms in the ligand and better σ–donor atoms on the macrocyclic ligands. From the ΔN values obtained, the Cu(I) species would all act as electron donors by means of π–backbonding to the CO ligand (in addition to the σ–bond interactions). Backbonding is thus enhanced by the presence of N atoms on the macrocyclic ligand [50].

At a local level, the Fukui function has been associated with reactivity at a certain site in a molecule [44, 58, 59]. Figures 3.2.7 and 3.2.8 show f^+ and local softness, s^+, values for the Cu(I) atoms in the fragments and compounds modelled. Large values of the Fukui function favour reactivity at a site when a reagent R approaches a substrate S. In this regard, the largest values for the Fukui function for nucleophilic attack, f^+, occur both in the fragment and the CO cationic

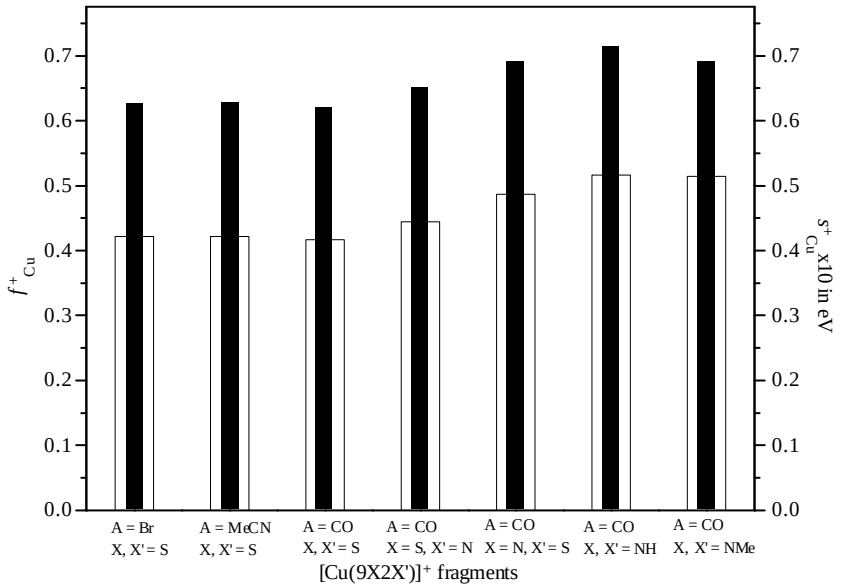

Figure 3.2.7. f^+ (solid bars) and s^+ (hollow bars) for the Cu atom in the [Cu(9X2X')] fragments obtained by removal of the ligand A in species [CuA(9S3)].

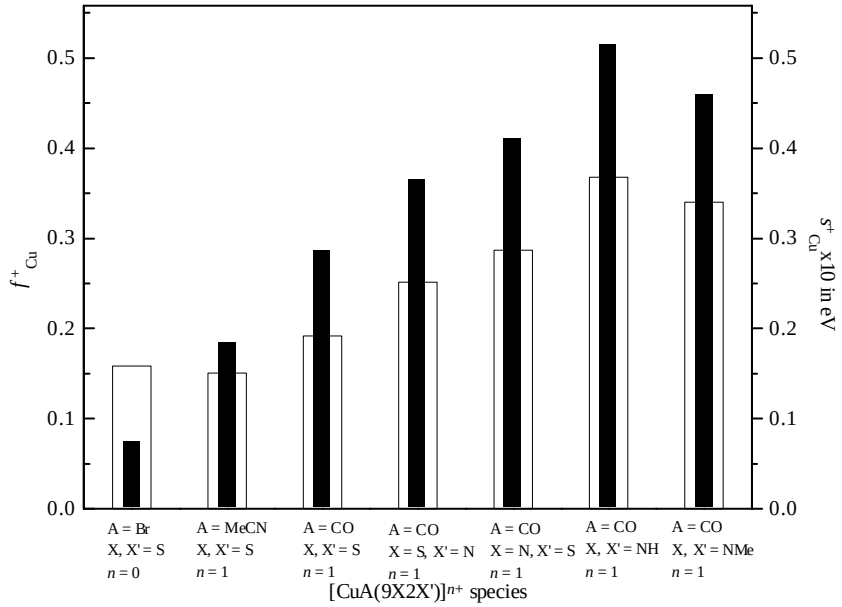

Figure 3.2.8. f^+ (solid bars) and s^+ (hollow bars) for the Cu atom in $[CuA(9X2X')]^{n+}$

species for the Cu(I) atom. In the species modelled with the 9S3 ligand, reactivity towards nucleophiles would increase in the order $Br^- < MeCN < CO$; the greatest reactivity being for the CO species. The reactivity for the iodide species would be expected to be lower than that of the

bromide species, which in turn explains the apparent stability of the [Cu(9S3)I] compound. Of the cationic CO complex species, it is interesting to observe that the lowest value obtained for f^{+}_{Cu} is for the 9S3 ligand while the greatest value obtained is for the 9N3 ligand. In this respect, the Cu(I) ion in the latter compound is the most reactive one towards other nucleophiles, which is consistent as well with the interaction energy values obtained for the compounds modelled, while the less reactive site in nucleophilic attack would be the Cu(I) atom coordinated to the 9S3 ligand. The same trend is observed in the $[Cu(9X2X')]^{+}$ fragments and the $[Cu(CO)(9X2X')]^{+}$ species, where f^{+} increases with an increasing number of N atoms.

3.2.6. The effect of the counter-ion

The calculation of the parameters employed in this discussion cannot be performed on the anions mentioned (BF_4^-, PF_6^- and BPh_4^-) due to the fact that their second electron affinities yield values that are greater (less negative) than the first electron affinities. Still, on a qualitative level, it may be expected that the tetraphenylborate anion is a softer species than the tetrafluoroborate and hexafluorophosphate anions. It must be noted that comparisons between experimental values obtained for the species $[Cu(CO)(9S3)]^{+}$, $[Cu(CO)(9N3)]^{+}$ and $[Cu(CO)(9NMe3)]^{+}$ do not take into account the effect of the counter-ion employed. In the triamine compounds $[Cu(CO)(2,2N3)]BPh_4$ and $[Cu(CO)(2,2N3)]BF_4$ which will be discussed in the following section, νCO values occur at 2080 cm^{-1} for the former and 2078 cm^{-1} for the latter, so it seems such a comparison would be allowed.

In terms of HSAB, it seems likely that the Cu(I) macrocyles with N donor atoms will be better stabilized by soft counter-ions like BPh_4^- as the cationic moieties are softer than the complex cation with the trithia macrocycle, which in turn would bind preferably with harder anions like BF_4^- and PF_6^-. It would be interesting to see if the trithia compound can indeed be obtained as the tetraphenylborate species. From a search performed on the CSD for Cu(I) cationic species containing the 9S3 ligand, not one single crystal structure was found to contain the tetraphenylborate anion as counter-ion, but rather the tetrafluoroborate, hexafluorophosphate or perchlorate anions occur instead.

3.3. Cu(I) triamine carbonyl compounds

The vast majority of Cu(I) carbonyl complexes that have been characterized by means of X-ray diffraction studies are tetrahedrally coordinated to nitrogen donor atoms and the CO ligand [6, 8-

13, 15, 17, 45]. It has long been stated that the basicity of the N donor atom plays an important role on the stabilization of the Cu(I) species when bound to a π-acid ligand like CO and η^2-C_2H_4 [3, 15, 45]. However, there exist few systematic studies that attempt to relate the stabilities of the Cu(I) carbonyl species to the electronic properties of the ligands themselves [60].

As Cu(I) forms stable carbonyl complexes with triamine ligands, the cationic species $[Cu(CO)(n,m\text{N3})]^+$ were investigated spectroscopically in the solid state and by means of DFT calculations. The triamine ligands $H_2N\text{-}(CH_2)_n\text{-}NH\text{-}(CH_2)_m\text{-}NH_2$ where n = 2, m = 2, 3 and n =3, m = 3, 4 will be referred to as n,mN3 in the present discussion. The structure of the compounds prepared is shown in figure 3.3.1.

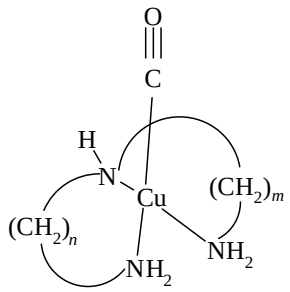

Figure 3.3.1. Structure for $[Cu(CO)(n,m\text{N3})]^+$ compounds, where n = 2, m = 2, 3 and n = 3, m = 3, 4.

3.3.1. Computational details

Calculations were carried out using Spartan02 DFT at the B3LYP level for the complex cations $[Cu(CO)(n,m\text{N3})]^+$ where n = 2, 3 and m = 2, 3, 4. The calculations were performed using the 6-31G** and 6-31 + G* basis sets in order to establish the performance of both. Geometry optimizations and vibrational analyses were performed for all the complex $[Cu(CO)(n,m\text{N3})]^+$ cations. In all cases studied, the vibrational analyses yielded all real frequency values. Vibrational assignments employed were those performed with the results obtained with the 6-31G** basis set, as a better match between experimental and observed frequencies was obtained. Parameters and HSAB descriptors were obtained for the $[Cu(CO)(n,m\text{N3})]^+$ species as well as for the $[Cu(n,m\text{N3})]^+$ fragments as was described in chapter 1, section 1.6.

3.3.2. Structure of the $[Cu(CO)(2,2N3)]^+$ species

In order to establish the reliability of the calculations performed by DFT on the complex triamine carbonyl cations, a comparison of calculated bond distances and angles with observed values was made for the compound where $n = m = 2$. The $[Cu(CO)(2,2N3)]BPh_4$ compound is the only one of the species studied for which the crystal structure has been determined by means of single crystal XRD studies [45].

Bond distances and angles in the calculated species are in good agreement with the observed values and standard deviation values of 0.00978 Å and 4.71° respectively, were obtained for the 6-31 G** basis set, and of 0.00934 Å and 3.90° for the 6-31 + G* basis set. These results considerably improve previous attempts in this work at modelling the triamine systems by means of molecular mechanics calculations using semi-empirical methods, where it was observed that ligand distances and angles were adequately estimated, but the Cu-L distances and angles varied significantly from the reported experimental values.

Graphs of calculated minus experimental bond distances, $\Delta r = r_{calc} - r_{exp}$, and angles, $\Delta\theta = \theta_{calc} - \theta_{exp}$, *vs*. the experimental values are shown in figures 3.3.2 and 3.3.3. It can be seen that both the H_2N-Cu-NH_2 and H_2N-Cu-NH angles are overestimated in the calculations. This trend was also observed in the Cu(I) carbonyl Schiff base complexes that will be discussed in section 3.4.

The structures obtained from the geometry optimization calculation performed for the different $[Cu(CO)(n,m\text{N3})]^+$ species are shown in figure 3.3.4. Selected calculated bond lengths and angles are shown in table 3.3.1.

3.3.3. Infrared spectra of $[Cu(CO)(2,2N3)]BPh_4$.

A full assignment of the bands occurring in the infrared spectra of $[Cu(CO)(2,2N3)]BPh_4$ and the labelled analogues $[Cu(^{13}CO)(2,2N3)]BPh_4$ and $[Cu(CO)(2,2N3\text{-}d_5)]BPh_4$, was carried out by means of the vibrational analyses performed with DFT calculations. The spectra for the $[Cu(CO)(2,2N3)]BPh_4$ and $[Cu(^{13}CO)(2,2N3)]BPh_4$ species are basically identical in the mid ir region, except for the shift obtained for the νCO stretching frequency. However, the spectrum of $[Cu(CO)(2,2N3\text{-}d_5)]BPh_4$ varies significantly as deuteration of the N atoms causes a shift in all of

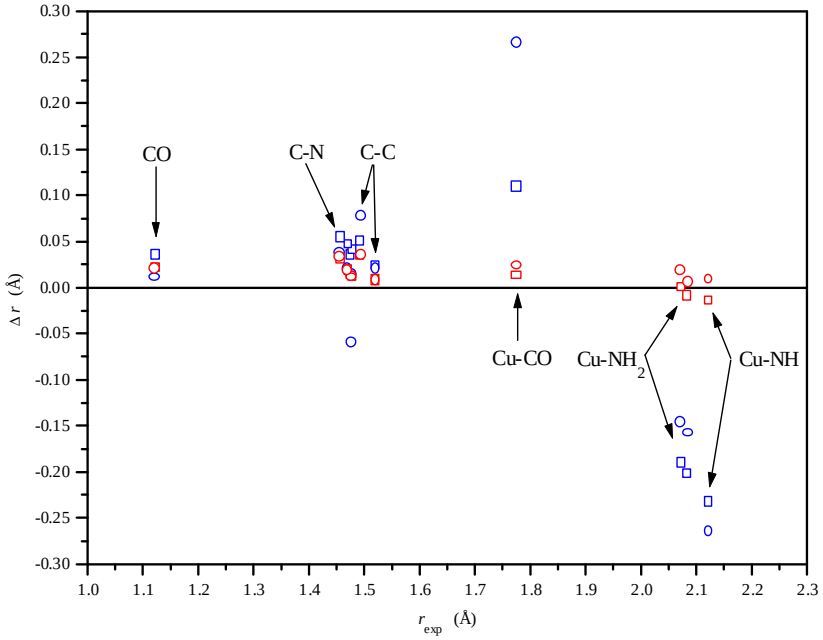

Figure 3.3.2. Comparison between calculated and observed bond lengths for [Cu(CO)(2,2N3)]BPh_4; $\Delta r = r_{calc} - r_{exp}$. Semi-empirical results are shown in blue and DFT results in red squares and red dots for the 6-31G** and 6-31 + G* basis sets, respectively. Standard deviation between experimental and calculated values for the DFT calculations are of 0.00978 Å (6-31G**) and 0.00934 Å (6-31 + G*).

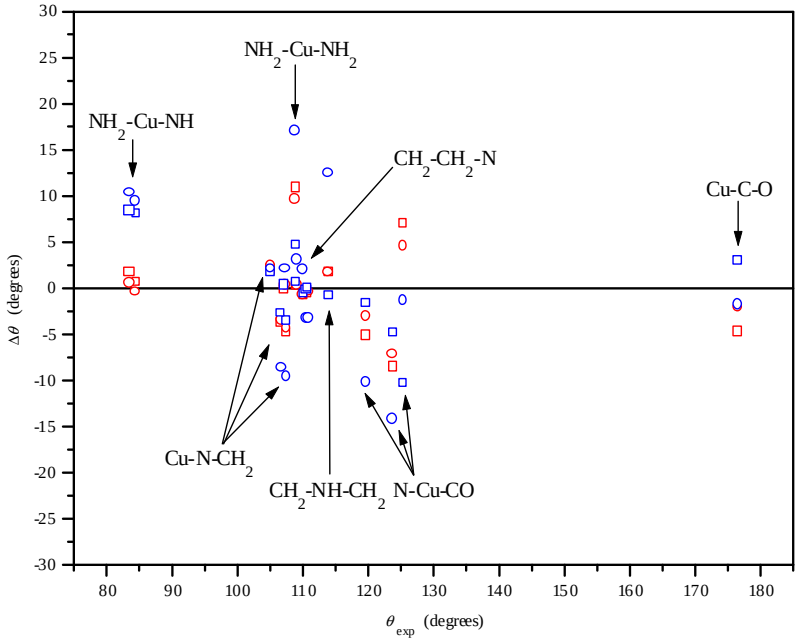

Figure 3.3.3. Comparison between calculated and observed bond angles for [Cu(CO)(2,2N3)]BPh_4; $\Delta\theta = \theta_{calc} - \theta_{exp}$. Semi-empirical results are shown in blue and DFT results in red squares and red dots for the 6-31G** and 6-31 + G* basis sets, respectively. Standard deviation between experimental and calculated values for the DFT calculations are of 4.71° (6-31G**) and 3.90° (6-31 + G*).

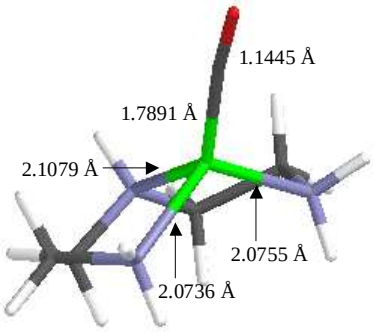

[Cu(CO)(2,2N3)]$^+$

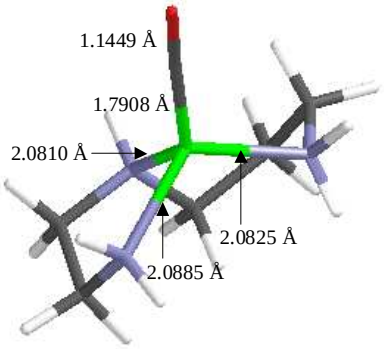

[Cu(CO)(2,3N3)]$^+$

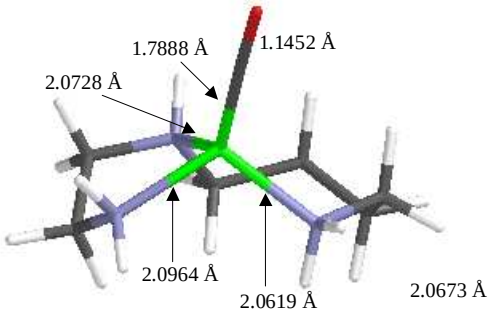

[Cu(CO)(2,4N3)]$^+$

2.1068 Å

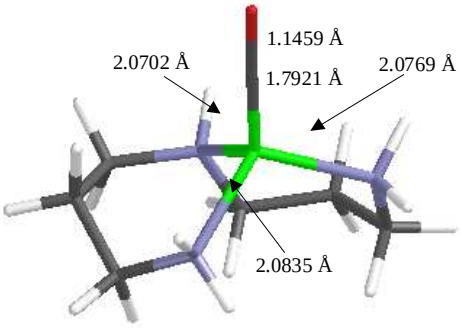

[Cu(CO)(3,3N3)]$^+$

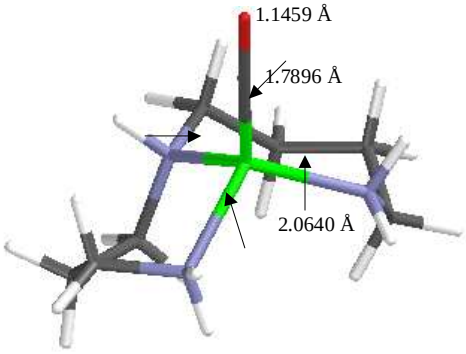

[Cu(CO)(3,4N3)]$^+$

Figure 3.3.4. Optimized structures obtained with the 6-31 G** basis set for the [Cu(CO)(*n*,*m*N3)]$^+$ species modelled showing the Cu-L and CO calculated bond distances.

the bands below the 1600 cm^{-1} region due to extensive coupling in the system as has been observed for other diamine, triamine and tetraamine systems [61-65]. Clearly, the extent of coupling experienced by these systems encumbers the assignment problem. A theoretical study including vibrational analyses for the prepared isotopomers, was carried out in order to arrive at a better understanding of their vibrational spectra.

The theoretical aspects relevant to the assignment problem will be discussed prior to the assignment of the experimental spectra.

Table 3.3.1. Selected bond lengths (Å) and angles (degrees) for [Cu(CO)(2,2N3)]BPh_4 [45] and calculated [Cu(CO)(*n*,*m*N3)]$^+$ complex cations.

Bond distance/angle	2,2N3 (exp)	2,2N3	2,3N3	2,4N3	3,3N3	3,4N3
Cu-CO	1.776(5)	1.7891	1.7908	1.7888	1.7921	1.7896
Cu-NH_2	2.073(4)	2.0736	2.0885	2.0964	2.0835	2.1068
	2.085(4)	2.0755	2.0825	2.0619	2.0769	2.0640
Cu-NH	2.123(3)	2.1079	2.0810	2.0728	2.0702	2.0673
C-O	1.123(6)	1.1445	1.1449	1.1452	1.1459	1.1459
Cu-C-O	176.57 (54)	171.83	172.46	177.13	175.80	177.15
H_2N-Cu-NH_2	108.90(15)	119.77	119.58	110.47	111.55	108.64
NH-Cu-CO	125.38(21)	132.40	130.79	122.87	122.93	118.12

3.3.3.1. Calculated frequencies

Vibrational analyses were performed on the cationic moieties $[CuAL]^+$, where A = CO, ^{13}CO, $C^{18}O$ and L = NH_2-CH_2-CH_2-NH-CH_2-CH_2-NH_2 (2,2N3 = 2,2N3-d_0), NH_2-CH_2-CH_2-ND-CH_2-CH_2-NH_2 (2,2N3-d_1), ND_2-CH_2-CH_2-NH-CH_2-CH_2-ND_2 (2,2N3-d_4), ND_2-CH_2-CH_2-ND-CH_2-CH_2-ND_2 (2,2N3-d_5), $^{15}NH_2$-CH_2-CH_2-^{15}NH-CH_2-CH_2-$^{15}NH_2$, NH_2-$^{13}CH_2$-$^{13}CH_2$-NH-$^{13}CH_2$-$^{13}CH_2$-NH_2, NH_2-CD_2-CH_2-NH-CH_2-CD_2-NH_2, NH_2-CH_2-CD_2-NH-CD_2-CH_2-NH_2, NH_2-CD_2-CD_2-NH-CD_2-CD_2-NH_2; and the Cu-65 isotopomer, $[^{65}Cu(CO)(2,2N3)]^+$. Vibrational analyses were performed for all of the aforementioned A and L ligands in the $[CuAL]^+$ compound by modifying only one isotopically labelled ligand at a time. For all isotopomers the optimized geometry obtained for the unlabelled $[Cu(CO)(2,2N3)]^+$ compound was employed.

The geometry-optimized compound obtained by DFT calculations has C_1 symmetry, and is consistent with the structure obtained by means of X-ray single crystal studies, as has been discussed previously. A total number of 63 normal modes of vibration was obtained for the $[Cu(CO)(2,2N3)]^+$ complex cation and all other isotopomers.

In their study of [Pd(2,2N3)X]X compounds (X = Cl, Br, I) and assuming a C_s symmetry for the square planar compound, Watt and Klett carried out ir assignments by means of the expected number of vibrations for each of the groups in the coordination compound [61]. They hence expected 12 vibrations arising from the NH_2 groups (6*A*' + 6*A*''), 3 from the N-H group (2*A*' + *A*''), 24 from the CH_2 groups (12*A*' + 12*A*''), and 12 vibrations from the N-C chain (6*A* + 6*A*''). A total number of 9 Pd-L vibrations were expected for the PdN_3X framework, including three νPd-N, one νPd-X and five bends, adding up to the total number of 60 expected normal modes.

By means of a similar analysis, the 63 vibrations expected for the $[Cu(CO)(2,2N3)]^+$ with a distorted tetrahedral geometry can be split into 12 vibrations arising from the NH_2 groups, 3 from the NH group, 24 from the CH_2 groups, 12 from the C-N skeleton, and 12 vibrations arising from the $[Cu(CO)N_3]$ unit which include the νCO vibration, one δCu-CO (*A*') and one πCu-CO (*A*").

Although this oversimplification in the assignment problem allows for an initial understanding of the systems studied, significant limitations are encountered due to the extent of coupling observed in such low symmetry systems. Assignments for all 63 calculated frequencies and the shifts obtained upon labelling for some of the isotopomers studied are shown in table 3.3.2. For NH_2, δNH_2 refers to diplacements in the plane constituted by the three NH_2 atoms (*e.g.*, scissoring mode) whereas πNH_2 refers to those out of plane (*e.g.*, twisting mode). However, for the N-H group, δN-H refers to displacements in the plane of the molecule (in which the Cu atom, CO ligand and both the N-H atoms lie), whereas πN-H refers to displacements out of this plane.

Comparison between the calculated normal modes in the $[Cu(CO)(2,2N3)]^+$ and $[Cu(CO)(2,2N3\text{-}d_5)]^+$ compounds, yields 5 vibrations with a $\Delta\nu > 930$ cm^{-1} (ν_1-ν_5), 2 with a $\Delta\nu \sim 430$ cm^{-1} (ν_{15}, ν_{16}, ν_{30}), 3 with a $\Delta\nu \sim 330$ cm^{-1} (ν_{31}, ν_{32}, ν_{33}), 1 with a $\Delta\nu \sim 260$ cm^{-1} (ν_{21}), 1 with a $\Delta\nu \sim 190$ cm^{-1} (ν_{46}), 3 with a $\Delta\nu \sim 105$ cm^{-1} (ν_{43}, ν_{44}, ν_{45}), 1 with a $\Delta\nu \sim 70$ cm^{-1} (ν_{40}) and others with smaller $\Delta\nu$ values. If only those vibrations with shifts greater than or equal to 105 cm^{-1} are taken into account, a total number of 15 vibrations sensitive to *d*-labelling of the N atoms is obtained, out of the 15 vibrations expected.

Table 3.3.2. Calculated shifts for the different $[Cu(CO)(2,2N3)]^+$ species modelled by means of DFT vibrational analyses. All frequencies in cm^{-1} and all $\Delta\nu$ values correspond to $\nu_{unlabelled} - \nu_{labelled}$ [a].

	unlabelled	^{13}CO	$C^{18}O$	^{15}N	$-d_1$	$-d_4$	$-d_5$	^{13}C	^{65}Cu	Assignment[b]
ν_1	3561.67	0	-0.25	**9.6**	-0.38	**938.83**	**938.52**	0.01	0	$\nu_a NH_2$
ν_2	3561.52	0	-0.29	**9.61**	-0.33	**938.75**	**938.51**	0.01	0	$\nu_a NH_2$
ν_3	3527.51	0	0.36	**7.89**	**947.44**	-0.01	**947.45**	0.02	0	νNH
ν_4	3488.31	0	0.12	**5.46**	0.11	**962.2**	**962.27**	0.01	0	$\nu_s NH_2$
ν_5	3487.89	0	0.02	**5.47**	-0.07	**960.94**	**961.91**	0.01	0	$\nu_s NH_2$
ν_6	3120.26	0	0.06	0.01	-0.59	-0.15	-0.75	**11.59**	0	$\nu_a CH_2$
ν_7	3118.36	0	0.08	0.01	-0.13	-0.18	-0.33	**11.71**	0	$\nu_a CH_2$
ν_8	3105.52	0	0.04	0.01	-0.22	-0.12	-0.35	**11.66**	0	$\nu_a CH_2$
ν_9	3103.13	0	-0.01	0	0	-0.09	-0.09	**11.68**	0	$\nu_a CH_2$
ν_{10}	3065.28	0	0.03	0	0	0	0.01	**6.4**	0	$\nu_s CH_2$
ν_{11}	3062.53	0	0.09	0	0.16	0	0.15	**6.56**	0	$\nu_s CH_2$
ν_{12}	3060.54	0	0.1	0	-0.03	-0.01	-0.04	**6.54**	0	$\nu_s CH_2$
ν_{13}	3056.84	0	-0.03	0	-0.01	-0.01	-0.02	**6.41**	0	$\nu_s CH_2$
ν_{14}	2176.15	**50.79**	**49.05**	0	-0.05	0.08	0.02	0.01	0.01	νCO
ν_{15}	1673.39	0	0.05	**3.76**	0.12	**439.86**	**439.98**	0.31	0	δNH_2
ν_{16}	1669.15	0	0	**3.76**	-0.03	**440.07**	**439.97**	0.31	0	δNH_2
ν_{17}	1520.84	0	-0.06	0.41	2.31	-0.38	1.98	4.08	0	δCH_2
ν_{18}	1518.62	0	-0.04	0.11	-0.02	-0.42	-0.4	4.1	0	δCH_2
ν_{19}	1514.81	0	0.08	0.18	0.17	-0.21	-0.1	4.26	0	δCH_2
ν_{20}	1500.28	0	0.04	0.11	1.76	-0.23	1.44	3.92	0	δCH_2
ν_{21}	1468.71	0	-0.08	**4.5**	**220.7**	0.65	**259.43**	3.35	0	πNH
ν_{22}	1442.58	0	0.08	1.14	0.47	6.82	7.58	13.68	0	CH_2 wag
ν_{23}	1428.79	0	0.05	1.49	-1	15.06	15.01	13.3	0	CH_2 wag
ν_{24}	1417.25	0.01	0.19	0.81	0.43	7.78	8	11.91	0.01	CH_2 wag
ν_{25}	1381.3	0	0.2	0.14	-3.14	-0.03	-3.16	11.24	0	CH_2 wag
ν_{26}	1360.78	0	0.21	3.59	7.77	19.87	35.59	5.27	0	CH_2 twist
ν_{27}	1332.76	0	0.19	3.7	-5.1	67.45	39.46	6.91	0	CH_2 twist
ν_{28}	1325.42	0	0.1	3.62	3.24	20.08	22.51	4.64	0	CH_2 twist
ν_{29}	1301.66	0	0.05	1.21	-6.05	1.93	-3.02	6.72	0	CH_2 twist
ν_{30}	1264.28	0	0.07	3.58	21.29	**416.51**	**423.6**	**14.87**	0	NH_2 twist
ν_{31}	1158.86	0	0.27	0.68	**208.82**	**333.56**	**334.07**	3.23	0	NH_2 twist
ν_{32}	1131.83	0	0.12	**5.74**	0.23	**330.06**	**329.32**	5.46	0	NH_2 wag
ν_{33}	1117.41	0	0.16	**5.66**	-0.76	**319.61**	**320.29**	7.81	0	NH_2 wag
ν_{34}	1092.16	0	0.1	**13.77**	-20.49	-24.46	104.49	**13.21**	0	νC-C + νC-NH_2
ν_{35}	1081.87	0	0.22	5.87	11.91	10.25	23.09	**12.32**	0	νC-NH_2
ν_{36}	1054.89	0.01	0.22	1.24	13.19	-152.02	-132.24	**13.51**	0.01	νC-C
ν_{37}	1047.71	0.01	0.14	**7.86**	-14.07	10.1	-3.21	**20.55**	0	νC-NH_2 + αC-C-N
ν_{38}	999.11	0	0.09	**4.89**	1.9	-47.96	-47.4	**16.53**	0	CH_2 rock + αC-N-C
ν_{39}	996.19	0	0.11	0.91	-18.75	-91.94	-92.49	8.6	0	αC-C-N + CH_2 rock
ν_{40}	969.83	0	0.08	5.31	**71.35**	-7.27	**78.93**	9.38	0	νC-N-C + δN-H
ν_{41}	903.1	0	-0.24	3.92	7.6	-56.38	-27.18	**17**	0	CH_2 rock
ν_{42}	868.35	0	0.21	6.75	7.47	10.16	16.89	**12.63**	0	CH_2 rock
ν_{43}	867.46	0	-0.27	7.26	17.5	-12.91	-9.43	**13.5**	0	CH_2 rock
ν_{44}	828.7	0.03	-0.21	**7.17**	**108.84**	-0.15	**110.13**	5.85	0.02	δNH + νC-N-C
ν_{45}	634.32	0.15	0.03	4.56	0.31	102.49	103.55	1.97	0.02	NH_2 rock
ν_{46}	613.27	0.07	-0.02	4.04	1.02	186.17	187.08	3.3	0.04	NH_2 rock
ν_{47}	507.73	0.06	-0.04	1.59	1.72	-43.83	-41.44	6.15	0.01	Ring def.
ν_{48}	499.9	0.09	0.11	1.72	3.23	49.29	54.38	9.47	0.06	Ring def.

Table 3.3.2. (cont.)

	unlabelled	^{13}CO	C^{18}O	^{15}N	-d_1	-d_4	-d_5	^{13}C	^{65}Cu	Assignment[b]
ν_{49}	477.22	**4.73**	**8.21**	0.82	0.51	-3.23	-1.06	0.16	**2.29**	νCu-CO
ν_{50}	436.89	1.33	1.71	**10.25**	**12.65**	**20.9**	**30.98**	0.5	0.01	νCu-NH + ν_sCu-N$_2$ + δCu-C≡O
ν_{51}	401.62	**2.54**	0.47	**7.7**	0.82	**20.09**	**20.49**	0.91	**0.21**	ν_aCu-N$_2$ + πCu-C≡O
ν_{52}	395.84	0.6	0.24	**3.62**	3.59	3.6	6.91	**4.6**	0.03	τC^{2}H$_2$ (*A'*) + δHN-Cu-CO
ν_{53}	330.62	**5.06**	0.37	**3.35**	5.67	7.97	11.7	0.56	0.17	ν_sCu-N$_2$ + νCu-NH + δCu-C≡O
ν_{54}	323.87	**5.01**	-0.1	1.83	0.59	**19.05**	**19.39**	1.52	0.09	π_aHN-Cu-N$_2$ + πCu-C≡O[c]
ν_{55}	285.3	3.5	0.55	3.15	0.37	8.94	9.93	0.81	**0.78**	δCu-C≡O + ν_sCu-N$_2$ + νCu-NH
ν_{56}	277.37	2.31	-0.4	1.89	0.52	7.59	8.4	1.53	**1.11**	πCu-C≡O + π_aHN-Cu-N$_2$[c]
ν_{57}	241	0.08	-0.72	1.82	0.56	10.67	10.84	3.15	0.05	τC^{1}H$_2$ (*A'*) + δ_sHN-Cu-N$_2$
ν_{58}	216.29	0.48	-0.4	0.96	-0.37	2.12	1.68	3.37	0.64	πHN-Cu-CO + τC^{1}H$_2$ (*A"*) + τC^{2}H$_2$ (*A"*)+ π_aHN-Cu-N$_2$
ν_{59}	187.15	0.52	1.04	0.88	0.17	2.19	2.38	2.12	**1.02**	δ_sCu-N$_2$
ν_{60}	117.6	0.06	-0.19	1.28	-0.31	6.26	5.98	0.87	0.44	δ_sCu-N$_2$ + τC^{1}H$_2$ (*A'*)
ν_{61}	70.37	0	-0.7	0.67	-1.18	3.79	2.65	0.65	0.03	τC^{2}H$_2$ (*A"*) + π_aHN-Cu-N$_2$ + πCu-C≡O
ν_{62}	56.41	0.02	0	0.3	-0.89	1.14	0.26	0.26	0.13	δHN-Cu-CO + τC^{2}H$_2$ (*A'*) + δCu-C≡O
ν_{63}	45	0.04	-0.09	0.04	-1.16	0.25	-0.9	0.54	0.07	τC^{1}H$_2$ (*A"*) + τC^{2}H$_2$ (*A"*) + πHN-Cu-CO

a Since $\Delta\nu$ corresponds to $\nu_{unlabelled} - \nu_{labelled}$, negative values reflect shifts to higher frequency.
b In the assignments performed in the low energy region, modes 49-63, NH_2 groups are represented by N and the secondary amine by NH.
c Modes 54 and 56 are coupled to the τC^1H_2 (*A"*) and τC^2H_2 (*A"*) modes.

The δNH_2 vibrations (ν_{15} and ν_{16}) are the less coupled of all the NH_2 bending vibrations (ν_{d5}/ν_{d0} ratios of 0.74 for both vibrations). The NH_2 twisting vibrations (ν_{30} and ν_{31}) occur before the wagging vibrations, and are the most coupled of all the NH_2 vibrations (ν_{d5}/ν_{d0} ratios of 0.66 and 0.71 respectively). In fact for both the -d_0 and -d_1 isotopomers, ν_{30} occurs at quite a similar frequency. However, ν_{31} shifts 208.82 cm^{-1} to lower energy upon -d_1 labelling due to the fact that the NH_2 twisting vibration for this isotopomer couples to the πN-H mode ν_{21}, as can be seen from the displacement diagrams shown in figures 3.3.5 and 3.3.6. The NH_2 twisting vibrations have usually been assigned as occurring at lower energy than the wagging vibrations [61-65]. This seems not to be the case, as despite the extensive coupling observed for this mode, the twisting mode occurs at a higher energy than the wagging mode for the -d_0, -d_4 and -d_5 isotopomers. The

analysis of the displacement diagrams obtained for the $[Cu(CO)L]^+$ isotopomers, where L = NH_2-CD_2-CH_2-NH-CH_2-CD_2-NH_2, NH_2-CH_2-CD_2-NH-CD_2-CH_2-NH_2, NH_2-CD_2-CD_2-NH-CD_2-CD_2-NH_2 is consistent with the aforementioned observations and further supports the trend in energy obtained for the NH_2 twisting and wagging vibrations. For the L = NH_2-CD_2-CD_2-NH-CD_2-CD_2-NH_2 compound, the first seven vibrations after the νCO mode are calculated to be exclusively NH_2 and NH vibrations, and again the NH_2 twisting mode is obtained at a higher energy than the NH_2 wagging mode. However, the twisting mode couples extensively to CH_2 vibrations, as can be seen from the values obtained for these vibrations in the L = NH_2-CD_2-CH_2-NH-CH_2-CD_2-NH_2 and NH_2-CH_2-CD_2-NH-CD_2-CH_2-NH_2 labelled compounds. Figure 3.3.7 shows the displacement diagrams obtained for the twisting modes ν_{30} and ν_{31} for the -d_2 labelled CH_2 groups and figure 3.3.8 shows the frequency values of some of the NH_2 and NH vibrations obtained for the CD_2 labelled compounds.

The shifts obtained for all 63 vibrations with progressive *d*-labelling of the N atoms (-d_0, -d_1, -d_4 and -d_5) are shown in figure 3.3.9 (A, B and C). The NH_2 wagging vibrations (ν_{32} and ν_{33}) shift ~320 cm^{-1} to lower energy upon *d*-labelling of the NH_2 groups and have ν_{d5}/ν_{d0} ratios of 0.71. ν_{34}, a C-C and C-N vibration due to its N-15 and C-13 sensitivity ($\Delta\nu$ ~ 14, 13 cm^{-1} to lower energy respectively) is coupled to the NH_2 symmetrical wagging vibration, ν_{33}, in the -d_0 and -d_1 isotopomers, but the coupling is lost for the -d_4 and -d_5 compounds as can be seen in figure 3.3.5. However, ν_{34} is obtained at a considerably lower energy for the -d_5 than for the -d_4 isotopomer, as ν_{34} couples to the πN-H mode ν_{21} for the -d_5 labelled compound.

The NH_2 rocking vibrations (ν_{45} and ν_{46}) have ν_{d5}/ν_{d0} ratios of 0.84 and 0.69 respectively. The very low value of 0.69 obtained for ν_{46} can be explained in terms of coupling between the ν_{46} and ν_{47} vibrations. In fact, for the -d_0 and -d_1 isotopomers, both vibrations are identical. The ν_{47} vibration occurs some 40 cm^{-1} at higher energy in the -d_4 and -d_5 isotopomers. Coupling between modes 46 and 47 in the -d_0 and -d_1 isotopomers would hence increase the energy for mode 46 and reduce it for mode 47, as can be seen in figure 3.3.9.C. This increase in energy for ν_{46} is responsible for the very low ν_{d5}/ν_{d0} ratio obtained.

The analysis for the NH_2 vibrations is complicated by the fact that deuteration of the NH_2 groups produces a noticeable variation in those vibrations associated to the C-N stretch, and hence some vibrations shift to higher energy in the -d_4 and -d_5 isotopomers. Assignments have been

performed on the basis of the displacement diagrams and the calculated shifts for the vibrations obtained shown in table 3.3.2.

As regards the 2,2N3-d_1 system, with *d*-labelling only on the secondary amine in the 2,2N3 ligand, a comparison between the $[Cu(CO)(2,2N3)]^+$ and $[Cu(CO)(2,2N3\text{-}d_1)]^+$ species provides two vibrations with large $\Delta\nu$ values, ($\Delta\nu \sim 950$ cm^{-1} for ν_3 and $\Delta\nu \sim 220$ cm^{-1} for ν_{21}). The next largest calculated shift occurs for ν_{31} with a $\Delta\nu \sim 210$ cm^{-1}. However, other sensitive vibrations are ν_{44} ($\Delta\nu \sim 110$ cm^{-1}) and ν_{40} with a $\Delta\nu \sim 70$ cm^{-1}. The first two vibrations mentioned correspond to two of the three modes predicted for the N-H group as mentioned by Watt and Klett [61], but coupling within the system is extensive and the next mode with a large sensitivity, ν_{31}, the asymmetric NH_2 twisting mode, is not an N-H mode *per se*, as both the atoms comprising the N-H bond shift in the same direction for the -d_0 and -d_4 isotopomers, and in opposite directions for the -d_1 and -d_5 isotopomers, which explains the lower energy shift upon deuteration of the secondary amine. It has also been mentioned previously, that this mode couples to the ν_{21} mode for the -d_1 labelled compound. It is ν_{44} that corresponds to the δN-H bend, the third mode expected for the N-H group, with almost half the sensitivity obtained for ν_{31}. This latter mode is highly coupled to vibrations from the C-N-C skeleton, and shows a $\Delta\nu \sim 7$ cm^{-1} and a $\Delta\nu \sim 6$ cm^{-1} upon N-15 and C-13 labelling respectively, within the 2,2N3 ligand. Displacement diagrams for some of the N-H vibrations previously mentioned are shown in figure 3.3.6.

The asymmetric stretch and the scissoring mode, $\nu_a CH_2$ and δCH_2, are obtained at a higher energy for the -CH_2-NH_2 groups than for the -CH_2-NH_2-CH_2- groups. All other CH_2 vibrations are highly coupled and all C-H bonds are displaced in the ligand. They do however, despite the coupling experienced to other modes in the ligand, seem to occur in small frequency ranges, as can be seen from table 3.3.2. No trend can be established as regards the frequency values obtained for the two different CH_2 groups in the 2,2N3 ligand. The CH_2 twisting mode, for example, is highly coupled for all of the N-d_i labelled compounds (i = 0, 1, 4, 5) and the ν_{26}, ν_{27}, ν_{28} and ν_{29} modes, all twisting modes, occur mainly for -CH_2-NH-CH_2- (ν_{26} and ν_{29}) and for -CH_2-NH_2 (ν_{27} and ν_{28}). The trend is maintained for the CD_2 labelled compounds, where ν_{27} and ν_{28} occur in the L = NH_2-CH_2-CD_2-NH-CD_2-CH_2-NH_2 labelled compound at the same frequency value for ν_{27} and 14 cm^{-1} to higher energy for ν_{28}. Both ν_{27} and ν_{28} are -CH_2-NH_2 vibrations in the -CD_2-NH-CD_2- labelled compound and it is ν_{26} and ν_{29} that shift to lower energy. A study of the

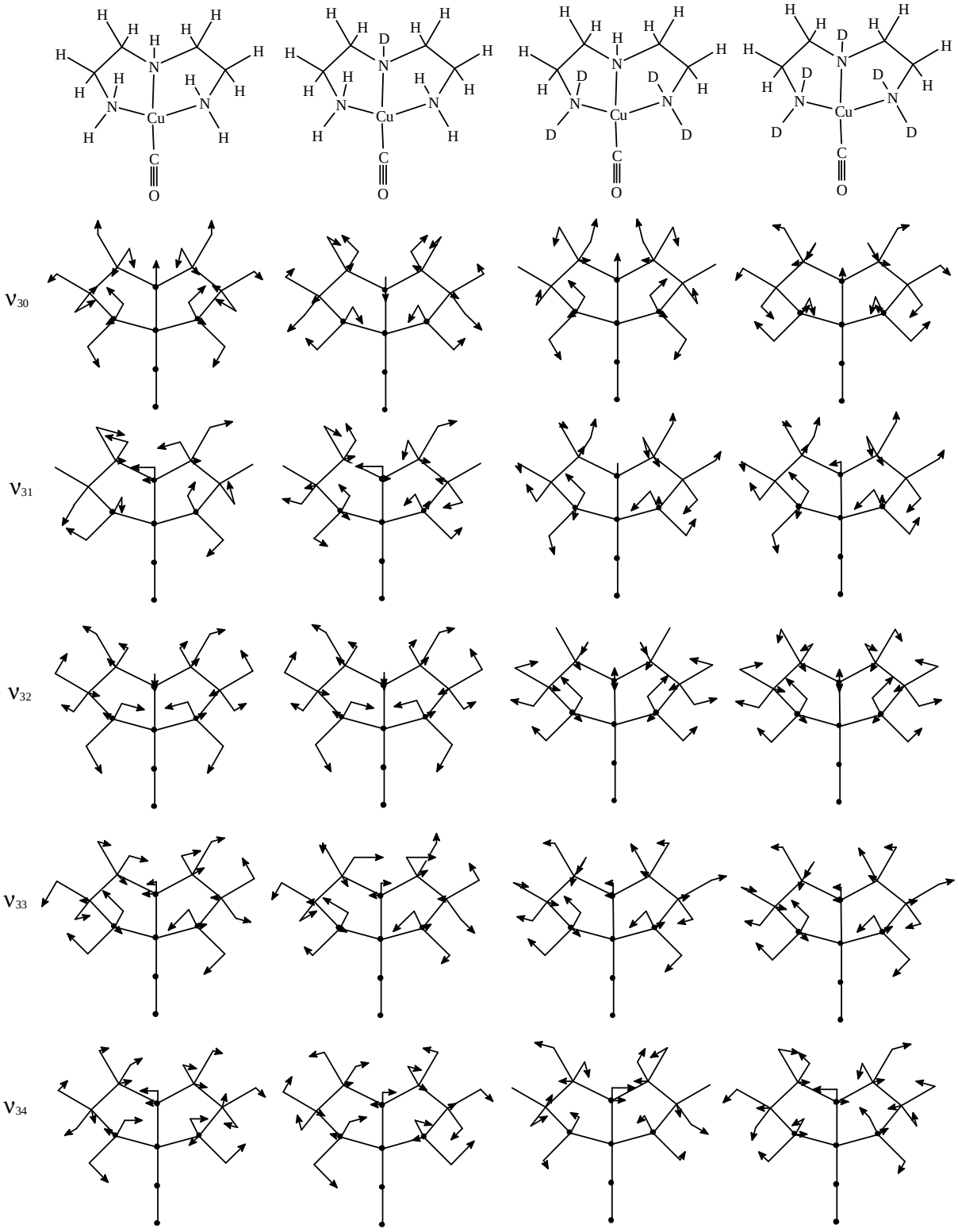

Figure 3.3.5. Projections on the *xy* plane for the NH_2 sensitive vibrations, $\nu_{30} - \nu_{34}$, obtained for the -d_0, -d_1, -d_4 and -d_5 N-labelled isotopomers.

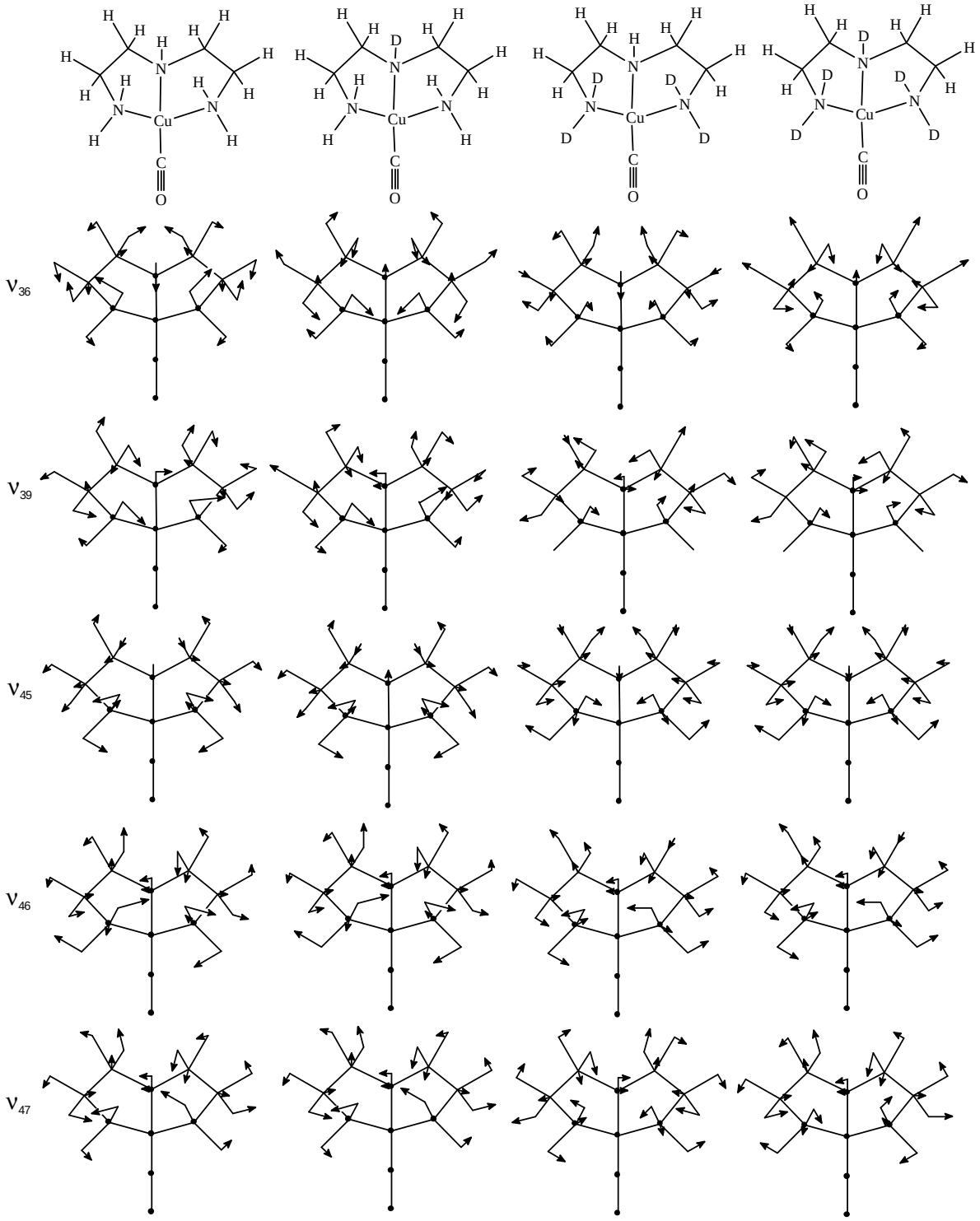

Figure 3.3.5 (continued). Projections on the *xy* plane for the NH_2 sensitive vibrations, ν_{36}, ν_{39}, and $\nu_{45} - \nu_{47}$, obtained for the -d_0, -d_1, -d_4 and -d_5 N-labelled isotopomers.

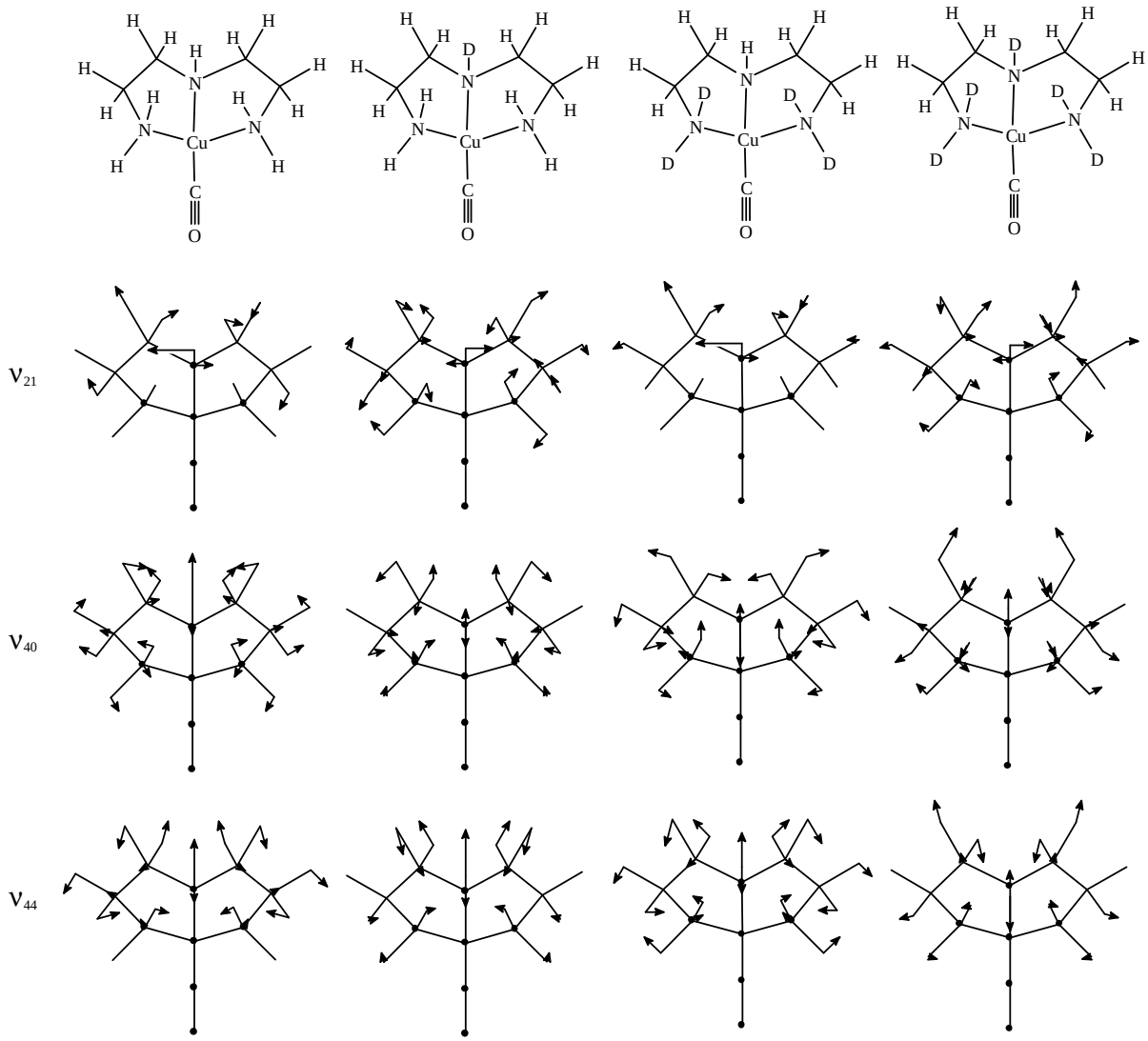

Figure 3.3.6. Projections on the *xy* plane for the N-H sensitive vibrations, ν_{21}, ν_{40} and ν_{44}, obtained for the -d_0, -d_1, -d_4 and -d_5 N-labelled isotopomers.

variations experienced upon -d_2 labelling of the CH_2 groups is currently underway, and will possibly in future shed some light on the vibrational coupling experienced by these systems.

Extensive coupling is observed for the C-C and C-N vibrations. Out of the twelve vibrations expected for the N-C ligand fragment, six are expected to be C-C and C-N stretching vibrations.

In a very rough approximation, the six stretching vibrations correspond to 2 νC-C, 2 νC-NH_2 and 2 νC-NH-C vibrations [61]. The $\Delta\nu$ values shown in table 3.3.2, obtained upon C-13 and N-15 labelling, are indicative of how highly coupled these modes are. Mode ν_{37}, the vibration with the highest C-13 sensitivity ($\Delta\nu \sim 20$ cm^{-1} to lower energy), also shows high sensitivity towards N-15 labelling ($\Delta\nu \sim 8$ cm^{-1} to lower energy). From the displacement diagrams obtained, the mode corresponds to a νC-NH_2 stretching mode coupled to a C-C bending mode. Mode 38 has been assigned to a coupled CH_2 rock and αC-N-C mode, where the rocking mode is the predominant vibration, hence its high sensitivity to C-13 labelling. Mode 39 has been assigned as a coupled αC-C-N + CH_2 rock due to its C-13 sensitivity. Modes 40 and 44 are coupled νC-N-C + δNH modes, with the former mode predominantly the νC-N-C vibration and the latter mode predominantly the δNH vibration as can be seen from the -d_1 and -d_5 sensitivities. The CH_2 torsional vibrations occur at low energy and are highly coupled to the metal-ligand vibrations. They occur predominantly as modes 52, 57, 58 and 61. Modes 62 and 63 are highly coupled to the torsional vibrations.

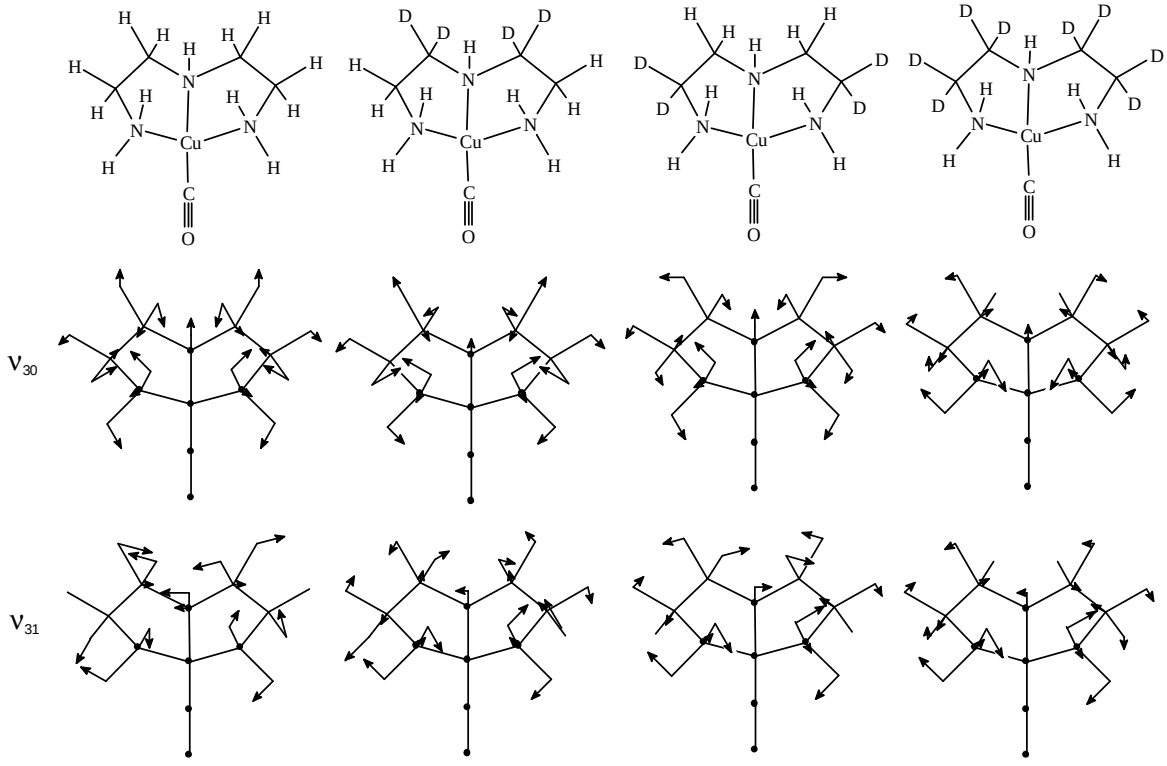

Figure 3.3.7. Projections on the *xy* plane for the NH_2 twisting vibrations, ν_{30} and ν_{31}, obtained for the CD_2 labelled isotopomers.

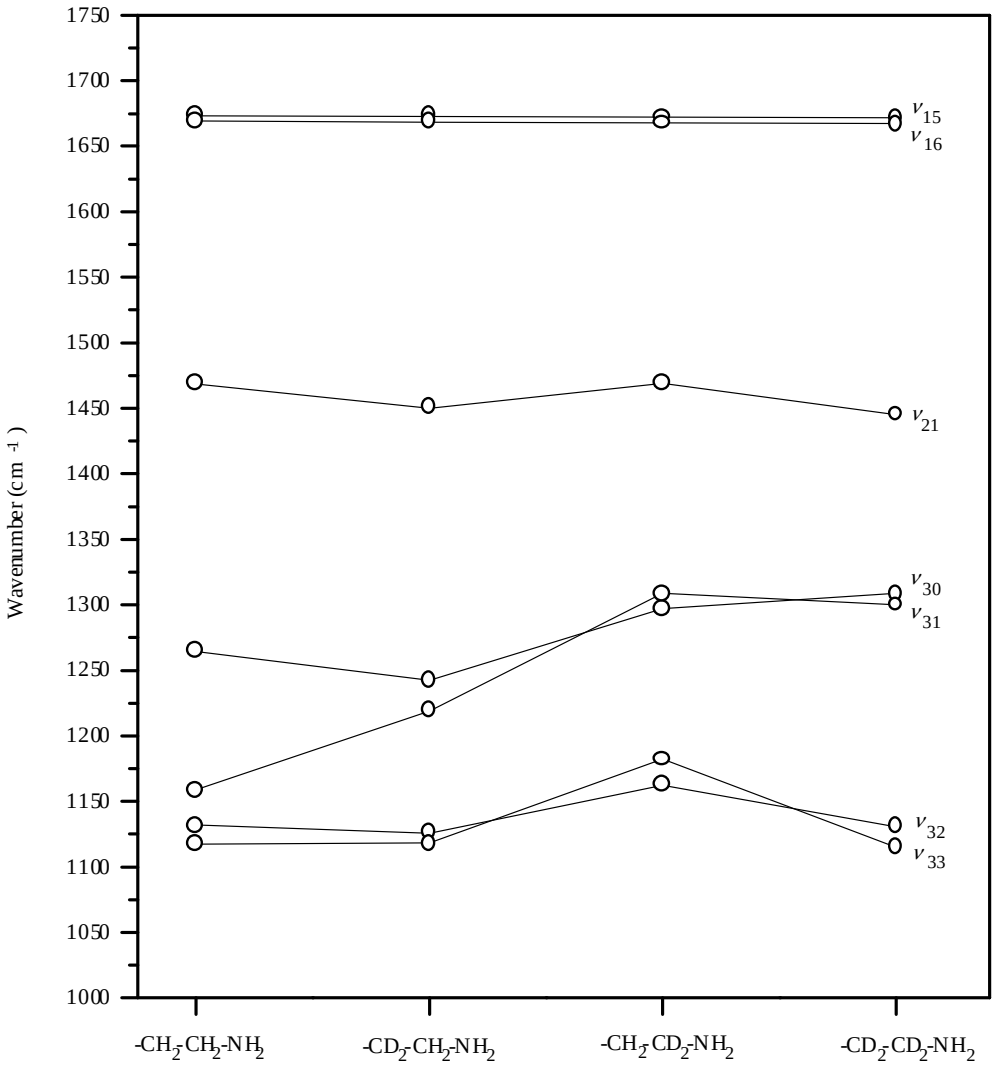

Figure 3.3.8. Calculated frequencies for some of the NH_2 and NH vibrations in CD_2 labelled compounds. Y fragments shown are for the $[Cu(CO)(Y\text{-}NH\text{-}Y)]^+$ isotopomers.

The analysis of the vibrations expected to occur in the low energy region follows the notation employed by Nakamoto for tetrahedral XWY_2Z compounds [66], where X = Cu, W = CO, Z = NH and Y = NH_2 in the present molecule. In the following discussion the nitrogen atoms from NH_2 groups will be represented by N. The tetrahedral skeleton $Cu(CO)(NH)N_2$ has C_s local symmetry and the modes can better be defined with respect to the mirror plane of the molecule, as in plane (*A*' symmetry) or out of plane (*A*" symmetry) vibrations.

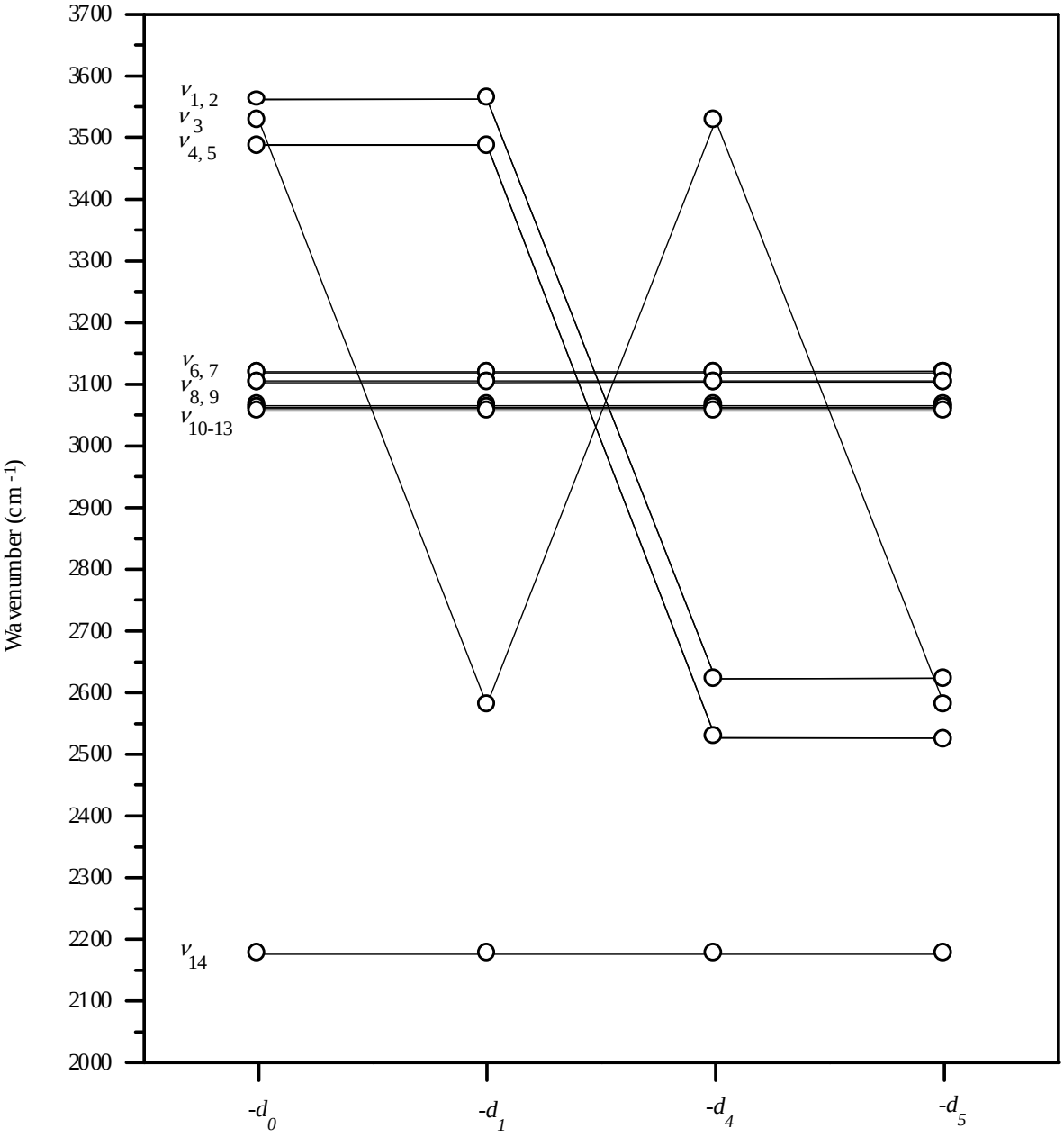

Figure 3.3.9.A. Calculated frequencies for vibrations $\nu_1 - \nu_{14}$ for the N-d_i-labelled $[Cu(CO)(2,2N3\text{-}d_i)]^+$ isotopomers, i = 0, 1, 4, 5.

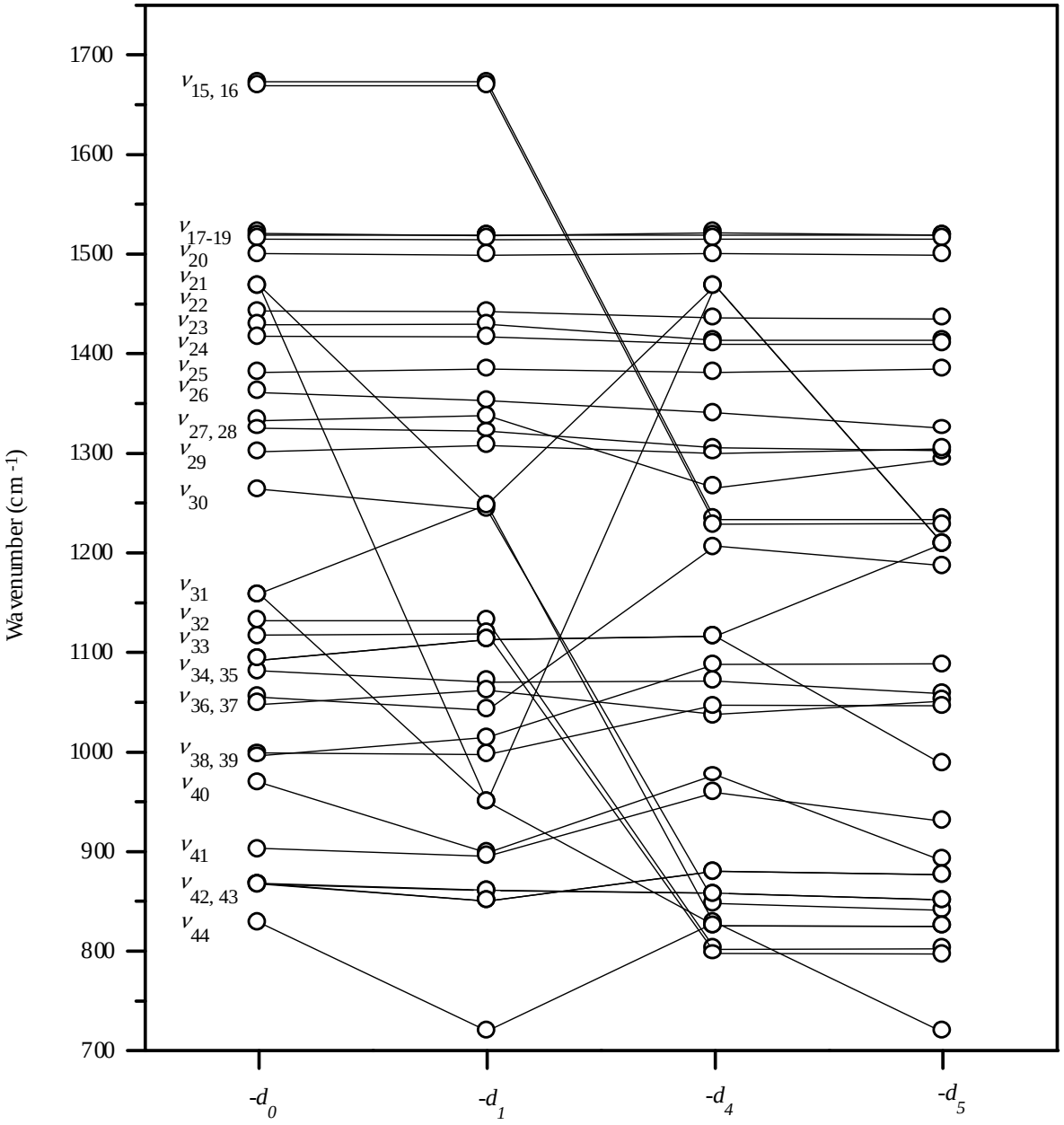

Figure 3.3.9.B. Calculated frequencies for vibrations $\nu_{15} - \nu_{44}$ for the N-d_i-labelled $[Cu(CO)(2,2N3\text{-}d_i)]^+$ isotopomers, i = 0, 1, 4, 5.

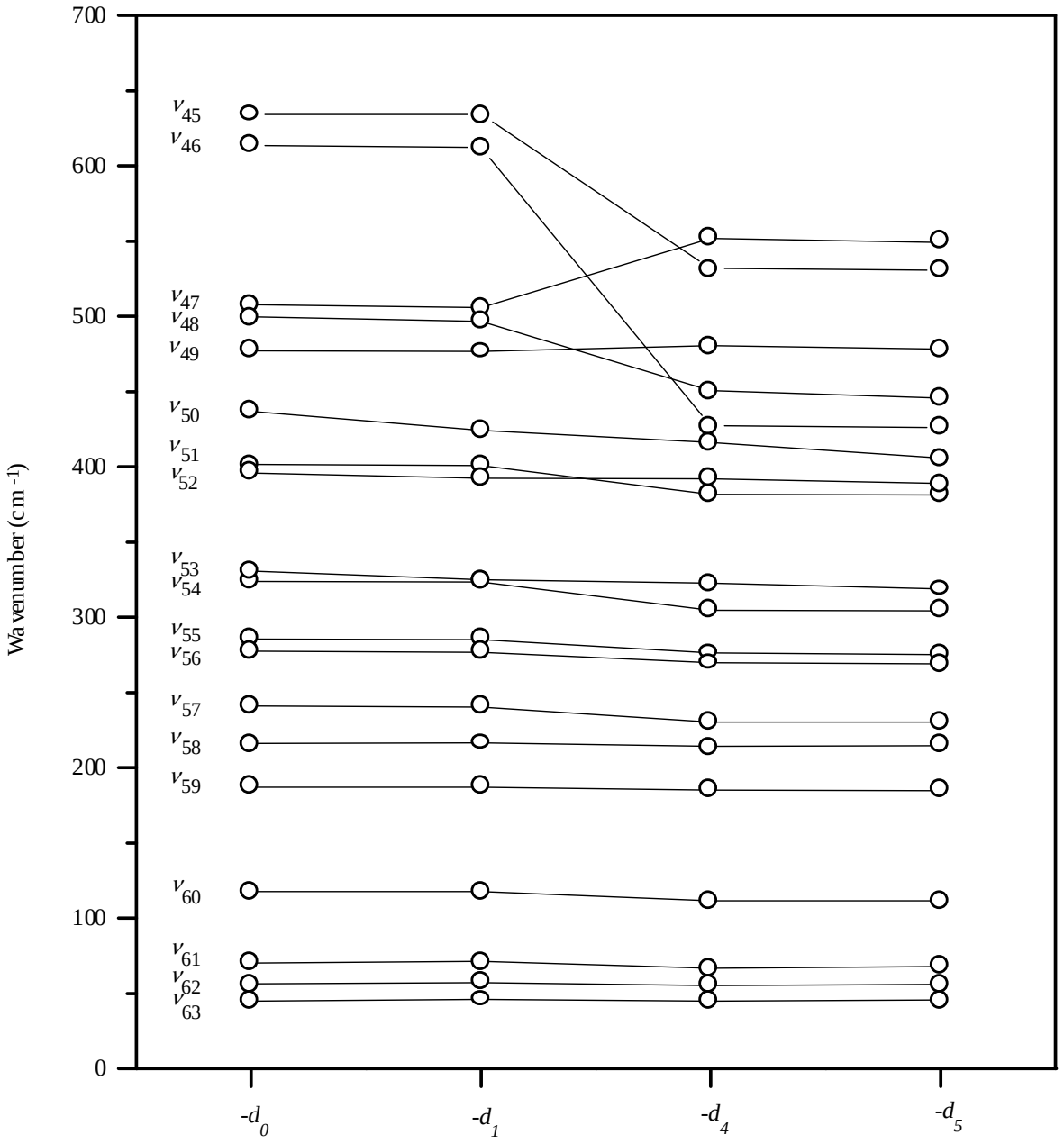

Figure 3.3.9.C. Calculated frequencies for vibrations $\nu_{45} - \nu_{63}$ for the N-d_i-labelled $[Cu(CO)(2,2N3\text{-}d_i)]^+$ isotopomers, i = 0, 1, 4, 5.

Fifteen vibrations of interest (9*A*' + 6*A*") are expected to occur in the low energy region. The fundamental vibrations of interest below 500 cm^{-1} fall into three categories.

1. Two Cu-C≡O bending vibrations, δCu-C≡O (*A*') in the mirror plane of the molecule and πCu-C≡O (*A*") out of the mirror plane.
2. Four torsional modes for the CH_2 groups in the triamine ligand. Methylene groups are labelled as C^1 and C^2 according to their position in the triamine ligand as shown in the 2,2N3 ligand, $H_2N\text{-}C^1H_2\text{-}C^2H_2\text{-}NH\text{-}C^2H_2\text{-}C^1H_2\text{-}NH_2$. Two τCH_2 (*A*') and two τCH_2 (*A*") vibrations are expected. The former vibrations (*A*' symmetry) involve the in-phase torsional modes of both the C^1 and C^2 methylene groups, and the latter vibrations (*A*" symmetry) the out-of-phase torsional modes of both the C^1 and C^2 methylene groups.
3. Nine vibrations (6*A*' + 3*A*") for the tetrahedral XWY_2Z skeleton, with the ligands viewed as a point mass. Table 3.3.3 shows the expected metal ligand vibrations and their symmetry.

A high degree of vibrational coupling is expected in these vibrations, the extent increasing as one moves into the far ir (the number of fundamentals of a given symmetry having similar energy is greater, in addition since bends are defined by two degrees of freedom perpendicular to the bond whereas stretches are defined only by one along the bond, bends are more likely to be best described by several Symmetry Adapted Linear Combinations in contrast to stretches –*viz*. bends are typically more coupled than stretches). The result is that in progressing into the far ir the bends in particular experience greater coupling with increasing number of other fundamentals so that it becomes increasingly more difficult to assign a particular vibrational frequency to a specific fundamental. This is particularly expected between the *A*" modes 58, 61 and 63, and is similarly expected between the *A*' modes 57, 59, 60, 61 and 62.

Given this, the assignments below 500 cm^{-1} presented here reflect the recognizable dominant fundamental contributors to the highly coupled vibrations. Here δ refers to a displacement in the mirror plane, π to a displacement out of the mirror plane, subscript s to symmetrical displacement of the two primary amine nitrogens (mirror image), subscript a to asymmetrical displacements (non-mirror image).

The *xy* projections of the fifteen vibrations occurring at lower energy (ν_{49} – ν_{63}) for the $[Cu(CO)(2,2N3)]^+$ compound are shown in figure 3.3.10. The *yz* projections along the OC-Cu-NH bonds are shown in figure 3.3.11 and *xz* projections for the tetrahedral framework are shown

in figure 3.3.12. Table 3.3.4 shows the assignments for the low energy vibrations together with the dominant fundamental occurring for that mode.

Table 3.3.3. Fundamental vibrations expected for XWY_2Z molecules. In the present study, X = Cu, W = CO, Z = NH and Y =N.

Symmetry	Nakamoto [66]	This work
A'	ν_s (XY_2)	ν_sCu-N_2
	ν (XW)	ν Cu-CO
	ν (XZ)	νCu-NH
	δ_s (XY_2)	δ_sCu-N_2
	δ_s (WXZ)	δHN-Cu-CO
	δ_s (ZXY_2)	δ_sHN-Cu-N_2 (umbrella mode)
A"	ν_a (XY_2)	ν_aCu-N_2
	δ (WXZ)	πHN-Cu-CO
	δ_a (ZXY_2)	π_aHN-Cu-N_2

Of primary interest regarding the vibrational coupling within the molecule in this region is that involving the carbonyl moiety. There is a lot of confusion in the literature regarding the order of assignment of the νM-CO, δM-C≡O and πM-C≡O vibrations of metal carbonyls. The intuitive order in decreasing frequency, as just presented, is often destroyed as a result of vibrational coupling of one or more of these fundamental vibrations. The extent of the coupling is influenced by the symmetry of the molecule, the nature of the metal and the nature of the other ligands. The complexity involved is illustrated by the varied assignments found in that other geometry associated with a coordination number of four, *viz*. square planar. Some studies (*e.g*. for $[Pt(CO)X_3]^-$ [67]) present the assignments as above, but a variety of alternate assignments can be found in the literature. Resolution of the confusion in the literature required normal coordinate analysis [68-70] and isotope labelling [71-73] studies. (Hence the present study of the tetrahedral geometry). Thus, for the *cis*$[Rh(CO)_2LX]$ system the sequence is δRh-C≡O > πRh-C≡O ≥ νRh-CO (the stretch is close to the out-of-plane bend, and may even be accidentally degenerate with it, depending on the ligand L) [68, 71, 74, 75]. In contrast, for the platinum analogue *cis*$[Pt(CO)_2LX]^+$ the sequence is πPt-C≡O > δPt-C≡O > νPt-CO [69], with the stretch close to the in-plane bend. Yet in the complexes $[Pt(CO)X_3]^-$ [70] and *trans*$[Pt(CO)LX_2]$ [72, 73] the sequences reflect that of *cis*$[Rh(CO)_2LX]$, *i.e.*, δPt-C≡O > πPt-C≡O ≥ νPt-CO (again the stretch is close to the out-of-plane bend, and may show accidental degeneracy with it, depending on the

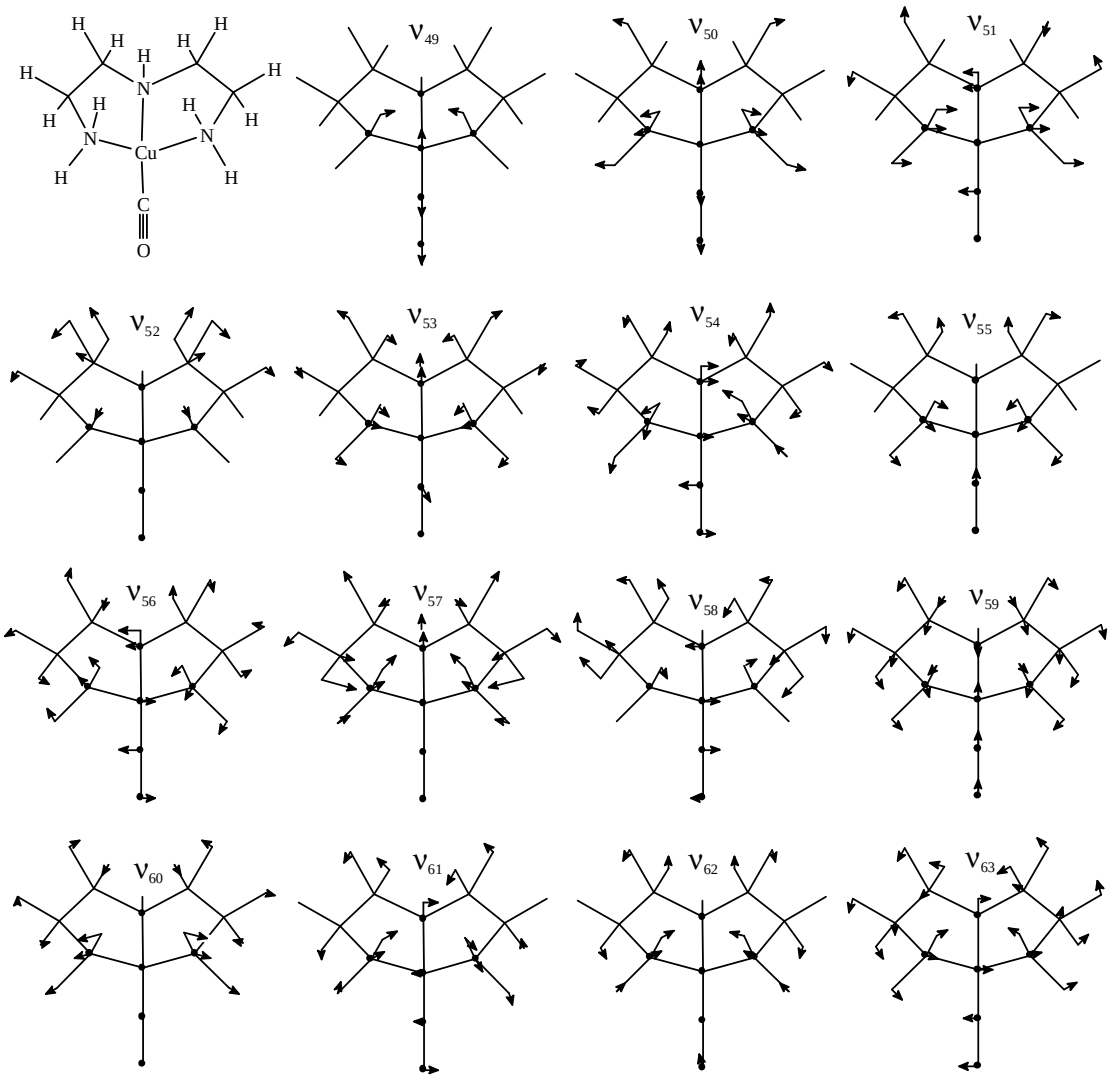

Figure 3.3.10. Projections on the *xy* plane for the low energy modes ($\nu_{49} - \nu_{63}$) calculated for the $[Cu(CO)(2,2N3)]^+$ complex cation.

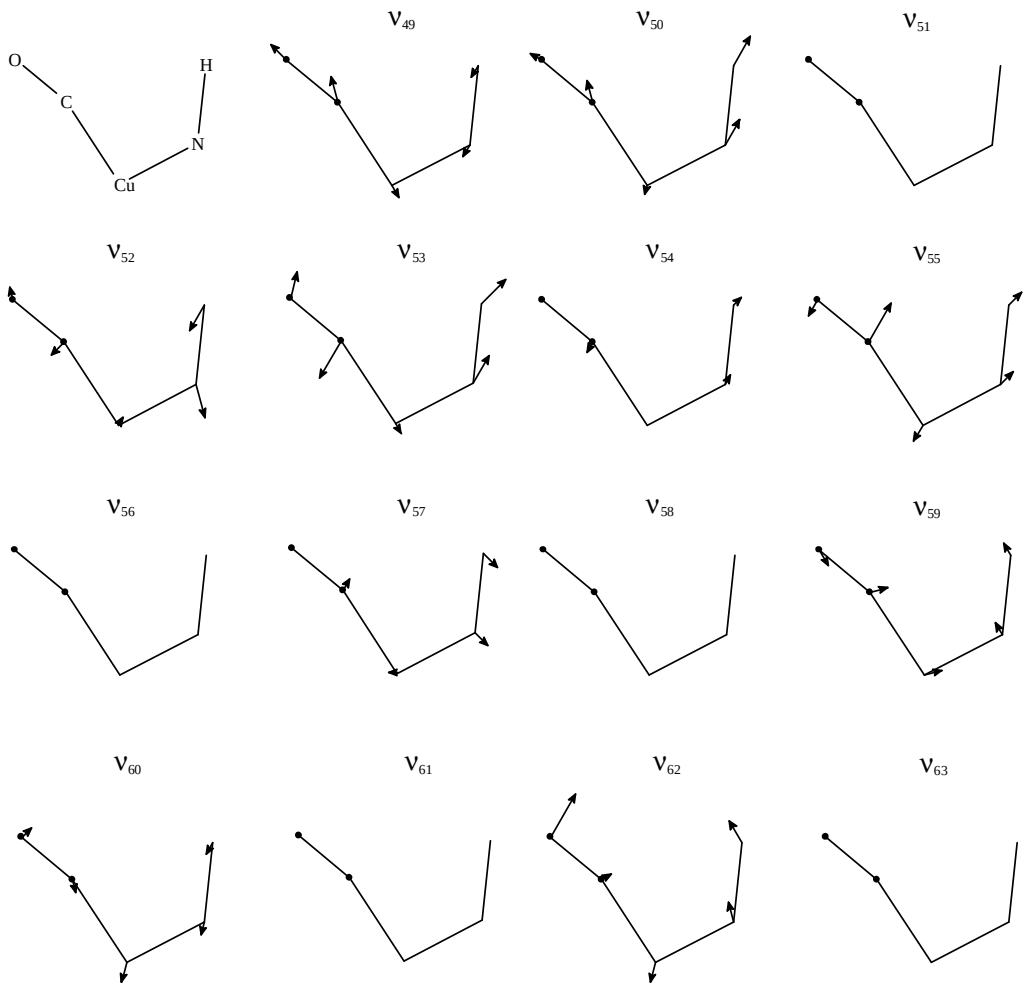

Figure 3.3.11. Projections on the *yz* plane for the low energy vibrations along the OC-Cu-NH bond.

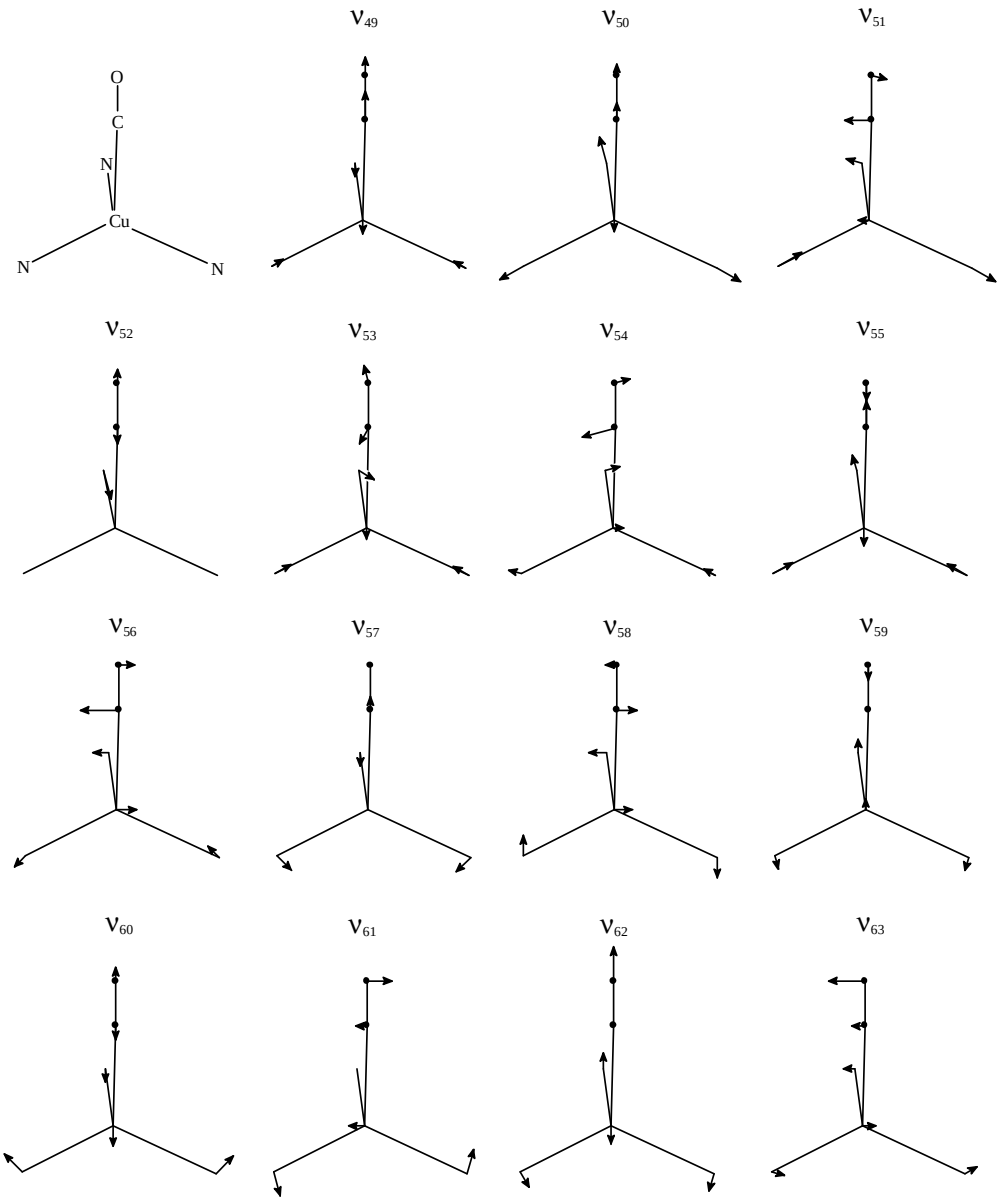

Figure 3.3.12. Projections on the *xz* plane for the low energy vibrations involving the $CuCON_3$ atoms.

ligand L). The assignment variations observed underline the importance of both isotope labelling studies and of molecular modelling studies in vibrational analysis.

The coupling of these modes in the present tetrahedral system and its significance to the assignment issue can now be considered. The observed order is significantly different than those determined for the square-planar systems; νCu-CO > δCu-C≡O > πCu-C≡O, with the stretch at a significant distance from the bends and which should (unlike that experienced by square planar systems) allow for the unambiguous assignment of the νM-CO in similar tetrahedral systems. Rather than the result of the stretch, this difference is due to the behaviour of the carbonyl bends both of which are found some 150 to 250 cm^{-1} lower than their square-planar counterparts. Both of these lower frequency fundamentals individually experience significant coupling, a consideration of which raises a caution to the possibility of a reversal of their assignment (similar to that noted with *cis*$[Pt(CO)_2LX]^+$) in other tetrahedral systems.

Table 3.3.4. Assignments for the low energy vibrations, ν_{49}-ν_{63}, and dominant fundamental occurring for each mode in the XWY_2Z molecule where X = Cu, W = CO, Z = NH and Y = N (=NH_2). Calculated frequencies in cm^{-1} are for the unlabelled $[Cu(CO)(2,2N3)]^+$ compound.

Vibration	Frequency	Symmetry	Assignment	Dominant fundamental(s)
ν_{49}	477	*A*'	νCu-CO	ν (XW)
ν_{50}	437	*A*'	νCu-NH + ν_sCu-N_2 + δCu-C≡O	ν (XZ)
ν_{51}	401	*A*"	ν_aCu-N_2 + πCu-C≡O	ν_a (XY_2)
ν_{52}	396	*A*'	τC^2H_2 + δHN-Cu-CO	τC^2H_2 (*A*'), δ_s (WXZ)[b]
ν_{53}	331	*A*'	ν_sCu-N_2 + νCu-NH + δCu-C≡O	ν_s (XY_2)
ν_{54}	324	*A*"	π_aHN-Cu-N_2 + πCu-C≡O [+ τC^1H_2 + τC^2H_2]	δ_a (ZXY_2)
ν_{55}	285	*A*'	δCu-C≡O + ν_sCu-N_2 + νCu-NH	δCu-C≡O
ν_{56}	277	*A*"	πCu-C≡O + π_aHN-Cu-N_2 [+ τC^1H_2 + τC^2H_2]	πCu-C≡O
ν_{57}	241	*A*'	τC^1H_2 + δ_sHN-Cu-N_2	τC^1H_2 (*A*'),δ_s (ZXY_2)
ν_{58}	216	*A*"	πHN-Cu-CO + τC^1H_2 + π_aHN-Cu-N_2 + τC^2H_2	δ (WXZ), τC^1H_2 (*A*")[c]
ν_{59}	187	*A*'	δ_sCu-N_2	δ_s (XY_2)[a]
ν_{60}	118	*A*'	δ_sCu-N_2 + τC^1H_2	δ_s (XY_2)
ν_{61}	70	*A*"	τC^2H_2 + π_aHN-Cu-N_2 + πCu-C≡O	τC^2H_2 (*A*")[c]
ν_{62}	56	*A*'	δHN-Cu-CO + τC^2H_2 + δCu-C≡O	δ_s (WXZ), τC^2H_2 (*A*')[b]
ν_{63}	45	*A*"	τC^1H_2 + τC^1H_2 + πHN-Cu-CO	τC^1H_2 (*A*")[c]

a Mode 59 is a strongly coupled mode. The principal δ_s (XY_2) mode from isotopic shifts and displacement diagrams is mode 60.
b Mode 52 is strongly coupled to mode 62.
c Modes 58 and 61 are strongly coupled to mode 63.

Two highly coupled modes in particular show significant δCu-C≡O contribution, these being modes 53 (331 cm^{-1}) and 55 (285 cm^{-1}). Based on their displacements and isotope sensitivities the former is predominantly the ν_sCu-N_2 (greater N-15 sensitivity, and while it has a larger ^{13}CO sensitivity than mode 55, its smaller C^{18}O sensitivity suggests that there is smaller δCu-C≡O contribution). For the same reasons the lower vibration better describes the bend, and has a larger metal displacement associated with the bend, as is evidenced by the greater metal isotope sensitivity.

Similarly, two highly coupled modes show significant πCu-C≡O contribution; modes 54 (326 cm^{-1}) and 56 (277 cm^{-1}). Based on their displacements and isotope sensitivities these are significantly coupled. The former is considered to be predominantly the π_aHN-Cu-N_2 based on the much greater NH/D sensitivity of this lower frequency vibration. Furthermore, the displacement of the Cu-C≡O bend in this mode is within a plane containing one of the Cu-NH_2 bonds (so accounting for its metal and C-13 isotope sensitivity) rather than being perpendicular to the molecular plane. It is in mode 56 that the Cu-C≡O displacement is perpendicular to the molecular plane, and the mode is thus a better descriptor for πCu-C≡O. The out-of-plane bend is coupled to several additional vibrations, but in addition to the evidence in the displacement diagram, it is best identified as mode 56 on the basis of its possessing a larger metal isotope sensitivity. A point of interest with mode 56 is the decoupling experienced by this vibration on C^{18}O labelling (seen by a shift of 0.4 cm^{-1} to higher wavenumber). This indicates that the coupling experienced by this mode is particularly susceptible to its environment. It is this fact, and that the δCu-C≡O and πCu-C≡O are observed only 7 cm^{-1} apart that raises the possibility that they may be found in reverse order in similar systems were the coupling experienced by δCu-C≡O to be slightly greater such that its frequency is lowered, or were the coupling experienced by πCu-C≡O be altered so as to be better described by mode 54.

An additional assignment complicated by vibrational coupling is that of δHN-Cu-CO. The displacements of two modes show substantial bending of the N-Cu-C angle so as to be assigned predominantly to this fundamental, namely mode 52 (396 cm^{-1}) and mode 62 (56 cm^{-1}). The other vibration is an *A*' CH_2 torsional vibration to which it couples. The higher frequency might be considered too high for the bend (being merely 40 cm^{-1} lower than the stretch), however the lower frequency is particularly too low in the far infra-red for consideration. In comparing the assignment of this vibration {δ_s (WXZ)} for a variety of simpler penta-atomic systems [66] its

location varies substantially between 150 and 365 cm^{-1}. This no doubt reflects the disparate influences of the reduced mass and the bond force constant (itself a balance of the bond order, difference in electronegativities, etc.) for the molecule. Both the δHN-Cu-CO and τC^2H_2 are strongly coupled, with mode 52 having large N-15 and -d_1 sensitivities as well as large sensitivities to C-13 and C^2-d_2 labelling of the 2,2N3 ligand. The displacement diagram for mode 62 shows δHN-Cu-CO character. However, although Cu-65 sensitivity is high, C-13 and O-18 sensitivities are negligible, a common feature observed in very low energy modes. Both modes 52 and 62 are better described as strongly coupled δHN-Cu-CO + τC^2H_2 vibrations.

Finally, the mode that best describes the unique symmetric umbrella bend involving all three nitrogens is clearly observed from the displacement diagram shown in figure 3.3.12 to mode 57.

3.3.3.2. Mid and far ir spectra for [Cu(CO)(2,2N3)]BPh_4 and its isotopomers

The mid and far ir spectra of the [Cu(CO)(2,2N3)]BPh_4, [Cu(^{13}CO)(2,2N3)]BPh_4 and [Cu(CO)(2,2N3-d_5)]BPh_4 compounds have been assigned on the basis of the theoretical study performed and the expected calculated shifts. In all cases, regression analyses provided straight lines with a good fit between experimental and calculated frequency values. Rescaling of the frequencies was deemed necessary as, contrary to what is observed for organic molecules where all calculated vibrations are obtained at higher frequencies, some M-L modes are calculated at slightly lower than observed values. The rescaling of frequencies hence decreases the calculated frequency values for high energy vibrations, and slightly increases the frequencies of those vibrations occurring at lower energies. Assignments will be discussed separately for the different groups involved in the complex Cu(I) cations.

The mid and far ir spectra for these compounds are shown in figures 3.3.13, 3.3.14 and 3.3.15. Assignments for the experimental and rescaled frequencies are shown in table 3.3.5.

3.3.3.2.1. N-H vibrations

Two frequencies are calculated for the NH_2 symmetric stretch, as the NH_2 groups vibrate symmetrically in-phase (*A*') and out-of-phase (*A*") with each other. These frequencies are calculated to have a $\Delta\nu$ value of 0.42 cm^{-1} and are observed as only one band in the experimental spectrum. This is also the case with the δNH_2 vibrations, where the scissoring mode occurs in-phase (*A*') and out-of-phase (*A*") and the $\Delta\nu_{calc}$ value is of 4.24 cm^{-1} but observed as a single band in the ir spectra for the compounds. The N-H stretching vibrations (ν_1–ν_5) occur in the 3500 cm^{-1}

region and shift some 860 cm^{-1} to lower energy upon deuteration. A weak intensity band is observed at 3160 cm^{-1} in the spectra for [CuA(2,2N3)]BPh_4, A = CO, ^{13}CO and at 2353 cm^{-1} for [Cu(CO)(2,2N3-d_5)]BPh_4. It has been assigned to the N-H bend overtone as it corresponds to 2 x δNH_2. The NH_2 scissoring vibrations (ν_{15} and ν_{16}) at 1592 cm^{-1} shift to 1185 cm^{-1} upon deuteration and a medium intensity band at 1435 cm^{-1} (ν_{21}) in the spectra of [Cu(CO)(2,2N3)]BPh_4 and [Cu(^{13}CO)(2,2N3)]BPh_4 slightly masked by the intense BPh_4 absorption at 1428 cm^{-1}, disappears upon deuteration and shifts to 1150 cm^{-1} in the spectrum of the deuterated compound and is indicative of πN-H. This last band is masked by another intense absorption of the BPh_4 anion occurring at 1154 cm^{-1}, but was observed in a concentrated spectrum of the deuterated sample at 1150 cm^{-1} and also appears in the spectrum of [Cu(CO)(2,2N3-d_5)]I at 1156 cm^{-1}. The assignment for these bands is consistent with that proposed by Watt and Klett [61] who observed bands at 1589 cm^{-1} and 1439 cm^{-1} in their study of Pd(II) compounds with diethylenetriamine. The authors pointed out that the δND_2 vibration was observed as an intense band at 1181 cm^{-1} but did not mention the shift obtained for the πN-D band. Although their assignment for this particular vibration was not totally satisfactory to them, the calculated values and observed experimental shifts further support the previously performed assignments.

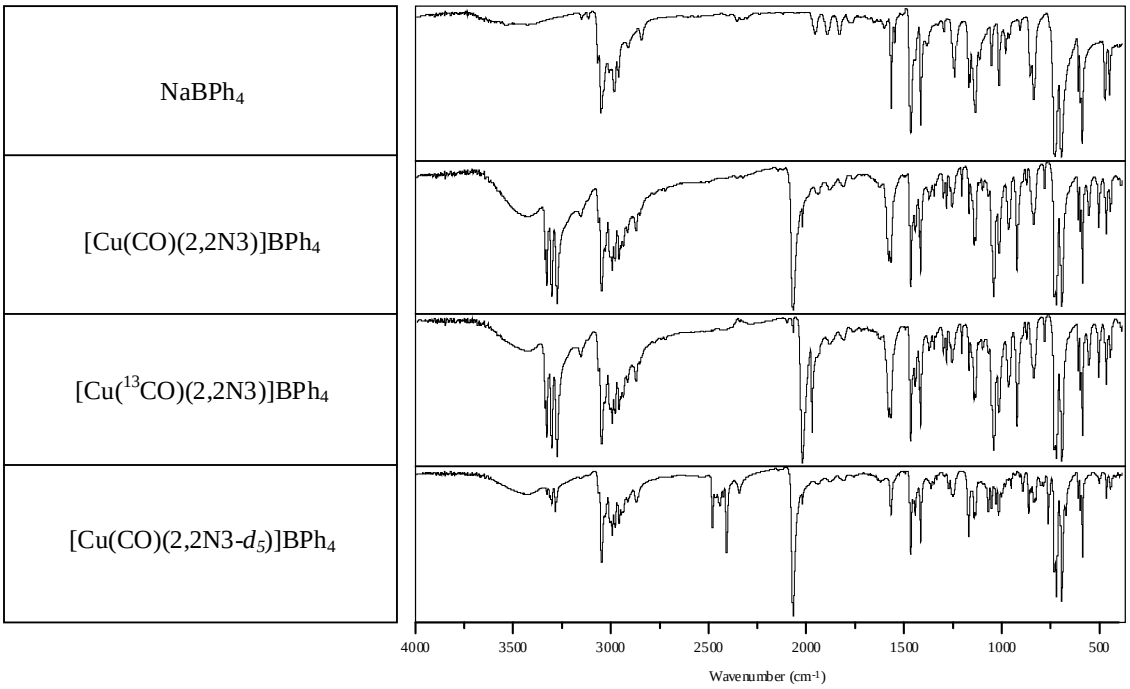

Figure 3.3.13. Mid ir spectra for $NaBPh_4$ and [CuAL]BPh_4 compounds, where A = CO, ^{13}CO; L = 2,2N3, 2,2N3-d_5.

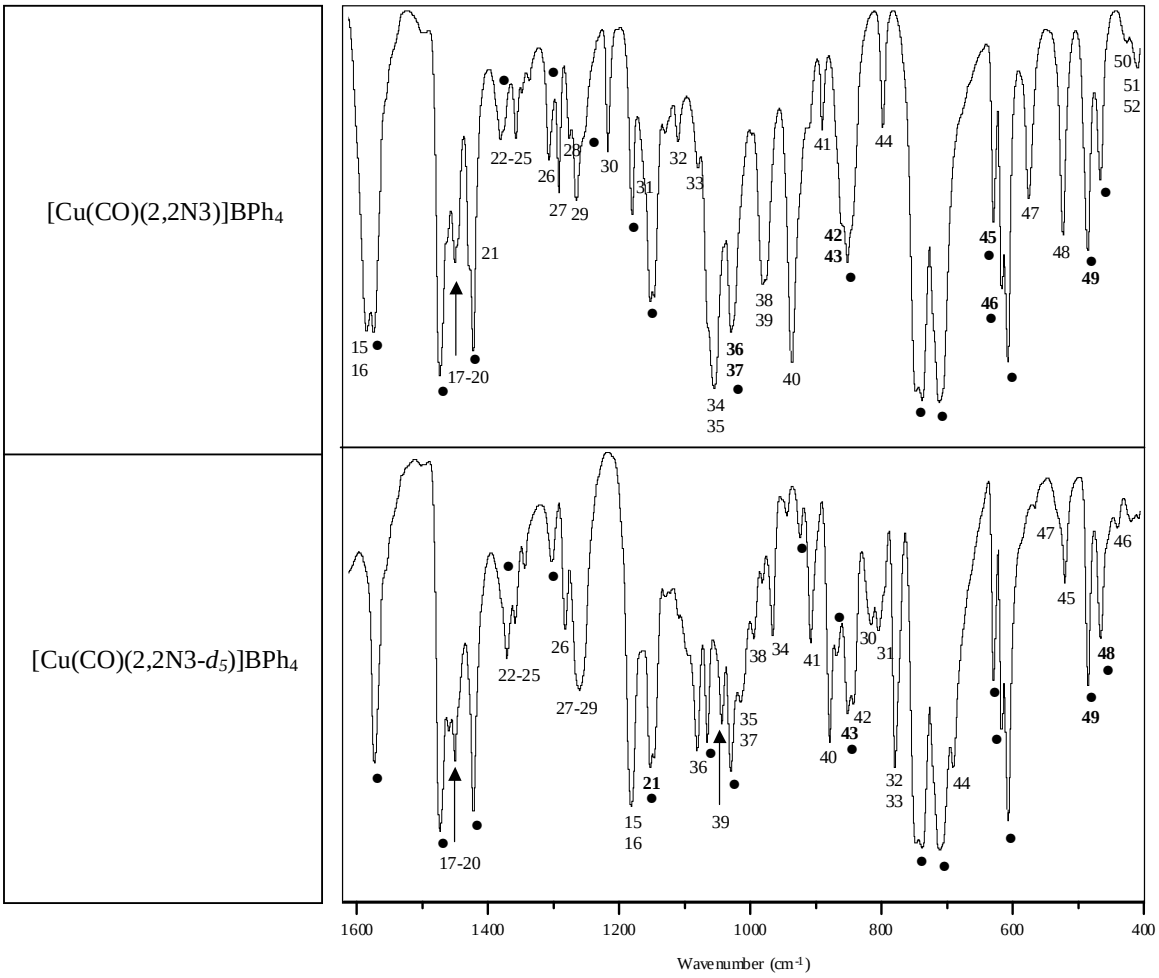

Figure 3.3.14. Mid ir spectra for $[Cu(CO)(2,2N3)]BPh_4$ and $[Cu(CO)(2,2N3\text{-}d_5)]BPh_4$. Numbering scheme follows the assignments shown in tables 3.3.2 and 3.3.5. Tetraphenylborate bands are shown with a dot and bold numbering is used to indicate bands from the $[Cu(CO)L]^+$ vibrations that are masked by BPh_4^- absorptions.

Watt and Klett [61] assigned the NH_2 wagging modes as occurring before the twisting modes. This seems not to be the case in light of the vibrational analyses performed by means of DFT calculations. The authors assigned the wagging vibrations at *ca.* 1310 and 1150 cm^{-1} and the twisting vibrations at *ca*. 1150 and 990 cm^{-1}. The band occurring at 1312 cm^{-1} (ν_{26}) has been assigned in the present work as a CH_2 twisting mode in good agreement with the calculated frequency values. Its shift to lower energy upon deuteration is due to the coupling experienced with the NH_2 twisting mode as seen from the displacement diagrams obtained for these vibrations. The band occurring at *ca.* 990 cm^{-1} assigned as a twisting vibration by the authors

occurs at too low a frequency value for an NH_2 twisting vibration. It has been assigned in this work as a CH_2 rock, coupled to a vibration of the C-N skeleton.

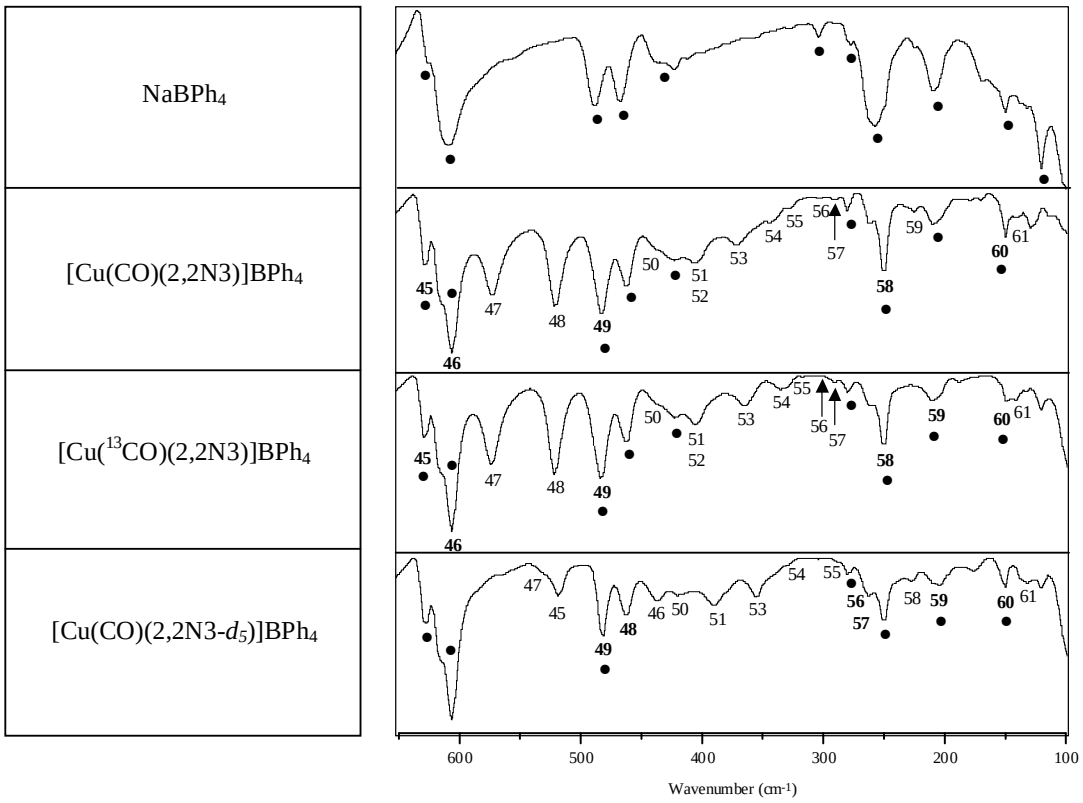

Figure 3.3.15 . Far ir spectra of $NaBPh_4$ and $[CuAL]BPh_4$ compounds (A = CO, ^{13}CO; L = 2,2N3, 2,2N3-d_5). Numbering scheme refers to assignments shown in tables 3.3.2, 3.3.4 and 3.3.5. Bold numbers represent bands masked by BPh_4^- absorptions. Tetraphenylborate absorptions are shown with a dot.

The NH_2 twisting mode, ν_{30}, is observed as a medium intensity absorption occurring at 1220 cm^{-1} for $[CuA(2,2N3)]BPh_4$, A = CO and ^{13}CO. This band shifts to 815 cm^{-1} in the spectrum for the -d_5 analogue. The remaining twisting mode, ν_{31}, is observed as a shoulder band at *ca*. 1166 cm^{-1} to the intense BPh_4^- absorption at 1155 and 1149 cm^{-1}. In the -d_5 labelled it shifts to 804 cm^{-1} compound. In the spectrum for [Cu(CO)(2,2N3)]I, the bands occurring at 1220 and 1170 cm^{-1} (ν_{30} and ν_{31}) are absent in the spectrum for the -d_5 labelled compound and shift to 821 and 807 cm^{-1}.

Table 3.3.5. Experimental and calculated rescaled frequencies (6-31G**) for [Cu(CO)(2,2N3)]BPh_4 and ^{13}CO and 2,2N3-d_5 isotopomers. All frequency values in cm^{-1}.

Vibration	[Cu(CO)(2,2N3)]BPh_4		[Cu(^{13}CO)(2,2N3)]BPh_4		[Cu(CO)(2,2N3-d_5)]BPh_4		Assignment
	Observed	Calculated	Observed	Calculated	Observed	Calculated	
ν_1	3344	3353	3344	3353	2489	2488	$\nu_a NH_2$
ν_2	3334	3353	3334	3353	2489	2488	$\nu_a NH_2$
ν_3	3311	3322	3311	3321	2453	2448	νNH
ν_4	3283	3285	3282	3285	2434	2397	$\nu_s NH_2$
ν_5	3283	3285	3282	3284	2417	2397	$\nu_s NH_2$
	3160		3160		2353		2 x δNH_2
ν_6	2956	2945	2956	2944	2953	2954	$\nu_a CH_2$
ν_7	2956	2943	2956	2942	2953	2952	$\nu_a CH_2$
ν_8	2946	2931	2945	2930	2945	2940	$\nu_a CH_2$
ν_9	2946	2929	2945	2928	2945	2938	$\nu_a CH_2$
ν_{10}	2896	2894	2896	2893	—	2902	$\nu_s CH_2$
ν_{11}	2880	2891	2879	2891	2877	2899	$\nu_s CH_2$
ν_{12}	2880	2889	2879	2889	2877	2898	$\nu_s CH_2$
ν_{13}	2880	2886	2879	2885	2877	2894	$\nu_s CH_2$
ν_{14}	2080	2070	2080		2079	2070	νCO
	2032		2032	2022	2032		ν^{13}CO
			1984*				$\nu^{13}C^{18}O$
ν_{15}	1592	1605	1592	1604	1185	1187	δNH_2
ν_{16}	1592	1601	1592	1600	1185	1183	δNH_2
ν_{17}	1467	1463	1465	1463	1465	1455	δCH_2
ν_{18}	1457	1461	1456	1461	1456	1455	δCH_2
ν_{19}	1457	1458	1456	1457	1456	1451	δCH_2
ν_{20}	1451	1444	1451	1444	—	1436	δCH_2
ν_{21}	1434	1415	1434	1415	1156[†]	1164	πNH
ν_{22}	1387	1391	1386	1390	1376	1376	CH_2 wag
ν_{23}	1381	1378	1379	1378	1363	1356	CH_2 wag
ν_{24}	1362	1367	1362	1367	1348	1352	CH_2 wag
ν_{25}	1342	1334	1342	1334	—	1329	CH_2 wag
ν_{26}	1312	1315	1311	1315	1287	1273	CH_2 twist[‡]
ν_{27}	1297	1289	1296	1289	1264[a]	1243	CH_2 twist
ν_{28}	1280	1282	1280	1282	1264[a]	1252	CH_2 twist
ν_{29}	1270	1260	1269	1260	1264[a]	1254	CH_2 twist
ν_{30}	1220	1226	1220	1225	815	820	NH_2 twist
ν_{31}	1164	1128	1166	1128	804	805	NH_2 twist
ν_{32}	1113	1103	1113	1103	779	784	NH_2 wag
ν_{33}	1083	1090	1082	1089	779	779	NH_2 wag
ν_{34}	1057	1066	1057	1066	967	957	νC-C + νC-NH_2
ν_{35}	1057	1057	1057	1056	1017	1024	νC-NH_2
ν_{36}	1031	1032	1031	1031	1084	1144	νC-C
ν_{37}	1031	1025	1031	1025	1017	1016	νC-NH_2 + αC-C-N
ν_{38}	982	980	982	980	996	1012	CH_2 rock + αC-N-C
ν_{39}	978	977	977	977	1045	1052	αC-C-N + CH_2 rock
ν_{40}	938	953	938	953	879	867	νC-N-C + δN-H
ν_{41}	891	891	891	891	908	903	CH_2 rock
ν_{42}	860	859	860	859	842	830	CH_2 rock
ν_{43}	860	858	860	858	852	854	CH_2 rock

Table 3.3.5. (cont.).

Vibration	[Cu(CO)(2,2N3)]BPh_4		[Cu(^{13}CO)(2,2N3)]BPh_4		[Cu(CO)(2,2N3-d_5)]BPh_4		Assignment
	Observed	Calculated	Observed	Calculated	Observed	Calculated	
ν_{44}	798	822	797	822	689	705	δNH + νC-N-C
ν_{45}	627[b]	642	627[b]	642	517	529	NH_2 rock
ν_{46}	614[b]	623	614[b]	622	436	432	NH_2 rock
ν_{47}	572	525	572	525	530[c]	547	Ring def.
ν_{48}	520	518	520	517	462[d]	450	Ring def.
ν_{49}	498[e]	497	—	492	—	480	νCu-CO[f]
ν_{50}	437	459	437	458	419	413	νCu-NH+ ν_sCu-N_2
ν_{51}	405	427	405	424	390	389	ν_aCu-N_2 + πCu-C≡O
ν_{52}	405	421	405	421	390	397	τCH_2 + δHN-Cu-CO
ν_{53}	371	361	364	356	354	331	ν_sCu-N_2 + νCu-NH + δCu-C≡O
ν_{54}	345	355	335	350	327	318	π_aHN-Cu-N_2 + πCu-C≡O
ν_{55}	328	319	318	316	290	290	δCu-C≡O + ν_sCu-N_2 + νCu-NH
ν_{56}	303	312	304	311	279[g]	284	πCu-C≡O + π_aHN-Cu-N_2
ν_{57}	290	278	291	278	262	248	τCH_2 + δ_sHN-Cu-N_2
ν_{58}	250[h]	255	250[h]	254	228	233	πHN-Cu-CO + τCH_2 + π_aHN-Cu-N_2
ν_{59}	225	228	—	227	205	206	δ_sCu-N_2
ν_{60}	150	164	149	164	133	137	δ_sCu-N_2 + τCH_2
ν_{61}	113	120	—	120	98	96	τCH_2 + π_aHN-Cu-N_2 + πCu-C≡O
ν_{62}	—	107	98	107	90	85	δHN-Cu-CO + τCH_2
ν_{63}	92	97	92	96	—	76	τCH_2 + πHN-Cu-CO

* Harmonic oscillator approximation yields a ratio of $\nu CO/\nu^{13}C^{18}O = 0.95311$.
† Masked by BPh_4^- band at 1154 cm^{-1} band appears at 1156 cm^{-1} in spectrum of [Cu(CO)(2,2N3-d_5)]I.
‡ CH_2 twisting vibrations are very coupled to the NH_2 twisting vibrations in the 2,2N3 compounds.
a Masked by BPh_4^- band at 1264 cm^{-1}.
b Masked by BPh_4^- bands at 627 and 615 cm^{-1}.
c Shoulder band.
d Masked by BPh_4^- absorption at 461 cm^{-1}. Occurs at 466 cm^{-1} in the spectrum of [Cu(CO)(2,2N3-d_5)]I.
e Occurs in the spectrum of [Cu(CO)(2,2N3)]BF_4.
f νCu-CO band is masked in all three isotopomers by the BPh_4^- bands at 481 and 461 cm^{-1} occurring in this region. A weak intensity band appears at 496 cm^{-1} in the spectrum of [Cu(CO)(2,2N3-d_5)]I. No band was observed in the spectrum of [Cu(CO)(2,2N3)]I as the νCu-CO bands possibly overlaps with the intense band observed for ν_{48} at 504 cm^{-1}.
g Masked by BPh_4^- absorption at 279 cm^{-1}. Occurs at 285 cm^{-1} in the spectrum of [Cu(CO)(2,2N3-d_5)]I.
h Masked by BPh_4^- absorption at 250 cm^{-1}. The band occurs at 252 cm^{-1} in the spectrum of [Cu(CO)(2,2N3)]I.

The NH_2 wagging modes, ν_{32} and ν_{33}, are observed as two bands occurring at 1113 and 1083 cm^{-1} in the spectra for [CuA(2,2N3)]BPh_4 (A = CO, ^{13}CO) and as one intense band at 779 cm^{-1} in the -d_5 isotopomer.

The δN-H vibration, ν_{44}, is coupled to the νC-N-C vibration and occurs at 798 cm^{-1} in the spectrum for [CuA(2,2N3)]BPh_4 (A = CO, ^{13}CO) and at 689 cm^{-1} in the -d_5 analogue. This vibration was not assigned by Watt and Klett [61].

The NH_2 rocking vibrations were previously assigned [61] as occurring at *ca*. 730 and 690 cm^{-1}. They have been assigned at a lower frequency value in the present work. Although both bands (ν_{45} and ν_{46}) in the [CuA(2,2N3)]BPh_4 (A = CO, ^{13}CO) are masked by the intense BPh_4^- absorptions occurring in the 630–600 cm^{-1} region, they occur at 650 and 600 cm^{-1} in the spectrum for the [Cu(CO)(2,2N3)]I compound and at 633 and 590 cm^{-1} in the spectrum for the [Cu(CO)(2,2N3)]BF_4 compound. The NH_2 rocking vibrations are the most sensitive of all the NH_2 vibrations to a change in anion.

3.3.3.2.2. CO vibrations

The νCO stretching frequency occurs at 2080 cm^{-1} and a weak shoulder band occurring at 2032 cm^{-1} can readily be assigned to $\nu^{13}CO$. The spectrum of the [Cu(^{13}CO)(2,2N3)]BPh_4 isotopomer shows a very weak band at 2080 cm^{-1} and two intense bands at 2032 cm^{-1} and 1984 cm^{-1}. The first one corresponds to the $\nu^{13}CO$ stretch and the second one to the $\nu^{13}C^{18}O$ stretch on the basis of the ratio obtained by means of the simple harmonic diatomic oscillator approximation.

Cu-CO bends are highly coupled vibrations that occur in the 300-400 cm^{-1} region. They will be further discussed in section 3.3.3.2.5.

3.3.3.2.3. CH_2 vibrations

The νC-H stretching vibrations occur in the 2950 and 2890 cm^{-1} region and are basically impervious to deuteration of the triamine system. The calculated frequency values for these eight vibrations show that they occur very close in energy and the bands overlap in the experimental spectra for the different isotopomers prepared. Asymmetric and symmetric stretches occur in the 2940-2950 cm^{-1} region for the former and at 2880-2890 cm^{-1} for the latter. The CH_2 scissoring modes (ν_{17}–ν_{20}) are the less coupled of the bending modes, and are observed as absorptions

occurring in the 1450-1460 cm^{-1} region. The CH_2 wagging modes ($\nu_{22}-\nu_{25}$) occur in the 1340-1390 cm^{-1} region and the shifts obtained upon deuteration of the compound increase as the coupling to the N-H vibrations increases. The 1110-1310 cm^{-1} region shows considerable coupling occurring between the CH_2 twisting vibrations ($\nu_{26}-\nu_{29}$) and the NH_2 twisting vibrations as well as the δN-H bending mode. The CH_2 rocking vibrations (ν_{38}, $\nu_{41}-\nu_{43}$) occur in the 800-980 cm^{-1} region, but couple extensively to the C-C and C-N modes as well as the NH_2 rocking modes.

3.3.3.2.4. C-C and C-N vibrations

Twelve normal modes of vibration are expected for the C-N skeleton [61], of which six are stretching modes and six are bending modes. Of these, 2 νC-C, 2 νC-NH-C and 2 νC-NH_2 are expected. The vibrations occurring in the 940–1060 cm^{-1} region are very coupled and cannot be assigned exclusively to one vibration in particular as was previously discussed. Bands $\nu_{34}-\nu_{40}$ (excluding ν_{38}, a CH_2 mode) have been assigned to the C-N and C-C vibrations on the basis of the isotopic shifts obtained for the C-13 and N-15 isotopomers (table 3.3.2) and the displacement diagrams obtained. Lower energy modes assigned as ring deformations are ν_{47} and ν_{48} and the CH_2 torsion modes occur predominantly as modes ν_{59}, and $\nu_{51}-\nu_{63}$ but are highly coupled to other Cu-L low energy vibrations.

3.3.3.2.5. Cu-N and Cu-CO vibrations

The νCu-CO stretching vibration, ν_{49}, is masked by absorptions due to the tetraphenylborate anion. The band is expected to occur at *ca*. 490 cm^{-1} and a band is indeed observed at 498 cm^{-1} in the spectrum for the $[Cu(CO)(2,2N3)]BF_4$ compound. However, the intense BPh_4^- absorptions occurring at 481 and 462 cm^{-1} mask the absorption for all the isotopomers studied. Three νCu-N frequencies are obtained for the compound, ν_{50}, ν_{51} and ν_{53}. The first of these, ν_{50}, occurs as a shoulder band at *ca*. 437 cm^{-1} where a weak absorption is also obtained for the $NaBPh_4$ compound. It is the principal νCu-NH vibration but is strongly coupled to the ν_sCu-N_2 from the displacement diagrams obtained (figures 3.3.10-3.3.12) and the calculated isotopic shifts obtained upon N-15 and -d_1, -d_4 and -d_5 labelling. Mode 50 has been assigned as occurring at 437 cm^{-1} and shifts to 419 cm^{-1} on -d_5 labelling. Mode 51, ν_aCu-N_2, occurs at 405 cm^{-1} and shifts to 390 cm^{-1} upon -d_5 labelling of the triamine system. Mode 53 is the third Cu-N vibration, ν_sCu-N_2, which is strongly coupled to the δCu-C≡O vibration, as can be seen from the displacement diagrams (figures 3.3.10-3.3.12) and the calculated shifts shown on table 3.3.2. This band occurs at 371

cm^{-1} in the far ir spectrum for the unlabelled compound and shifts to 364 cm^{-1} upon ^{13}CO labelling and to 354 cm^{-1} upon -d_5 labelling, further supporting the extent of coupling occurring in the low energy region as previously stated. Mode 55 has been assigned as the predominant δCu-C≡O vibration, which [1] in the spectrum for the unlabelled compound occurs at 328 cm^{-} and shifts to 318 cm^{-1} upon ^{13}CO labelling. It is, however, highly coupled to the ν_sCu-N_2 and νCu-NH vibrations and shifts to 290 cm^{-1} on -d_5 labelling. The out-of-plane bend, πCu-C≡O, is strongly coupled to the π_aHN-Cu-N_2 vibration and occurs as modes 54 and 56. Mode 54 at 345 cm^{-1} in the unlabelled compound, shifts to 335 cm^{-1} and 327 cm^{-1} upon ^{13}CO and -d_5 labelling respectively. Mode 56 in the unlabelled compound occurring at 303 cm^{-1} is obtained at 304 cm^{-1} and *ca*. 280 cm^{-1} respectively in the spectra for the ^{13}CO and -d_5 isotopomers. Assignments for the low energy modes 56-63 are complicated by the fact that absorptions for the [CuAL]BPh_4 compounds (A = CO, ^{13}CO; L = 2,2N3, 2,2N3-d_5) are extremely weak and masked by tetraphenylborate absorptions occurring in this region, as can be seen in figure 3.3.15. The assignments performed for these fundamentals rely strongly on the spectra obtained for the iodide derivatives [Cu(CO)L]I (L = 2,2N3, 2,2N3-d_5), which are shown in figure 3.3.16. Table 3.3.6 shows the experimental frequencies obtained for the low energy vibrations in the [Cu(CO)L]Y (L = 2,2N3 and 2,2N3-d_5; Y = BPh_4, I) compounds. In the spectrum for the unlabelled iodide derivative the symmetric umbrella bend, δ_sHN-Cu-N_2, occurs at 282 cm^{-1} and shifts to 274 cm^{-1} upon -d_5 labelling. Mode 58, assigned as the πHN-Cu-CO bend, occurs at 252 cm^{-1} and shifts to 238 cm^{-1} upon -d_5 labelling for the iodide derivatives. This mode is coupled to a CH_2 torsional mode and a π_aHN-Cu-N_2 vibration, and is masked by a medium to weak intensity tetraphenylborate absorption occurring at 250 cm^{-1} in the [CuA(2,2N3)]BPh_4 (A = CO, ^{13}CO) derivatives. Mode 59, a δ_sCu-N_2 coupled mode, occurs at 224 cm^{-1} in the unlabelled iodide derivative and shifts to 218 cm^{-1} upon -d_5 labelling. Mode 60, the principal δ_sCu-N_2 vibration in the unlabelled iodide derivative, occurs at 167 cm^{-1} and shifts to 153 cm^{-1} upon -d_5 labelling. The remaining modes, 61 to 63, correspond to highly coupled τCH_2 vibrations.

3.3.4. [Cu(CO)(*n*,*m*N3)]$^+$ compounds

As was previously mentioned, the [Cu(CO)(*n*,*m*N3)]$^+$ complex cations and [Cu(*n*,*m*N3)]$^+$ fragments were modelled by means of DFT using the 6-31G** and 6-31 + G* basis sets. Calculated parameters (ionization potential, *I*; electron affinities, *A*; electronegativities, χ; global hardness, η, and global softness, *S*) are shown in table 3.3.7. Fukui function values for nucleophilic and electrophilic attacks for the donor atoms in the triamine ligands, in the CO

species as well as the Cu(I) atom are shown in table 3.3.8. Although the differences are subtle, it can be seen that the compound with the largest η value is that with the 2,2N3 ligand and the one with the lowest value is that with the 3,3N3 ligand.

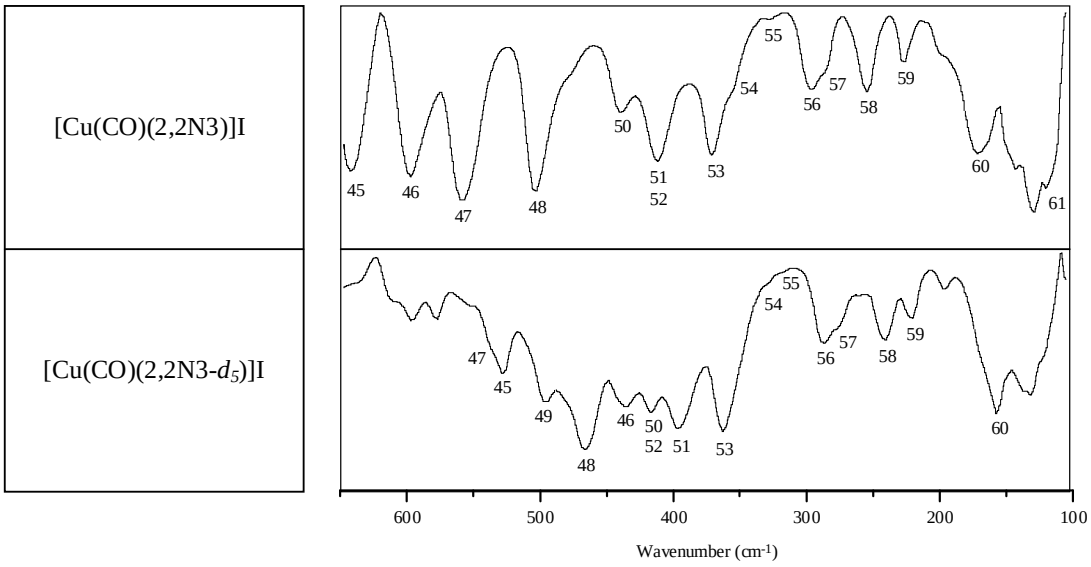

Figure 3.3.16 . Far ir spectra of [Cu(CO)L]I compounds (L = 2,2N3, 2,2N3-d_5). Numbering scheme refers to assignments shown in tables 3.3.2, 3.3.4 and 3.3.5.

Table 3.3.6. Experimental frequencies and assignments in the low energy region for [Cu(CO)L]Y compounds, where L = 2,2N3; 2,2N3-d_5 and Y = BPh_4, I. All frequency values in cm^{-1}.

Vibration	[Cu(CO)(2,2N3)Y		[Cu(CO)(2,2N3-d_5)Y		Assignment
	Y = BPh_4	Y = I	Y = BPh_4	Y = I	
ν_{49}	498[a]	—	—	496	νCu-CO
ν_{50}	437	439	419	416	νCu-NH+ ν_sCu-N_2 + δCu-C≡O
ν_{51}	405	411	390	395	ν_aCu-N_2 + πCu-C≡O
ν_{52}	405	411	390	395	τCH_2 + δHN-Cu-CO
ν_{53}	371	370	354	361	ν_sCu-N_2 + νCu-NH + δCu-C≡O
ν_{54}	345	354	327	325	π_aHN-Cu-N_2 + πCu-C≡O
ν_{55}	328	327	290	317	δCu-C≡O + ν_sCu-N_2 + νCu-NH
ν_{56}	303	293	279[b]	285	πCu-C≡O + π_aHN-Cu-N_2
ν_{57}	290	282	262	274	τCH_2 + δ_sHN-Cu-N_2
ν_{58}	250[b]	252	228	238	πHN-Cu-CO + τCH_2 + π_aHN-Cu-N_2
ν_{59}	225	224	205	218	δ_sCu-N_2
ν_{60}	150	167	133	153	δ_sCu-N_2 + τCH_2
ν_{61}	113	115	98	98	τCH_2 + π_aHN-Cu-N_2 + πCu-C≡O
ν_{62}	—	98	90	88	δHN-Cu-CO + τCH_2
ν_{63}	92	80	—	71	τCH_2 + πHN-Cu-CO

a Value obtained in the spectrum for [Cu(CO)(2,2N3)]BF_4.
b Masked by tetraphenylborate absorption.

Table 3.3.7. Calculated parameters for $[Cu(CO)(n,mN3)]^+$ complex cations and $[Cu(n,mN3)]^+$ fragments obtained with the 6-31G** and 6-31 + G* basis sets. All values in eV.

Compound	6-31G**					6-31 + G*				
	I	*A*	χ	η	*S*	*I*	*A*	χ	η	*S*
$[Cu(CO)(2,2N3)]^+$	11.67	–2.50	4.59	7.09	0.0706	11.86	–2.96	4.45	7.41	0.0675
$[Cu(2,2N3)]^+$	10.69	–3.08	3.81	6.88	0.0727	11.00	–3.44	3.78	7.22	0.0693
$[Cu(CO)(2,3N3)]^+$	11.59	–2.42	4.58	7.00	0.0714	11.76	–2.93	4.41	7.35	0.0681
$[Cu(2,3N3)]^+$	10.55	–3.03	3.76	6.79	0.0737	10.86	–3.39	3.74	7.12	0.0702
$[Cu(CO)(2,4N3)]^+$	11.61	–2.36	4.62	6.99	0.0716	11.79	–2.89	4.45	7.34	0.0681
$[Cu(2,4N3)]^+$	10.69	–2.93	3.88	6.81	0.0734	11.07	–3.30	3.88	7.19	0.0696
$[Cu(CO)(3,3N3)]^+$	11.40	–2.35	4.53	6.87	0.0723	11.57	–2.87	4.35	7.22	0.0693
$[Cu(3,3N3)]^+$	10.31	–2.86	3.73	6.58	0.0760	10.65	–3.22	3.72	6.93	0.0721
$[Cu(CO)(3,4N3)]^+$	11.46	–2.30	4.58	6.88	0.0727	11.65	–2.85	4.40	7.25	0.0690
$[Cu(3,4N3)]^+$	10.32	–2.89	3.72	6.61	0.0757	10.72	–3.29	3.72	7.00	0.0714

An interesting feature of the triamine systems prepared, is the variation of the νCO stretching frequencies, the highest of these values obtained for the 2,2N3 species and the lowest for the 3,3N3 species. These are also the compounds for which the largest and lowest values of η were obtained by means of both basis sets employed. The mid ir spectra of these compounds in the νNH and νCO regions is shown in figure 3.3.17 and the values obtained for some of the vibrations occurring in this region are shown in table 3.3.9. The $[Cu(CO)(n,mN3)]BPh_4$ compounds were prepared due to the enhanced stability towards oxidation that appears to be linked to the very voluminous tetraphenylborate anion. The $[Cu(CO)(n,mN3)]BPh_4$ compounds are very insoluble and basically quantitative yields were obtained. Successful preparation of [Cu(CO)(2,2N3)]I and $[Cu(CO)(2,2N3)]BF_4$ was achieved, however, the compounds were obtained in very poor yields, and are difficult to isolate and extremely moisture and air-sensitive, with fast oxidation to Cu(II) observed.

From the experimental and calculated values it can be seen that the 2,2N3 system has the highest value associated to the CO stretch. The frequencies for the 2,3N3, 3,3N3 and 3,4N3 systems vary only slightly between 2070 and 2064 cm^{-1}. The calculated CO stretching frequencies follow the same trend as the experimental values, despite the fact that the differences are subtle, especially between the 3,3N3 and 3,4N3 systems. Interestingly, the trend observed for the CO stretching frequencies is the same as that obtained for the η values, suggesting its employment as a good indicator of global hardness.

Table 3.3.8. Fukui function values for nucleophilic (f^+) and electrophilic (f^-) attack for the Cu, C, O and N_i, (i = 1, 2, 3) atoms in the triamine systems obtained with the 6-31G** and 6-31 + G* basis sets. Columns on the left show the values obtained for the fragments after removal of the CO ligand.

Compound	Atom	6-31G**				6-31 + G*			
		f^+		f^-		f^+		f^-	
$[Cu(CO)(2,2N3)]^+$	N_1	–0.054	–0.065	–0.029	–0.014	–0.191	–0.435	–0.020	0.008
	N_2	–0.049	–0.032	–0.009	0.003	–0.094	–0.050	0.050	–0.004
	N_3	–0.054	–0.065	–0.029	–0.014	–0.191	–0.434	–0.020	0.008
	ΣN_i	–0.157	–0.162	–0.067	–0.025	–0.476	–0.919	0.010	0.012
	Cu	0.730	0.533	0.480	0.306	0.080	0.510	0.422	0.474
	C		0.109		0.075		0.347		–0.134
	O		0.117		0.124		0.078		0.127
$[Cu(CO)(2,3N3)]^+$	N_1	–0.061	–0.068	–0.032	–0.020	–0.169	–0.528	–0.057	–0.001
	N_2	–0.047	–0.033	–0.014	0.000	–0.092	–0.088	0.021	–0.028
	N_3	–0.054	–0.062	–0.032	–0.014	–0.235	–0.433	–0.038	0.006
	ΣN_i	–0.162	–0.163	–0.078	–0.034	–0.496	–1.049	–0.074	–0.023
	Cu	0.716	0.529	0.480	0.302	0.018	0.541	0.445	0.470
	C		0.105		0.076		0.319		–0.144
	O		0.113		0.122		0.074		0.125
$[Cu(CO)(2,4N3)]^+$	N_1	–0.062	–0.071	–0.025	–0.016	–0.166	–0.667	–0.005	0.027
	N_2	–0.045	–0.036	–0.043	0.001	0.037	–0.099	–0.027	–0.017
	N_3	–0.052	–0.063	–0.025	–0.026	0.086	–0.477	–0.014	0.015
	ΣN_i	–0.159	–0.170	–0.093	–0.041	–0.043	–1.243	–0.046	0.025
	Cu	0.719	0.537	0.485	0.302	–0.180	0.782	0.418	0.414
	C		0.098		0.070		0.319		–0.170
	O		0.111		0.120		0.072		0.118
$[Cu(CO)(3,3N3)]^+$	N_1	–0.053	–0.074	–0.032	–0.018	0.072	–0.700	–0.047	0.018
	N_2	–0.045	–0.038	–0.020	–0.001	0.054	–0.030	0.014	–0.006
	N_3	–0.066	–0.057	–0.037	–0.022	–0.118	–0.533	–0.038	0.025
	ΣN_i	–0.164	–0.169	–0.089	–0.041	0.008	–1.255	–0.071	0.037
	Cu	0.725	0.540	0.464	0.281	–0.322	0.826	0.434	0.387
	C		0.096		0.070		0.401		–0.152
	O		0.111		0.116		0.068		0.117
$[Cu(CO)(3,4N3)]^+$	N_1	–0.055	–0.070	–0.027	–0.008	–0.243	–0.722	–0.026	0.038
	N_2	–0.048	–0.036	–0.025	0.002	–0.034	–0.024	–0.030	–0.005
	N_3	–0.059	–0.062	–0.043	–0.036	–0.061	–0.556	–0.076	0.002
	ΣN_i	–0.162	–0.168	–0.095	–0.042	–0.338	–1.302	–0.132	0.035
	Cu	0.705	0.546	0.478	0.286	–0.195	0.938	0.468	0.348
	C		0.095		0.068		0.324		–0.144
	O		0.111		0.115		0.068		0.110

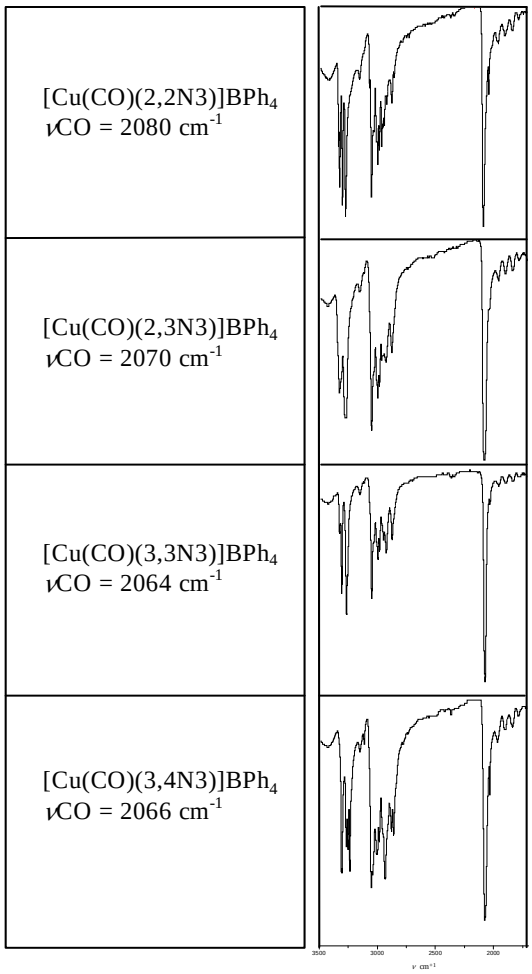

Figure 3.3.17. Mid ir spectra showing the νNH and νCO regions for the [Cu(CO)(*n*,*m*N3)]BPh_4 compounds.

ΔN, N_{CO}, N_{Cu} and N_{Di} values were calculated as was described in section 3.2.4 and are shown in table 3.2.7. In general, the systems follow the expected trend of more backbonding (larger ΔN) is experienced the more basic the triamine system bound to the Cu(I) atom. Larger ΔN values are obtained for the 2,3N3, 3,3N3 and 3,4N3 ligands and the lowest value is obtained for the 2,2N3 ligand. The values are consistent with the trend observed for the CO stretching frequency and would point to the fact π-backbonding from the metal to the CO ligand is slightly larger for the systems that have the most basic amines bound to the Cu(I) ion, as would be expected. However,

ΔN values must be taken with caution, as they are merely an approximation, as has been stated previously [40, 46, 47].

Table 3.3.9. Experimental and calculated frequency values (cm^{-1}) for some of the vibrations appearing in the mid ir spectra for the [Cu(CO)(*n*,*m*N3)]BPh_4 (*n* = 2, *m* = 2, 3 and *n* = 3, *m* = 3, 4) compounds prepared. Calculated values (unadjusted) are for the cationic species $[Cu(CO)(n,mN3)]^+$ from vibrational analyses using the 6-31G** basis set.

	2,2N3		2,3N3		3,3N3		3,4N3	
Vibration	Exp.	Calc.	Exp.	Calc.	Exp.	Calc.	Exp.	Calc.
$\nu_a NH_2$	3344	3561	3335	3563	3335	3548	3314	3549
	3334	3561	3335	3554	3335	3539	3277	3533
νN-H	3311	3527	3318	3513	3317	3505	3262	3480
$\nu_s NH_2$	3283	3488	3286	3500	3275	3487	3262	3480
	3283	3487	3277	3486	3275	3479	3246	3473
νCO	2080	2176	2070	2173	2064	2165	2066	2166
δNH_2	1592	1673	1581	1673	1582	1669	1586	1668
	1592	1669	1581	1672	1582	1669	1586	1664
νCu-CO[a]	498[b]	477		474		462		462

a Experimental frequencies for the νCu-CO vibration have been left unassigned. Although weak intensity bands appear in the 450-500 cm^{-1} region in the far ir spectra for these compounds, unambiguous assignments could not be performed.
b From $[Cu(CO)(2,2N3)]BF_4$

The number of electrons transferred from the CO ligand to the Cu ion, N_{CO}, is greater for the 2,2N3 system, where σ-bonding is expected to be more significant than for the other more basic triamines. The number of electrons on the Cu atom due to its interaction with CO was calculated by means of a Mulliken population analysis as $N_{Cu} = N_{Cu}[Cu(CO)L]^+ - N_{Cu}[CuL]^+$ and the number of electrons on the donor atoms that are transferred due to the interaction of the $[CuL]^+$ system with CO was calculated as $N_{Di} = \Sigma(N_{Di}[CuL]^+ - N_{Di}[Cu(CO)L]^+)$ as was discussed in section 3.2.4. N_{CO} and N_{Cu} exhibit a linear dependence, and both quantities decrease with increasing basicity of the *n*,*m*N3 ligands. The results are in good agreement with the expected trend of less electron transfer from the CO ligand to the Cu(I) atom, the more basic the triamine ligand employed. It is interesting to note that the calculated νCu-CO frequencies decrease with increasing basicity of the *n*,*m*N3 ligand, with the same trend being observed for the experimental CO stretching frequency. Graphs of N_{CO} *vs*. N_{Cu} and N_{CO}, N_{Cu} *vs*. average pK_a are shown in figures 3.3.18 and 3.3.19.

At a local level, employment of the Fukui function values as a reactivity index at the metal centre in both the triamine fragments and the carbonyl compounds, reveals no significant differences

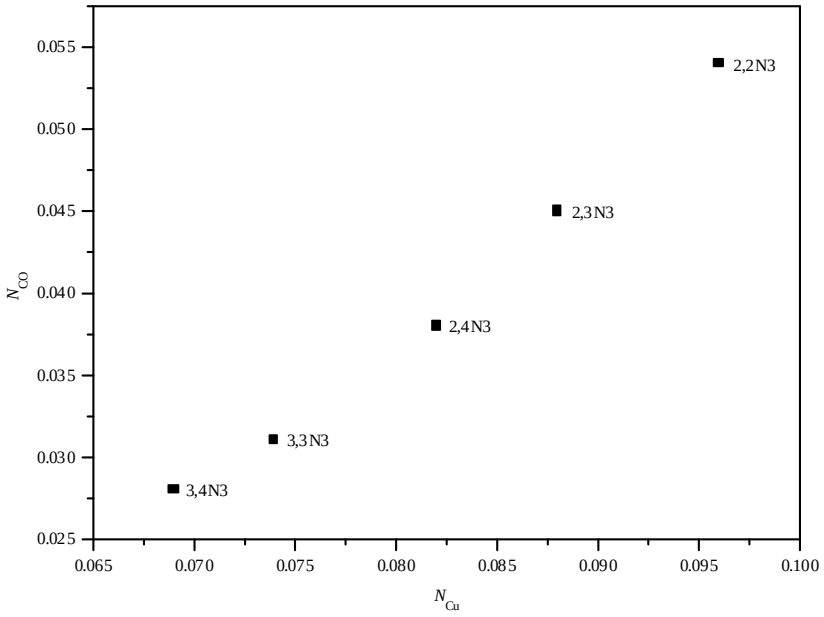

Figure 3.3.18. Graph of N_{CO} *vs.* N_{Cu} for $[Cu(CO)(n,mN3)]^+$ compounds.

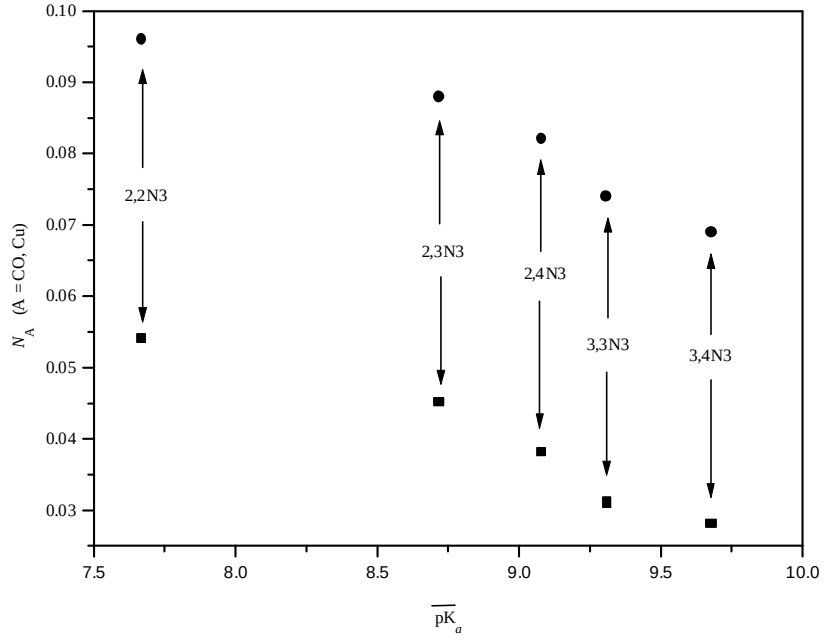

Figure 3.3.19. Graph of N_{CO} (squares) and N_{Cu} (circles) for $[Cu(CO)(n,mN3)]^+$ compounds *vs.* average pK_a value for *n*,*m*N3 ligands.

and values vary very little from one another. For the triamine fragments, $[Cu(n,m\text{N3})]^+$, f^+_{Cu} values follow the trend 2,2N3 > 3,3N3 > 2,4N3 > 2,3N3 > 3,4N3 although differences are quite subtle (values obtained with the 6-31G** basis set have been employed). f^+_{Cu} values in the carbonyl compounds, $[Cu(CO)(n,m\text{N3})]^+$, vary in the following sequence, 3,4N3 > 3,3N3 > 2,4N3 > 2,2N3 > 2,3N3. No stronger conclusions can be drawn from these results except that interaction with the CO ligand modifies the electronic distribution around the Cu(I) ion and alters the reactivity of the atom in the compound towards a nucleophile.

Ambundo *et al.* [2] studied the influence of the coordination geometry upon Cu(II/I) redox potentials for twelve copper tripodal ligand complexes. Their results showed that Cu(I) stability constants are relatively invariant and that the Cu(I) ion exhibits little preference for one type of donor atom over another or for ring size of the chelated systems. Few studies have been performed on the redox potentials of Cu(I) triamine carbonyl systems. Zanello and Leoni [60] studied the electrochemical behaviour of the compounds with the 2,2N3 ligand and the N-methyl derivative of the 3,3N3 ligand, $H_2N\text{-}(CH_2)_3\text{-}N(CH_3)\text{-}(CH_2)_3\text{-}NH_2$. Their results revealed that the carbonyl compound with the N-methyl derivative of the 3,3N3 ligand can be more easily oxidized to the Cu(II) species than the 2,2N3 carbonyl compound and more easily reduced to the Cu(0) species as well. In an oxidation reaction the f^-_{Cu} values could be employed if electron loss is considered as a reaction with an electrophile. Larger values of f^-_{Cu} would be expected for the N-methyl derivative of the 3,3N3 ligand over the 2,2N3 ligand. Unfortunately, no data could be found for the $[Cu(CO)(3,3\text{N3})]^+$ compound. The values obtained in this work would point towards oxidation being simpler for the 2,2N3 derivative than for the 3,3N3 derivative.

3.3.5. Interaction energies for the $[Cu(CO)(n,m\text{N3})]^+$ compounds

Interaction energies between the $[Cu(n,m\text{N3})]^+$ fragments and CO were calculated for the compounds modelled and are shown in table 3.3.10. The values obtained are indicative of increasing stability in the reaction between the $[Cu(n,m\text{N3})]^+$ as an electrophile and CO in the following order: 2,2N3 > 2,3N3 > 2,4N3 > 3,3N3 > 3,4N3, as would be expected in terms of increasing basicity of the ligands employed. The more electron enriched the Cu(I) atom, the less the interaction energy with the CO ligand. It is interesting to note that $(\Delta E_{int})_{Cu}$ follows the trend established by the average pK_a values for the ligands, with the less basic ligand 2,2N3 having a greater interaction energy with CO than the other systems. Although σ-bonding from the CO ligand to the Cu(I) ion is not the only feature present in the Cu-CO bond in these systems, it seems that the average electronic properties of the triamine ligands are actually transmitted to the

Cu(I) ion in terms of its reactivity towards nucleophiles. As the Cu(I) atom becomes more electron enriched due to its interaction with a better σ-donor, it will become a poorer electrophile. The λ values calculated as $\lambda = N_{Cu} = N_{Cu}[Cu(CO)(n,mN3)] - N_{Cu}[Cu(n,mN3)]$, are also consistent with the Cu(I) species becoming a poorer electrophile as its electron density is enriched by interaction with the different *n*,*m*N3 ligands. A graph of average interaction energies *vs.* average pK_a values for the triamine systems is shown in figure 3.3.20.

Table 3.3.10. Interaction energies, $(\Delta E_{int})_{Cu}$, for the interaction between $[Cu(n,mN3)]^+$ fragments and CO. Values in kcal/mol.

Compound	λ	ΔE_v	ΔE_μ	$(\Delta E_{int})_{Cu}$
$[Cu(CO)(2,2N3)]^+$	0.096	–1.74	–9.51	–11.26
$[Cu(CO)(2,3N3)]^+$	0.088	–1.82	–8.74	–10.56
$[Cu(CO)(2,4N3)]^+$	0.082	–1.64	–8.14	–9.78
$[Cu(CO)(3,3N3)]^+$	0.074	–1.91	–7.21	–9.12
$[Cu(CO)(3,4N3)]^+$	0.069	–1.89	–6.82	–8.71

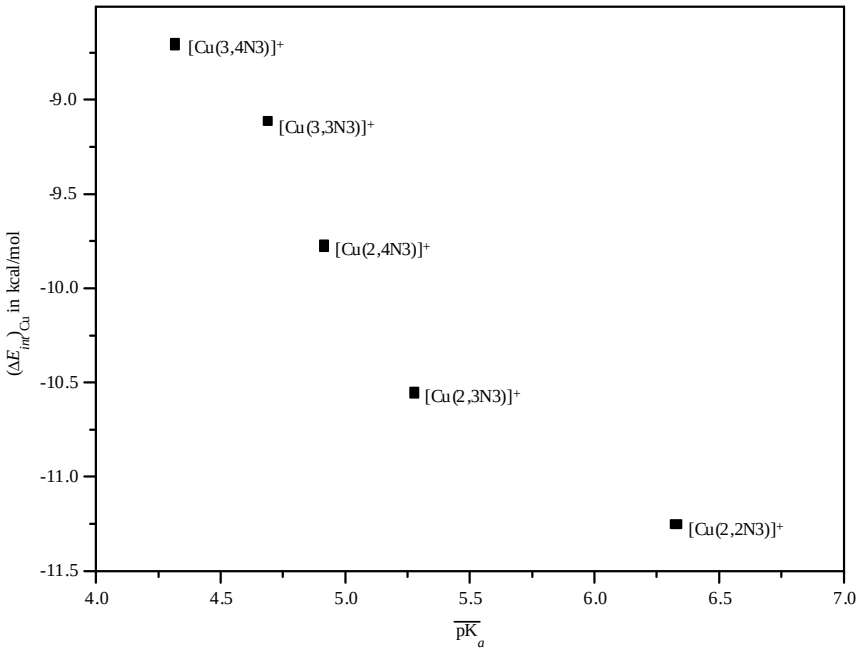

Figure 3.3.20. Interaction energies, $(\Delta E_{int})_{Cu}$, between $[Cu(n,mN3)]^+$ fragments and CO *vs.* average pK_a values for the *n*,*m*N3 ligands.

3.4. Cu(I) carbonyl compounds with Schiff bases

Cu(I) carbonyl compounds with Schiff base ligands form stable compounds and several of these have been characterized by means of XRD studies [4, 76-79]. Schiff base derivatives were prepared in the present study by reaction of the 2,2N3 ligand with *p*-substituted benzaldehydes to determine the effect of the substituents on the aromatic ring on the CO stretching frequency. The structure of the $[Cu(CO)\{2,2N3(C_6H_4X)_2\}]BPh_4$ compounds is shown in figure 3.4.1. Single crystals were obtained and the crystal structure determined for the compound where X = H. The compounds were modelled by means of DFT calculations at the B3LYP level with the 6-31G** basis set and HSAB descriptors were calculated as was previously described. Unfortunately, vibrational analyses could not be performed successfully for the simplest of the systems studied, $[Cu(CO)\{2,2N3(C_6H_5)_2\}]^+$, perhaps due to the large number of electrons in the system.

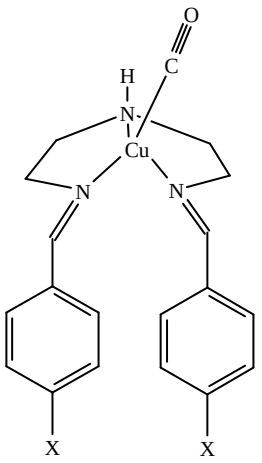

Figure 3.4.1. Structure for the $[Cu(CO)\{2,2N3(C_6H_4X)_2\}]^+$ derivatives, X = NO_2, Me, MeO, F, Cl, Br, H, NMe_2.

3.4.1. Crystal structure of $[Cu(CO)\{2,2N3(C_6H_5)_2\}]BPh_4$ {*N*-Benzylidene-*N*'-[2-(benzyilidene-amino)-ethyl]-ethane-1,2-diamine}carbonylcopper(I) tetraphenylborate

Crystallographic data for the title compound is shown in table 3.4.1. Crystal structure parameters, bond lengths and angles, and average isotropic displacement parameters are shown in appendix 3.

Table 3.4.1. Crystallographic data for $[Cu(CO)\{2,2N3(C_6H_5)_2\}]BPh_4$

	$[Cu(CO)\{2,2N3(C_6H_5)_2\}]BPh_4$
Empirical formula	$C_{43}H_{41}BCuN_3O$
Fw	690.14
Crystal system	monoclinic
space group	P21/n (no. 14)
a (Å)	10.295(2)
b (Å)	23.869(5)
c (Å)	14.474(3)
α (deg)	90.00
β (deg)	91.07(3)
γ (deg)	90.00
V (Å^3)	3556.3(12)
Z	4
ρ_{calcd} (gcm^{-3})	1.2890(5)
Temp (K)	193(2)
λ (Mo Kα) (Å)	0.71073
μ (Mo Kα) (cm^{-1})	6.52
min-max 2θ (deg)	2.55-26.72
R	0.1088
WR	0.1412

The structure and labelling scheme for the compound is shown in figures 3.4.2 and 3.4.3. Selected bond lengths and angles for the compound are shown in table 3.4.2.

Table 3.4.2. Selected bond lengths (Å) and bond angles (degrees) for $[Cu(CO)\{2,2N3(C_6H_5)_2\}]^+$

Cu(1)-C(1)	1.797(4)	Cu(1)-C(1)-O(1)	176.8(4)
Cu(1)-N(1)	2.102(3)	N(1)-Cu(1)-C(1)	122.33(15)
Cu(1)-N(2)	2.067(3)	N(2)-Cu(1)-C(1)	132.41(15)
Cu(1)-N(3)	2.078(3)	N(3)-Cu(1)-C(1)	115.03(15)
C(1)-O(1)	1.121(4)	N(1)-Cu(1)-N(2)	85.29(12)
N(2)-C(6)	1.269(4)	N(1)-Cu(1)-N(3)	84.17(13)
N(3)-C(13)	1.271(5)	N(2)-Cu(1)-N(3)	104.88(11)

The coordination geometry for the Cu(I) atom is a distorted tetrahedron. Cu–N distances in the compound are slightly shorter for the imino nitrogens than the Cu–NH distance, 2.067(3) and 2.078(3) Å for the former and 2.102(3) Å for the latter. Interestingly, the differences observed for the Cu-N distances in the Schiff base carbonyl derivative are minimal when compared to those observed by Patch, *et al.* [17] in their dinuclear dicarbonyls with benzimidazole chelates where the Cu-N aromatic distances are close to 2 Å while the Cu-N(amine) distance is almost 2.6 Å.

The Cu–C distance is 1.797(4) Å and falls within the values usually reported for Cu(I) carbonyl compounds [4, 17, 76-79]. Selected bond lengths for related compounds are shown in table 3.4.3.

Table 3.4.3. Selected bond lengths in Å for Cu(I) carbonyl Schiff base compounds.

Compound	Cu-N	Cu-CO	Cu-Y	C-O
$[Cu(CO)\{2,2N3(C_6H_5)_2\}]BPh_4$	2.067(3), 2.078(3)	1.797(4)	2.102(3)	1.121(5)
$[Cu_2(CO)_2(TC–5,5)]$[79][a]	1.940(4), 1.938(6)	1.771(7)		1.128(9)
	1.922(5), 1.937(6)	1.749(9)		1.12(1)
$[Cu(CO)(C_2N_2Ph_2)I]$ [76][b]	2.058(8), 2.077(9)	1.800(9)	2.624(2)	1.12(2)
$[Cu(CO)(dad)(O_3SCF_3)]$ [78][c]	2.094(5), 2.070(4)	1.820(6)	2.64(1)	–
$[Cu(CO)(LBF_2)]$ [77][d]	2.165(2), 2.163(2),	1.780(3)		1.112(4)
	2.100(2), 2.108(2)			
NEt_4[Cu(CO)(DFGB)][4][e]	2.135	1.780(5)		1.122(7)
$[Cu_2(HL\text{-}Et)(CO)_2](CF_3SO_3)_2$ [17][f]	2.01(1), 1.96(1)	1.82(2)	2.59(1)	–
	2.03(1), 2.00(1)	1.77(2)	2.31(1)	

a TC-5,5 is the deprotonated tropocoronand ligand.
b $C_2N_2Ph_2$ is ethylenebis(benzaldimine); Y = I.
c dad is glyoxalbis(2,4-dimethylpentyl-3-imine); Y = O from O_3SCF_3.
d LBF_2 is difluoro-3,3'-(trimethylenedinitrilo)bis(2-butanone oximato)borate.
e DFGB is difluoro(glyoximato)borato.
f HL-Et is bis((1-ethyl-2-benzimidazolyl)methyl); Y = N.

The N-Cu-N angles formed between the Cu atom and the N donor atoms within the chelating ligand are quite similar, 85.29(12) and 84.18(13)° while the N2-Cu1-N3 angle is considerably larger and close to its value in an ideal tetrahedron with a value of 104.87(11)°. The structure is similar to that reported by Pasquali *et al.* [45] for the $[Cu(CO)(2,2N3)]BPh_4$ compound. Cu-N distances in both compounds are similar, and there is basically no difference between the Cu-NH_2 distances in the diethylenetriamine compound and its Schiff base derivative.

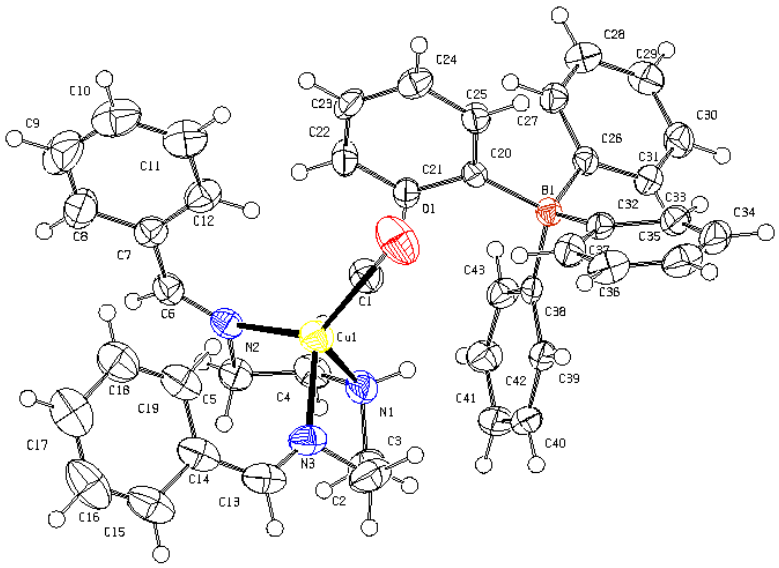

Figure 3.4.2. PLATON [80] drawing of $[Cu(CO)\{2,2N3(C_6H_5)_2\}]BPh_4$ showing the labelling scheme employed for all atoms.

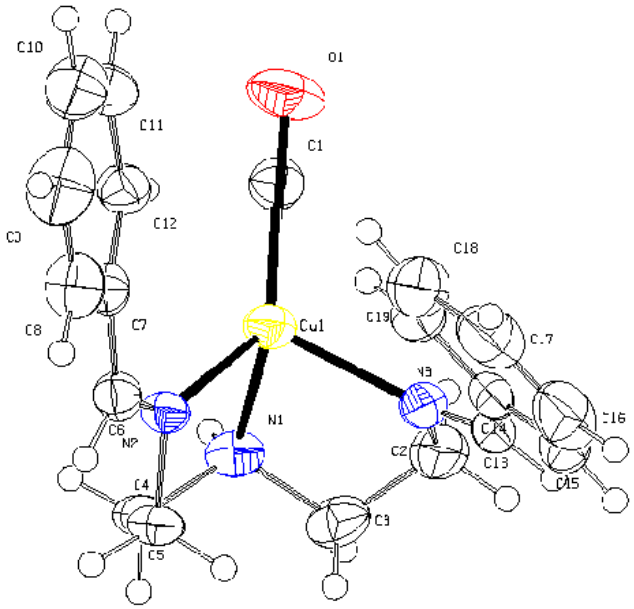

Figure 3.4.3. PLATON [80] drawing of the cationic moiety $[Cu(CO)\{2,2N3(C_6H_5)_2\}]^+$ and labelling scheme.

3.4.2. Molecular modelling of $[Cu(CO)\{2,2N3(C_6H_5)_2)\}]^+$ and $[Cu\{2,2N3(C_6H_4X)_2\}]^+$ species

Geometry optimization was performed on the $[Cu(CO)\{2,2N3(C_6H_5)_2\}]^+$ moiety and the cationic structure obtained closely resembled a conformational isomer of the cationic moiety obtained in the X-ray diffraction study. Hence, a conformer analysis of the optimized geometry obtained by DFT calculations was performed using MM. The comformers obtained through the molecular mechanics calculations were then optimized by means of DFT calculations to yield two stable species with identical energies. The structure of both conformers, one of which resembles the crystal structure, is shown in figure 3.4.4.

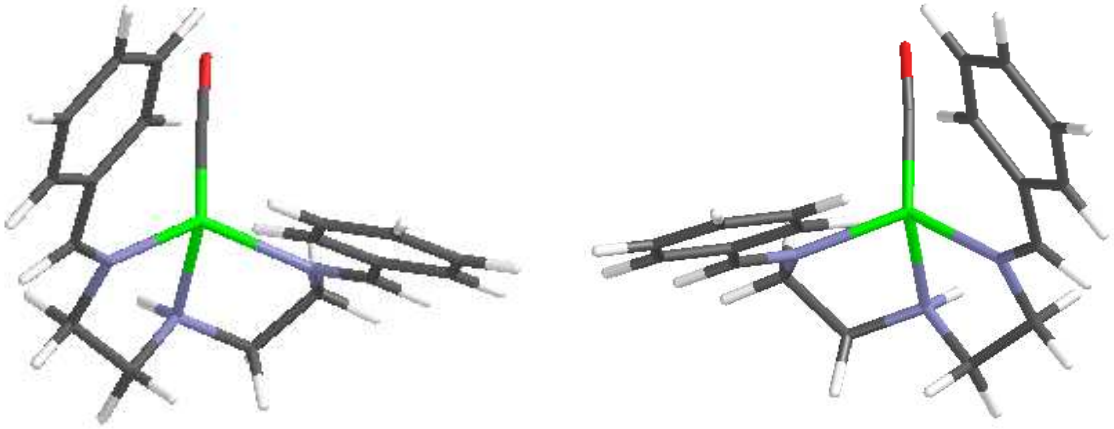

Figure 3.4.4. Stable conformers obtained by MM and DFT calculations for the cationic $[Cu(CO)\{2,2N(C_6H_5)_2\}]^+$ compound. The structure on the left most closely resembles that obtained by means of single crystal XRD.

Calculated bond distances and bond angles for the conformer that more resembles the crystal structure of the compound obtained were compared to experimental values. The calculated values are in good agreement with the experimental values obtained and graphs of calculated minus experimental bond distances, $\Delta r = r_{calc} - r_{exp}$, and angles, $\Delta\theta = \theta_{calc} - \theta_{exp}$, *vs.* the experimental values are shown in figures 3.4.5 and 3.4.6. Standard deviation values are 0.0163 Å and 4.493° for bond lengths and bond angles respectively. It can be seen from figure 3.4.6, that the N-Cu-N bond is most overestimated in the calculations. This was also observed for the $[Cu(CO)(2,2N3)]^+$ species as was previously mentioned. Bond lengths are slightly longer for the calculated molecules in the gaseous phase than those observed in the solid state.

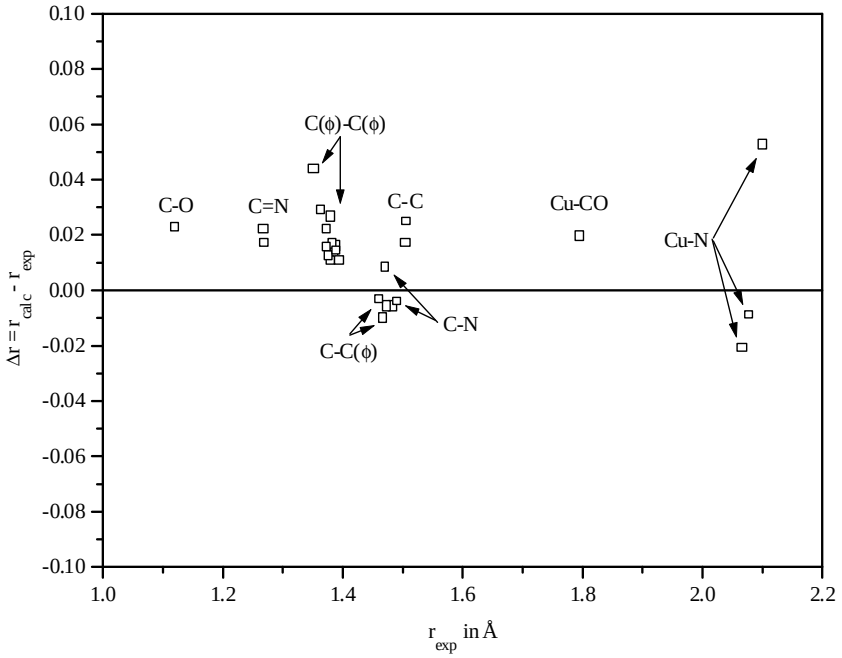

Figure 3.4.5. Graph of $\Delta r = r_{calc} - r_{exp}$ *vs.* r_{exp} for $[Cu(CO)\{2,2N3(C_6H_5)_2\}]^+$. Standard deviation between experimental and calculated values is 0.0163 Å.

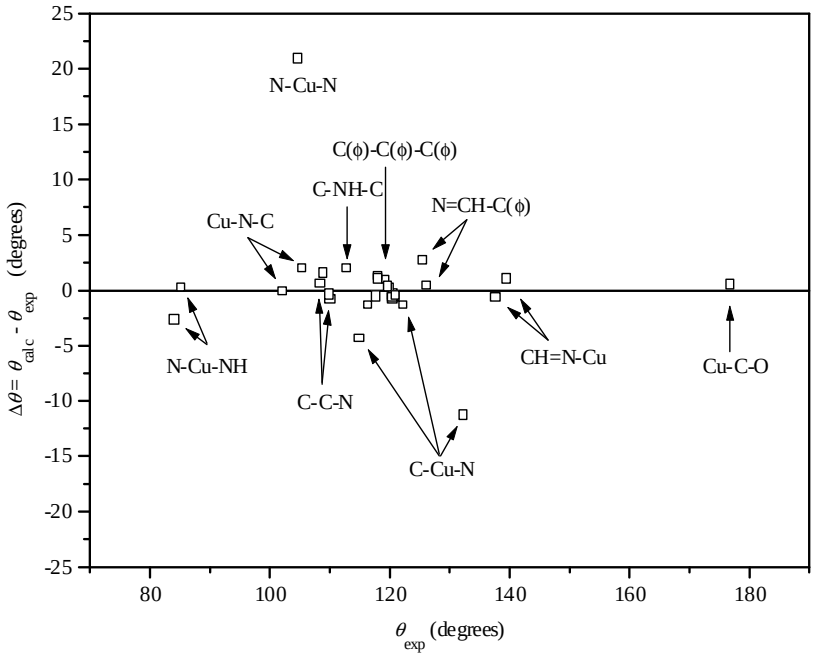

Figure 3.4.6. Graph of $\Delta\theta = \theta_{calc} - \theta_{exp}$ *vs.* θ_{exp} for $[Cu(CO)\{2,2N3(C_6H_5)_2\}]^+$. Standard deviation between experimental and calculated values is 4.493°.

Table 3.4.4. Parameters for $[Cu(CO)\{2,2N3(C_6H_4X)_2\}]^+$ cations in eV for geometry optimizations with 6-31G** basis set. First row for each X substituent shows parameters for the $[Cu(CO)\{2,2N3(C_6H_4X)_2\}]^+$ cations and second row for the $[Cu\{2,2N3(C_6H_4X)_2\}]^+$ fragments. All X substituents in position 4.

X	σ^a	I	A	χ	η	S	HOMO	LUMO
NO_2	0.78	11.02	–4.49	3.26	7.75	0.0645	–9.66	–5.78
		10.36	–4.43	2.97	7.40	0.0676	–8.59	–5.75
F	0.34	10.51	–3.54	3.49	7.02	0.0712	–9.18	–4.91
		9.90	–3.63	3.13	6.77	0.0739	–8.11	–4.97
Cl	0.23	10.44	–3.71	3.36	7.08	0.0706	–9.19	–5.04
		9.88	–3.63	3.13	6.76	0.0740	–8.16	–5.08
Br	0.23	10.36	–3.73	3.31	7.05	0.0710	–9.14	–5.03
		9.83	–3.81	3.01	6.82	0.0733	–8.15	–5.09
H	0.0	10.45	–3.47	3.49	6.96	0.0719	–9.10	–4.83
		9.81	–3.56	3.13	6.68	0.0748	–8.01	–4.90
CH_3	–0.17	10.23	–3.34	3.44	6.79	0.0737	–8.95	–4.67
		9.63	–3.43	3.10	6.53	0.0766	–7.88	–4.73
OCH_3	–0.27	9.90	–3.21	3.34	6.55	0.0763	–8.62	–4.54
		9.42	–3.31	3.05	6.36	0.0786	–7.77	–4.60
$N(CH_3)_2$	–0.60	8.93	–2.81	3.06	5.87	0.0851	–7.72	–4.06
		8.69	–2.94	2.87	5.81	0.0860	–7.33	–4.17

a Values taken from references 81 and 82.

Global parameters were calculated for all $[Cu(CO)\{2,2N3(C_6H_4X)_2\}]^+$ species and $[Cu\{2,2N3(C_6H_4X)_2\}]^+$ fragments modelled and are shown in table 3.4.4. It can be seen that the global hardness of a given molecule follows the trend established by the Hammett substituent parameters. Global hardness increases for electron-withdrawing substituents and decreases with electron-donating substituents (increasing global softness) as would be expected according to the HSAB theory. Figure 3.4.7 shows global hardness values for the $[Cu(CO)\{2,2N3(C_6H_4X)_2\}]^+$ species and the $[Cu\{2,2N3(C_6H_4X)_2\}]^+$ fragments *vs*. the Hammett substituent parameter. A comparison between hardness values for the Cu(I) complex cation with the 2,2N3 ligand and its Schiff base derivative $\{2,2N3(C_6H_5)_2\}$ shows that the former is a slightly harder species than the latter, with η values of 7.09 and 6.96 eV respectively. Interestingly, the difference between η values between the $[Cu(CO)\{2,2N3(C_6H_4X)_2\}]^+$ complex cations and the $[Cu\{2,2N3(C_6H_4X)_2\}]^+$ fragments, $\Delta\eta$, increases for electron-withdrawing substituents and is smaller for electron-donating substituents. Hence, reaction of the $[Cu\{2,2N3(C_6H_4X)_2\}]^+$ fragments with CO produces increasingly harder species than the hypothetical fragments the more electron-withdrawing the substituent is. According to Pearson's maximum hardness principle [52-54] and if $\Delta\eta$ can be considered as a driving force in the reaction of a $[CuL]^+$ fragment with CO to yield the $[Cu(CO)L]^+$ species, then the interaction of the $[CuL]^+$ species with CO would be favoured when

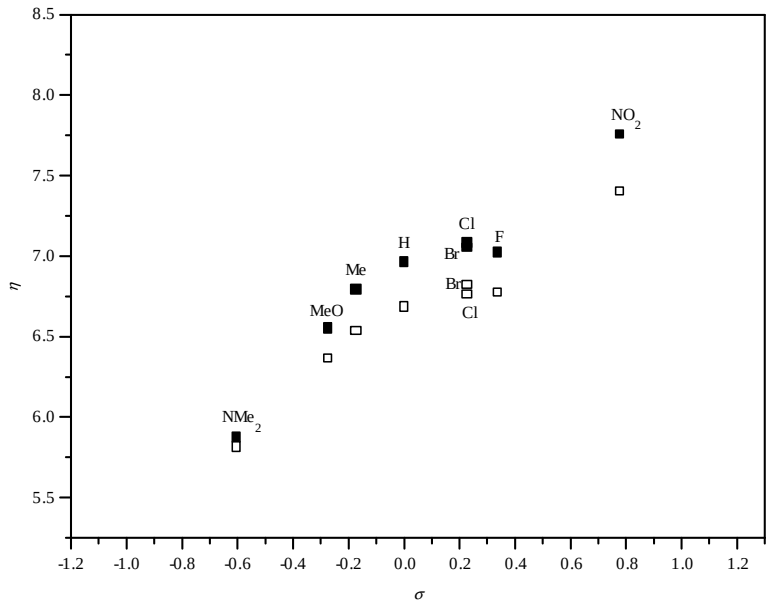

Figure 3.4.7. Global hardness, η, values for $[Cu(CO)L]^+$ compounds (solid squares) and $[CuL]^+$ fragments (hollow squares) *vs.* Hammett substituent parameter. L = 2,2N3$(C_2H_4X)_2$ and X = NO_2, F, Cl, Br, H, Me, MeO, NMe_2.

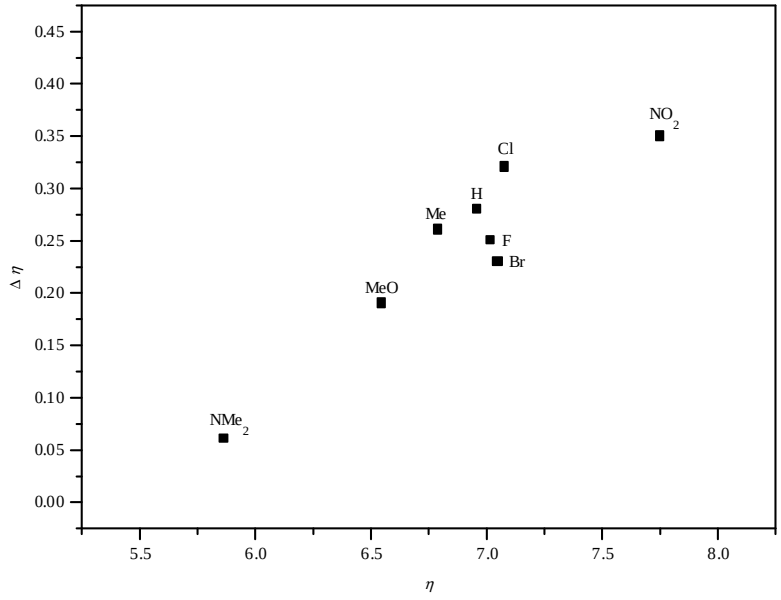

Figure 3.4.8. $\Delta\eta = \eta\{[Cu(CO)L]^+\} - \eta\{[CuL]^+\}$ *vs.* $\eta\{[Cu(CO)L]^+\}$, L = 2,2N3$(C_2H_4X)_2$ and X = NO_2, F, Cl, Br, H, Me, MeO, NMe_2.

L contains electron-withdrawing substituents. Figure 3.4.8 shows a graph of $\Delta\eta$ *vs.* η for the Schiff base derivatives.

Condensed Fukui functions calculated for the Cu(I) and donor atoms in the $[Cu(CO)\{2,2N3(C_6H_4X)_2\}]^+$ complex cations and $[Cu\{2,2N3(C_6H_4X)_2\}]^+$ fragments are shown in table 3.4.5. condensed Fukui function values for nucleophilic attack, f^+_{Cu}, for the $[Cu\{2,2N3(C_6H_4X)_2\}]^+$ fragments follow the trend NMe_2 > OMe > F > Me > H > Br > Cl > NO_2. The trend observed for the complex cations $[Cu(CO)\{2,2N3(C_6H_4X)_2\}]^+$ is NMe_2 > OMe > F > Me > H > Cl > Br > NO_2. Condensed local softness values for the Cu(I) atoms in the complex cations and fragments, $s^+_{Cu} = S f^+_{Cu}$, are shown in table 3.4.6. Condensed local softness values, s^+_{Cu}, *vs.* the substituent parameter for the compounds modelled are shown in figures 3.4.9 and 3.4.10. The trend obtained for the $[Cu(CO)\{2,2N3(C_6H_4X)_2\}]^+$ compounds has a good correlation with σ except for X = F, for which a larger than expected local softness is obtained. However, calculations involving X = F and NO_2 substituents have failed to yield the expected values in the past [59]. The trend obtained for the $[Cu\{2,2N3(C_6H_4X)_2\}]^+$ fragments correlates well with σ except for X = F and more noticeably for X = Cl, for which a very low value is obtained, where one close to that for the X = Br derivative is expected. No reasonable explanation could be given to account for this abnormal value. With very few exceptions, the local softness values obtained show that the Cu(I) ion becomes locally harder with electron-withdrawing substituents and softer with electron-donating substituents. These results are in good agreement with what would be expected from HSAB theory.

3.4.3. Infrared spectra of $[Cu(CO)\{2,2N3(C_6H_4X)_2\}]BPh_4$ compounds

The main aim of the study performed on Cu(I) carbonyl X-substituted Schiff base derivatives was to determine the effect of the different X substituents on the vibrational spectra of $[Cu(CO)\{2,2N3(C_6H_5)_2\}]BPh_4$ compounds and to determine the metal-ligand vibrations where possible. In order to facilitate this, labelling of $[Cu(CO)\{2,2N3(C_6H_5)_2\}]BPh_4$ was performed by deuterium-exchange of the NH group and ^{13}CO labelling. The spectra are quite complex due to the number of bands associated to the tetraphenylborate anion employed and the phenyl groups from the Schiff base ligand. A full vibrational assignment is hence, out of the scope of this work. However, some important conclusions can be arrived at by means of the labelling studies and the calculations performed for the triamine system $[Cu(CO)(2,2N3)]BPh_4$.

Table 3.4.5. Condensed Fukui function values for nucleophilic attack (f^+) and for electrophilic attack (f^-) for Cu and donor atoms in the $[Cu(CO)\{2,2N3(C_6H_4X)_2\}]^+$ compounds (right columns) and $[Cu\{2,2N3(C_6H_4X)_2\}]^+$ fragments (left columns) obtained with the 6-31G** basis set.

X	atom	f^+		f^-	
	N_1	0.018	0.020	–0.047	–0.031
	N_2	–0.014	–0.012	0.005	0.005
	N_3	0.021	0.022	–0.046	–0.030
NO_2	Cu	0.057	0.026	0.343	0.212
	C		0.012		0.053
	O		0.031		0.079
	N_1	0.004	0.015	–0.044	–0.019
	N_2	–0.022	–0.016	0.002	–0.002
	N_3	0.007	0.025	–0.045	–0.022
F	Cu	0.256	0.057	0.336	0.176
	C		0.027		0.047
	O		0.043		0.071
	N_1	0.019	0.017	–0.042	–0.016
	N_2	–0.016	–0.015	0.000	–0.003
	N_3	0.026	0.026	–0.043	–0.019
Cl	Cu	0.070	0.046	0.320	0.157
	C		0.020		0.043
	O		0.039		0.064
	N_1	0.006	0.017	–0.040	–0.013
	N_2	–0.020	–0.014	–0.001	–0.004
	N_3	0.009	0.026	–0.041	–0.016
Br	Cu	0.222	0.044	0.306	0.140
	C		0.020		0.039
	O		0.038		0.059
	N_1	0.008	0.025	–0.046	–0.025
	N_2	–0.022	–0.016	0.003	0.000
	N_3	0.004	0.017	–0.046	–0.024
H	Cu	0.247	0.053	0.341	0.193
	C		0.024		0.051
	O		0.042		0.075
	N_1	0.003	0.014	–0.043	–0.015
	N_2	–0.022	–0.016	0.001	–0.003
	N_3	0.007	0.024	–0.044	–0.019
CH_3	Cu	0.251	0.055	0.325	0.161
	C		0.025		0.045
	O		0.042		0.067
	N_1	–0.001	0.010	–0.034	0.000
	N_2	–0.022	–0.016	–0.004	–0.007
	N_3	0.004	0.023	–0.038	–0.007
OCH_3	Cu	0.275	0.062	0.287	0.103
	C		0.029		0.032
	O		0.044		0.051
	N_1	–0.005	0.009	–0.018	0.013
	N_2	–0.022	–0.016	–0.008	–0.009
	N_3	0.001	0.019	–0.023	0.008
$N(CH_3)_2$	Cu	0.284	0.063	0.205	0.038
	C		0.031		0.015
	O		0.043		0.031

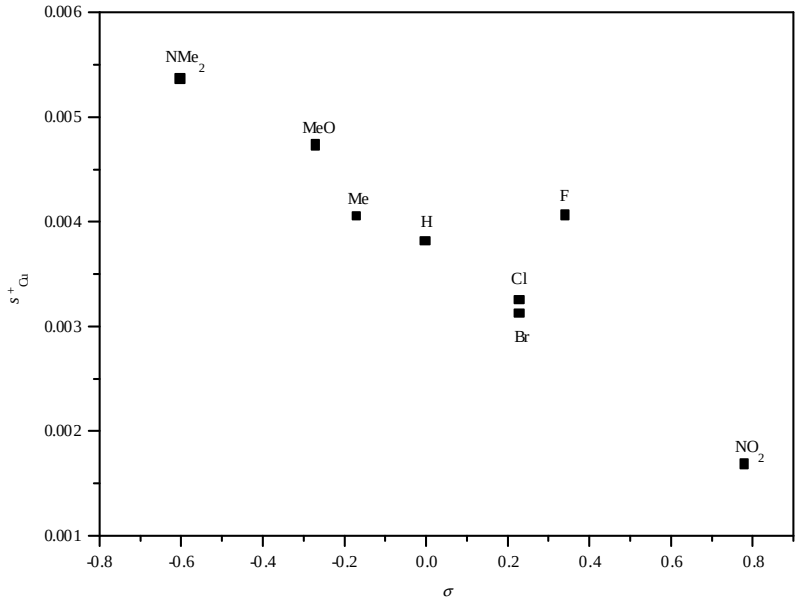

Figure 3.4.9. Condensed local softness, s^+_{Cu}, *vs.* Hammett substituent parameter for $[Cu(CO)L]^+$ compounds, L = {2,2N3($C_6H_4X)_2$} and X = NO_2, F, Cl, Br, H, Me, MeO, NMe_2.

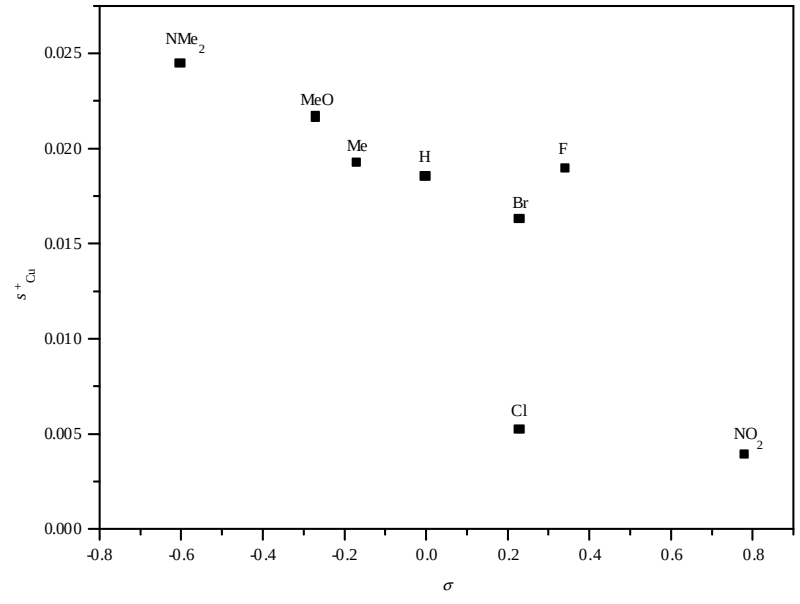

Figure 3.4.10. Condensed local softness, s^+_{Cu}, *vs.* Hammett substituent parameter for $[CuL]^+$ fragments, L = {2,2N3($C_6H_4X)_2$} and X = NO_2, F, Cl, Br, H, Me, MeO, NMe_2.

Table 3.4.6. Global softness, condensed Fukui function and condensed local softness values for the Cu(I) atoms in $[Cu(CO)L]^+$ compounds and $[CuL]^+$ fragments; L = $2,2N3(C_6H_4X)_2$ and X = NO_2, F, Cl, Br, H, Me, MeO, NMe_2. Global softness and condensed local softness values have been multiplied by a factor of 10. S and s^+_{Cu} values in eV.

X	$[Cu(CO)\{2,2N3(C_6H_4X)_2\}]^+$			$[Cu\{2,2N3(C_6H_4X)_2\}]^+$		
	S	f^+_{Cu}	s^+_{Cu}	S	f^+_{Cu}	s^+_{Cu}
NO_2	0.645	0.026	0.168	0.676	0.057	0.0385
F	0.712	0.057	0.406	0.739	0.256	0.1892
Cl	0.706	0.046	0.325	0.740	0.070	0.0518
Br	0.710	0.044	0.312	0.733	0.222	0.1627
H	0.719	0.053	0.381	0.748	0.247	0.1848
Me	0.737	0.055	0.405	0.766	0.251	0.1923
MeO	0.763	0.062	0.473	0.786	0.275	0.2162
NMe_2	0.851	0.063	0.536	0.860	0.284	0.2442

Table 3.4.7 shows some of the bands that could be assigned for the $[Cu(CO)\{2,2N3(C_6H_5)_2\}]BPh_4$ compound by means of the isotopic labelling studies performed and comparison with $[Cu(CO)(2,2N3)]BPh_4$. Mid ir spectra for the labelled compounds are shown in figures 3.4.11 and 3.4.12. Far ir spectra are shown in figure 3.4.13.

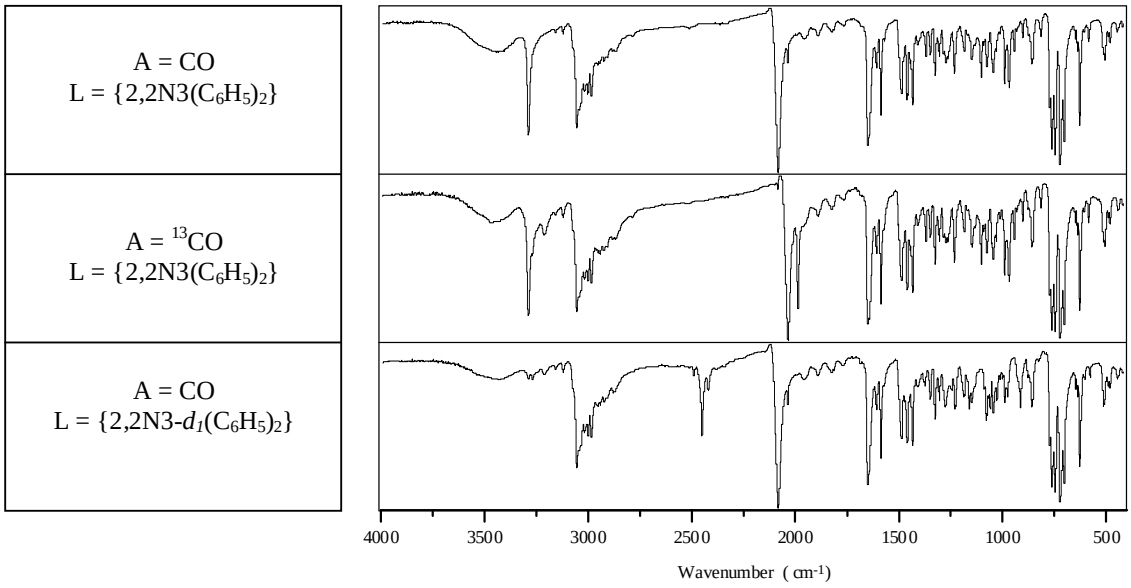

Figure 3.4.11. Mid ir spectra for $[CuAL]BPh_4$ compounds.

The νN-H stretching vibration occurs at 3292 cm^{-1} in the [CuA{2,2N3(C_6H_5)$_2$}]BPh_4 (A = CO, ^{13}CO) and shifts to 2448 cm^{-1} upon -d_1 labelling. The πN-H vibration appears at 1436 cm^{-1} in the spectra for the CO and ^{13}CO compounds, and appears in the spectrum of the -d_1 labelled species at 1150 cm^{-1}. This band could not be observed in the spectra of the 2,2N3 system as it overlapped with intense bands appearing in the region. The present study further confirms the assignment performed previously. The δN-H vibration appears at 802 cm^{-1} in the spectra for the CO and ^{13}CO compounds and is absent in the spectrum of the -d_1 labelled species as it overlaps with the intense absorptions due to the phenyl rings in the 680–780 cm^{-1} region.

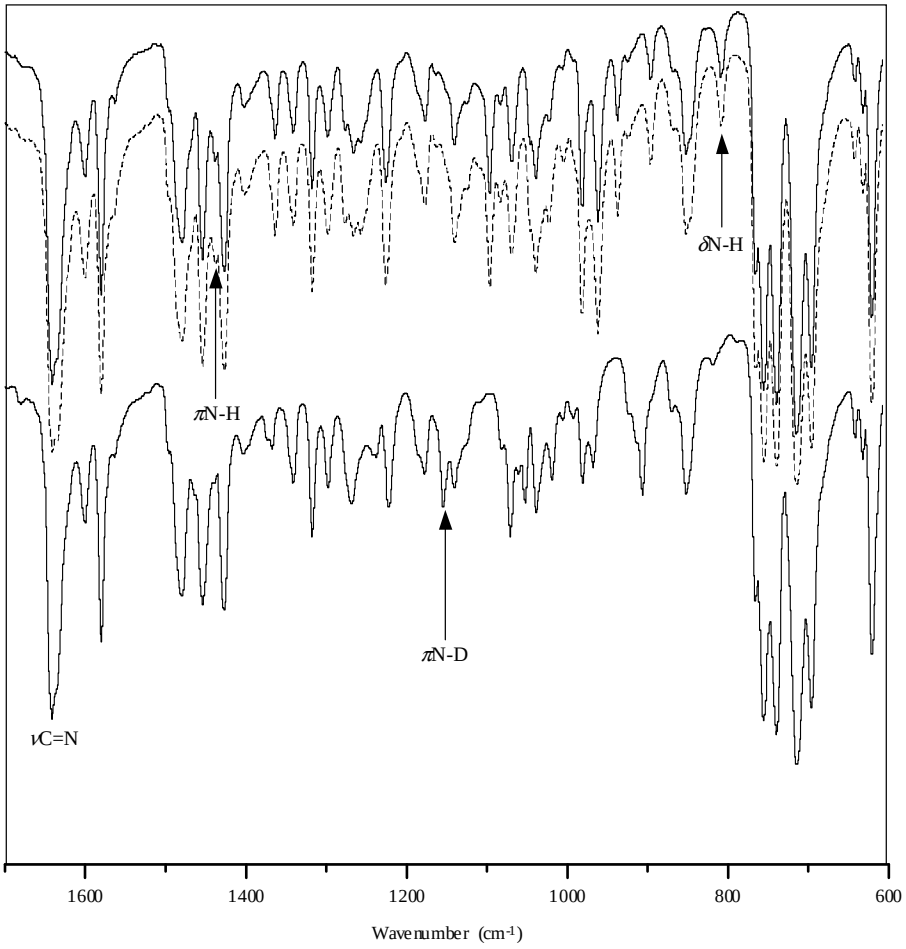

Figure 3.4.12. Mid ir spectra for [CuAL]BPh_4 compounds. Top spectrum A = CO, L = {2,2N3(C_6H_5)$_2$}; dashed line A = ^{13}CO, L = {2,2N3(C_6H_5)$_2$}; bottom spectrum A = CO, L = {2,2N3-d_1(C_6H_5)$_2$}.

The CO stretch appears at 2078 cm^{-1} in the spectra for the unlabelled and -d_1 labelled compounds, and shifts to 2031 cm^{-1} upon ^{13}CO labelling. A medium intensity band at 1983 cm^{-1} has been assigned to the $^{13}C^{18}O$ stretch. Close inspection of the νCO band in the spectrum of the ^{13}CO labelled species shows a very weak intensity band occurring as a shoulder at *ca*. 2007 cm^{-1}. It has been assigned to the $^{13}C^{17}O$ stretch in good agreement with the value obtained by means of the simple harmonic diatomic oscillator approximation ($\nu^{13}C^{17}O/\nu CO = 0.96$).

Table 3.4.7. Assignments for some of the bands observed in the spectra for [CuAL]BPh_4; A = CO, ^{13}CO and L = {2,2N3$(C_6H_5)_2$}, {2,2N3-$d_1(C_6H_5)_2$}. All frequency values in cm^{-1}.

Vibration†	A = CO L = {2,2N3$(C_6H_5)_2$}	A = ^{13}CO L = {2,2N3$(C_6H_5)_2$}	A = CO L = {2,2N3-$d_1(C_6H_5)_2$}
νN-H	3292	3292	2448
νCO	2077	2080	2077
$\nu^{13}CO$	2032	2031	2032
$\nu^{13}C^{17}O$		2007	
$\nu^{13}C^{18}O$		1983	
νC=N	1640, 1634	1640, 1634	1640, 1634
πN-H	1436	1436	1150
δN-H	802	803	—[a]
νCu-CO	—[b]	—[b]	—[b]
νCu-NH + ν_sCu-N_2 + δCu-C≡O	430	427	430
ν_aCu-N_2 + πCu-C≡O	403	402	402
τCH_2 + δHN-Cu-CO	391	391	388
ν_sCu-N_2 + νCu-NH + δCu-C≡O	366	363	368
πCu-C≡O + π_aHN-Cu-N_2	345	339	345
δCu-C≡O + ν_sCu-N_2 + νCu-NH	323	321	322
π_aHN-Cu-N_2 + πCu-C≡O	301	300	302
τCH_2 + δ_sHN-Cu-N_2	290	291	290
πHN-Cu-CO + τCH_2 + π_aHN-Cu-N_2	256	257	256
δ_sCu-N_2	230	231	230

† Assignments are based on those performed for the [Cu(CO)(2,2N3)]BPh_4 compound.
a Masked by intense absorption bands due the phenyl vibrations.
b Masked by intense bands at 498 and 491 cm^{-1} due to absorptions from the phenyl rings in the {2,2N3$[C_6H_5]_2$} ligand and the tetraphenylborate anion.

The C=N stretching vibration appears as a broad band which consists of two bands that overlap, occurring at 1640 and 1634 cm^{-1} for all isotopomers.

The νCu-CO band is expected to occur between 500 and 480 cm^{-1} based on the study performed for the $[Cu(CO)(2,2N3)]^+$ system. Two bands occur in this region, one at 498 cm^{-1} which is a shoulder band to the intense absorption at 491 cm^{-1}. Both absorptions are observed at the same

frequency values for the CO and ^{13}CO compounds ruling out their assignment as the Cu-CO stretch, which is expected to occur in the range 500-490 cm^{-1}. The νCu-CO absorption is expected to be of weak intensity, and is more than likely masked by the ligand and tetraphenylborate anion absorptions occurring in this region.

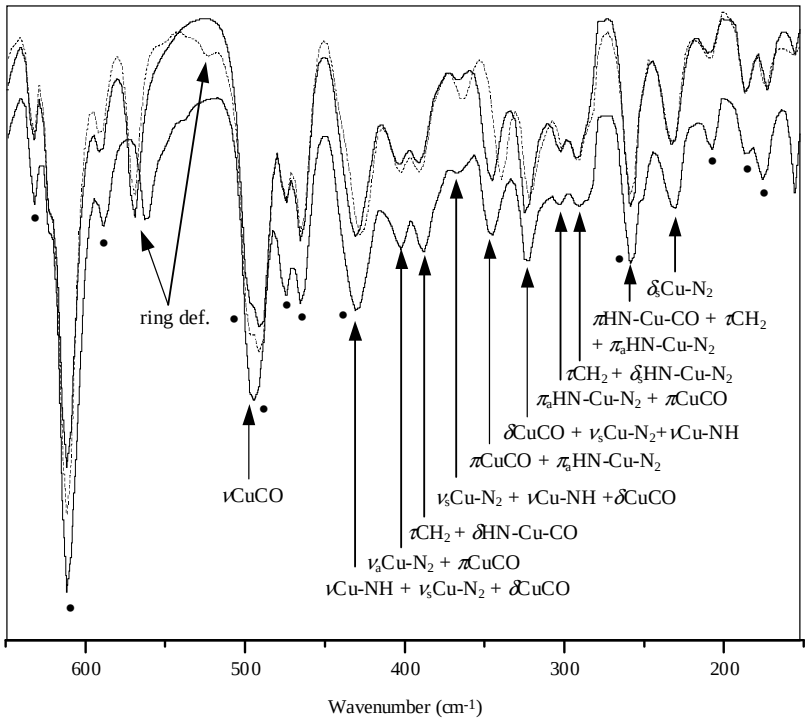

Figure 3.4.13. Far ir spectra of $[CuAL]BPh_4$ compounds. Top spectrum, A = CO, L = {2,2N3$(C_6H_5)_2$}; dotted line, A = ^{13}CO, L = {2,2N3$(C_6H_5)_2$}; bottom spectrum, A = CO, L = {2,2N3-$d_1(C_6H_5)_2$}. Tetraphenylborate and ligand (L) absorptions are shown with a dot. νCu-CO vibration is expected to occur *ca*. 498 cm^{-1} and is masked by phenyl absorptions in the 490-500 cm^{-1} region.

Three Cu-N vibrations are expected to occur in the far ir spectra, and have been assigned as the modes occurring at 430, 403 and 366 cm^{-1} by comparison with the far ir spectra for the $[Cu(CO)(2,2N3)]BPh_4$ compound. The three Cu-N vibrations are coupled to the Cu-C≡O bends, as can be seen from the shifts obtained upon ^{13}CO substitution. The band observed at 391 cm^{-1} has been assigned as a CH_2 torsional vibration coupled to the in-plane HN-Cu-CO bend and shifts 3 cm^{-1} to lower energy upon -d_1 substitution.

The largest shift to lower energy obtained upon ^{13}CO substitution occurs for the band at 345 cm^{-1} which is obtained at 339 cm^{-1} for the ^{13}CO labelled compound. It has been assigned to the πCu-C≡O vibration while the band obtained at 323 cm^{-1} has been assigned as the δCu-C≡O vibration. Most of the bands obtained in the 300-400 cm^{-1} region show sensitivity to ^{13}CO labelling, indicative of the extent of coupling expected for these vibrations, as obtained for the $[Cu(CO)(2,2N3)]^+$ system.

Cu-N bending modes and CH_2 torsional modes are obtained at lower energies and are expected to be very coupled modes as previously discussed for the $[Cu(CO)(2,2N3)]^+$ system.

Mid ir spectra of the X-substituted Schiff base derivatives are shown in figure 3.4.14. Table 3.4.8 shows some of the frequencies determined in the present study for the series of $[Cu(CO)L]BPh_4$ compounds prepared, where L = $2,2N3(C_6H_4X)_2$ and X = NO_2, F, Cl, Br, H, Me, MeO, NMe_2.

Neither the νN-H nor the νC=N vibrations appear to be X-sensitive and no trend could be established for those vibrations. However, the νCO vibration is obtained at higher energies for electron-withdrawing substituents and at lower energies for electron-releasing substituents. In fact, the νCO frequencies follow the same trend established by the global hardness values calculated for the $[Cu(CO)\{2,2N3(C_6H_4X)_2\}]^+$ complex cations, as is shown in figure 3.4.15. Although merely an approximation, the ΔN values calculated are in good agreement with the expected trend, as can be seen from the values in table 3.4.8. Figure 3.4.16 shows a graph of ΔN values *vs*. experimental νCO frequencies.

The νCO frequencies are greater for those substituents that would reduce the electron density around the Cu(I) atom. Substituents that increase the electron density would result in a poor σ-bond interaction with the CO ligand and a lower νCO frequency. π-backbonding is expected to be greater for those compounds with substituents that are good electron donors or that enrich the electronic density for the Cu(I) atom. Hence, backbonding would be greater for the NMe_2 derivative and smaller for the NO_2 derivative.

Given the difficulty in identifying the νCu-CO and so preventing using it to interpret the effect of the substituent on the σ-donation and π-backbonding within the $[Cu(CO)\{2,2N3(C_6H_4X)_2\}]^+$ system, other suitable bands showing X sensitivity were sought. νCu-N frequencies could be

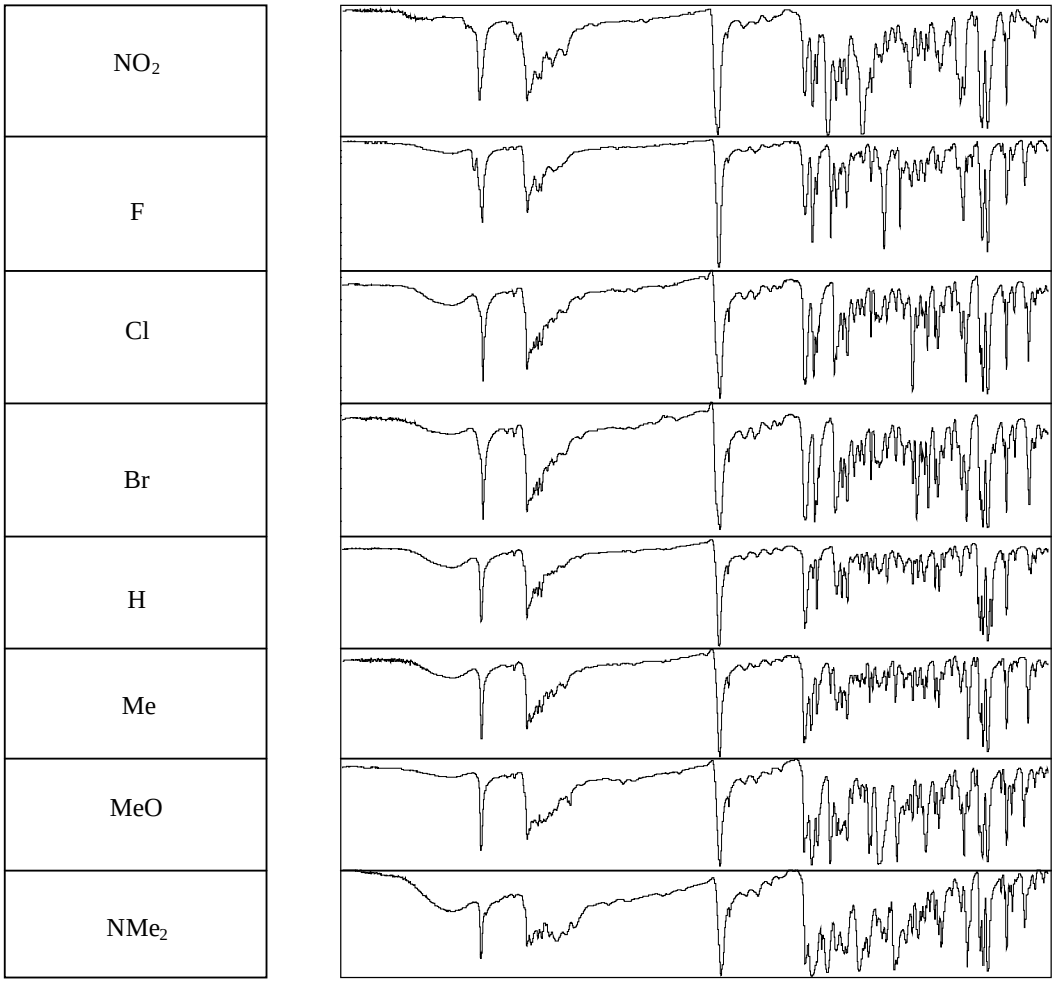

Figure 3.4.14. Mid ir spectra for X-substituted Schiff base derivatives $[Cu(CO)\{2,2N3(C_6H_4X)_2\}]BPh_4$, X = NO_2, F, Cl, Br, H, Me, MeO, NMe_2.

assigned for the X-substituted Schiff base derivatives and are shown in table 3.4.8. The general trend observed is that the νCu-N frequency increases with electron-withdrawing substituents and decreases with electron-donating substituents. The band occurring at 403 cm^{-1} in the X = H compound, appears to be the least coupled of the three νCu-N vibrations. Its assignment in the X = H compound as a coupled ν_aCu-N_2 + πCu-C≡O is consistent with the fact that substituent effects should be more noticeable for the imine N atoms than the secondary NH group, as the former are directly bonded to the X substituted aromatic systems. Frequency values for the aforementioned νCu-N vibration show the same trend as that observed for the νCO vibration as a function of the calculated global hardness values, as is shown in figure 3.4.17. In fact, a linear

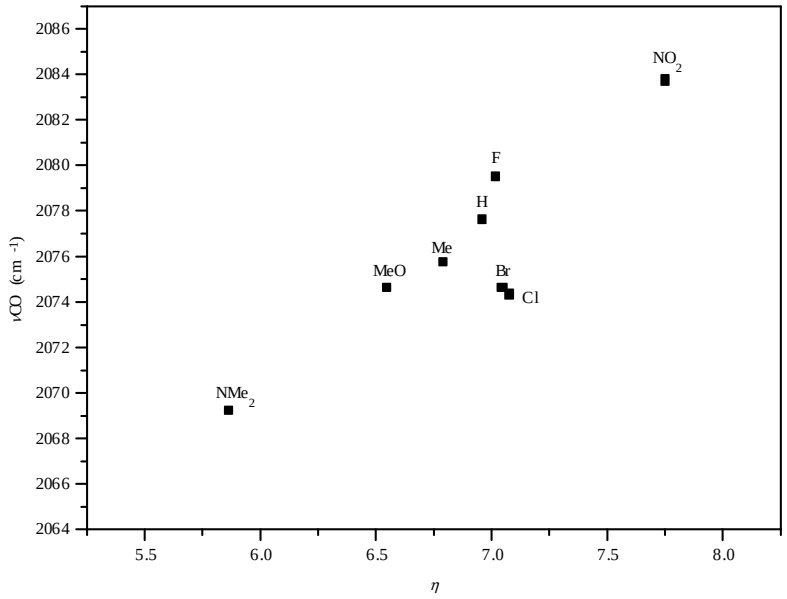

Figure 3.4.15. Graph of νCO *vs.* η for $[Cu(CO)L]^+$ compounds where L = {2,2N3(C_6H_4X)$_2$} and X = NO_2, F, Cl, Br, H, Me, MeO, NMe_2.

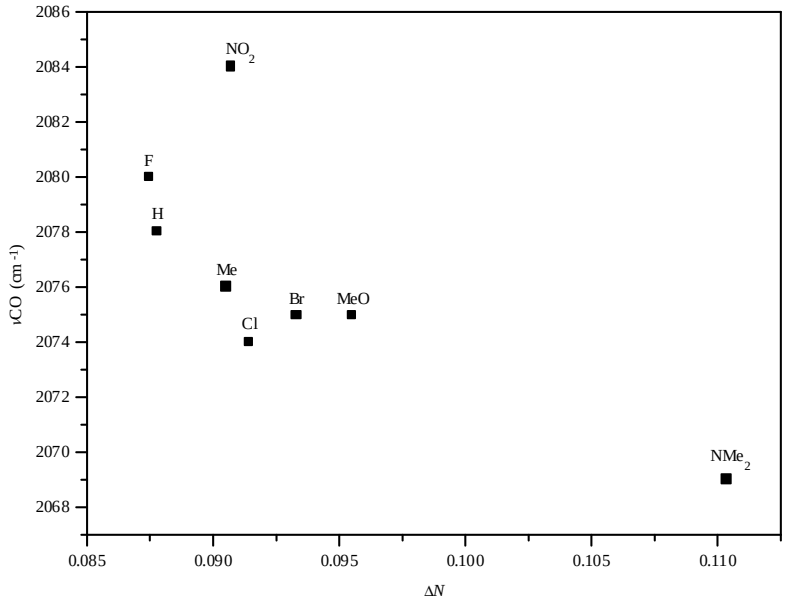

Figure 3.4.16. Graph of νCO *vs.* ΔN for $[Cu(CO)L]^+$ compounds where L = {2,2N3(C_6H_4X)$_2$} and X = NO_2, F, Cl, Br, H, Me, MeO, NMe_2.

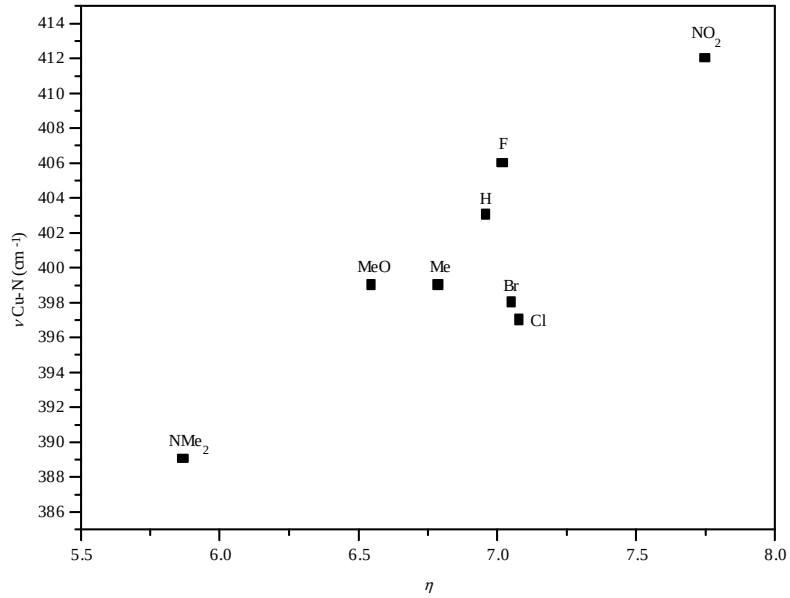

Figure 3.4.17. Graph of νCuN *vs.* η for $[Cu(CO)L]^+$ compounds where L = {2,2N3(C_6H_4X)$_2$} and X = NO_2, F, Cl, Br, H, Me, MeO, NMe_2.

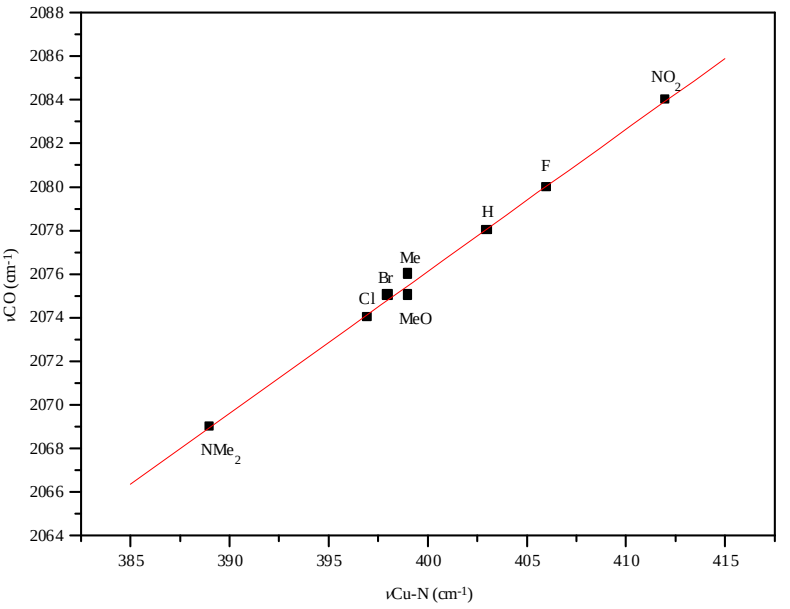

Figure 3.4.18. Experimental νCO *vs.* νCuN frequencies for $[Cu(CO)L]^+$ compounds where L = {2,2N3(C_6H_4X)$_2$} and X = NO_2, F, Cl, Br, H, Me, MeO, NMe_2. (R = 0.9979).

correlation is obtained for νCuO *vs.* νCu-N (figure 3.4.18), with lower νCu-N frequencies observed for electron-releasing substituents than for electron-withdrawing substituents. The more electron enriched the Cu(I) atom, the poorer the Cu-CO σ-bond interaction, and greater Cu→CO π-backbonding is expected. Consequently, higher νCO frequencies are obtained for the compounds with electron-withdrawing substituents, and lower ones for those with electron-donating substituents. The experimental νCu-N and νCO frequencies are in good agreement with the expected trend. It is interesting to note that while νCO correlates with νCu-N, there is no correlation between the frequencies for νN-H vibration and νCu-N.

Table 3.4.8. Calculated ΔN values for Cu→CO π-backbonding and selected experimental frequencies (cm^{-1}) for the Schiff base derivatives [Cu(CO){2,2N3($C_6H_4X)_2$}]BPh_4.

X	σ^a	ΔN	νN-H	νCO	νC=N	νCu-N[b]		
NO_2	0.78	0.091	3298	2084	1640[c]	439	412	382
F	0.34	0.087	3287	2080	1640[c]	437	406	378
Cl	0.23	0.091	3283	2074	1642, 1636	430	397	372
Br	0.23	0.093	3283	2075	1641, 1636	436	398	375
H	0.0	0.088	3292	2078	1641, 1633	431	403	367
CH_3	-0.17	0.091	3290	2076	1645, 1638	431	399	373
OMe	-0.27	0.096	3292	2075	1644, 1633	423	399	—[d]
NMe_2	-0.60	0.110	3292	2069	1638, 1632	424	389	—[d]

a Values taken from references 81 and 82.
b Cu-N vibrations follow the assignment shown in table 3.4.7 for the X = H compound. Values taken from references 81 and 82.
c Broad band.
d Very weak absorption not observed for these compounds.

The remaining two νCu-N vibrations (assigned at 431 and 367 cm^{-1} in the X = H compound) appear to be very coupled vibrations, and no correlation was obtained with the calculated global parameters or the experimental frequencies for the νN-H, νCO and νC=N vibrations.

3.5. References

1. Bruce, M.I.; *J. Organomet. Chem*., **44**, 1972, 209–226.
2. Ambundo, E.A.; Deydier, M.V.; Grall, A.J.; Aguera-Vega, N.; Dressel, L.T.; Cooper, T.H.; Heeg, M.J.; Ochrymowycz, L.A.; Rorabacher, D.B.; *Inorg. Chem.*; **38**, 1999, 4233–4242.
3. Hathway, B.J.; *Comprehensive Coordination Chemsitry. The Synthesis, Reactions, Properties and Applications of Coordination Compounds.* Vol. 5, London, Great Britain, 1987, pp. 534–750.
4. McCool, M.W.; Marsh, R.E.; Ingle, D.M.; Gagné, R.R.; *Acta Cryst.*, **B37**, 1981, 935–937**.**
5. Ivanovna, S.M.; Ivanov, S.V.; Miller, S.M.; Anderson, O.P.; Solntsev, K.A.; Strauss, S.H.; *Inorg. Chem.*; **38**, 1999, 3756–3757.
6. Ugozzoli, F.; Manotti-Lanfredi, A.M.; Marsich, N.; Camus, A.; *Inorg. Chim. Acta*; **256**, 1997, 1–7.
7. Thompson, J.S.; Whitney, J.F.; *J. Am. Chem. Soc*.; **105**, 1983, 5488–5490.
8. Thompson, J.S.; Whitney, J.F.; *Inorg. Chem.*; **23**, 1984, 2813–2819.
9. Conry, R.R.; Guanzhen Ji; Tipton, A.A.; *Inorg. Chem.*; **38**, 1999, 906–913.
10. Churchill, M.R.; DeBoer, B.G.; Rotella, F.J.; Salah, O.M.A.; Bruce, M.I.; *Inorg. Chem.*; **14**, 1975, 2051–2056.
11. Imai, S.; Fujisawa, K.; Kobayashi, T.; Shirasawa, N.; Fujii, H.; Yoshimura, T.; Kitajima, N.; Moro-oka, Y.; *Inorg. Chem*.; **37**, 1998, 3066–3070.
12. Kitajima, N.; Fujisawa, K.; Fujimoto, C.; Moro-oka, Y.; Hashimoto, S.; Kitagawa, T.; Toriumi, K.; Tatsumi, K.; Nakamura, A.; *J. Am. Chem. Soc.*; **114**, 1992, 1277–1291.
13. Rasika Dias, H.V.; Hui-Ling Lu; *Inorg. Chem.*; **34**, 1995, 5380–5382.
14. Hirsch, J.; DeBeer George, S.; Solomon, E.I.; Hedman, B.; Hodgson, K.O.; Burstyn, J.N.; *Inorg. Chem.*, **40**, 2001, 2439–2441.
15. Chaudhuri, P.; Oder, K.; *J. of Organomet. Chem.;* **367**, 1989, 249–258.
16. Mahapatra, S.; Kaderli, S.; Llobet, A.; Neuhold, Y.M.; Palanché, T.; Halfen, J.A.; Young, Jr., V.G.; Kaden, T.A.; Que, Jr., L.; Zuberbühler, A.D.; Tolman, W.B.; *Inorg. Chem.*; **36**, 1997, 6343–6356.
17. Patch, M.G.; Choi, H.; Chapman, D.R.; Bau, R.; McKee, V.; Reed, C.A.; *Inorg. Chem.*; **29**, 1990, 110–119.
18. Pasquali, M.; Marini, G.; Floriani, C.; Gateani-Manfredotti, A.; Guastini, C.; *Inorg. Chem.*; **19**, 1980, 2525–2531.
19. Penfield, K.W., Gay, R.R.; Himmelwright, R.S.; Eickman, N.C.; Norris, V.A.; Freeman, H.C.; Solomon, E.I.; *J. Am. Chem. Soc*.; **103**, 1981, 4382–4388.

20. Colman, P.M.; Freeman, H.C.; Guss, J.M.; Murata, M.; Norris, V.A.; Ramshaw, J.A.M.; Venkatappa, M.P.; *Nature*; **272**, 1978, 319–324.
21. Amundsen, A.R.; Whelan, J.; Bosnich, B.; *J. Am. Chem. Soc.*; **99**, 1977, 6730–6739.
22. Sanaullah; Kano, K.; Glass, R.S.; Wilson, G.S.; *J. Am. Chem. Soc.*; **115**, 1993, 592–600.
23. Sanaullah; Hungerbühler, H.; Schöneich, C.; Morton, M.; Van der Velde, D.G.; Wilson, G.S.; Asmus, K.D.; Glass, R.S.; *J. Am. Chem. Soc.*; **119**, 1997, 2134–2145.
24. Thompson, J.S.; Marks, T.J.; Ibers, J.A.; *J. Am. Chem. Soc.*; **101**, 1979, 4180–4192.
25. Wu, H.; Lucas, R.; *Inorg. Chem.*; **32**, 1993, 526–531.
26. Addison, A.W.; Nageswara Rao, T.; Sinn, E.; *Inorg. Chem.*; **23**, 1984, 1957–1967.
27. Bermejo, E.; Carballo, R.; Castiñeiras, R.; Lombao, A.; Hiller, W.; Strähle, J.; *Polyhedron*; **10**, 1991, 1579–1585.
28. Masuda, H.; Sugimori, T.; Kohzuma, T.; Odani, A.; Yamauchi, O.; *Bull. Chem. Soc. Jpn.*; **65**, 1992, 786 –793.
29. Diaddario Jr., L.L.; Dockal, E.R.; Glick, M.D.; Ochrymowycz, L.A.; Rorabacher, D.B.; *Inorg. Chem.*; **24**, 1985, 356–363.
30. Navon, N.; Golub, G.; Cohen, H.; Paoletti, P.; Valtancoli, B.; Bencini, A.; Meyerstein, D.; *Inorg. Chem.*; **38**, 1999, 3484–3488.
31. Schatz, M.; Becker, M.; Thaler, F.; Hampel, F.; Schindler, S.; Jacobson, R.R.; Tyeklár, Z.; Murthy, N.N.; Ghosh, P.; Chen, Q.; Zubieta, J.; Karlin, K.D.; *Inorg. Chem.*; **40**, 2001, 2312–2322.
32. Arnold, P.J.; Davies, S.C.; Dilworth, J.R.; Durrant, M.C.; Griffiths, D.V.; Hughes, D.L.; Richards, R.L.; Sharpe, P.C.; *J. Chem. Soc., Dalton Trans.*; 2001, 736–746.
33. Boeyens, J.C.A.; Dobson, S.M.; Hancock, R.D.; *Inorg. Chem.*; **24,** 1985, 3073–3076.
34. Blake, A.J.; Danks, J.P.; Harrison, A.; Parsons, S.; Schooler, P.; Whittaker, G.; Schröder, M.; *J. Chem. Soc., Dalton Trans.*; 1998, 2335–2340.
35. Blake, A.J.; Danks, J.P.; Fallis, I.A.; Harrison, A.; Li, W.S.; Parsons, S.; Ross, S.A.; Whittaker, G.; Schröder, M.; *J. Chem. Soc., Dalton Trans.*; 1998, 3969–3976.
36. Blake, A.J.; Danks, J.P.; Fenske, D.; Schröder, M.; *New J. Chem.*; **23**, 1999, 345–346.
37. Küpers, H-J.; Wieghardt, K.; Tsay, Y-H.; Krüger, C.; Nuber, B.; Weiss, J.; *Angew. Chem. Int. Ed. Engl.*; **26**, 1987, 575–576.
38. Structure obtained from Cambridge Crystallographic Data Centre, 2003; reference code VOFMIM.
39. Clarkson, J.A.; Yagbasan, R.; Blower, P.J.; Cooper, S.R.; *J. Chem. Soc., Chem. Commun.*; 1989, 1244–1245.

40. Pearson, R.G.; *J. Organic Chem.;* **54**, 1989, 1423–1430.
41. Structure obtained from Cambridge Crystallographic Data Centre, 2003; reference code FITDUH.
42. Martínez, A.; Salcedo, R.; Sansores, L.E.; Medina, G.; Gasque, L.; *Inorg. Chem.*; **40**, 2001, 301–306.
43. Chandrakumar, K.R.S.; Pal, S.; *J. Phys. Chem. A*; **106**, 2002, 11775–11781.
44. Méndez, F.; Gázquez, J. L.; *J. Am. Chem. Soc*.; **116**, 1994, 9298–9301.
45. Pasquali, M.; Marchetti, F.; Floriani, C.; *Inorg. Chem.;* **17**, 1978, 1684–1688.
46. Pearson, R.G.; *Inorg*. *Chem.*; **23**, 1984, 4675–4679.
47. Pearson, R.G.; *J. Am. Chem. Soc.;* **107**, 1985, 6801–6806.
48. Plitt, H.S.; Bär, M.R.; Ahlrichs, R.; Schnöckel, H.; *Inorg. Chem.*; **31**, 1992, 463–465.
49. Håkansson, M.; Jagner, S.; *Inorg*. *Chem.*; **29**, 1990, 5241–5244.
50. Pearson, R.G.; *J. Am. Chem. Soc.;* **85**, 1963, 3533–3539.
51. Pearson, R.G.; *Surv. Progr*. *Chem.*; **5**, 1969, 1–52.
52. Parr, R.G.; Gázquez, J.L.; *J. Phys. Chem.*; **97**, 1993, 3939–3940.
53. Parr, R.G.; Chattaraj, P.K.; *J. Am. Chem. Soc*.; **113**, 1991, 1854–1855.
54. Pearson, R.G.; *J. Chem. Educ*.; **64**, 1987, 561–567.
55. Mulliken, R.S.; *J. Phys. Chem.*; **56**, 1952, 801–822.
56. Mulliken, R.S.; *J. Am. Chem. Soc*.; **74**, 1952, 811–824.
57. Weiss, J.; *J. Chem. Soc*.; 1942, 245–252.
58. Parr, R.G.; Yang, W.; *J. Am. Chem. Soc.*; **106**, 1984, 4049–4050 .
59. De Proft, F.; Amira, S; Choho, K.; Geerlings, P; *J. Phys. Chem.*; **98**, 1994, 5227–5233.
60. Zanello, P.; Leoni, P.; *Can. J. Chem.*; **63**, 1985, 922–927.
61. Watt, G.W.; Klett, D.S.; *Spectrochim. Acta*; **20**, 1964, 1053–1064.
62. Buckingham, D.A.; Jones, D.; *Inorg. Chem.*; **4**, 1965, 1387–1392.
63. Kuo, K.W.; Madan, S.K.; *Inorg. Chem.*; **8**, 1969, 1580–1584.
64. Bennett, A.M.A.; Foulds, G.A.; Thornton, D.A.; *Spectrochim. Acta*; **45A**, 1989, 219–223.
65. Bennett, A.M.A.; Foulds, G.A.; Thornton, D.A.; Watkins, G.M.; *Spectrochim. Acta*; **46A**, 1990, 13–22.
66. Nakamoto, K.; *Infrared and Raman Spectra of Inorganic and Coordination Compounds. Part A: Theory and Applications in Inorganic Chemistry*. 5th edition; John Wiley & Sons, New York, USA, 1997, pp. 189–209.
67. Denning, R.G.; Ware, M.J.; *Spectrochim. Acta*; **24A**, 1968, 1785–1793.

68. Hall, P.S.; Jackson, G.E.; Moss, J.R.; Thornton, D.A.; Verhoeven, P.F.M.; Watkins, G.M.; *Spectrosc. Letters*; **26**, 1993, 1247–1267.
69. Browning, J.; Goggin, P.L.; Goodfellow, R.J.; Norton, M.G.; Rattray, A.J.; Taylor, B.F.; Mink, J.; *J. Chem. Soc. Dalton Trans.*; 1977, 2061–2067.
70. Goggin, P.L.; Norton, M.G.; *Inorg. Chim. Acta*; **26**, 1978, 125–128.
71. Hall, P.S.; Jackson, G.E.; Moss, J.R.; Thornton, D.A.; Watkins, G.M.; *J. Alloys and Compounds*; **197**, 1993, 69–74.
72. Foulds, G.A.; Thornton, D.A.; Watkins, G.M.; *Spectrochim. Acta*; **484A**, 1992, 577–596.
73. Foulds, G.A.; Hall, P.S.; Thornton, D.A.; Watkins, G.M.; *Spectrochim. Acta*; **484A**, 1992, 597–604.
74. Stammreich, H.; Kawai, K.; Tavares, Y.; Krumholz, P.; Behmoiras, J.; Bril, S.; *J. Chem. Phys.*; **32**, 1960, 1482–1487.
75. Adams, D.M.; Trumble, W.R.; *J. Chem. Soc. Dalton Trans.*; 1974, 690–692.
76. Toth, A.; Floriani, C.; Pasquali, M.; Chiesi-Villa, A.; Gaetani-Manfredotti, A.; Guastini, C.; *Inorg. Chem.*; **24**, 1985, 648–653.
77. Gagné, R.R.; Allison, J.L.; Gall, R.S.; Koval, C.A.; *J. Am. Chem. Soc.*; **99**, 1977, 7170–7178.
78. Stamp, L.; Dieck, H.T.; *Inorg. Chim. Acta*; **129**, 1987, 107–114.
79. Villacorta, G.M.; Lippard, S.J.; *Inorg. Chem.*; **26**, 1987, 3672–3676.
80. A.L.Spek (2003) PLATON, A Multipurpose Crystallographic Tool, Utrecht University, Utrecht, The Netherlands.
81. Connors. K.A.; *Chemical Kinetics: The Study of Reaction Rates in Solution*; John Wiley & Sons, New York, USA, 1990.
82. Exner, O.; *Correlation Analysis of Chemical Data*; Plenum Publishing Corporation, Prague, Czechoslovakia, 1988.

4. Experimental

4.1. Preparation of *N*-oxide ligands

The preparation of the *N*-oxide ligands used in the syntheses of Zeise's salt derivatives follows that described in the literature for these compounds [1-3].

4.1.1. Synthesis of pyO and py-d_5O

The synthesis of pyO was carried out in small amounts in order to optimize the yield of the labelled derivatives. Due to the very hygroscopic nature of pyO, the compound was obtained as the hydrochloride, pyO·HCl, which is easier to manipulate in small amounts.

Distilled pyridine (0.5 mL; 6 mmol) was added to 5 mL of glacial acetic acid (85 mmol) in a round bottom flask. A condenser was fitted to the flask and 0.7 mL of 30% H_2O_2 were added slowly. The reaction mixture was heated to approximately 75 °C for six hours and an additional 0.7 mL of 30% H_2O_2 were added (total H_2O_2/py molar ratio of 2). The reaction was left heating overnight and the reaction mixture was concentrated in a water bath at reduced pressure. An excess of solid Na_2CO_3 was added to the concentrated reaction mixture until alkaline as measured by pH paper. The mixture was concentrated to dryness and the pyO extracted 3 times with 5 mL fractions of dry, distilled $CHCl_3$. The solution was concentrated in a water bath at reduced pressure and 5 mL of a diluted HCl solution (1:1 in H_2O) were added to the concentrated fraction. The mixture was concentrated in a water bath at reduced pressure and isopropanol was added to the remaining fraction. A white creamy solid formed which was redissolved in hot isopropanol and recrystallized twice to yield a white crystalline product. Approximately 0.52 g of pyO·HCl was obtained.

The deuterated analogue, py-d_5O, was prepared as above, using py-d_5 99 % isotopic purity from Aldrich.

Yields of 65 % were obtained for the pyO·HCl and py-d_5O·HCl preparation reactions.

4.1.2. Preparation of quinO and quin-d_7O

Quinoline (0.5 mL; 4 mmol) was added to 5 mL of glacial acetic acid (85 mmol) in a round bottom flask fitted with a condenser. To this mixture, 30 % H_2O_2 was added slowly (5 mL; 4 mmol) and the reaction was heated for 6 hours at 75 °C. An additional 5 mL of H_2O_2 were added

and the reaction was left heating overnight at 75° C. The reaction mixture was concentrated in a water bath at reduced pressure and solid Na_2CO_3 was added until an alkaline pH was obtained as measured with pH paper. The mixture was evaporated to dryness in a water bath at reduced pressure and the solid obtained was extracted 3 times with 5 mL fractions of distilled $CHCl_3$. The $CHCl_3$ fractions were mixed and evaporated to dryness in a water bath under reduced pressure. A light brown solid was obtained and broken under dry diethyl ether to remove unreacted quinoline. The solid was vacuum filtered and dried in a desiccator. Approximately 0.44 g of product was obtained.

The deutertated analogue, quin-d_7O, was prepared by the same method as described above using quin-d_7, 97 atom %D, from Merck, Sharp and Dohme.

Yields of 75 % were obtained for the quinO and quin-d_7O preparation reactions.

4.1.3. Preparation of py-^{18}O and quin-^{18}O

The preparation of the O-18 labelled isotopomers was performed at microscale using $H_2{}^{18}O_2$ which was prepared in a discharge tube from $H_2{}^{18}O$ (95 % O-18 purity, from Aldrich) [3-6].

The reaction was carried out several times with 0.1 mL of regular water in order to optimize H_2O_2 production in the discharge tube before employment of labelled $H_2{}^{18}O$.

The discharge tube design follows that described in reference 4. A 2.0 m long glass tube was fitted with aluminium electrodes connected to a 200 V power supply. Four traps were fitted at 10, 30, 60 and 180 cm from the point of water entry. The highest yields in the preparation of H_2O_2 were obtained for trap 3, which was fitted to a high vacuum pump (pressure readings varied from 0.075 to 0.18 mbar) to evacuate the system. Water was fed through a capillary at the point of entry and reaction times varied as water intake was observed to depend on room temperature (for which reason a water bath at ~15 °C was used) and capillary size. In a typical run, 0.1 mL of water were totally evacuated in an 8 to 10 hour interval. Recovery of H_2O_2 in the U-tube trap at liquid N_2 temperature was of 90 %. H_2O_2 content by titration with standardized $KMnO_4$ was close to 70 %. When yields were consistently obtained, 0.1 mL of $H_2{}^{18}O$ were fed and the collected $H_2{}^{18}O_2$ was used immediately in the preparation of py-^{18}O and quin-^{18}O.

Platinum electrodes instead of aluminium electrodes were initially employed in the preparation of H_2O_2, but owing to the high work function of platinum, a sustainable discharge was not achieved and H_2O_2 yields were extremely low. Aluminium electrodes are passivated by a layer of hydroxide/oxide that may eventually lead to an $^{18}O/^{16}O$ H_2O_2 mixture, as was obtained in this work. O-18 enrichment would be expected to have been greater, had a sustainable discharge been obtained with the platinum electrodes.

4.1.3.1. Synthesis of py-^{18}O

Dry distilled pyridine (0.1 mL; 1.2 mmol) was added to a round bottom flask. Glacial acetic acid (3 mL) was used to wash out the $H_2{}^{18}O_2$ obtained from the discharge tube. It was assumed from yields in previous runs with H_2O that the amount of $H_2{}^{18}O_2$ collected was close to 2 mmol. A condenser was fitted and the reaction was left overnight at 75 °C. The reaction mixture was concentrated in a water bath at reduced pressure and solid Na_2CO_3 was added until a basic pH was obtained as measured with pH paper. The mixture was evaporated to dryness and the product was extracted into dry distilled $CHCl_3$ which was evaporated at a high vacuum to yield py-^{18}O. The product was obtained in a very poor yield and characterized only by means of its mid ir spectrum which showed the bands expected for pyO. O-18 enrichment in the ligand could not be measured due to insufficient sample. The appearance of two bands for some of the vibrations sensitive to O-18 labelling in the mid ir spectrum indicate that a pyO/py-^{18}O mixture was obtained as is discussed in section 2.1. The product was used immediately in the preparation of $[Pt(C_2H_4)(pyO/py^{18}O)]Br_2$.

4.1.3.2. Synthesis of quin-^{18}O

Glacial acetic acid (3 mL) was used to wash out the $H_2{}^{18}O_2$ obtained from the discharge tube and added to quinoline (0.15 mL; 1.1 mmol) in a round bottom flask. A condenser was fitted and the reaction was left overnight at 75 °C. The mixture was then concentrated in a water bath at reduced pressure and the remaining fraction was made basic by addition of solid Na_2CO_3 as measured by pH paper. The mixture was evaporated to dryness and extracted into dry distilled $CHCl_3$ which was evaporated to dryness under a high vacuum. Mid ir of the brown compound obtained showed that it was contaminated with quinoline, so the product was separated by using a chromatography plate with a $CHCl_3$/MeOH mixture (10:1, $CHCl_3$:MeOH, on silica gel F_{254}). The purified product was obtained in a 50 % yield and mid and far ir spectra were collected and mass spectra were recorded for the labelled compound. Mass spectra for the compound show two peaks at 146.3 and 148.3 (m/z ratios) for the positive ion (quinO/quin-^{18}O + H) and two peaks at 144.5

and 146.4 (m/z ratios) for the negative ion (quinO/quin-^{18}O – H). From the relative abundance values, a mixture of quinO/quin-^{18}O in a 3 to 2 ratio was obtained. The compound was used in the preparation of [Pt(C_2H_4)(quinO/quin-^{18}O)Br_2].

From the mass spectroscopy results obtained for the quinO/quin-^{18}O mixture, and the splitting of some O-18 sensitive bands observed in the spectra for the [Pt(C_2H_4)(pyO/py-^{18}O)Br_2] and [Pt(C_2H_4)(quinO/quin-^{18}O)Br_2] compounds, it seems reasonable to assume that a similar enrichment was obtained for the pyO/py-^{18}O mixture.

4.2. Zeise's salt derivatives

Zeise's salt derivatives [PtALX$_2$] (A = C_2H_4, C_2D_4, CO, ^{13}CO and L = pyO, py-d_5O, pyO/py-^{18}O, quinO, quin-d_7O, quinO/quin-^{18}O) were obtained by reaction of K[Pt(C_2H_4)X$_3$] and K[Pt(C_2D_4)X$_3$] (X = Cl, Br) with the L ligands.

4.2.1. Preparation of Zeise's salt

Zeise's salt derivatives were prepared in a similar manner to the synthesis described by Chatt and Searle [7]. Potassium tetrachloroplatinate, K_2PtCl_4, (1.0 g; 2.4 mmol) was dissolved in 50 mL of water and 1 mL of concentrated HCl was added to the red solution. The solution was transferred to a two necked round bottom flask and glass valves were fitted to allow for the creation of a vacuum and the introduction of C_2H_4 into the flask. Ethylene was pumped into the flask under a vacuum strong enough to cause the red solution to bubble. The reaction was left stirring for a period of 5 to 10 days with a magnetic stirrer agitating the solution inside the flask. When the C_2H_4 pressure was negative (an indication of the reaction taking place) more C_2H_4 was pumped into the flask to create a positive pressure in order to favour the production of Zeise's salt. The red solution slowly turned bright yellow, a colour change indicative of the formation of K[Pt(C_2H_4)Cl_3]. The yellow solution was filtered through cotton wool in a Pasteur pipette to remove any platinum oxide that could have formed during the reaction. Removal of this oxide proved essential in avoiding the Pt(II) in the Zeise's salt solution decomposing to platinum oxide during purification of Zeise's salt. The filtered solution was concentrated in a water bath at reduced pressure with the water bath temperature not exceeding 25 °C (at higher temperatures oxidation to platinum oxide was observed). Distilled acetone was added to extract the K[Pt(C_2H_4)Cl_3] species formed. The precipitated KCl and unreacted K_2PtCl_4 were removed by filtration and the extracted K[Pt(C_2H_4)Cl_3] in acetone was concentrated in a water bath as described above. More acetone was added to allow for further removal of KCl and K_2PtCl_4.

Zeise's salt was not obtained as a solid due to the acidic conditions at which the syntheses were performed. Instead, distilled water was added to the concentrated yellow solution making up to 20 mL total volume. This solution (~ 0.1 M) was used in the preparation of the $[PtALX_2]$ derivatives. The solution was stored under C_2H_4 and in a dark place to avoid decomposition of $K[Pt(C_2H_4)Cl_3]$.

The bromide derivative was obtained by addition of a 20-fold excess of KBr during the preparation of the C_2H_4 derivative starting from K_2PtCl_4. HBr was added instead of HCl and when the solution turned a golden-yellow colour, it was concentrated in a water bath not exceeding 25 °C and the product was extracted into distilled dry acetone. The crystalline solid (KBr and KCl) was filtered off and the extract was concentrated to add water and a 20-fold excess of KBr which was left stirring overnight under positive C_2H_4 pressure. The procedure was repeated several times to yield a solution of $K[Pt(C_2H_4)Br_3]$ which was stored as mentioned previously for the chloride derivative.

4.2.2. Preparation of $K[Pt(C_2D_4)X_3]$

Ethylene-*d*$_4$ (99.5 % isotopic purity from MSD Isotopes, Merck) was used for the preparation of the labelled compounds. Potassium tetrachloroplatinate (1.00 g; 2.4 mmol) was dissolved in approximately 50 mL of water and the solution was added to the sealed glass tube connected to the flask containing C_2D_4 and stopped with a septum. The glass seal separating the solution and the C_2D_4 was broken with a magnetic stirrer and the solution was left stirring until it turned yellow indicating the formation of $K[Pt(C_2D_4)Cl_3]$. It was removed using a syringe from the flask which was then rinsed with water several times to add more K_2PtCl_4 in H_2O with a 20-fold excess of KBr to produce $K[Pt(C_2D_4)Br_3]$ as described above. The solutions of $K[Pt(C_2D_4)X_3]$ were used immediately in the preparation of the $[Pt(C_2D_4)LX_2]$ compounds.

4.2.3. Preparation of $[PtALX_2]$; A = C_2H_4, C_2D_4, L = pyO and py-*d*$_5$O and X = Cl, Br.

The $[PtALX_2]$ derivatives were prepared following the method described for the $[Pt(C_2H_4)(pyO)Cl_2]$ derivative.

6 mL of a $K[Pt(C_2H_4)Cl_3]$ solution of approximate 0.1 M concentration were concentrated in a water bath not exceeding 25 °C at reduced pressure. The concentrate was removed with a Pasteur pipette and taken to approximately 3 mL with distilled water. An excess of pyO·HCl was added to the solution (0.12 g; 0.9 mmol) and stirred with a magnetic stirrer in an ice bath. The solution was

neutralized with solid Na_2CO_3 until a pH between 5 and 6 was obtained. As the pH increased a bright yellow compound precipitated from the solution. The compound was filtered and washed several times with cold water. Approximately 0.15 g of the compound were obtained (65% yield).

Crystals suitable for XRD were obtained for the $[Pt(C_2H_4)(pyO)Cl_2]$ derivative by diffusion of distilled dry hexane into a $CHCl_3$ solution of $[Pt(C_2H_4)(pyO)Cl_2]$. The crystal structure for this compound is described in section 2.3.1.1. Crystal structure parameters, bond lengths and angles, and average isotropic displacement parameters are shown in appendix 1.

The derivatives were characterized by ^1H and ^{13}C nmr, microanalysis and mid and far ir and raman spectra. Nmr and microanalyses results are shown in tables 4.1-4.3; vibrational spectra are thoroughly discussed in section 2.3.2.

Compounds are light and moisture sensitive. They were hence stored in a desiccator kept in the dark to avoid decomposition.

4.2.4. Preparation of $[Pt(C_2H_4)(py\text{-}^{18}O)Br_2]$

The pyO/py-^{18}O mixture obtained from reaction with $H_2{}^{18}O_2$ was used immediately in the preparation of the Zeise's salt derivative. 1 mL of a 0.1 M aqueous solution of $K[Pt(C_2H_4)Br_3]$ was added to the pyO/py-^{18}O mixture in an ice bath which was neutralized by addition of solid Na_2CO_3 until a pH between 5 and 6 was reached. No precipitate was formed so the product was extracted with 2 mL distilled $CHCl_3$. The yellow $CHCl_3$ extract was evaporated to dryness under a high vacuum and a golden yellow powder was obtained. Yields were extremely low and all of the sample was used to run mid and far ir spectra. The spectra obtained have a band to band correspondence with the spectra for $[Pt(C_2H_4)(pyO)Br_2]$ except for the splitting of several bands which are sensitive to O-18 labelling as is discussed in section 2.3.2.

4.2.5. Preparation of $[PtALX_2]$; A = C_2H_4, C_2D_4, L = quinO, quin-d_7O and X = Cl, Br.

The $[PtALX_2]$ derivatives were prepared following the method described for the $[Pt(C_2H_4)(quinO)Cl_2]$ derivative.

6 mL of a $K[Pt(C_2H_4)Cl_3]$ solution of approximate 0.1 M concentration were concentrated in a water bath not exceeding 25 °C at reduced pressure. The concentrate was removed with a Pasteur

pipette and taken to approximately 3 mL with distilled water. An excess of quinO was added to the solution (0.13 g; 0.9 mmol) and stirred with a magnetic stirrer in an ice bath. A pale yellow precipitate formed immediately upon addition of the quinO ligand. The mixture was stirred in an ice bath and neutralized with solid Na_2CO_3 until a pH between 5 and 6 was obtained. The yellow solid was vacuum filtered and washed several times with cold water. Approximately 0.20 g of the compound were obtained (75 % yield).

The derivatives were characterized by ^{1}H and ^{13}C nmr, microanalysis and mid and far ir and raman spectra. Nmr and microanalysis results are shown in tables 4.1-4.3; vibrational spectra are thoroughly discussed in section 2.3.2.

4.2.6. Preparation of $[Pt(C_2H_4)(quin\text{-}^{18}O)Br_2]$

6 mL of a 0.1 solution of $K[Pt(C_2H_4)Br_3]$ were concentrated to approximately 2 mL in a water bath not exceeding 25 °C under reduced pressure. The quinO/quin-^{18}O mixture (0.08 g; 0.55 mmol) obtained was added to the concentrate and a yellow solid formed immediately. The mixture was neutralized with solid Na_2CO_3 in an ice bath until a pH between 5 and 6 was obtained. The yellow solid obtained was vacuum filtered immediately and washed several times with cold water. Approximately 0.14 g of $[Pt(C_2H_4)(quinO/quin\text{-}^{18}O)Br_2]$ were obtained (50 % yield). The compound was characterized by nmr, ir and raman spectroscopy.

4.2.7. Preparation of $[PtALX_2]$; A = CO, ^{13}CO, L = pyO, py-d_5O, quinO, quin-d_7O and X = Cl, Br.

All CO and ^{13}CO derivatives were prepared from the corresponding $[Pt(C_2H_4)LX_2]$ derivative by exactly the same procedure which is described below for $[Pt(CO)(pyO)Cl_2]$.

0.1 g of $[Pt(C_2H_4)(pyO)Cl_2]$ were dissolved in approximately 5 mL of dry distilled $CHCl_3$. The yellow solution was filtered through a Pasteur pipette with cotton wool and CO was bubbled through the solution until a colour change from bright yellow to pale yellow was observed. The $[Pt(CO)(pyO)Cl_2]$ derivative was precipitated by addition of distilled dry hexane. Yields were practically quantitative.

The ^{13}CO derivatives were prepared in the same way using ^{13}CO (99 % C-13 purity from Aldrich).

Crystals suitable for XRD were obtained for the [Pt(CO)(quinO)Br_2] derivative by diffusion of distilled dry hexane into a $CHCl_3$ solution of [Pt(CO)(quinO)Br_2]. The crystal structure for this compound is described in section 2.3.1.2. Crystal structure parameters, bond lengths and angles, and average isotropic displacement parameters are shown in appendix 2.

Carbonyl Zeise's salt derivatives are considerably less stable than the ethylene derivatives and must be prepared under anhydrous conditions and stored in the dark as they are light sensitive and decompose easily. The quinO carbonyl derivatives appear to be more stable than the pyO derivatives.

All compounds were stored in a desiccator and kept in the dark to avoid decomposition.

The carbonyl derivatives were characterized by ^{1}H and ^{13}C nmr, microanalysis and mid and far ir and raman spectra. Nmr and microanalysis results are shown in tables 4.1-4.3; vibrational spectra are thoroughly discussed in section 2.3.2.

4.2.8. Nmr spectra

The experimental procedures followed were carried out as follows. The ^{1}H (400 MHz), and ^{13}C (100 MHz) nmr spectra were recorded on an Avance Bruker 400 MHz spectrometer using standard pulse sequences. Chemical shifts are reported in ppm and referenced to the residual undeuterated solvent resonances ($CDCl_3$ ^{1}H 7.25, ^{13}C 77.00) and coupling constants are reported in Hz.

The chemical shifts obtained for all compounds prepared (tables 4.1 and 4.2) are in good agreement with reported values [1, 8, 9]. Integration of peaks in the ^{1}H spectra obtained is consistent with the expected structure.

All of the C_2H_4 derivatives show the olefin protons at *ca*. 4.4 ppm, a value that is consistent with a square planar structure [9]. Pt-H coupling constants of *ca*. 35 Hz were obtained for all C_2H_4 derivatives.

C_2H_4 signals are absent for all the C_2D_4 derivatives as expected.

Table 4.1. ^{1}H nmr spectra of Zeise's salt derivatives. Values in parenthesis correspond to the number of protons obtained by integration of the observed peaks.

Compound	Chem. shift (ppm)	$J_{(Pt-H)}$ (Hz)
$[Pt(C_2H_4)(pyO)Cl_2]$	8.595, 8.580 (2); 7.920,7.901, 7.882 (1); 7.686, 7.669, 7.651 (2)	
	4.451[b], 4.366[a], 4.280[b] (4)	34.01
$[Pt(C_2D_4)(pyO)Cl_2]$	8.600, 8.597, 8.583, 8.580 (2); 7.923, 7.921, 7.919, 7.902, 7.885, 7.882 (1); 7.684, 7.680, 7.667, 7.652, 7.648 (2)	
$[Pt(C_2H_4)(py\text{-}d_5O)Cl_2]$	4.459[b], 4.374[a], 4.288[b]	34.01
$[Pt(CO)(pyO)Cl_2]$	8.573, 8.559 (2); 8.002, 7.984, 7.965 (1); 7.719, 7.701, 7.684 (2)	
$[Pt(^{13}CO)(pyO)Cl_2]$	8.574, 8.559 (2); 8.003, 7.984, 7.965 (1); 7.720, 7.702, 7.685 (2)	
$[Pt(CO)(py\text{-}d_5O)Cl_2]$	—[c]	
$[Pt(C_2H_4)(pyO)Br_2]$	8.592, 8.577 (2); 7.920, 7.901, 7.881 (1); 7.741, 7.723, 7.705 (2)	
	4.591[b], 4.507[a], 4.422[b] (4)	33.61
$[Pt(C_2D_4)(pyO)Br_2]$	8.602, 8.587 (2); 7.924, 7.905, 7.886 (1); 7.693, 7.676, 7.658 (2)	
$[Pt(C_2H_4)(py\text{-}d_5O)Br_2]$	4.582[b], 4.497[a], 4.410[b]	36.73
$[Pt(CO)(pyO)Br_2]$	8.540, 8.526 (2); 7.984, 7.966, 7.949 (2); 7.721, 7.705, 7.688 (1)	
$[Pt(^{13}CO)(pyO)Br_2]$	8.542, 8.527 (2); 7.986, 7.968, 7.950 (2); 7.721, 7.706, 7.689 (1)	
$[Pt(CO)(py\text{-}d_5O)Br_2]$	—[c]	
$[Pt(C_2H_4)(quinO)Cl_2]$	8.983, 8.959, 8.939 (2); 8.382, 8.361 (1); 8.073, 8.052, 8.031 (2); 7.854, 7.836, 7.816 (1); 7.668, 7.652, 7.633 (1)	
	4.431[b], 4.347[a], 4.264[b] (4)	33.61
$[Pt(C_2D_4)(quinO)Cl_2]$	9.007, 8.985 (1); 8.951, 8.937 (1); 8.374, 8.354 (1); 8.085, 8.066, 8.048, 8.030 (2); 7.862, 7.844, 7.825 (1); 7.662, 7.646, 7.642, 7.626 (1)	
$[Pt(C_2H_4)(quin\text{-}d_7O)Cl_2]$	4.444[b], 4.359[a], 4.275[b]	34.01
$[Pt(CO)(quinO)Cl_2]$	8.937, 8.930, 8.908 (2); 8.499, 8.478 (1); 8.136, 8.117, 8.097 (2); 7.921, 7.902, 7.883 (1); 7.728, 7.713, 7.707, 7.692 (1)	
$[Pt(^{13}CO)(quinO)Cl_2]$	8.906, 8.904 (1); 8.895, 8.881 (1); 8.465, 8.444 (1); 8.106, 8.084, 8.065 (2); 7.890, 7.870, 7.852 (1); 7.694, 7.678, 7.673, 7.658 (1)	
$[Pt(CO)(quin\text{-}d_7O)Cl_2]$	—[c]	
$[Pt(C_2H_4)(quinO)Br_2]$	8.977, 8.955 (1); 8.908, 8.906, 8.893, 8.890 (1); 8.356, 8.335 (1); 8.088, 8.085, 8.071, 8.067, 8.063, 8.049, 8.030 (2); 7.869, 7.866, 7.849, 7.846, 7.831, 7,828 (1); 7.671, 7.656, 7.650, 7.635 (1)	
	4.574[b], 4.488[a], 4.403[b] (4)	34.41
$[Pt(C_2D_4)(quinO)Br_2]$	8.963, 8.941 (1); 8.910, 8.895 (1); 8.360, 8.339 (1); 8.072, 8.070, 8.052, 8.048, 8.030, 8.027 (2); 7.857, 7.838, 7.819 (1); 7.675, 7.659, 7.654, 7.639 (1)	
$[Pt(C_2H_4)(quin\text{-}d_7O)Br_2]$	4.574[b], 4.489[a], 4.404[b]	34.01
$[Pt(C_2H_4)(quin\text{-}^{18}O)Br_2]$	8.938, 8.918 (1); 8.813 (1); 8.202 (1); 8.009, 7.989 (2); 7.825, 7.806, 7.788 (1); 7.571 (1)	
	4.582[b], 4.494[a], 4.408[b] (4)	35.21
$[Pt(CO)(quinO)Br_2]$	8.868, 8.866, 8.853, 8.830 (2); 8.454, 8.433 (1); 8.102, 8.099, 8.085, 8.081, 8.077, 8.068, 8.064, 8.062 (2); 7.895, 7.892, 7.878, 7.874, 7.857, 7.854 (1); 7.710, 7.694, 7.689, 7.673 (1)	
$[Pt(^{13}CO)(quinO)Br_2]$	8.869, 8.866, 8.861, 8.855, 8.852, 8.839 (2); 8.450, 8.429 (1) 8.104, 8.101, 8.086, 8.082, 8.063 (2); 7.895, 7.893, 7.878, 7.874, 7.857, 7.855 (1); 7.705, 7.690, 7.684, 7.669 (1)	
$[Pt(CO)(quin\text{-}d_7O)Br_2]$	—[c]	

a C_2H_4 signal.
b Pt satellites.
c No peaks obtained.

Table 4.2. ^{13}C nmr spectra of Zeise's salt derivatives.

Compound	Chemical shift (ppm)	$J_{(Pt-C)}$ (Hz)
$[Pt(C_2H_4)(pyO)Cl_2]$	142.097, 136.934, 126.283; 61.072[a]	
$[Pt(C_2D_4)(pyO)Cl_2]$	142.080, 136.909, 126.293; 60.968[a], 60.720[a], 60.468[a], 60.221[a]	
$[Pt(C_2H_4)(py\text{-}d_5O)Cl_2]$	141.929, 141.640, 141.345; 137.017, 136.763, 136. 511; 126.227, 125.971, 125.703; 62.661[b], 61.576[a], 60.471[b]	109.17
$[Pt(CO)(pyO)Cl_2]$	145.392; 142.547, 137.754, 126.543	
$[Pt(^{13}CO)(pyO)Cl_2]$	154.834[b], 145.408[c], 145.373[d], 135.981[b]; 142.558, 137.759, 126.551	948.48
$[Pt(CO)(py\text{-}d_5O)Cl_2]$	145.413[c]; 142.495, 142.202, 141.913; 137.585, 137.304, 137.045; 126.326, 126.066, 125.806	
$[Pt(C_2H_4)(pyO)Br_2]$	141.560[c], 136.462, 126.777; 59.573[a]	
$[Pt(C_2D_4)(pyO)Br_2]$	141.550, 136.438, 126.782	
$[Pt(C_2H_4)(py\text{-}d_5O)Br_2]$	142.201, 141.905, 141.614; 136.547, 136.266, 135.984; 125.999, 125.742, 125.479; 59.222[b], 58.176[a], 57.153[b]	105.25
$[Pt(CO)(pyO)Br_2]$	145.253[c]; 142.603; 137.614; 126.446	
$[Pt(^{13}CO)(pyO)Br_2]$	154.415[b], 145.262[c], 145.226[d], 136.112[b]; 154.415, 136.112, 126.453	921.00
$[Pt(CO)(py\text{-}d_5O)Br_2]$	145.272[c]; 142.534, 142.251, 141.957; 137.436, 136,784, 136.131; 126.250, 126.001, 125.726	
$[Pt(C_2H_4)(quinO)Cl_2]$	142.448, 139.281, 137.958, 134.137, 129.913, 128.568, 119.556 119.372; 61.104[a]	
$[Pt(C_2D_4)(quinO)Cl_2]$	142.491, 139.427, 137.889, 134.157, 129.971, 129.907, 128.545 119.542	
$[Pt(C_2H_4)(quin\text{-}d_7O)Cl_2]$	142.440, 142.133, 141.796; 139.280; 137.913, 137.766, 137.627; 133.949, 133.685, 133.436; 129.775; 129.641, 129.347, 129.150; 128.315, 128.080, 127.802; 119.377, 119.113, 118.820; 119.311, 119.047, 118.768; 62.186[b], 61.094[a], 60.046[b]	109.88
$[Pt(CO)(quinO)Cl_2]$	146.203[c]; 143.714, 139.982, 139.388, 134.971, 130.590, 130.494, 129.051, 119.840, 119.828	
$[Pt(^{13}CO)(quinO)Cl_2]$	155.190[b], 145.797[c], 145.762[d], 136.409[b]; 143.312, 139.589, 138.979, 134.566, 130.186, 130.095, 128.646, 119.435	945.15
$[Pt(CO)(quin\text{-}d_7O)Cl_2]$	155.187[b], 145.812[c], 136.446[b]; 143.284, 143.006, 142.705; 139.431; 138.849, 138.581, 138.330; 134.296, 134.050, 133.798; 129.904; 129.904, 129.648, 129.397; 128.457, 128.212, 127.962; 119.228, 118.974, 118.711	943.34
$[Pt(C_2H_4)(quinO)Br_2]$	142.551, 139.414, 137.740, 134.131, 129.896, 128.578, 119.671, 119.467; 58.035[a]	
$[Pt(C_2D_4)(quinO)Br_2]$	142.604, 139.327, 137.842, 134.095, 130.254, 129.874, 128.580, 119.571, 119.493; 57.720[a], 57.462[a], 57.211[a], 56.982[a], 56.726[a]	
$[Pt(C_2H_4)(quin\text{-}d_7O)Br_2]$	142.565, 142.265, 141.986; 139.339; 137.612, 137.341, 137.121; 133.898, 133.619, 133.414; 129.765; 129.619, 129.377, 129.128; 128.373, 128.110, 127.868; 119.582, 119.201, 118.950; 119.296, 119.047, 118.724; 59.087[b], 58.076[a], 57.028[b]	101.73
$[Pt(C_2H_4)(quin\text{-}^{18}O)Br_2]$	128.463, 119.731	
$[Pt(CO)(quinO)Br_2]$	145.577[c]; 143.231, 139.514, 138.891, 134.527, 130.189, 130.021, 128.665, 119.547, 119.310	
$[Pt(^{13}CO)(quinO)Br_2]$	154.674[b], 145.560[c], 145.525[d], 136.446[b]; 143.213, 139.542, 138.841, 134.511, 130.177, 130.022, 128.636, 119.581, 119.276	917.08
$[Pt(CO)(quin\text{-}d_7O)Br_2]$	154.694[b], 145.577[c], 136.483[b]; 143.415, 143.135, 142.876; 139.486; 138.552, 138.422, 138.081; 134.248, 133.979, 133.779; 129.892; 129.881, 129.677, 129.371; 128.513, 128.211, 128.03; 119.434, 119.064, 118.841	917.38

a C_2H_4 signal;
b Pt satellites;
c CO signal;
d $^{13}C^{18}O$ signal (very weak)

Table 4.3. Microanalytical data for $[PtALX_2]$ compounds.[a]

Compound	% C calc. (exp.)	% H calc. (exp.)	% N calc. (exp.)
$[Pt(C_2H_4)(pyO)Cl_2]$	21.61 (21.92)	2.33 (2.26)	3.60 (3.48)
$[Pt(C_2D_4)(pyO)Cl_2]$	21.38 (21.58)	2.31 (2.28)	3.56 (3.39)
$[Pt(C_2H_4)(py\text{-}d_5O)Cl_2]$	21.33 (21.52)	2.31 (2.25)	3.55 (3.65)
$[Pt(CO)(pyO)Cl_2]$	18.52 (18.43)	1.30 (1.50)	3.60 (3.63)
$[Pt(^{13}CO)(pyO)Cl_2]$	18.47 (18.19)	1.29 (1.43)	3.59 (3.51)
$[Pt(CO)(py\text{-}d_5O)Cl_2]$	18.28 (18.34)	1.28 (1.10)	3.55 (3.43)
$[Pt(C_2H_4)(pyO)Br_2]$	17.59 (17.87)	1.90 (1.82)	2.93 (2.81)
$[Pt(C_2D_4)(pyO)Br_2]$	17.44 (18.03)	1.88 (1.80)	2.91 (3.08)
$[Pt(C_2H_4)(py\text{-}d_5O)Br_2]$	17.40 (17.65)	1.88 (1.73)	2.90 (2.75)
$[Pt(CO)(pyO)Br_2]$	15.08 (15.37)	1.05 (1.12)	2.93 (2.99)
$[Pt(^{13}CO)(pyO)Br_2]$	15.05 (15.06)	1.05 (1.13)	2.92 (2.96)
$[Pt(CO)(py\text{-}d_5O)Br_2]$	14.92 (15.00)	1.04 (0.90)	2.90 (2.82)
$[Pt(C_2H_4)(quinO)Cl_2]$	30.08 (30.69)	2.52 (2.43)	3.19 (3.63)
$[Pt(C_2D_4)(quinO)Cl_2]$	29.81 (30.17)	2.50 (2.39)	3.16 (3.22)
$[Pt(C_2H_4)(quin\text{-}d_7O)Cl_2]$	29.61 (29.99)	2.49 (2.38)	3.14 (3.07)
$[Pt(CO)(quinO)Cl_2]$	27.35 (27.62)	1.61 (1.57)	3.19 (3.05)
$[Pt(^{13}CO)(quinO)Cl_2]$	27.28 (27.99)	1.60 (1.51)	3.18 (3.15)
$[Pt(CO)(quin\text{-}d_7O)Cl_2]$	26.92 (27.27)	1.58 (1.46)	3.14 (3.00)
$[Pt(C_2H_4)(quinO)Br_2]$	25.02 (25.65)	2.10 (1.98)	2.65 (2.52)
$[Pt(C_2D_4)(quinO)Br_2]$	24.83 (25.12)	2.09 (2.32)	2.63 (2.61)
$[Pt(C_2H_4)(quin\text{-}d_7O)Br_2]$	24.69 (25.05)	2.07 (1.95)	2.62 (2.65)
$[Pt(CO)(quinO)Br_2]$	22.75 (22.86)	1.34 (1.39)	2.65 (2.73)
$[Pt(^{13}CO)(quinO)Br_2]$	22.70 (23.61)	1.33 (1.44)	2.65 (2.69)
$[Pt(CO)(quin\text{-}d_7O)Br_2]$	22.45 (22.49)	1.32 (1.02)	2.62 (2.63)

a Microanalyses were performed by Mr. P. Benincasa, University of Cape Town and by Ms. T. Naidoo, University of Natal.

The bromide Zeise's salt derivatives show a well defined single C_2H_4 signal at a slightly higher value than the corresponding Cl derivatives. This was used as evidence that full conversion of $K[Pt(C_2H_4)Cl_3]$ to $K[Pt(C_2H_4)Br_3]$ was achieved before reaction with the L ligands.

^{13}C nmr spectra are particularly interesting for the C_2D_4, py-d_5O, quin-d_7O and ^{13}CO analogues. In the ethylene-d_4 derivatives, due to coupling with the D nuclei with a $I = 1$ value, the number of peaks expected for the ethylene carbons is calculated as $2I + 1$. The signal is extremely weak and long runs have to be performed in order to obtain the 5 expected ^{13}C signals. A cluster of peaks was obtained for the $[Pt(C_2D_4)(pyO)Cl_2]$, $[Pt(C_2D_4)(quinO)Cl_2]$ and $[Pt(C_2D_4)(quinO)Br_2]$ compounds. They were not observed in the $[Pt(C_2D_4)(pyO)Br_2]$ derivative which was run for a shorter period of time.

The ^{13}C signals in the py-d_5O and quin-d_7O derivatives split into three weak intensity peaks according to $2I$ +1. They were observed in all of the compounds and are particularly interesting in

the quin-d_7O derivatives. Out of the nine ^{13}C signals obtained for the quinO derivatives, seven of these appear as weak triplets and two (139.431, 129.904 ppm, values for the ^{13}C nmr spectrum for [Pt(CO)(quin-d_7O)Cl_2]) as single peaks that correspond to the two C atoms in the fused quinO ring system.

The ^{13}C spectra for the ^{13}CO derivatives yield an extremely intense signal at *ca*. 146 ppm which corresponds to the ^{13}CO ligand. Pt-C coupling was observed in the nmr spectra for all the ^{13}CO derivatives. An extremely weak shoulder band to the ^{13}CO signal was obtained for all ^{13}CO derivatives. It has been assigned to $^{13}C^{18}O$ signal, as the mid-ir spectra show that a significant amount of this isotopomer is present in the ^{13}CO used.

Pt-C coupling was also observed for some of the C_2H_4 compounds, especially those with py-d_5O and quin-d_7O, due to the long runs performed.

4.2.9. Infrared spectra

Infrared spectra were recorded on a Perkin-Elmer Spectrum 2000 FT-IR spectrometer. Mid ir spectra were recorded in the region 4000 to 400 cm^{-1} with 4 scans and at a resolution of 4 cm^{-1}. Far ir spectra were recorded in the region 650 to 30 cm^{-1} and the number of scans was typically 64, but varied for some samples like the *N*-oxide ligands and the some of the Zeise's salt derivatives for which up to 200 scans were used to minimize noise signals occurring below 200 cm^{-1}. Spectra were recorded at a resolution of 4 cm^{-1}.

Mid ir spectra for pyO and quinO ligands were obtained on CsI windows. Due to the extremely hygroscopic nature of these compounds, the sample was added to one of the CsI windows and heated for approximately 15 minutes in an oven at 100 °C. The other CsI window was placed covering the sample, heated for an additional 5 minutes, and allowed to cool in a desiccator before ir spectra were recorded.

Far ir spectra for the pyO and quinO ligands were obtained as described above using polyethylene windows.

All mid ir spectra for the Zeise's salt derivatives were run in KBr pellets and all far ir spectra in polyethylene pellets.

The chloride derivatives show an intense absorption at *ca.* 327 cm^{-1} (ν_aPt-Cl) which is absent in the bromide derivatives and which in turn show an intense absorption at *ca.* 250 cm^{-1} (ν_aPt-Br). Together with the nmr data, this further confirms that full chloride to bromide exchange was obtained in the preparation of the bromide derivatives of Zeise's salt.

4.2.1.0. Raman spectra

Raman spectra were collected by Prof. S. O. Paul at UNISA.

Raman spectra were collected in a Bruker RFS100 FT-Raman spectrometer with a Nd-YAG laser (1064 nm radiation) and a liquid nitrogen cooled Ge detector. Samples were in a powdered form in small Al holders. The laser excitation power at the samples ranged from 3 to 30 mW, depending on the fluorescence of the sample. This fluorescence also necessitated a large number of scans: either 512 or 1064 scans were co-added and averaged.

The spectra were recorded at a resolution of 4 cm^{-1} with a zero-filling factor of 2 in the region 3500 to 100 cm^{-1}.

Raman spectra were recorded for all of the Zeise's salt derivatives prepared, with the exception of $[Pt(C_2H_4)(pyO/py\text{-}^{18}O)Br_2]$.

4.2.11. Molecular modelling

Zeise's salt derivatives were modelled using molecular mechanics with the Cerius2 and Spartan02 program packages. DFT calculations were performed with Spartan02 at the B3LYP level employing the basis set LACVP** for Pt(II) and 6-31G** for the remaining atoms.

4.3. Preparation of [Cu(CO)(*n*,*m*N3)]BPh_4 compounds

Preparation of the triamine carbonyl derivatives was achieved by the following method outlined for the 2,2N3 compound. All other compounds were prepared accordingly.

Syntheses were carried out using distilled, dry, degassed solvents employing Schlenk line techniques. All triamine ligands were supplied by Aldrich and used without further purification. Reactions were performed under high purity nitrogen free of oxygen by passage through an oxygen trap (<30 ppb oxygen). CO was similarly purified by passage through an oxygen trap.

0.5 g (2.6 mmol) of CuI were added to 5 mL of distilled, dry methanol, under a stream of purified N_2. A Cu(0) coil was added to the suspension to reproportionate any Cu(II) species that could form upon addition of the ligand. An excess of the triamine (300 μL; 2.75 mmol) was added to the CuI suspension under a stream of purified CO. The CuI dissolved immediately yielding a pale blue solution that turned colourless after stirring under a CO atmosphere. 0.83 g of $NaBPh_4$ (2.4 mmol) were added to the colourless solution under a stream of CO and a white solid precipitated immediately. The white solid was vacuum filtered under a stream of purified CO by fitting a glass frit to the Schlenk tube. The compounds are quite stable when completely dry, but rapid oxidation to Cu(II) was observed when complete dryness had not been achieved or in the presence of moisture. The compounds were stored under CO and undergo decomposition slowly.

The 3,4N3 system was handled as a solid under N_2 in a glove box as it melts quickly, is extremely hygroscopic and has an overwhelming stench. Once placed in the Schlenk tube under N_2 this was stopped and weighed. Dry distilled MeOH was added under a stream of N_2 together with a Cu(0) coil and, CuI was added to the solution under a stream of CO to produce a light blue solution which turned colourless after stirring under a CO atmosphere. The product was precipitated by addition of $NaBPh_4$ as described above.

Yields obtained in the preparation of the [Cu(CO)(*n*,*m*N3)]BPh4 systems were quite high (85-95%). Due to the facile oxidation to Cu(II), the compounds were not purified any further.

Infrared spectra (mid and far ir) were run immediately after preparation of the compounds. Microanalyses are shown in table 4.4.

Table 4.4. Microanalytical data for [Cu(CO)(*n*,*m*N3)]BPh_4 compounds.[a]

Compound	% C calc. (exp.)	% H calc. (exp.)	% N calc. (exp.)
[Cu(CO)(2,2N3)]BPh_4	67.77 (67.62)	6.47 (6.43)	8.18 (8.04)
[Cu(^{13}CO)(2,2N3)]BPh_4	67.64 (68.26)	6.46 (6.45)	8.16 (8.13)
[Cu(CO)(2,3N3)]BPh_4	68.28 (67.56)	6.69 (6.66)	7.97 (7.80)
[Cu(CO)(3,3N3)]BPh_4	68.73 (68.82)	6.89 (6.86)	7.76 (7.68)
[Cu(CO)(3,4N3)]BPh_4†	69.01 (66.01)	7.07 (6.79)	7.56 (7.42)

a Microanalyses were performed by Mr. P. Benincasa, University of Cape Town and by Ms. T. Naidoo, University of Natal.

† Contaminated with unreacted CuI. Calculated values of %C = 66.83, %H = 6.84, %N = 7.31 are obtained for [Cu(CO)(3,4N3)]BPh_4·0.1CuI.

4.3.1. Preparation of [Cu(^{13}CO)(2,2N3)]BPh_4

The compound was prepared as mentioned above, except that a vacuum was generated in the Schlenk tube with the CuI methanolic suspension and the Cu(0) coil under N_2. The tube was filled with ^{13}CO (99 % C-13 purity from Aldrich) and was left stirring for 2 days until the blue solution was colourless. $NaBPh_4$ was added under a stream of purified N_2 as described previously and it was filtered under a stream of purified N_2. Mid and far ir spectra were collected immediately.

4.3.2. Preparation of [Cu(CO)(*n*,*m*N3-d_5)]BPh_4 derivatives

To a dry Schlenk tube containing 150 μL (1.34 mmol) of C2,2N3 was added 1 mL of deuterated methanol (monodeuterium methyl alcohol, 99.5 % D purity from Aldrich). In order to obtain complete exchange of the amine protons, the methanol was evaporated under a stream of N_2 by heating the Schlenk tube in a water bath at 50 °C. Once the solvent evaporated, more MeOD was added (0.5 mL) and the procedure repeated for a total of 5 times. CuI and a Cu(0) coil were added under a stream of CO. The compound was precipitated by addition of $NaBPh_4$ under a stream of CO and was filtered under a stream of CO. Mid and far ir spectra of the compound were run immediately to prevent exchange of the deuterated amines.

All compounds prepared are white but turn slightly blue upon exposure to air or greyish brown over time when stored under CO or N_2 and kept in a desiccator.

4.3.3. Preparation of [Cu(CO)(2,2N3)]I and [Cu(CO)(2,2N3-d_5)]I

0.5 g (2.6 mmol) of CuI were added to 5 mL of distilled, dry methanol, under a stream of purified N_2. A Cu(0) coil was added to the suspension to reproportionate any Cu(II) species that could form upon addition of the ligand. An excess of the triamine (300 μL; 2.75 mmol) was added to the CuI suspension under a stream of purified CO. The pale blue solution was left stirring until it turned colourless. The solution was cooled in an acetone/ice bath until precipitation of a white crystalline solid was observed which was vacuum filtered under a stream of purified CO by fitting a glass frit to the Schlenk tube.

The -d_5 derivative was prepared by D-exchange of the ligand with MeOD prior to addition of CuI as mentioned above for the [Cu(CO)(2,2N3-d_5)]BPh_4 derivative.

The compounds are extremely unstable and fast oxidation to Cu(II) was observed. Mid and far ir spectra for the compounds were run immediately after preparation.

4.3.4. Preparation of $[Cu(CO)(2,2N3)]BF_4$

Preparation of the $[Cu(CO)(2,2N3)]BF_4$ derivative follows that described for the $[Cu(CO)(2,2N3)]BPh_4$ compound except that $NaBF_4$ (0.26 g; 2.4 mmol) was added instead of $NaBPh_4$. Precipitation of the compound was obtained by cooling in an acteone/ice bath.

The compound is unstable and oxidation to Cu(II) was observed. Mid and far ir spectra of the compound were run immediately after preparation.

4.3.5. Molecular modelling

Cu(I) systems were modelled using semiempirical methods with the Cerius2 and Spartan02 program packages. DFT calculations were performed with Spartan02 at the B3LYP level employing the 6-31G** and 6-31 + G* basis sets.

4.4. Preparation of the Schiff base derivatives of diethylenetriamine, $[Cu(CO)\{2,2N3(C6H4X)2\}]BPh_4$ compounds; X = NO_2, F, Cl, Br, H, Me, MeO, NMe_2.

All Schiff base derivatives were prepared following the same reaction scheme that will be outlined below for the reaction of diethylenetriamine (2,2N3) with benzaldehyde. All other substituted benzaldehydes employed have the X substituent in position 4.

1 mL of diethylenetriamine (9.16 mmol) was added to 5 mL of dried distilled methanol. To this solution were added 2 mL of benzaldehyde (20 mmol). The reaction mixture was heated in an oil bath and refluxed under N_2 for a period of 2 hours after which the hot, slightly yellow methanolic solution was added to a Schlenk tube containing 1.71 g of CuI (9 mmol) under N_2. The Schiff base reacts immediately with the CuI to yield a yellow compound that may, for some of the Schiff bases employed, turn orange or brick red. Addition of CO to the Schlenk tube is followed by the slow redissolution and precipitation of the cream coloured carbonyl derivatives upon addition of the $NaBPh_4$ counter-ion (3.08 g; 9 mmol). As the reaction products are not totally soluble in MeOH, the reaction was left stirring under a CO atmosphere for approximately two days in the presence of a Cu(0) coil and then vacuum filtered under a stream of N_2 or CO. The dry compounds slowly turn yellow when not stored under a CO atmosphere. With electron-donating substituents like NMe_2, the compounds easily turn green due to oxidation to the Cu(II) species.

Yields for all reaction were close to 90 %.

Mid and far ir spectra for the compounds were recorded immediately after preparation. Microanalysis results for the Schiff base systems prepared are shown in table 4.5. Most compounds (X = Cl, Br, Me, MeO) analyze satisfactorily for the monohydrated compound $[Cu(CO)\{2,2N3(C_6H_4X)_2\}]BPh_4 \cdot H_2O$. Larger than expected values of N are obtained for the X = F derivative although results for C and H are satisfactory. It is likely that the compound is contaminated with unreacted 2,2N3 ligand, which would increase the N content in the compound. In fact, a very weak intensity band is observed in the mid ir spectrum for this compound (X = F), at slightly lower frequency than the intense νN-H band. The compound with X = NMe_2 analyzes satisfactorily for the trihydrated compound $[Cu(CO)\{2,2N3(C_6H_4NMe_2)_2\}]BPh_4 \cdot 3H_2O$.

Table 4.5. Microanalytical data for $[Cu(CO)\{2,2N3(C_6H_4X)_2\}]BPh_4 \cdot H_2O$ compounds.[a]

X	% C calc. (exp.)	% H calc. (exp.)	% N calc. (exp.)
NO_2	64.71 (62.93)	5.18 (4.87)	8.77 (9.17)
F†	69.40 (69.80)	5.55 (5.67)	5.65 (6.21)
Cl	66.46 (66.66)	5.32 (5.24)	5.41 (5.48)
Br	59.64 (59.33)	4.77 (4.71)	4.85 (4.86)
H	72.93 (71.83)	6.12 (5.83)	5.93 (5.99)
Me	73.41 (72.46)	6.43 (6.39)	5.71 (5.76)
MeO	70.35 (70.35)	6.17 (6.10)	5.47 (5.56)
NMe_2‡	67.98 (68.07)	6.92 (6.65)	8.43 (8.59)

a Microanalyses were performed by Ms. T. Naidoo, University of Natal.
† Possibly contaminated with 2,2N3.
‡ Calculated values for $[Cu(CO)\{2,2N3(C_6H_4X)_2\}]BPh_4 \cdot 3H_2O$.

The compounds decarbonylate over time, and loss of CO in transit may have an effect on the microanalytical results obtained.

Crystals suitable for XRD were obtained for the $[Cu(CO)\{2,2N3(C_6H_5)_2\}]BPh_4$ compound by cooling of the mother liquor in a Schlenk tube filled with CO in a freezer for several days. The crystal structure for this compound is discussed in section 3.4.1. Crystal structure parameters, bond lengths and angles, and average isotropic displacement parameters are shown in appendix 3.

Infrared spectra for all Cu(I) compounds were recorded on a Perkin-Elmer Spectrum 2000 FT-IR spectrometer. Mid ir spectra were run as KBr pellets and far ir spectra as polyethylene pellets. Number of scans and resolution are the same as those stated above for the Zeise's salt derivatives.

References

1. Watkins, G.M.; *Ligand Isotope Vibrational Studies of Metal (II) Complexes With Particular Reference to Heterocyclic N-oxides*, PhD Thesis, University of Cape Town, 1988.
2. Ochiai, E; *J. Org. Chem.*; **18**, 1953, 534.
3. Sørensen, G.O.; Tang-Pedersen, Å.; Pedersen, E.J.; *J. Mol. Struct.*; **101**, 1983, 263–268.
4. Ball, R.E.; Edwards, J.O.; Jones, P.; *J. Inorg. Nucl. Chem.*; **28**, 1966, 2460–2461.
5. Jarnagin, R.C.; Wang, J.H.; *J. Am. Chem. Soc.*; **80**, 1957, 786–787.
6. Rodebush, W.H.; Keizer, C.R.; McKee, F.S.; Quagliano, J.V.; *J. Am. Chem. Soc.*; **69**, 1947, 538–540.
7. Chatt, I.; Searle, M.L.; *Inorg. Synth.*; **5**, 1957, 210–211.
8. Hall, P.S.; Thornton, D.A.; Foulds, G.A.; *Polyhedron*; **6**, 1987, 85–94.
9. Foulds, G.A.; Hall, P.S.; Thornton, D.A.; Watkins, G.M.; *Spectrochim. Acta*; **84A**, 1992, 597–604.

Appendix 1

Crystal structure parameters, bond lengths and angles, and average isotropic displacement parameters for $[Pt(C_2H_4)(pyO)Cl_2]$.

Crystal structure parameters

Crystal Data			
Formula			C7 H9 Cl2 N O Pt
Formula Weight			389.13
Crystal System			Monoclinic
Space group		C2	(No. 5)
a, b, c [Angstrom]	18.391(4)	6.7850(14)	8.5432(17)
alpha, beta, gamma [deg]	90	112.46(3)	90
V [Ang**3]			985.2(4)
Z			4
D(calc) [g/cm**3]			2.624
Mu(MoKa) [/mm]			14.736
F(000)			712
Crystal Size [mm]		0.09 x 0.10 x 0.10	
Data Collection			
Temperature (K)			193
Radiation [Angstrom]		MoKa	0.71073
Theta Min-Max [Deg]			3.8, 28.3
Dataset		-24: 24 ; -9: 9 ; -11: 11	
Tot., Uniq. Data, R(int)		4575, 2408, 0.028	
Observed data [I > 2.0 sigma(I)]			2319
Refinement			
Nref, Npar			2408, 110
R, wR2, S		0.0230, 0.0541, 1.07	
w = 1/[s^2^(Fo^2^)+(0.0224P)^2^]		where P=(Fo^2^+2Fc^2^)/3	
Max. and Av. Shift/Error			0.00, 0.00
Flack x			-0.016(10)
Min. and Max. Resd. Dens. [e/Ang^3]			-1.08, 1.19

- PLATON Reference : Spek, A.L. (1990), Acta Cryst. A46, C-34

Bond lengths and angles

Bond Lengths (Angstrom). - (Bonds are ordered on the first label, left to right and top to bottom) - esd in last digit in ().

Pt(1) - Cl(1)	2.2913(17)	Pt(1) - Cl(2)	2.2835(19)	Pt(1) - O(1)	2.047(5)	Pt(1) - C(6)	2.112(7)
Pt(1) - C(7)	2.115(8)	O(1) - N(1)	1.368(7)	N(1) - C(1)	1.323(8)	N(1) - C(5)	1.343(8)
C(1) - C(2)	1.375(10)	C(2) - C(3)	1.397(10)	C(3) - C(4)	1.362(9)	C(4) - C(5)	1.395(9)
C(6) > C(7)	1.391(13)						

C(1) - H(1)	0.9501	C(2) - H(2)	0.9501	C(3) - H(3)	0.9506	C(4) - H(4)	0.9490
C(5) - H(5)	0.9497	C(6) - H(6A)	0.9899	C(6) - H(6B)	0.9903	C(7) - H(7A)	0.9902
C(7) - H(7B)	0.9898						

Bond/Valence Angles (Degrees) - (Angles are ordered on the middle label, left to right and top to bottom) - esd in last digit in ().

Cl(1) - Pt(1) - Cl(2)	178.96(7)	Cl(1) - Pt(1) - O(1)	85.15(14)	Cl(1) - Pt(1) - C(6)	90.9(2)
Cl(1) - Pt(1) - C(7)	90.0(2)	Cl(2) - Pt(1) - O(1)	93.90(14)	Cl(2) - Pt(1) - C(6)	90.1(2)
Cl(2) - Pt(1) - C(7)	90.7(2)	O(1) - Pt(1) - C(6)	161.0(3)	O(1) - Pt(1) - C(7)	159.6(3)
C(6) - Pt(1) - C(7)	38.4(4)	Pt(1) - O(1) - N(1)	120.5(4)	O(1) - N(1) - C(1)	119.7(5)
O(1) - N(1) - C(5)	117.6(5)	C(1) - N(1) - C(5)	122.5(6)	N(1) - C(1) - C(2)	120.6(6)
C(1) - C(2) - C(3)	118.3(6)	C(2) - C(3) - C(4)	120.2(6)	C(3) - C(4) - C(5)	119.3(6)
N(1) - C(5) - C(4)	119.0(5)	Pt(1) - C(6) - C(7)	70.9(4)	Pt(1) - C(7) - C(6)	70.7(4)

N(1) - C(1) - H(1)	119.69	C(2) - C(1) - H(1)	119.66	C(1) - C(2) - H(2)	120.91
C(3) - C(2) - H(2)	120.81	C(2) - C(3) - H(3)	119.95	C(4) - C(3) - H(3)	119.88
C(3) - C(4) - H(4)	120.40	C(5) - C(4) - H(4)	120.28	N(1) - C(5) - H(5)	120.48
C(4) - C(5) - H(5)	120.52	Pt(1) - C(6) - H(6A)	116.51	Pt(1) - C(6) - H(6B)	116.52
C(7) - C(6) - H(6A)	116.51	C(7) - C(6) - H(6B)	116.55	H(6A) - C(6) - H(6B)	113.52
Pt(1) - C(7) - H(7A)	116.57	Pt(1) - C(7) - H(7B)	116.57	C(6) - C(7) - H(7A)	116.55
C(6) - C(7) - H(7B)	116.56	H(7A) - C(7) - H(7B)	113.52		

Average (an)isotropic displacement parameters

(An)isotropic, Equivalent and Main Axes Displacement Parameters - Unusual Values Marked with a # - [Optional Coordinate Split-up]

Atom	Label	U11 or Uiso	U22	U33	U23	U13	U12	Ueq(sUeq)	U1	U2	U3	U3/U1
1	Pt1	0.02084(12)	0.02165(12)	0.02782(13)	0.00012(12)	0.00880(8)	-0.00160(9)	0.02358(7)	0.0194	0.0229	0.0284	1.46
		[0.0493	0.0046	0.2914]	[0.0478	0.0036	0.2840]					
2	Cl1	0.0209(6)	0.0407(8)	0.0597(9)	0.0064(7)	0.0150(6)	0.0020(6)	0.0406(4)	0.0194	0.0389	0.0633	3.25
		[0.1734	-0.1346	0.3940]	[0.1676	-0.1450	0.3672]					
3	Cl2	0.0277(7)	0.0293(8)	0.0679(10)	0.0003(8)	0.0078(6)	0.0065(6)	0.0448(5)	0.0219	0.0347	0.0776	3.54
		[-0.0712	0.1410	0.2127]	[-0.0765	0.1438	0.1797]					
4	O1	0.018(2)	0.028(2)	0.062(3)	-0.003(2)	0.009(2)	-0.0051(16)	0.0379(14)	0.0158	0.0300	0.0678	4.29
		[0.0098	-0.2796	0.2682]	[0.0034	-0.2778	0.2342]					
5	N1	0.017(2)	0.020(2)	0.045(3)	-0.0022(19)	0.0096(18)	-0.0013(19)	0.0280(14)	0.0163	0.0202	0.0475	2.92
		[-0.0703	-0.3154	0.2013]	[-0.0749	-0.3130	0.1785]					
6	C1	0.032(3)	0.025(3)	0.044(3)	0.000(2)	0.016(2)	-0.001(2)	0.0332(17)	0.0248	0.0308	0.0441	1.78
		[-0.1097	-0.3434	0.0323]	[-0.1129	-0.3434	0.0191]					
7	C2	0.032(3)	0.027(3)	0.043(3)	-0.002(2)	0.005(2)	0.000(2)	0.0368(17)	0.0266	0.0294	0.0543	2.04
		[-0.1886	-0.3977	-0.0282]	[-0.1902	-0.3953	-0.0454]					
8	C3	0.026(3)	0.027(3)	0.051(4)	0.003(3)	0.008(3)	0.002(2)	0.0367(19)	0.0241	0.0285	0.0573	2.37
		[-0.2247	-0.4188	0.0882]	[-0.2281	-0.4212	0.0670]					
9	C4	0.030(3)	0.032(3)	0.056(4)	0.001(3)	0.021(3)	-0.002(2)	0.0380(19)	0.0250	0.0329	0.0561	2.25
		[-0.1831	-0.3880	0.2559]	[-0.1881	-0.3892	0.2363]					
10	C5	0.026(3)	0.032(3)	0.038(3)	0.002(2)	0.011(2)	0.000(2)	0.0324(17)	0.0259	0.0314	0.0398	1.54
		[-0.1060	-0.3294	0.3073]	[-0.1078	-0.3330	0.2981]					
11	C6	0.050(4)	0.019(3)	0.095(6)	0.009(3)	0.034(4)	-0.013(3)	0.053(3)	0.0093	0.0526	0.0965	10.40#
		[0.1024	0.2797	0.2760]	[0.0898	0.2697	0.2228]					
12	C7	0.044(4)	0.034(4)	0.090(6)	-0.025(4)	0.022(4)	-0.015(3)	0.057(3)	0.0203	0.0493	0.1016	5.00#
		[0.1038	0.2578	0.4353]	[0.0950	0.2774	0.3941]					
13	H1	0.04000						0.04000				
14	H2	0.04400						0.04400				
15	H3	0.04400						0.04400				
16	H4	0.04500						0.04500				
17	H5	0.03900						0.03900				
18	H6A	0.06300						0.06300				
19	H6B	0.06300						0.06300				
20	H7A	0.06900						0.06900				
21	H7B	0.06900						0.06900				

The Displacement Factor has the Form of Exp(-T) where T = 8*(pi**2)*Uiso*sin(theta/lambda)**2, for Isotropic Atoms,

T = 2*(pi**2)*(U11*(h*as)**2+U22*(k*bs)**2+U33*(l*cs)**2+2*U23*k*l*bs*cs+2*U13*h*l*as*cs+2*U12*h*k*as*bs),for Anisotr. Atoms

Ueq = 1/3 Sum(i,j) (Uij*as(i)*as(j)*a(i).a(j))

U1, U2, U3 are the three Main Axes Components of Uij

Reference U(eq): R.X. Fischer & E. Tillmanns, Acta Cryst. (1988). C44, 775-776

Appendix 2

Crystal structure parameters, bond lengths and angles, and average isotropic displacement parameters for [Pt(CO)(quinO)Br_2].

Crystal structure parameters

Crystal Data	
Formula	C10 H7 Br2 N O2 Pt
Formula Weight	528.05
Crystal System	Triclinic
Space group	P-1 (No. 2)
a, b, c [Angstrom]	8.2115(16) 8.3089(17) 9.4738(19)
alpha, beta, gamma [deg]	85.14(3) 74.01(3) 81.90(3)
V [Ang**3]	614.5(2)
Z	2
D(calc) [g/cm**3]	2.854
Mu(MoKa) [/mm]	17.902
F(000)	476
Crystal Size [mm]	0.20 x 0.25 x 0.30
Data Collection	
Temperature (K)	193
Radiation [Angstrom]	MoKa 0.71073
Theta Min-Max [Deg]	3.4, 28.3
Dataset	0: 10 ; -10: 11 ; -12: 12
Tot., Uniq. Data, R(int)	3048, 3048, 0.000
Observed data [I > 2.0 sigma(I)]	2785
Refinement	
Nref, Npar	3048, 146
R, wR2, S	0.0244, 0.0623, 1.07
w = 1/[s^2^(Fo^2^)+(0.0359P)^2^+0.8517P]	where P=(Fo^2^+2Fc^2^)/3
Max. and Av. Shift/Error	0.00, 0.00
Min. and Max. Resd. Dens. [e/Ang^3]	-1.62, 1.41

- PLATON Reference : Spek, A.L. (1990), Acta Cryst. A46, C-34

Bond lengths and angles

Bond Lengths (Angstrom). - (Bonds are ordered on the first label, left to right and top to bottom) - esd in last digit in ().

Pt(1) - Br(1)	2.4240(7)	Pt(1) - Br(2)	2.4242(7)	Pt(1) - O(1)	2.045(3)	Pt(1) - C(1)	1.823(5)
O(1) - N(1)	1.361(4)	O(2) - C(1)	1.131(6)	N(1) - C(2)	1.316(5)	N(1) - C(10)	1.384(5)
C(2) - C(3)	1.398(7)	C(3) - C(4)	1.360(7)	C(4) - C(5)	1.406(6)	C(5) - C(6)	1.418(6)
C(5) - C(10)	1.422(6)	C(6) - C(7)	1.378(7)	C(7) - C(8)	1.402(7)	C(8) - C(9)	1.368(7)
C(9) - C(10)	1.393(6)						

C(2) - H(2)	0.9501	C(3) - H(3)	0.9499	C(4) - H(4)	0.9505	C(6) - H(6)	0.9499
C(7) - H(7)	0.9501	C(8) - H(8)	0.9497	C(9) - H(9)	0.9500		

Bond/Valence Angles (Degrees) - (Angles are ordered on the middle label, left to right and top to bottom) - esd in last digit in ().

Br(1) - Pt(1) - Br(2)	178.83(3)	Br(1) - Pt(1) - O(1)	93.94(9)	Br(1) - Pt(1) - C(1)	89.34(14)		
Br(2) - Pt(1) - O(1)	85.71(9)	Br(2) - Pt(1) - C(1)	90.99(14)	O(1) - Pt(1) - C(1)	176.53(16)		
Pt(1) - O(1) - N(1)	118.5(2)	O(1) - N(1) - C(2)	118.7(3)	O(1) - N(1) - C(10)	117.5(3)		
C(2) - N(1) - C(10)	123.8(3)	Pt(1) - C(1) - O(2)	178.2(4)	N(1) - C(2) - C(3)	119.9(4)		
C(2) - C(3) - C(4)	120.0(4)	C(3) - C(4) - C(5)	120.2(4)	C(4) - C(5) - C(6)	123.2(4)		
C(4) - C(5) - C(10)	119.0(4)	C(6) - C(5) - C(10)	117.8(4)	C(5) - C(6) - C(7)	119.8(4)		
C(6) - C(7) - C(8)	120.6(4)	C(7) - C(8) - C(9)	121.5(5)	C(8) - C(9) - C(10)	118.6(4)		
N(1) - C(10) - C(5)	117.1(4)	N(1) - C(10) - C(9)	121.2(4)	C(5) - C(10) - C(9)	121.8(4)		

N(1) - C(2) - H(2)	120.09	C(3) - C(2) - H(2)	120.01	C(2) - C(3) - H(3)	119.95		
C(4) - C(3) - H(3)	120.05	C(3) - C(4) - H(4)	119.88	C(5) - C(4) - H(4)	119.87		
C(5) - C(6) - H(6)	120.12	C(7) - C(6) - H(6)	120.12	C(6) - C(7) - H(7)	119.70		
C(8) - C(7) - H(7)	119.69	C(7) - C(8) - H(8)	119.24	C(9) - C(8) - H(8)	119.30		
C(8) - C(9) - H(9)	120.69	C(10) - C(9) - H(9)	120.73				

Average (an)isotropic displacement parameters

(An)isotropic, Equivalent and Main Axes Displacement Parameters - Unusual Values Marked with a # - [Optional Coordinate Split-up]

Atom	Label	U11 or Uiso	U22	U33	U23	U13	U12	Ueq(sUeq)	U1	U2	U3	U3/U1
1	Pt1	0.01883(11)	0.02086(11)	0.01497(10)	0.00135(6)	-0.00353(6)	-0.00229(6)	0.01856(6)	0.0143	0.0191	0.0223	1.56
		[0.3449	0.2912	0.5505]	[0.3447	0.2846	0.5487]					
2	Br1	0.0354(3)	0.0362(2)	0.0207(2)	-0.00671(18)	-0.00571(18)	-0.00708(19)	0.03054(14)	0.0184	0.0328	0.0404	2.19
		[0.2774	0.4367	0.7735]	[0.2883	0.4246	0.7759]					
3	Br2	0.0302(2)	0.0382(3)	0.0201(2)	-0.00803(18)	-0.00222(17)	-0.00265(18)	0.03016(14)	0.0173	0.0332	0.0401	2.32
		[0.4043	0.1583	0.3196]	[0.4065	0.1422	0.3242]					
4	O1	0.0194(14)	0.0365(17)	0.0145(14)	0.0030(12)	-0.0017(11)	-0.0026(12)	0.0244(9)	0.0133	0.0214	0.0384	2.89
		[0.0927	0.3128	0.5511]	[0.0955	0.2936	0.5481]					
5	O2	0.0199(16)	0.050(2)	0.045(2)	-0.0054(17)	-0.0114(15)	-0.0025(14)	0.0377(11)	0.0182	0.0434	0.0515	2.82
		[0.7125	0.2709	0.5302]	[0.7113	0.2501	0.5382]					
6	N1	0.0137(15)	0.0303(18)	0.0118(15)	0.0007(13)	-0.0008(12)	-0.0020(13)	0.0193(9)	0.0104	0.0164	0.0310	2.97
		[-0.0278	0.3109	0.6818]	[-0.0250	0.2931	0.6804]					
7	C1	0.034(3)	0.026(2)	0.022(2)	-0.0023(17)	-0.0051(18)	-0.0059(18)	0.0275(14)	0.0216	0.0252	0.0357	1.65
		[0.5769	0.2701	0.5381]	[0.5669	0.2733	0.5375]					
8	C2	0.024(2)	0.027(2)	0.025(2)	-0.0009(17)	-0.0084(17)	0.0008(17)	0.0254(12)	0.0204	0.0254	0.0303	1.48
		[-0.1145	0.4435	0.7275]	[-0.1181	0.4373	0.7285]					
9	C3	0.024(2)	0.037(3)	0.031(2)	-0.0077(19)	-0.0039(18)	0.0077(18)	0.0321(14)	0.0175	0.0337	0.0453	2.59
		[-0.2427	0.4501	0.8571]	[-0.2509	0.4331	0.8607]					
10	C4	0.023(2)	0.049(3)	0.020(2)	-0.0042(19)	0.0002(17)	-0.0016(19)	0.0320(14)	0.0164	0.0298	0.0498	3.03
		[-0.2811	0.3114	0.9372]	[-0.2795	0.2884	0.9386]					
11	C5	0.022(2)	0.035(2)	0.020(2)	-0.0011(17)	-0.0057(16)	-0.0065(17)	0.0254(12)	0.0198	0.0209	0.0353	1.78
		[-0.1867	0.1573	0.8882]	[-0.1819	0.1463	0.8882]					
12	C6	0.034(2)	0.048(3)	0.020(2)	0.0051(19)	-0.0045(19)	-0.020(2)	0.0335(14)	0.0170	0.0274	0.0559	3.28
		[-0.2191	0.0107	0.9678]	[-0.2007	-0.0101	0.9654]					
13	C7	0.042(3)	0.036(3)	0.034(3)	0.011(2)	-0.017(2)	-0.018(2)	0.0354(17)	0.0221	0.0282	0.0559	2.53
		[-0.1198	-0.1338	0.9150]	[-0.1008	-0.1456	0.9066]					
14	C8	0.037(3)	0.028(2)	0.036(3)	-0.0022(19)	-0.008(2)	-0.0039(19)	0.0340(16)	0.0279	0.0351	0.0390	1.40
		[0.0179	-0.1345	0.7782]	[0.0125	-0.1335	0.7748]					
15	C9	0.027(2)	0.031(2)	0.025(2)	0.0001(18)	-0.0079(18)	-0.0042(18)	0.0275(12)	0.0242	0.0269	0.0314	1.30
		[0.0434	0.0122	0.6982]	[0.0456	0.0072	0.6974]					
16	C10	0.0209(19)	0.027(2)	0.0137(17)	0.0008(15)	-0.0068(15)	-0.0054(15)	0.0200(11)	0.0123	0.0198	0.0278	2.27
		[-0.0573	0.1586	0.7547]	[-0.0495	0.1464	0.7531]					
17	H2	0.03100						0.03100				
18	H3	0.03800						0.03800				
19	H4	0.03900						0.03900				
20	H6	0.04000						0.04000				
21	H7	0.04200						0.04200				
22	H8	0.04100						0.04100				
23	H9	0.03300						0.03300				

The Displacement Factor has the Form of Exp(-T) where T = 8*(pi**2)*Uiso*sin(theta/lambda)**2, for Isotropic Atoms,

T = 2*(pi**2)*(U11*(h*as)**2+U22*(k*bs)**2+U33*(l*cs)**2+2*U23*k*l*bs*cs+2*U13*h*l*as*cs+2*U12*h*k*as*bs),for Anisotr. Atoms

Ueq = 1/3 Sum(i,j) (Uij*as(i)*as(j)*a(i).a(j))

U1, U2, U3 are the three Main Axes Components of Uij

Reference U(eq): R.X. Fischer & E. Tillmanns, Acta Cryst. (1988). C44, 775-776

Appendix 3

Crystal structure parameters, bond lengths and angles, and average isotropic displacement parameters for $[Cu(CO)\{2,2N3(C_6H_5)_2\}]BPh_4$.

Crystal structure parameters

Crystal Data	
Formula	C19 H21 Cu N3 O, C24 H20 B
Formula Weight	690.15
Crystal System	Monoclinic
Space group	P21/n (No. 14)
a, b, c [Angstrom]	10.295(2) 23.869(5) 14.474(3)
alpha, beta, gamma [deg]	90 91.07(3) 90
V [Ang**3]	3556.1(13)
Z	4
D(calc) [g/cm**3]	1.289
Mu(MoKa) [/mm]	0.652
F(000)	1448
Crystal Size [mm]	0.08 x 0.09 x 0.20
Data Collection	
Temperature (K)	193
Radiation [Angstrom]	MoKa 0.71073
Theta Min-Max [Deg]	2.5, 26.7
Dataset	-12: 12 ; -26: 30 ; -18: 17
Tot., Uniq. Data, R(int)	11906, 7242, 0.047
Observed data [I > 2.0 sigma(I)]	4634
Refinement	
Nref, Npar	7242, 447
R, wR2, S	0.0562, 0.1412, 1.01
w = 1/[s^2^(Fo^2^)+(0.0493P)^2^+3.5339P]	where P=(Fo^2^+2Fc^2^)/3
Max. and Av. Shift/Error	0.77, 0.00
Min. and Max. Resd. Dens. [e/Ang^3]	-0.50, 0.34

- PLATON Reference : Spek, A.L. (1990), Acta Cryst. A46, C-34

Bond lengths and angles

Bond Lengths (Angstrom). - (Bonds are ordered on the first label, left to right and top to bottom) - esd in last digit in ().

Cu(1) - O(1)	2.9166	Cu(1) - N(1)	2.1020	Cu(1) - N(2)	2.0674	Cu(1) - N(3)	2.0780
Cu(1) - C(1)	1.7972	O(1) - C(1)	1.1206	N(1) - C(3)	1.4918	N(1) - C(4)	1.4724
N(2) - C(5)	1.4842	N(2) - C(6)	1.2686	N(3) - C(2)	1.4748	N(3) - C(13)	1.2712
C(2) - C(3)	1.5083	C(4) - C(5)	1.5060	C(6) > C(7)	1.4687	C(7) - C(8)	1.3887
C(7) - C(12)	1.3813	C(8) - C(9)	1.3768	C(9) - C(10)	1.3857	C(10) - C(11)	1.3530
C(11) - C(12)	1.3811	C(13) > C(14)	1.4607	C(14) - C(15)	1.3954	C(14) - C(19)	1.3904
C(15) - C(16)	1.3632	C(16) - C(17)	1.3825	C(17) - C(18)	1.3736	C(18) - C(19)	1.3734

N(1) - H(1)	0.9591	C(2) - H(2A)	0.9900	C(2) - H(2B)	0.9900	C(3) - H(3A)	0.9900
C(3) - H(3B)	0.9900	C(4) - H(4A)	0.9900	C(4) - H(4B)	0.9900	C(5) - H(5A)	0.9900
C(5) - H(5B)	0.9900	C(6) - H(6)	0.9500	C(8) - H(8)	0.9500	C(9) - H(9)	0.9500
C(10) - H(10)	0.9500	C(11) - H(11)	0.9500	C(12) - H(12)	0.9500	C(13) - H(13)	0.9500
C(15) - H(15)	0.9500	C(16) - H(16)	0.9500	C(17) - H(17)	0.9500	C(18) - H(18)	0.9500
C(19) - H(19)	0.9500						

Bond/Valence Angles (Degrees) - (Angles are ordered on the middle label, left to right and top to bottom) - esd in last digit in ().

O(1) - Cu(1) - N(1)	122.74	O(1) - Cu(1) - N(2)	133.25	O(1) - Cu(1) - N(3)	113.81
O(1) - Cu(1) - C(1)	1.24	N(1) - Cu(1) - N(2)	85.29	N(1) - Cu(1) - N(3)	84.17
N(1) - Cu(1) - C(1)	122.33	N(2) - Cu(1) - N(3)	104.88	N(2) - Cu(1) - C(1)	132.41
N(3) - Cu(1) - C(1)	115.02	Cu(1) - O(1) - C(1)	1.98	Cu(1) - N(1) - C(3)	107.17
Cu(1) - N(1) - C(4)	105.42	C(3) - N(1) - C(4)	112.90	Cu(1) - N(2) - C(5)	105.45
Cu(1) - N(2) - C(6)	137.76	C(5) - N(2) - C(6)	116.56	Cu(1) - N(3) - C(2)	102.17
Cu(1) - N(3) - C(13)	139.46	C(2) - N(3) - C(13)	117.85	Cu(1) - C(1) - O(1)	176.78
N(3) - C(2) - C(3)	108.47	N(1) - C(3) - C(2)	109.90	N(1) - C(4) - C(5)	110.09
N(2) - C(5) - C(4)	108.98	N(2) - C(6) - C(7)	125.49	C(6) - C(7) - C(8)	119.53
C(6) - C(7) - C(12)	122.26	C(8) - C(7) - C(12)	118.02	C(7) - C(8) - C(9)	120.97
C(8) - C(9) - C(10)	119.65	C(9) - C(10) - C(11)	119.93	C(10) - C(11) - C(12)	120.55
C(7) - C(12) - C(11)	120.84	N(3) - C(13) - C(14)	126.31	C(13) - C(14) - C(15)	119.03
C(13) - C(14) - C(19)	122.99	C(15) - C(14) - C(19)	117.97	C(14) - C(15) - C(16)	120.87
C(15) - C(16) - C(17)	120.56	C(16) - C(17) - C(18)	119.30	C(17) - C(18) - C(19)	120.52
C(14) - C(19) - C(18)	120.77				

Cu(1) - N(1) - H(1)	116.30	C(3) - N(1) - H(1)	109.74	C(4) - N(1) - H(1)	105.39
N(3) - C(2) - H(2A)	110.00	N(3) - C(2) - H(2B)	110.00	C(3) - C(2) - H(2A)	110.00
C(3) - C(2) - H(2B)	110.00	H(2A) - C(2) - H(2B)	108.37	N(1) - C(3) - H(3A)	109.68
N(1) - C(3) - H(3B)	109.68	C(2) - C(3) - H(3A)	109.68	C(2) - C(3) - H(3B)	109.68
H(3A) - C(3) - H(3B)	108.18	N(1) - C(4) - H(4A)	109.64	N(1) - C(4) - H(4B)	109.64
C(5) - C(4) - H(4A)	109.64	C(5) - C(4) - H(4B)	109.64	H(4A) - C(4) - H(4B)	108.15
N(2) - C(5) - H(5A)	109.89	N(2) - C(5) - H(5B)	109.89	C(4) - C(5) - H(5A)	109.89
C(4) - C(5) - H(5B)	109.89	H(5A) - C(5) - H(5B)	108.30	N(2) - C(6) - H(6)	117.26
C(7) - C(6) - H(6)	117.26	C(7) - C(8) - H(8)	119.52	C(9) - C(8) - H(8)	119.52
C(8) - C(9) - H(9)	120.17	C(10) - C(9) - H(9)	120.17	C(9) - C(10) - H(10)	120.03

C(11) - C(10) - H(10)	120.03	C(10) - C(11) - H(11)	119.72	C(12) - C(11) - H(11)	119.72
C(7) - C(12) - H(12)	119.58	C(11) - C(12) - H(12)	119.58	N(3) - C(13) - H(13)	116.84
C(14) - C(13) - H(13)	116.84	C(14) - C(15) - H(15)	119.56	C(16) - C(15) - H(15)	119.56
C(15) - C(16) - H(16)	119.72	C(17) - C(16) - H(16)	119.72	C(16) - C(17) - H(17)	120.35
C(18) - C(17) - H(17)	120.35	C(17) - C(18) - H(18)	119.74	C(19) - C(18) - H(18)	119.74
C(14) - C(19) - H(19)	119.61	C(18) - C(19) - H(19)	119.61		

Average (an)isotropic displacement parameters

(An)isotropic, Equivalent and Main Axes Displacement Parameters - Unusual Values Marked with a # - [Optional Coordinate Split-up]

Residue = 1

Atom	Label	U11 or Uiso	U22	U33	U23	U13	U12	Ueq(sUeq)	U1	U2	U3	U3/U1
1	Cu1	0.03739	0.04246	0.04148	-0.00353	0.00185	0.01037	0.04043	0.0284	0.0417	0.0511	1.80
		[0.2920	0.3924	0.3578]	[0.2827	0.3900	0.3597]					
2	O1	0.05066	0.05176	0.10364	-0.00690	0.02124	0.01312	0.06844	0.0324	0.0629	0.1100	3.39
		[0.0639	0.4575	0.4084]	[0.0510	0.4579	0.3894]					
3	N1	0.03570	0.04139	0.04539	0.00566	0.00544	0.00593	0.04077	0.0318	0.0380	0.0524	1.65
		[0.3143	0.3090	0.4073]	[0.3085	0.3075	0.4022]					
4	N2	0.02905	0.03210	0.04075	-0.00389	0.00090	0.00417	0.03396	0.0257	0.0338	0.0424	1.65
		[0.3674	0.3628	0.2404]	[0.3686	0.3637	0.2344]					
5	N3	0.04204	0.04991	0.03583	-0.01099	-0.00615	0.01311	0.04268	0.0298	0.0327	0.0655	2.20
		[0.4513	0.4093	0.4439]	[0.4388	0.4060	0.4486]					
6	C1	0.03891	0.05083	0.04590	-0.00214	0.00337	0.00244	0.04518	0.0373	0.0464	0.0518	1.39
		[0.1445	0.4325	0.3807]	[0.1429	0.4300	0.3828]					
7	C2	0.06608	0.06923	0.03587	-0.00332	-0.00764	0.02165	0.05716	0.0335	0.0472	0.0908	2.71
		[0.4383	0.3678	0.5188]	[0.4176	0.3637	0.5211]					
8	C3	0.04974	0.05742	0.04255	0.01452	-0.00327	0.01210	0.04995	0.0289	0.0511	0.0699	2.42
		[0.4242	0.3109	0.4790]	[0.4115	0.3063	0.4732]					
9	C4	0.03749	0.03582	0.05461	-0.00214	0.00195	0.00848	0.04262	0.0279	0.0451	0.0548	1.97
		[0.3446	0.2756	0.3265]	[0.3440	0.2760	0.3173]					
10	C5	0.03746	0.03747	0.04485	0.00147	0.00474	0.01336	0.03988	0.0239	0.0431	0.0526	2.20
		[0.4387	0.3105	0.2634]	[0.4263	0.3083	0.2592]					
11	C6	0.03252	0.03929	0.03803	-0.00408	0.00345	-0.00004	0.03658	0.0309	0.0357	0.0431	1.39
		[0.3818	0.3818	0.1540]	[0.3838	0.3804	0.1575]					
12	C7	0.03894	0.03430	0.03438	-0.00317	-0.00501	-0.00564	0.03594	0.0263	0.0375	0.0440	1.68
		[0.3233	0.4303	0.1144]	[0.3146	0.4310	0.1163]					
13	C8	0.05991	0.06103	0.04217	0.00507	0.00485	-0.00838	0.05432	0.0389	0.0551	0.0689	1.77
		[0.3575	0.4536	0.0329]	[0.3690	0.4513	0.0326]					
14	C9	0.08896	0.06197	0.05876	0.02623	-0.00582	-0.01998	0.06998	0.0325	0.0693	0.1082	3.33
		[0.3147	0.4955	-0.0126]	[0.2891	0.4991	-0.0055]					
15	C10	0.07892	0.03805	0.07380	0.01335	-0.02071	-0.00410	0.06386	0.0334	0.0568	0.1014	3.04
		[0.2028	0.5194	0.0250]	[0.1813	0.5205	0.0354]					
16	C11	0.06328	0.03723	0.06398	-0.00045	-0.00712	0.00875	0.05493	0.0344	0.0570	0.0733	2.13
		[0.1534	0.4988	0.1066]	[0.1397	0.4981	0.1130]					
17	C12	0.05069	0.04045	0.04020	0.00174	-0.00303	0.00739	0.04383	0.0346	0.0418	0.0551	1.59
		[0.2138	0.4545	0.1524]	[0.2047	0.4537	0.1533]					
18	C13	0.04340	0.05444	0.04711	-0.02412	-0.01152	0.01816	0.04847	0.0255	0.0332	0.0867	3.40
		[0.5571	0.4392	0.4425]	[0.5398	0.4343	0.4536]					
19	C14	0.03828	0.04216	0.05767	-0.02301	-0.00518	0.00720	0.04611	0.0251	0.0367	0.0766	3.05
		[0.5811	0.4774	0.3877]	[0.5888	0.4811	0.3737]					
20	C15	0.04011	0.06739	0.07826	-0.03142	-0.00845	0.00510	0.06204	0.0374	0.0421	0.1066	2.85
		[0.7077	0.4987	0.3922]	[0.7137	0.5035	0.3762]					
21	C16	0.04802	0.06675	0.10647	-0.03175	0.01366	-0.01594	0.07359	0.0383	0.0545	0.1280	3.34

		[0.7548	0.5382	0.3318]	[0.7435	0.5424	0.3120]					
22	C17	0.06142	0.05281	0.08856	-0.01398	0.01446	-0.00315	0.06743	0.0478	0.0565	0.0980	2.05
		[0.6691	0.5581	0.2588]	[0.6601	0.5595	0.2476]					
23	C18	0.05014	0.05337	0.07504	-0.00323	-0.00017	-0.00504	0.05953	0.0462	0.0569	0.0755	1.64
		[0.5404	0.5376	0.2529]	[0.5404	0.5380	0.2447]					
24	C19	0.03641	0.05175	0.06408	-0.01194	-0.00187	0.00241	0.05078	0.0360	0.0445	0.0718	1.99
		[0.4997	0.4973	0.3164]	[0.5017	0.4995	0.3064]					
25	H1	0.04360						0.04360				
26	H2A	0.06860						0.06860				
27	H2B	0.06860						0.06860				
28	H3A	0.05994						0.05994				
29	H3B	0.05994						0.05994				
30	H4A	0.05115						0.05115				
31	H4B	0.05115						0.05115				
32	H5A	0.04785						0.04785				
33	H5B	0.04785						0.04785				
34	H6	0.04389						0.04389				
35	H8	0.06518						0.06518				
36	H9	0.08398						0.08398				
37	H10	0.07664						0.07664				
38	H11	0.06592						0.06592				
39	H12	0.05259						0.05259				
40	H13	0.05816						0.05816				
41	H15	0.07444						0.07444				
42	H16	0.08831						0.08831				
43	H17	0.08092						0.08092				
44	H18	0.07144						0.07144				
45	H19	0.06094						0.06094				

Residue = 2

Atom	Label	U11 or Uiso	U22	U33	U23	U13	U12	Ueq(sUeq)	U1	U2	U3	U3/U1
1	C20	0.02255	0.02747	0.02781	0.00170	-0.00009	-0.00355	0.02595	0.0207	0.0266	0.0305	1.48
		[0.8776	0.3090	0.3457]	[0.8811	0.3077	0.3431]					
2	C21	0.03058	0.04004	0.03129	0.00740	0.00599	0.00475	0.03390	0.0251	0.0296	0.0470	1.87
		[0.9854	0.3018	0.2859]	[0.9783	0.2992	0.2813]					
3	C22	0.04047	0.05027	0.03546	0.00330	0.01210	-0.00310	0.04192	0.0253	0.0493	0.0512	2.03
		[0.9963	0.3377	0.2075]	[1.0033	0.3329	0.2073]					
4	C23	0.04637	0.04033	0.02557	0.01074	-0.00521	-0.00918	0.03749	0.0199	0.0353	0.0572	2.88
		[0.9246	0.3774	0.1874]	[0.9077	0.3802	0.1915]					
5	C24	0.04700	0.03174	0.03766	0.00481	-0.00515	0.00173	0.03887	0.0280	0.0386	0.0500	1.79
		[0.8180	0.3873	0.2455]	[0.8078	0.3874	0.2481]					
6	C25	0.03239	0.03290	0.03355	0.00224	0.00422	0.00173	0.03290	0.0292	0.0314	0.0381	1.30
		[0.7982	0.3530	0.3232]	[0.7947	0.3525	0.3212]					
7	C26	0.02587	0.02715	0.02964	0.00310	0.00610	0.00601	0.02748	0.0198	0.0254	0.0373	1.89
		[0.7426	0.2223	0.4064]	[0.7348	0.2210	0.4022]					
8	C27	0.03376	0.02875	0.03119	0.00415	0.00341	0.00548	0.03120	0.0245	0.0294	0.0397	1.62

		[0.6873	0.2186	0.3166]	[0.6801	0.2176	0.3141]					
9	C28	0.04335	0.03122	0.03779	-0.00202	-0.00753	0.00184	0.03755	0.0306	0.0322	0.0499	1.63
		[0.5978	0.1771	0.2887]	[0.5895	0.1769	0.2917]					
10	C29	0.03655	0.02660	0.05487	-0.00007	-0.00313	-0.00293	0.03939	0.0258	0.0366	0.0558	2.17
		[0.5527	0.1381	0.3580]	[0.5564	0.1380	0.3479]					
11	C30	0.04045	0.03546	0.04670	0.01271	0.00589	-0.00382	0.04081	0.0247	0.0424	0.0553	2.23
		[0.6092	0.1406	0.4463]	[0.6053	0.1384	0.4365]					
12	C31	0.03456	0.03729	0.03194	0.00788	0.00117	-0.00171	0.03459	0.0260	0.0347	0.0431	1.66
		[0.6963	0.1814	0.4673]	[0.6983	0.1789	0.4626]					
13	C32	0.02935	0.03392	0.02790	0.00450	0.00113	0.00705	0.03038	0.0231	0.0278	0.0403	1.75
		[0.8180	0.3091	0.5228]	[0.8104	0.3070	0.5205]					
14	C33	0.03666	0.04316	0.03136	0.00427	0.00274	0.00813	0.03703	0.0299	0.0314	0.0498	1.67
		[0.7273	0.2966	0.5906]	[0.7194	0.2944	0.5887]					
15	C34	0.04739	0.06387	0.02953	0.00120	0.00741	0.01796	0.04684	0.0263	0.0385	0.0758	2.88
		[0.7119	0.3333	0.6661]	[0.6936	0.3281	0.6644]					
16	C35	0.05921	0.04720	0.03379	-0.00997	-0.00614	0.01872	0.04682	0.0279	0.0363	0.0763	2.73
		[0.7817	0.3809	0.6747]	[0.7622	0.3781	0.6780]					
17	C36	0.05736	0.03669	0.04470	-0.00508	-0.00956	0.00546	0.04638	0.0342	0.0396	0.0654	1.91
		[0.8688	0.3936	0.6094]	[0.8563	0.3929	0.6131]					
18	C37	0.04104	0.03959	0.03564	0.00050	0.00302	0.00048	0.03873	0.0347	0.0394	0.0420	1.21
		[0.8837	0.3582	0.5373]	[0.8802	0.3580	0.5367]					
19	C38	0.02611	0.03037	0.02344	0.00769	0.00601	-0.00004	0.02657	0.0160	0.0274	0.0362	2.26
		[0.9869	0.2330	0.4642]	[0.9805	0.2302	0.4583]					
20	C39	0.03204	0.03702	0.02637	0.00259	0.00376	0.00286	0.03177	0.0247	0.0312	0.0394	1.59
		[1.0691	0.2452	0.5368]	[1.0632	0.2432	0.5350]					
21	C40	0.03641	0.05189	0.02881	0.00311	-0.00224	0.00560	0.03907	0.0270	0.0364	0.0539	2.00
		[1.1820	0.2154	0.5576]	[1.1744	0.2108	0.5565]					
22	C41	0.03649	0.05091	0.04685	0.00884	-0.00149	0.01769	0.04478	0.0228	0.0467	0.0648	2.85
		[1.2204	0.1715	0.5043]	[1.2052	0.1668	0.4989]					
23	C42	0.04304	0.04100	0.04112	-0.00224	0.00058	0.01463	0.04172	0.0271	0.0411	0.0569	2.10
		[1.1401	0.1561	0.4263]	[1.1269	0.1538	0.4272]					
24	C43	0.03948	0.03441	0.03331	0.00316	-0.00093	0.00462	0.03575	0.0289	0.0361	0.0422	1.46
		[1.0247	0.1857	0.4088]	[1.0181	0.1850	0.4087]					
25	B1	0.02626	0.02498	0.02839	0.00158	0.00342	0.00138	0.02651	0.0240	0.0244	0.0311	1.29
		[0.8535	0.2677	0.4344]	[0.8506	0.2674	0.4324]					
26	H21	0.04068						0.04068				
27	H22	0.05031						0.05031				
28	H23	0.04499						0.04499				
29	H24	0.04665						0.04665				
30	H25	0.03948						0.03948				
31	H27	0.03744						0.03744				
32	H28	0.04507						0.04507				
33	H29	0.04727						0.04727				
34	H30	0.04897						0.04897				
35	H31	0.04151						0.04151				
36	H33	0.04444						0.04444				
37	H34	0.05621						0.05621				

38	H35	0.05618	0.05618
39	H36	0.05565	0.05565
40	H37	0.04647	0.04647
41	H39	0.03812	0.03812
42	H40	0.04688	0.04688
43	H41	0.05373	0.05373
44	H42	0.05007	0.05007
45	H43	0.04290	0.04290

The Displacement Factor has the Form of Exp(-T) where T = 8*(pi**2)*Uiso*sin(theta/lambda)**2, for Isotropic Atoms,

T = 2*(pi**2)*(U11*(h*as)**2+U22*(k*bs)**2+U33*(l*cs)**2+2*U23*k*l*bs*cs+2*U13*h*l*as*cs+2*U12*h*k*as*bs),for Anisotr. Atoms

Ueq = 1/3 Sum(i,j) (Uij*as(i)*as(j)*a(i).a(j))

U1, U2, U3 are the three Main Axes Components of Uij

Reference U(eq): R.X. Fischer & E. Tillmanns, Acta Cryst. (1988). C44, 775-776

Index of figures

Index of tables